NORTHWESTERN UNIVERSITY

Control of Hierarchical Order and Development of Stimuli-Responsive
Self-Assembled Materials Across Multiple Length Scales

A DISSERTATION

SUBMITTED TO THE GRADUATE SCHOOL
IN PARTIAL FULFILLMENT OF THE REQUIREMENTS

for the degree

DOCTOR OF PHILOSOPHY

Field of Chemistry

By

Stacey Chin

EVANSTON, ILLINOIS

March 2019

Abstract

Control of Hierarchical Order and Development of Stimuli-Responsive Self-Assembled Materials Across Multiple Length Scales

Stacey Chin

One of the grand challenges in materials chemistry and nanochemistry is the development of functional materials through ordered, hierarchical structures using synthetic building blocks. Nature has done this through evolution of molecular components such as nucleic acids, saccharides, lipids, amino acids, and inorganic crystals. The precise spatial positioning of these components gives rise to highly complex functions, such as the movement of muscles or the growth of tissues. In the context of these biological systems, this work developed novel stimuli-responsive materials based on interactions and hierarchical ordering of low molecular weight molecules known as peptide amphiphiles (PAs). The first system of supramolecular-covalent hybrid polymers was created by synthetically modifying a peptide amphiphile capable of self-assembling into supramolecular filaments with an initiator for atom-transfer radical polymerization. This enabled the growth of thermo-responsive oligo(ethylene glycol) methacrylate (OEGMA) polymers covalently attached to the nanofiber surface. Arrangement of these nanofibers in an aligned tubular scaffold resulted in macroscopic anisotropic actuation of the hybrid material, with a stronger response perpendicular to the direction of alignment. This behavior emulates the anisotropic actuation observed in biological muscle tissue, which is driven chemically. Computational and experimental results indicated that the anisotropy was due to its hierarchical structuring, in part from the tethered nature of the thermo-responsive molecular structures to the supramolecular filaments as well as due to the structural reinforcement of the microstructure. From this work, explorations of how to further control the macroscopic domains of alignment were carried out using a direct ink-writing approach to apply shear. 3D printing was used to order the supramolecular assemblies into various patterns of align-

ment within the hybrid structure. With printed patterns of alignment, structures were able to display curling instead of shrinking behavior, attributed to differences in drag force and therefore alignment between layers of printed material. In order to create more uniformly patterned alignment, cellulose nanocrystals were then incorporated into the PA printing solution, which significantly improved the rheological properties of the ink such that large free-standing structures could be printed without the addition of cross-linking calcium ions. In order to create similar printed structures but without the need for rheological additives, an all-PA ink system was developed containing β-cyclodextrin and adamantane moieties for supramolecular host-guest cross-linking. These all-PA materials were also printable and maintain their structure without the addition of ionic cross-linkers or other rheological additives, which could be important for biological applications of these materials. Finally, the formation of hierarchical peptide amphiphile structures was investigated on a microscopic level by using annealing processes in confined environments. The reversible formation of micron-sized, highly ordered liquid crystalline superstructures was observed upon heating, consisting of thousands of bundled PA nanofibers packed in a hexagonal lattice. It is suggested that the inter-fiber spacing decreases significantly at elevated temperatures due to increased ion condensation and the entropic release of water bound to the PA surface. This effect is analogous to the lower critical solution temperature behavior observed in thermo-responsive polymers such as OEGMA, but has not been previously observed within supramolecular assemblies. Taken together, these findings demonstrate the versatility of PA molecules towards controlling the formation of hierarchically ordered materials and their applications in the development of stimuli-responsive functional materials.

Acknowledgements

It takes a village, and I am grateful for mine. You all have helped make me who I am today.

- **Professor Stupp**, thank you for giving me the opportunity to work in the lab. I have learned more than I could ever imagine in my time here, and I am grateful for the support that you have given me to grow as a scientist.

- **Professors Milan Mrksich, SonBinh Nguyen, and Fraser Stoddart** — thank you for serving on my committee and providing feedback and asking the tough questions about my research.

- **Liam Palmer** — for being the fountain of knowledge that keeps our group afloat. Your feedback and suggestions were always incredibly helpful.

- **Professor! Martin Conda-Sheridan** — for being my first mentor in the lab, and teaching me everything I know about synthesizing molecules, running columns, and Argentinian footballers (still not much).

- **Christopher Synatschke** — my partner in fancy food adventures! (and also sometimes science). Without you, PA-polymer hybrids, this thesis, and many many food comas never would have happened, so I am eternally grateful.

- **Hiroaki Sai** — for being an excellent all-night Argonne buddy, for being willing to drop everything and help out at any hour, and for always pushing to make our science bigger and better (even if it means talking research during happy hour.)

- **Nick Sather & Kristen Wek** — team 3D printing! Thank you for helping me out with my crazy ideas (especially when they don't work or do something completely weird).

LIST OF ABBREVIATIONS

AFM Atomic Force Microscopy

ATRP Atom-Transfer Radical Polymerization

BDNF Brain-Derived Neurotrophic Factor

BiB Bromoisobutyryl Bromide

Bpy 2,2'-Bipyridine

CaCl$_2$ Calcium Chloride

CAD Computer-Aided Design

CDCl$_3$ Deuterated Chloroform

CLSM Confocal Laser-Scanning Microscopy

CNC Cellulose Nanocrystal

CPP Critical Packing Parameter

cryo-TEM Cryogenic Transmission Electron Microscopy

CsCl Cesium Chloride

CsOH Cesium Hydroxide

CuBr Copper (I) Bromide

DCM Dichloromethane

DEGMA Diethyleneglycol Methyl Ether Methacrylate

DIEA *N,N*-Diisopropylethyl Amine

DIW Direct Ink Writing

DLS Dynamic Light Scattering

DMAEMA Dimethylaminoethyl Methacrylate

DMF Dimethylformamide

DMSO Dimethyl Sulfoxide

DNA Deoxyribonucleic Acid

DSC Differential Scanning Calorimetry

DSS 4,4-Dimethyl-4-Silapentane-1-Sulfonic Acid

EDC 1-Ethyl-3-(3-dimethylaminopropyl)carbodiimide

ESI Electrospray Ionization

FEA Finite Element Analysis

FGF-2 Fibroblast Growth Factor 2

FITC Fluorescein Isothiocyanate

Fmoc 9-Fluorenylmethyloxycarbonyl

GPC Gel Permeation Chromotography

HBTU 2-(1H-Benzotriazol-1-yl)-1,1,3,3-tetramethyluronium Hexafluorophosphate

HFIP Hexafluoisopropanol

HPLC High-Performance Liquid Chromatography

LC Liquid Crystal

LC-MS Liquid Chromatography-Mass Spectrometry

LCST Lower Critical Solution Temperature

MAXS Medium-Angle X-Ray Scattering

MCM-41 Mobil Composition of Matter No. 41

MD Molecular Dynamics

MeOH Methanol

MIM Molecularly Interlocked Machines

Mn Number-averaged Molecular Weight

Mtt 4-Methyltrityl

NaCl Sodium Chloride

NaOH Sodium Hydroxide

NaPS Sodium Persulfate

NBAA *N,N'*-Methylenebisacrylamide

NH$_4$OH Ammonium Hydroxide

NIPAM N-isopropylacrylamide

NMR Nuclear Magnetic Resonance

OEGMA$_{500}$ Oligo(Ethylene Glycol) Methyl Ether Methacrylate, Mn 500

PA Peptide Amphiphile

PDI Polydispersity Index

PEG Polyethylene Glycol

PEGMA Polyethylene Glycol Methacrylate

POM Polarized Optical Microscopy

PS Poly(Styrene)

PVP Poly(2-Vinylpyridine)

PyBOP Benzotriazol-1-yl-oxytripyrrolidinophosphonium Hexafluorophosphate

RDF Radial Distribution Function

RT Room Temperature

SAM Self-Assembled Monolayer

SAXS Small-Angle X-Ray Scattering

SEM Scanning Electron Microscopy

TAMRA Carboxytetramethylrhodamine

TEM Transmission Electron Microscopy

TEMPO (2,2,6,6-Tetramethylpiperidin-1-yl)oxyl

TFA Trifluoroacetic Acid

THF Tetrahydrofuran

TIPS Triisopropyl Silane

TREN Tris(2-aminoethyl)amine

Tris Tris(hydroxymethyl)aminomethane

USAXS Ultrasmall-Angle X-Ray Scattering

UV Ultraviolet

VT Variable Temperature

WAXS Wide-Angle X-Ray Scattering

To my family and to Alex,

for their love and support that got me through grad school.

CONTENTS

List of Tables

List of Figures

1 Introduction

1.1 BIOLOGICAL INSPIRATION FOR FUNCTIONAL HIERARCHICAL MATERIALS

Evolved over millennia, nature has developed a rich complexity of structures with diversity of functions. These structures have served as inspiration for scientists throughout the course of history, as researchers have tried to replicate these complex functions, such as the mechanical strength of trees,[1] the structural integrity of bones,[2,3] or the work-performing behavior of muscles,[4,5] using synthetic materials.[6] These complex functions are integrally tied to the way these materials are structured — through the hierarchical ordering of small, molecular building blocks. In contrast to traditional top-down materials fabrication where bulk materials are miniaturized to the micro or nano scale through processing,[7] these natural building blocks are arranged from the bottom up, from simple nanostructures into increasingly complex structures that influence the macroscopic functions of the materials (Fig. 1.1).

The hierarchal structure of plant cell walls contributes to the enormous mechanical strength of wood materials (Fig. 1.2). The cell wall not only protects and shapes the cell body inside, and
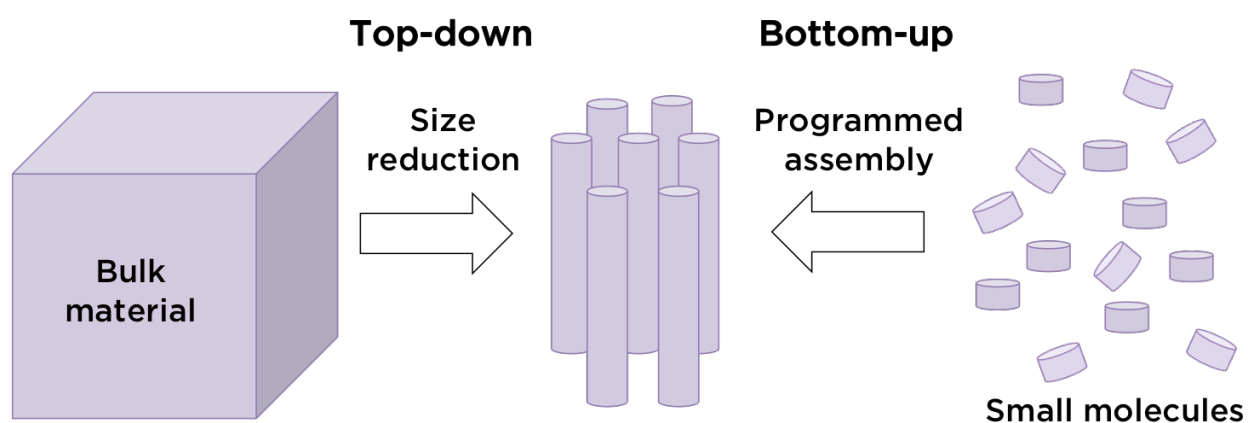
Figure 1.1: Top-down assembly (left) takes bulk materials and reduces their size through processing techniques to reach the desired length scale. Bottom-up assembly (right) takes atoms or molecular building blocks, and arranges them in a precise manner to create the desire material and features.
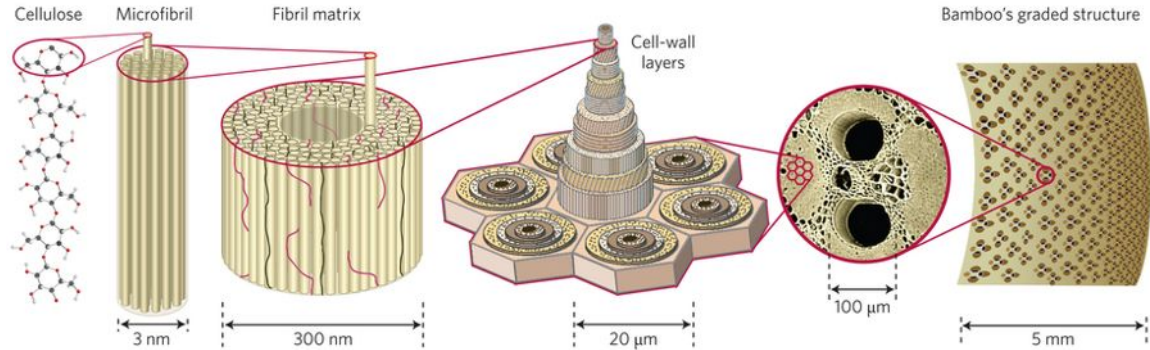
Figure 1.2: In bamboo and other wood materials, hydrogen bonding within cellulose chains forms fibrillar structures. These fibrils arrange into hollow honeycomb-like structures, surrounded by a matrix of lignin and hemicellulose, which gives bamboo its characteristic tensile strength. Reproduced from Wegst *et al.*[6]

also provides an ordered scaffold for further macroscopic structures.[1,8] The cell walls composed of aligned cellulose fibrils, which provides reinforcement for the matrix of lignin and hemicellulose that surrounds them. Cellulose is a straight-chain polysaccharide made of repeating glucose units. Each repeat unit is only ∼1 nm long, but due to the formation of hydrogen bonds, can form larger hexagonal or rectangular or fibrillar structures that further bundle into macrofibrils (∼10-25 nm in diameter). These macrofibrils have ∼20 nm-long regions of crystalline cellulose, with ordered hydrogen bonding between amorphous regions with disordered hydrogen bonds. The further higher-order arrangement of these cellulose macrofibrils into honeycomb-like structures gives the cell walls and overall wood structure their characteristic macroscopic mechanical strength.

Another material that exhibits excellent mechanical properties due to its structural hierarchy is the compact bone in the human skeleton (Fig. 1.3). Compact bone is made of a combination of cells embedded in an organized matrix of organic collagen and inorganic hydroxyapatite ($Ca_{10}(PO_4)_6(OH)_2$)) nanocrystals.[6,9] Collagen is composed of polypeptide chains that fold into tropocollagen triple helices (∼300 nm long, ∼1.5 nm in diameter) due to glycine residues every third amino acid. These collagen fibrils form a scaffold for the growth of 50 nm x 25 nm x 3 nm hydroxyapatite nanocrystals uniformly along their length. These mineralized collagen fibrils then form a bundled superstructure of fibers, which are further organized into lamellar concentric

arrays of ~100 nm-diameter hollow cylinders called osteons. These osteons surround the nerves and blood vessels within the bone, protecting them from damage and providing structural integrity to support the rest of the body.

Skeletal muscles are another example of a material whose function, the development of motion and ability to perform mechanical work, is dependent on its structural hierarchy (Fig. 1.4).[11] The overall contraction of muscles that leads to their work-performing ability is fundamentally due to the nanoscale motion of two proteins: actin and myosin.[12–14] Actin, a small protein of 42 kDa, assembles with other actin subunits into filamentous structures that provide a 'track' for the movement of myosin protein heads to slide across, generating force in what is known as a power stroke. However, a single actin-myosin power stroke only generates a force of ~2-5 pN across a distance of 5 nm;[15] in order to transduce this energy to a larger lengthscale, motion must be a concerted effort of thousands of actin and myosin proteins working together and moving in tandem. Each subunit of actin and myosin proteins, which are held together by proteins called titin, are structured in a fibrous subunit called a sarcomere, which are roughly 2 μm in length.[16] These sarcomeres bundle together into myofibrils, which further bundle into muscle fibers that create the entire skeletal muscle. This arrangement is extensive, with hundreds of thousands of sarcomeres running along the length of a typical muscle. This hierarchical ordering allows the 2 pN forces of single actomyosin contractions to create many Newtons worth of macroscopic, work-performing force.

While nature so elegantly organizes its available building blocks into hierarchical structure, programming and predicting the interactions and assemblies that new molecules will form has proven to be quite difficult for synthetic chemists. Therefore, researchers often try and mimic the structures and interactions that are found in natural systems within a new synthetic design. One such design element are the anisotropic fibrous structures that appear repeatedly in structural hierarchy, which can often branch length scales and promote directional functional properties within the material. Replicating these types of assemblies and controlling structural order can be done using biologically
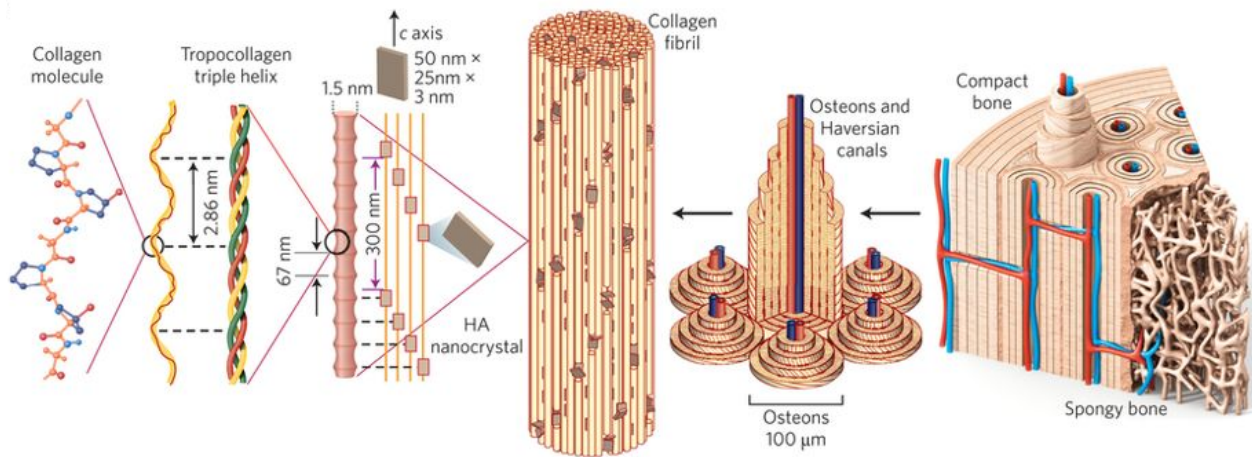
Figure 1.3: In compact bone, tropocollagen triple helices are formed due to hydrogen bonding from repeated glycine residues. These helices bundle into collagen fibrils, which allow for the mineralization of hydroxyapatite crystals along their length. The mineralized fibrils are then arranged into concentric arrays of hollow cylinders, called osteons, which surround nerves and blood vessels while providing mechanical strength. Reproduced from Wegst *et al.*[6]
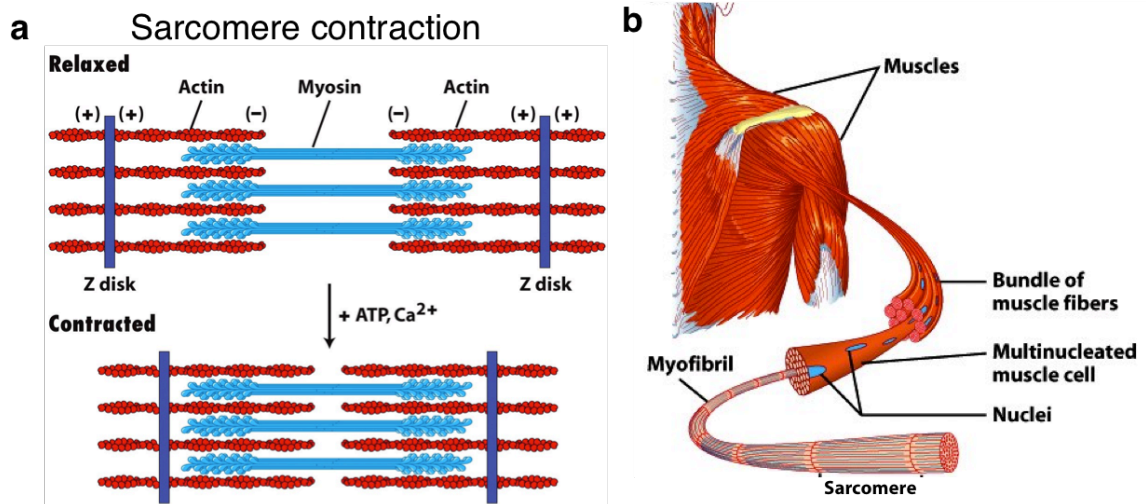
Figure 1.4: (a) In skeletal muscle, actin and myosin proteins make up the contractile unit, called a sarcomere, with a titin protein scaffold. (b) Sarcomeres bundle together into myofibrils, which further bundle into muscle fibers that create the macroscopic skeletal muscle. Modified from Lodish *et al.*[10]

derived building blocks, such as polypeptides or polysaccharides, but can also be developed using *de novo* chemical compounds and interactions not typically found in nature.

1.2 ARTIFICIAL ACTUATORS & STIMULI-RESPONSIVE POLYMERS

One active field of research that relies on hierarchical structure is the field of artificial actuators. Inspired by the structure of skeletal muscles, described above, scientists strive to make mechanically robust synthetic materials that have the ability to transduce stimuli such as light, temperature, or chemical energy into mechanical energy such as movement or lifting another object. In these systems, structural anisotropy is essential to creating directionality of this motion, which allows the energy to be more efficiently directed into a work-performing task. Artificial actuators are of great interest in the field of soft robotics, due to their flexibility and adaptability to different process, as well as their increased safety as compared to their traditional metal robotics counterparts.

On the nanoscale, artificial actuators and the actuating motion has been explored through the bottom-up design of synthetic molecules, such as the molecular motors pioneered by the lab of Fraser Stoddart.[18,19] Mechanically interlocked molecules (MIMs) consist of two or more synthetic components that cannot be separated (due to steric repulsions) without breaking a covalent
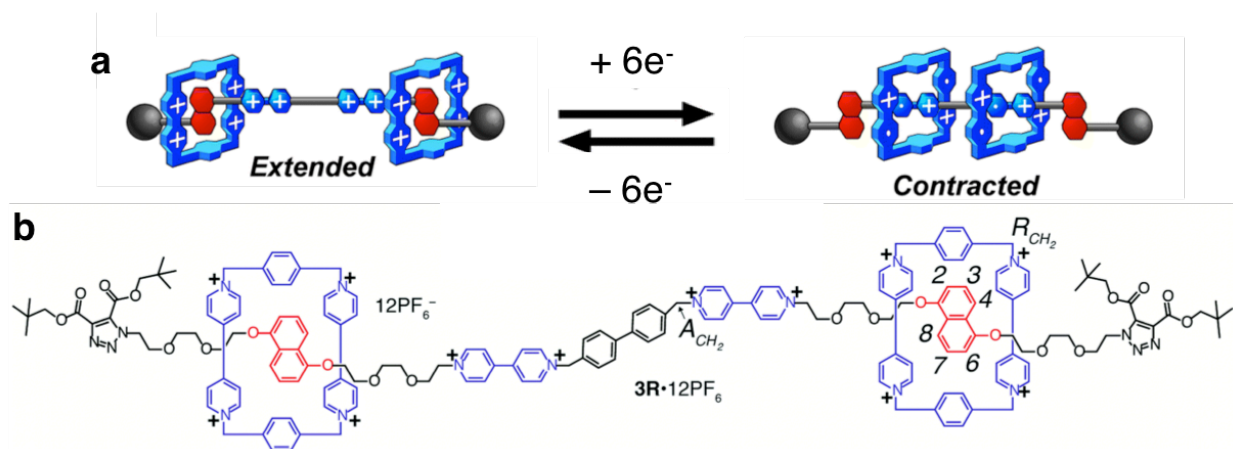
Figure 1.5: (a) Actuation schematic of a muscle-inspired rotaxane system. (b) Chemical structure of rotaxane molecule. Modified from Witus *et al.*[17]

bond, and are thus extremely stable as well as able to be chemically well-characterized. Rotaxane molecules, a type of MIM, can include recognition sites that serve as extended and contracted states for translational molecular motion. Rotaxanes often actuate through electrochemical means, relying on a change in redox state and therefore charge and dipolar interactions between two portions of the molecule (Fig. 1.5a).[17] However, these molecules are often synthetically very challenging to make (Fig. 1.5b), and therefore the potential to scale up these molecules into a functional, macroscopic material is limited.

Due to their ease of scalability and simple chemistries, macromolecular polymer systems have been widely explored in the artificial actuator literature, particularly within the field of stimuli-responsive hydrogels.[20–22] Hydrogels are covalently crosslinked polymer networks that are highly swollen in water, often containing over 90% water by mass. Polymer hydrogels make attractive materials candidates due to their ease of synthesis, scalability, and especially their ability to undergo reversible volumetric changes that can be multiple times the initial material volume. Due to extensive monomer development over the past century, there are also a large number of chemistries and functionalities that are available for use within stimuli-responsive materials. Typical stimuli include temperature,[23] light,[24,25] electric field,[26,27] and pH,[28] with the most common system being thermoresponsive polymers such as poly(NIPAM) or poly(DMAEMA).[29]

Typically, these thermoresponsive polymers undergo reversible volumetric contraction in water through a property known as a lower critical solution temperature, or LCST. Polymers with LCST behavior undergo a transition from a hydrophilic state to a hydrophobic state above a specific transition temperature causing collapse and precipitation from solution.[31–34] On the molecular level, below the LCST these polymer chains form hydrogen bonds with water, solvating the polymer chains in solution (Fig. 1.6). As the temperature is increased, however, entropic effects dominate, and it becomes thermodynamically more favorable for the water molecules that were previously interacting with the polymer chains to interact and hydrogen bond with water molecules in solution. The polymer chains, no longer solvated, collapse into a random globule conformation, effectively pre-

cipitating from solution. In a dispersed polymer solution, this results in turbidity within the sample and eventual settling of the polymer aggregates. If the polymers are crosslinked within a hydrogel network, this results in shrinkage of the bulk hydrogel and expulsion of water, or syneresis, from the network structure. This transition is fully reversible, and upon cooling the hydrogen bonds will reform, causing resolution and re-swelling of the polymer chains. This hydrophilic to hydrophobic transition is common among many other stimuli-responsive polymers as well,[25,35] although the thermodynamic driving forces may be different in other chemistries.

However, structural anisotropy is difficult to create in a polymeric hydrogel due to the random entangled network formed upon polymerization. This typically results in only isotropic contraction, where the polymer network shrinks the same amount in each direction. In these cases, a global stimulus cannot be applied throughout the material to induce directional or anisotropic motion. By applying externally biased stimuli, such as temperature gradients, peristaltic or earthworm-type motion can be demonstrated.[36,37] In light-responsive systems, shining light on specific parts of the structure can also induce directional motion.[38] Such examples rely on complexity within the spatiotemporal application of the respective stimulus, while the material itself remains relatively simple.
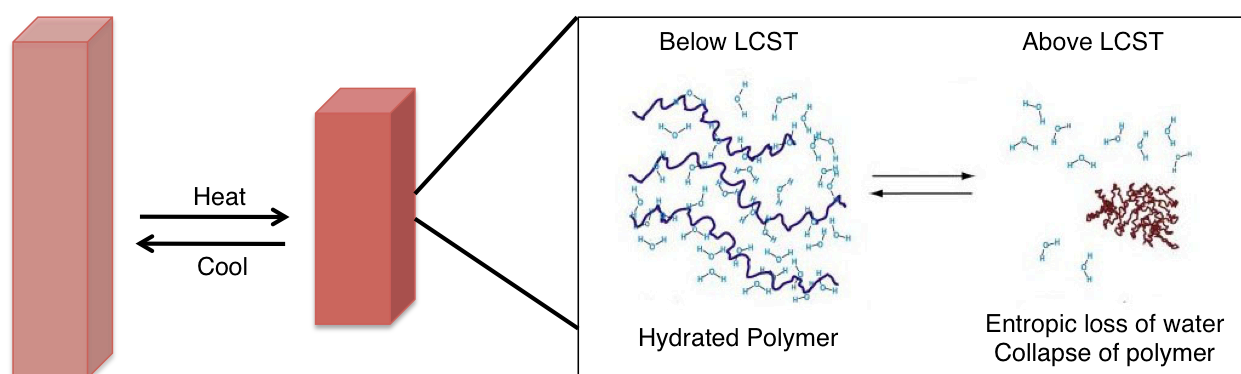
Figure 1.6: Below the LCST, polymer chains are hydrated by water hydrogen bonds and hydrogels are swollen. Above transition temperature, entropic effects dominate, with water molecules no longer solubilizing the polymer chain. The polymer chain collapses, leading to contraction of the hydrogel. Modified from Pennadam *et al.*[30]
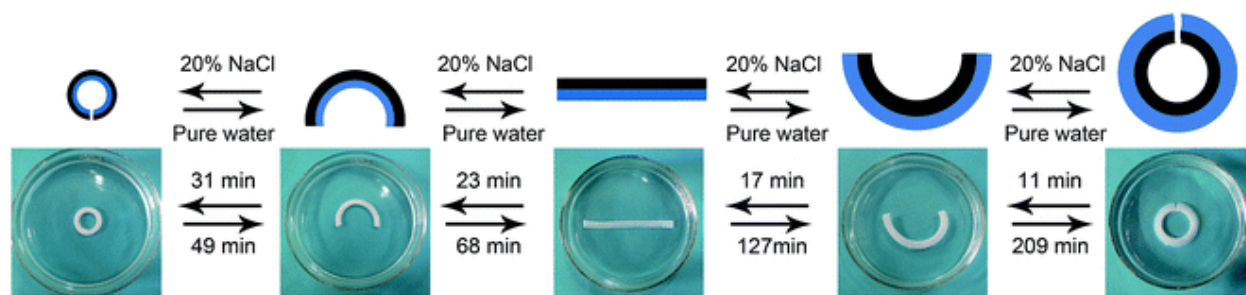
Figure 1.7: Schematic representation of bidirectional bending and shape switching behaviors of hydrogel bilayer. Reproduced from Xu *et al.*[39]

A logical evolution of artificial actuator systems is to increase complexity in the material by introducing additional components to reinforce the material, add directionality, or other desirable functions. Bilayers of nonresponsive-responsive materials, for example, can show curling behavior due to mismatches in the mechanical properties as one material contracts (Fig. 1.7).[39,40] This curling behavior can lead to anisotropy, depending on the configuration within the sample geometry.[41] In another example from the Aida lab, incorporation of titania nanosheets in a thermoresponsive hydrogel led to composite materials with strong and rapid anisotropic actuation in response to changes in temperature.[42] To induce the anisotropic orientation and therefore actuation, a strong magnetic field was used to orient the nanosheets within the polymer matrix. LCST-behavior of the polymer at increased temperature causes an increase in permittivity, causing electrostatic repulsion between nanosheets.

These examples demonstrate the need for increased complexity in order to develop anisotropic actuation. The inclusion of directional information within the material is critical for achieving anisotropy. The short persistence length of most traditional covalent polymers prevents the stable orientation of individual chains and therefore long-range order without the application of intense forces such as high shear, which is not feasible for a number of systems and detracts from the scalability of such materials. As such, non-covalent systems, such as supramolecular assembled structures, have become of interest due to their ability to easily form high-aspect ratio anisotropic assemblies.

1.3 SUPRAMOLECULAR ASSEMBLY

1.3.1 *Driving forces for supramolecular assembly*
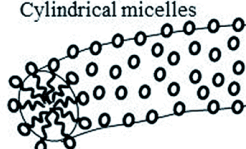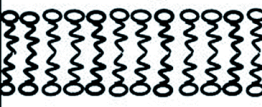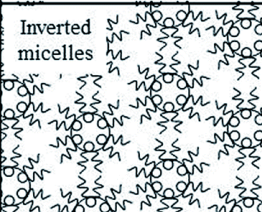
The term supramolecular chemistry was coined by Jean-Marie Lehn in 1978 to describe "chemistry beyond the molecule," or chemical interactions that occur outside of a covalent bond.[43] As a field that has burgeoned over the last thirty years,[44] supramolecular focuses on the breadth of noncovalent interactions that can occur between different molecules, such as Van der Waals forces, π-π stacking, hydrogen bonding, and electrostatic interactions. These noncovalent interactions, while weaker in strength than a typical covalent bond, play an integral role in the arrangement and bottom-up building of hierarchical structures from molecular building blocks. The dynamic nature of these noncovalent interactions due to the fine balance of attractive forces (such as π-π stacking) and repulsive forces (such as electrostatic repulsion of like-charged species), can also allow for the reconfiguration of assemblies with small changes in the environment. These rearrangements can result in distinct phases or assembly states depending on the energy landscape of the molecules, leading to a rich variety of supramolecular assemblies that can arise from a single molecular structure.[45,46] The extreme promise of supramolecular chemistry was rewarded in 1987, when the scientists Donald Cram, Jean-Marie Lehn, and Charles Pederson were awarded the Nobel Prize in chemistry for their development of the field.[47] Supramolecular chemistry was acknowledged again in 2016, when Fraser Stoddart, Jean-Pierre Sauvage, and Ben Feringa were awarded the Nobel Prize in for molecular machines, which rely heavily on the advances in knowledge about intermolecular interactions.[48]

Some of the most highly studied supramolecular systems are amphiphilic surfactant molecules that contain both hydrophilic and hydrophobic moieties; however, predicting the final assembled state of surfactant-like molecules can be challenging. In 1976, Jacob Israelachvili proposed a theory describing a 'critical packing parameter' (CPP), which generally describes rules for how simple

surfactants can pack based on geometric constraints due to the balance of attractive and repulsive forces present (Fig. 1.8).[49] The CPP is defined as follows:

$$CPP = \frac{V}{a_o l_c} \tag{1}$$

Where V is the volume of the surfactant molecule, a_o is the surface area of the headgroup, and l_c is the critical length of the hydrophobic chain.

Critical Packing Parameter $(v/a_0 l_c)$	Critical Packing Shape	Structures Formed
< 1/3	Cone	Spherical micelles
1/3 – 1/2	Truncated cone	Cylindrical micelles
1/2 -1	Truncated cone	Flexible bilayers, vesicles
~1	Cylinder	Planar bilayers
>1	Inverted truncated cone or wedge	Inverted micelles

Figure 1.8: Critical packing shape and structures formed for varying critical packing parameter values of a simple amphiphile molecule. Modified from Salim *et al.*[50]

Generally, as the CPP increases, the assembly becomes more dominated by the hydrophobic alkyl chains, resulting in less overall surface curvature as the effective size of the headgroup decreases. While the CPP is a useful starting point for predicting behavior and has been used extensively to describe traditional surfactant assembly, it does not account for specific intermolecular interactions between molecules such as hydrogen bonding or electrostatics. As chemists design molecules with increasing complexity that go far past simple surfactants, the Israelachvilli packing principles may not encompass the multitude of interactions that contribute to the overall assembly of these complex molecules.

1.3.2 *Peptide-based supramolecular materials*

One type of these more complex self-assembling molecules are peptide-based materials. Nature has evolved to assemble peptides into complex protein structures with high fidelity using the interplay of hydrophobic and hydrogen-bonding intra- and inter-molecular interactions between peptide side chains (Fig. 1.9). These programmable interactions make peptides a prime candidate for the rational design of synthetic self-assembled structures.

Scientists have studied natural peptide-based materials such as amyloid fibrils, spider silk, and collagen and elastin extracellular matrix proteins to learn about the intermolecular interactions that cause the assembly into anisotropic structures. Using these hydrogen bonding and hydrophobic interactions, researchers have developed synthetic peptide sequences that assemble into fibrillar structures, such as RADA 16-I,[51] KVLFF,[52] KFE8,[53] or simple diphenylalanines.[54] In particular, taking advantage of β-sheet hydrogen bonding, interactions that are integral in the formation of amyloid fibrils, has been a rich avenue in the design of anisotropic supramolecular structures due to the directional nature of the bond formation.[55]

Inspired by the amphiphilic lipid molecules that compose cellular membranes, additional hydrophobic interactions can be added to direct assembly by lipidating a short amino acid sequence. The class of molecules, termed peptide amphiphiles (PAs) was developed in the late 1990s,[56] and has
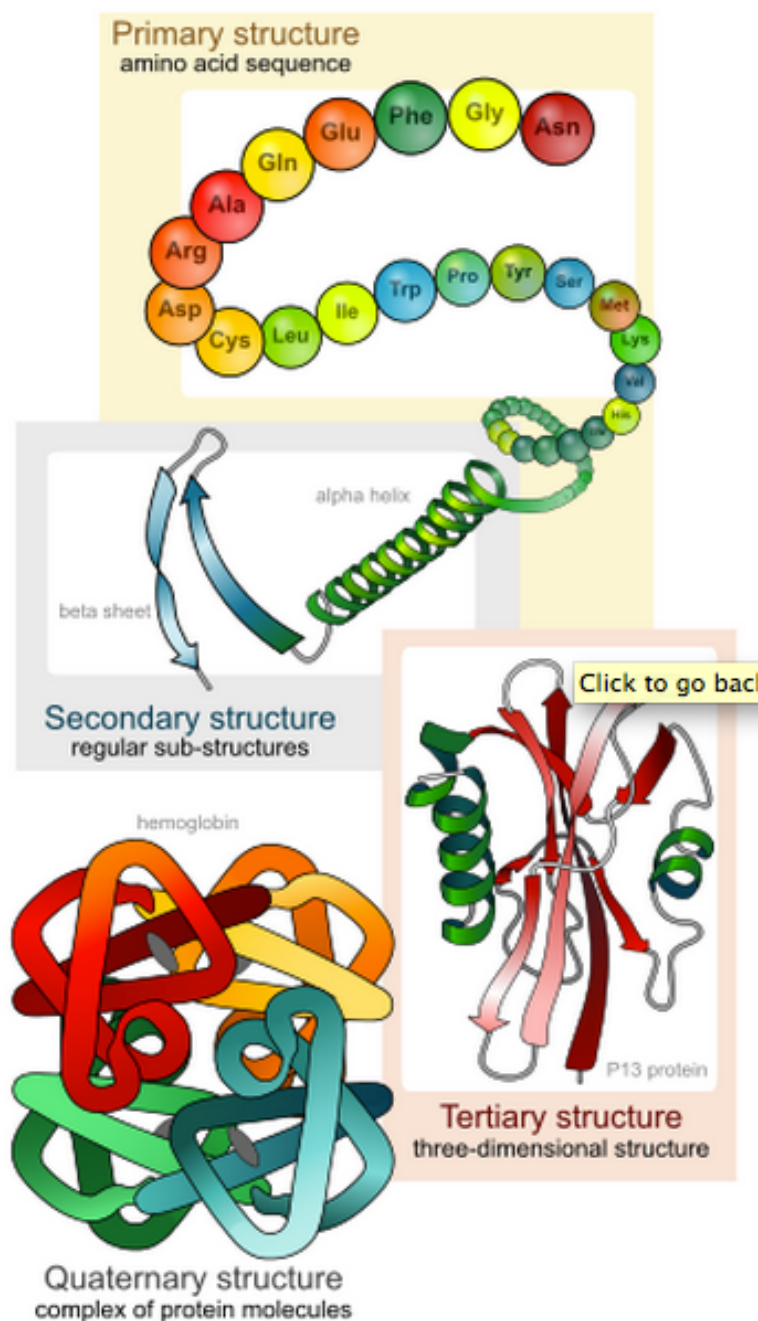
Figure 1.9: Bottom-up folding of polypeptide structures. Primary structure is comprised of the amino acid sequence, which fold into to regular secondary structures such as α-helices or β-sheets. These domains can further fold into three-dimensional tertiary structure, and multiple tertiary structures can complex into a functional quaternary structure. Shown is the tetrameric quaternary structure of hemoglobin. Image from the public domain.

subsequently been extensively studied by the Stupp group and others over the past two decades.[57,58] These molecules are short peptide sequences attached to a hydrophobic alkyl tail (Fig. 1.10). The alkyl tail, typically 12-16 carbons long, is covalently attached to hydrophobic amino acid residues such as valine or alanine, which have propensity to form β-sheet hydrogen bonds in aqueous solution. The β-sheet structure forms directional hydrogen bonds, unlike other secondary structures such as α-helices, which can elongate the self-assembled structure outside of the typical micellar structure that would be expected from simple surfactant behavior.[59] These β-sheet hydrogen bonds, in combination with the terminal hydrophilic charged amino acids, cause the peptide amphiphiles to assemble into highly anisotropic nanostructures. Typically, these take the form of cylindrical nanofibers or nanoribbons with a more rectangular or elongated ellipsoid cross-section, but can also form sheet-like or helical assemblies depending on amino acid sequence.[46,60,61] Due to the biocompatibility and structural similarity of PA-based materials to the native extracellular matrix, our group has used these molecules extensively as biomaterials and scaffold for tissue regeneration.[62–64] The modular nature of the solid-phase peptide synthesis methods used to make these molecules allows us to easily modify these peptides to add additional functionality, such as bioactive epitope sequences. With the extensive protecting group chemistry that has been developed for peptides, it is also rather simple to add small molecule to the peptide structure through orthogonal chemistry.[65–67]
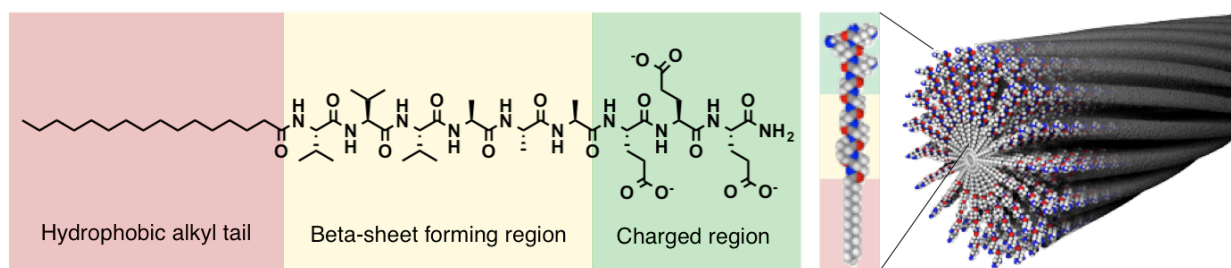
Figure 1.10: PA sequences contain a hydrophobic alkyl tail (red) covalently attached to a β-sheet forming peptide region (yellow). Charged amino acids (green) are added for solubility. These PA molecules can assemble into nanofiber morphologies. Additional functionalities, such as bioactive epitopes, can also be added after the charged region.
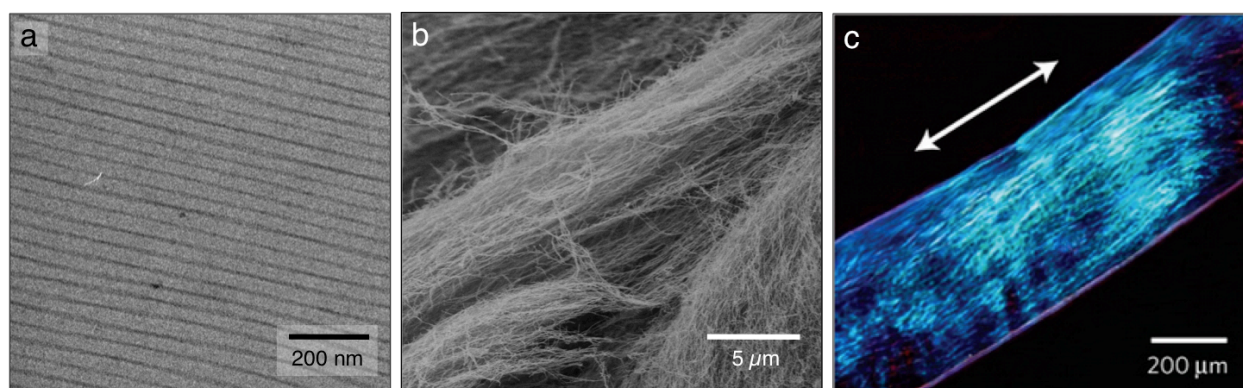
Figure 1.11: (a) Cryo-TEM of PA nanofibers showing nanoscale alignment after applied shear force. (b) SEM of microscopically aligned bundled PA structures. (c) Cross-polarized optical microscopy showing macroscale alignment of an extruded PA string. Panel B modified from Chin *et al.*[68] Panel C modified from Zhang *et al.*[69]

One of the strengths of these self-assembled PA materials is their ability to form hierarchical structures informed by their molecular design (Fig. 1.11). Due to the anisotropic nature of the peptide amphiphile assemblies, they form lyotropic liquid crystalline solutions at certain concentrations. The domains of alignment can easily be aligned into larger monodomains through the application of even weak shear forces such as pipetting (Fig. 1.11c).[69] These 1D filamentous nanofibers are able to mechanically entangle and bundle together to create porous aligned superstructures. The alignment of these nanostructures can be frozen in place by the addition of multivalent counterions such as calcium, which can both charge screen and bridge the ionic amino acids, causing the nanofiber materials to form a hydrogel network that can be used as a structural scaffold.[68] The alignment of within the hydrogel structure can direct both the mechanical properties of the gel as well as cellular response to the material, particularly in cell types such as cardiomyocytes and neurons, whose functionality is highly dependent on the cellular alignment.[70,71]

Aggregation and superstructure formation can be induced by additional functionalities, such as epitope sequence or DNA base-pairing interactions.[72,73] This versatility makes PAs a prime candidate for use in the further development of hierarchical materials.

1.4 LIQUID CRYSTALLINE MATERIALS

Liquid crystals are a state of matter that, due to their simultaneous liquid-like and crystal-like nature, displays unique physical properties.[74] The liquid-like properties allow these materials to flow, shear, and form droplets, whereas the crystalline-like nature give the molecules regular spacing as well as anisotropic optical,[75] electrical,[76] and magnetic properties.[77] Typical liquid crystal-forming molecules are structurally anisotropic, such as azobenzene,[78] nanocrystalline cellulose,[79] or surfactant micelles,[80] which allows for the close, crystalline-like packing of the molecules.

The formation of the liquid crystalline (LC) phase is typically temperature-dependent (thermotropic).[81] Depending on how the molecules are arranged, different classes of liquid crystals can form, such as nematic, smectic, or cholesteric phases, each of which have characteristic packing and optical properties (Fig. 1.12. In some colloidal dispersions, liquid crystals can also be formed depending on concentration (lyotropic liquid crystals), where solvent molecules also play a role in the assembly of the LC phase. These can include amphiphilic surfactant molecules, viruses,[82] or colloidal nanocrystals,[83,84] among others. Lyotropic liquid crystals may also pack in different phases, such as lamellar or hexagonal columnar phases depending on the concentration of amphiphile and solvent. As mentioned in section 1.3.2, PA molecules form lyotropic liquid crystalline solutions upon aggregation.

Due to the anisotropic nature of molecules, it is easy to gain extensive molecular scale orientational order, forming domains of aligned molecules that are often on the order of micrometers. However, this order rarely extends to the macroscale without the application of an external force or field. This can be done mechanically using applied strain,[86] through surface patterning,[87] or by using magnetic or electric fields.[76,88]

Liquids crystalline materials have been used extensively in the field of optics, where they are commonly used in displays or lenses.[89,90] More recently, their ability to switch between LC and isotropic phases have been used for shape-memory polymers and actuating materials.[91−93] However, in these cases, the shape change is typically not reversible without human intervention to reset
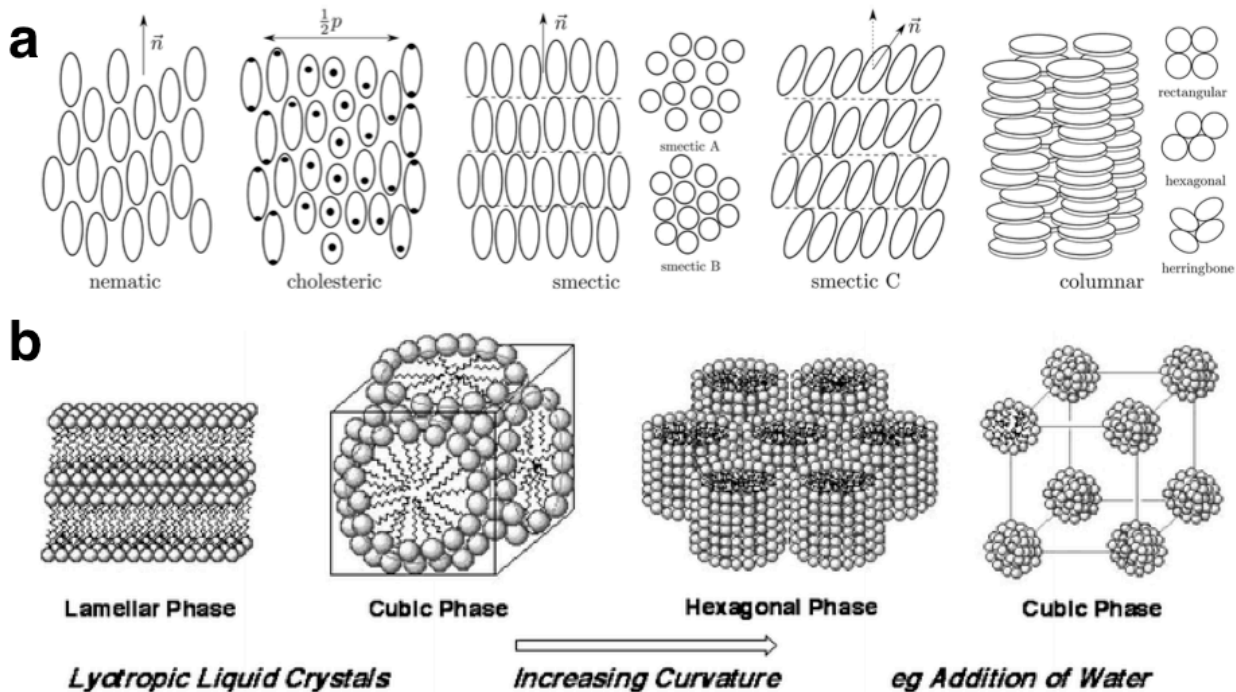
Figure 1.12: (a) Thermotropic liquid crystal phases. (b) Lyotropic liquid crystal phases. Panel A modified from Andrienko.[74] Panel B modified from Goodby *et al.*[85]

the desired shape of the elastomer. Researchers have also taken advantage of their ability to be shear aligned using extrusion-based techniques. Recent advances in the field of 3D printing have been especially potent for the complex spatial patterning of alignment within LC materials.[94,95] The functionality of these materials shows promise for the hierarchical ordering of functional materials.

1.5 THESIS OVERVIEW

This thesis is based on developing new molecular systems that utilize directed assembly to control the overall hierarchical structure and therefore function of the resulting materials. Taking inspiration from biological systems, we use peptide amphiphile building blocks as the basis for our bottom-up design of anisotropic structures, and explore their assembly into higher ordered superstructures for functional anisotropic materials.

This work begins by taking inspiration from the structure of skeletal muscles, and their ability to transduce chemical energy into mechanical energy. In Chapter 2, synthesis of covalent-supramolecular hybrid materials is explored to create anisotropic artificial actuators. By embedding highly anisotropic peptide amphiphile nanofibers into a matrix of thermoresponsive but isotropic covalent polymers, we create a hybrid hydrogel material that actuates anisotropically, dependent on the direction of alignment. We further investigate the mechanisms of this anisotropic contraction through computational and experimental means, concluding that the anisotropy is due to a combination of factors, with both the composite-like microstructure as well as the grafted-from nanostructure contributing to the observed behavior. This knowledge gives us a basis for the further design of covalent-supramolecular hybrid polymers with even more complex actuation behavior.

Chapter 3 builds upon the previous work, expanding the scope of fabrication techniques to a direct ink writing 3D printing method. This technique allows for precise programming of alignment using a top-down approach. 3D printed covalent-supramolecular hybrid polymers are fabricated with different patterns of alignment. When heated, printed materials with net alignment show anisotropic curling behavior, unlike prints lacking net alignment. This is attributed to gradients in alignment that occur during the printing process. We further include cellulose nanocrystals into the hybrid ink to act as a rheological additive to increase the stiffness of the inks in order to build even larger, more complex structures. The resulting materials are significant more mechanically robust and able to be easily handled, even before ionic cross-linking with divalent calcium ions. The 3D

printing methods are then extended to a new PA-only system containing supramolecular host-guest cross-links, taking advantage of the strong noncovalent binding affinity between β-cyclodextrin and adamantane. PA solutions containing both host and guest components form shear-thinning hydrogels without the addition of calcium cross-linking and can be printed as multilayer, freestanding hydrogel structures.

In Chapter 4, we move from the macroscale to the microscale, looking at how to control structure and hierarchical order of PA nanostructures using thermal processing, or annealing, within spatially confined environments. Using variable-temperature X-ray scattering and confocal laser-scanning microscopy techniques on a model PA system, we observe a sharp increase of translational order and formation of a hexagonal lyotropic liquid crystal phase upon heating. The formation of the lyotropic LC phase also correlates with the bundling of PA nanofibers into regular, micron-sized superstructures. This is attributed to an LCST-like entropic effect due to a change in hydration state of the nanofibers at high temperature. The LCST behavior is shown to be highly dependent on the ionicity of the nanofiber surface; however superstructure bundling can occur with or without the presence of crystalline Bragg peaks that indicate high degrees of translational order. The LCST behavior is shown to be generalizable to other PA sequences, and this phenomenon is indicative of a general strategy to control superstructure formation and alignment within a liquid crystalline peptide solution.

Finally, taking into account the knowledge gained from the work detailed in the previous chapters, Chapter 5 discusses the next steps for progressing in the development of aligned functional hierarchical materials. Further development of the supramolecular-covalent hybrid polymer system in proposed in the context of creating more complex actuation motion, as well as expansion of the 3D printing methods to build larger, more robust structures. Additional studies within the rich phase space of PA LCST behavior are also proposed to further determine the dynamic PA-solvent interactions that govern the superstructure formation and inform us of design rules for the bottom-up creation of hierarchical ordered peptides.

2 Covalent-Supramolecular Hybrid Polymers as Anisotropic Artificial Actuators

2.1 OBJECTIVES AND SIGNIFICANCE

Imparting innate directionality into a synthetic material can be quite difficult; however, the structure of skeletal muscle can provide inspiration on how to achieve reversible, macroscopic, anisotropic motion in soft materials. One key aspect of their structure that informs their function is the precise organization of individual proteins such as actin, myosin, and titin into anisotropic structures called sarcomeres. Their further hierarchical organization into muscle fibers allows the transduction of nanoscale protein motion to the performance of macroscale mechanical work. Inspired by this hierarchical structure, we report on the bottom-up design of macroscopic tubes that exhibit anisotropic actuation driven by a thermal stimulus. The tube is built from a hydrogel in which extremely long supramolecular nanofibers are aligned using weak shear forces, followed by radial growth of thermoresponsive polymers from their surfaces. The hierarchically ordered tube exhibits reversible anisotropic actuation with changes in temperature, with much greater contraction perpendicular to the direction of nanofiber alignment. We identify two critical factors for the anisotropic actuation, macroscopic alignment of the supramolecular scaffold and its covalent bonding to polymer chains. Using finite element analysis and molecular calculations, we conclude polymer chain confinement and mechanical reinforcement by rigid supramolecular nanofibers are responsible for the anisotropic actuation. The work reported suggests strategies to create soft active matter with molecularly encoded capacity to perform complex tasks.

2.2 BACKGROUND

Nature creates mechanically useful materials through the bottom-up arrangement of nanoscale building blocks into hierarchically ordered structures that bridge length scales and create macroscopic objects. In a human biceps macroscopic forces are exerted through directional and concerted motion of millions of actuating components.[11] These components are made up of actin and myosin supramolecular polymers linked to a macromolecular scaffold known as titin, which collectively form the sarcomere.[14] The aligned structure of sarcomeres over macroscopic scales provides great inspiration for the development of soft materials that behave as anisotropic actuators.

When attempting to replicate the functions of skeletal muscle, polymer gels are extremely promising materials due to their ability to undergo large volumetric changes with a variety of stimuli.[26,29,96,97] For example, pH-responsive hydrogels successfully adjusted the focal length of optical lenses with only isotropic swelling behavior.[98] Directional actuation can be achieved in molecularly isotropic materials through the application of complex external forces such as thermal gradients, photo-masking of specific locations, or external fields.[24,27,37] Alternatively, a directional bias in the material itself can be introduced through the use of processing techniques such as the construction of multilayered polymer sheets with different moduli,[23,99] or top-down photopatterning of polymer films.[22,100] In supramolecular materials, it is possible to introduce a directional bias of non-covalent assemblies using external forces,[69] however, very few examples of using such materials as actuators have been reported. One such rare example is a recent contribution that demonstrated the photo-triggered actuation of hierarchically organized molecular motors in aligned supramolecular gels.[101] Other important examples are liquid crystalline (LC) elastomers, where LC phases can lead to reversible deformation of materials,[102,103] and shape memory polymers that can recover previously programmed shapes upon application of thermal stimuli.[104,105] However, these LC and polymeric systems are typically hydrophobic and require high temperature processing to create specific shapes.

A different approach to anisotropic actuation has been the use of organic-inorganic composite materials to introduce directionality in the microstructure.[106] In one example, anisotropic actuation was achieved by incorporating titania nanosheets aligned by a strong, external magnetic field within a thermoresponsive hydrogel.[42] In another example, oriented patterns of 3D-printed cellulose fibers and clay particles in a thermoresponsive polymer matrix could form complex shapes through predictable self-folding.[94] These systems, however, still require complex processing steps to attain the desired actuation. It remains of great interest in materials science to design anisotropic actuators based on intrinsically ordered systems containing supramolecular and covalent polymers that align under weak shear forces, which takes inspiration from the hierarchical organization of proteins in skeletal muscle.

We report here on the bottom-up molecular design of a macroscopic soft actuator that deforms anisotropically in an aqueous environment without requiring high temperature or high stress processing, which are typically needed in such systems.[107] The material has a hybrid composition consisting of two components, a supramolecular polymer that under very weak shearing forces provides the anisotropic framework, and transfers this anisotropy to the thermoresponsive motion of the covalent polymer linked to the supramolecular skeleton. Consequently, the hierarchical structure formed in the shape of a macroscopic tube exhibits anisotropic actuation reversibly driven by thermal changes. To build the anisotropic skeleton we use water soluble peptide amphiphile (PA) molecules that under certain conditions are thermodynamically driven to form effectively infinite nanoscale fibers,[45] resulting in a LC solution that is easily shear aligned to encode directional information.[69,70] These PA molecules are chemically designed to initiate the polymerization of the thermoresponsive polymer using atom-transfer radical polymerization (ATRP). As described below, the required steps for bottom-up assembly of this muscle-inspired hierarchically ordered actuator utilize easily applied shear using simple benchtop procedures.

2.3 RESULTS & DISCUSSION

2.3.1 *Material synthesis & characterization*

Fig 2.1 shows a schematic representation of the fabrication process used to prepare the hybrid actuator material. We synthesized a PA (PA1, Fig. 2.1a, blue color) that contains a bromoisobutyryl moiety coupled to the ϵ-amino group of a lysine residue in order to initiate the growth of covalent polymer chains by ATRP.[108] Coassembly of PA1 with PA2 (filler) results in the formation of supramolecular nanofibers containing 10 mol% initiator functionalized molecules (Fig. 2.1b). Thermal annealing was used to lengthen the nanofibers[45] and create an aqueous lyotropic liquid crystal at 1 wt% in buffer (Fig. 2.1c, Fig. 2.2).

We found that this liquid crystal can be extensively shear aligned in a tubular mold containing a rotating metal rod in the center (Fig. 2.1d).[70] By retracting the central rod, the chamber containing PA is exposed to $CaCl_2$ solution and this in turn causes gelation of the liquid crystal into a tube shaped object. Based on earlier work, we hypothesized that the supramolecular fibers would orient circumferentially in the tube walls (Fig. 2.1e). Lastly, the tubular hydrogels are then transferred to a polymerization bath containing a methanol/water solution. This solution contains diethylene glycol methyl ether methacrylate (DEGMA) and oligo(ethylene glycol) methyl ether methacrylate ($OEGMA_{500}$) monomers (molar ratio 95:5 DEGMA:$OEGMA_{500}$), *N,N'*-methylenebisacrylamide crosslinker, catalyst, and reducing agent in order to carry out ATRP[109,110] and generate covalent chains grafted from the supramolecular scaffold (Fig. 2.1f). Due to the controlled nature of ATRP, polymer chains can only grow from the initiator sites on PA1. Unless otherwise noted, chains had an expected degree of polymerization of 1500, and crosslinker was added at a concentration equivalent to 1 wt% of the monomers, resulting in approximately one crosslink per 75 monomer units. Crosslinking is expected to occur both within polymer chains on the same nanofiber as well as between nanofibers.
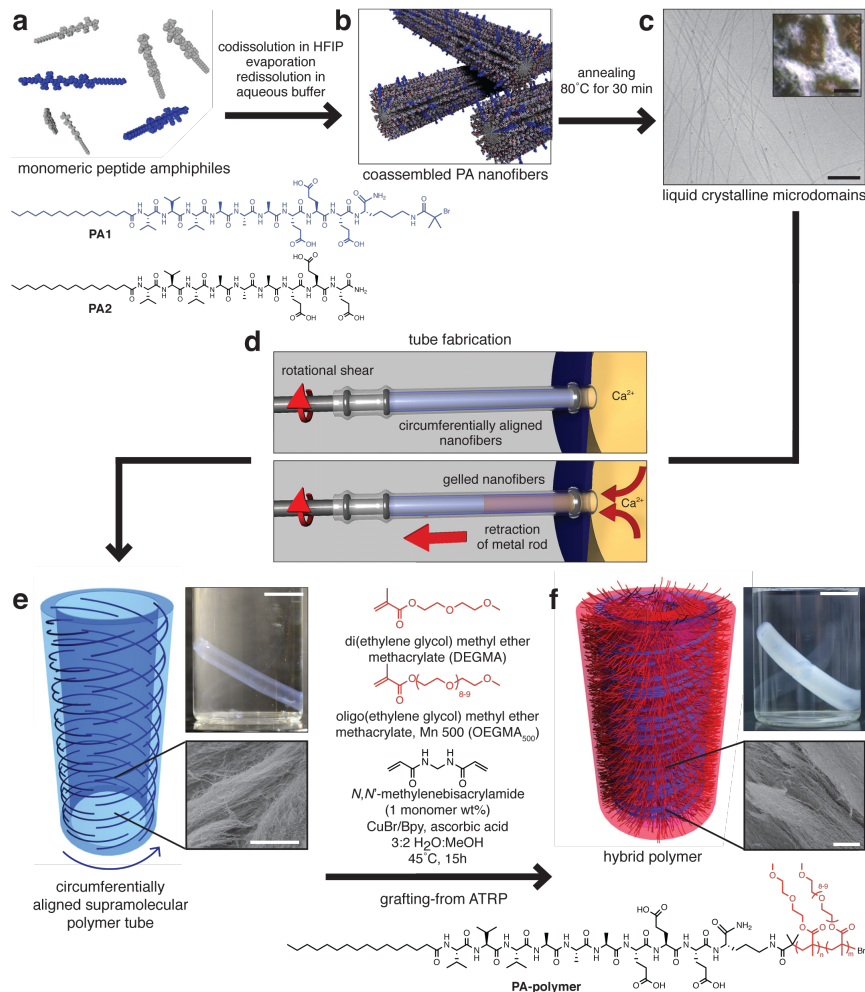
Figure 2.1: (a) PA1 and PA2 are codissolved in hexafluoroisopropanol (HFIP) to ensure complete dissolution and molecular mixing. Removal of HFIP and redissolution in aqueous buffer gives (b), coassembled peptide amphiphile (PA) nanofibers. Subsequent annealing at 80°C for 30 minutes gives a liquid crystalline solution of high aspect-ratio PA nanofibers. (c) Cryogenic transmission electron microscopy shows long nanofibers (scale bar is 200 nm), and polarized optical microscopy (inset, scale bar is 200 μm) shows birefringent domains. (d) To fabricate the PA tubes, rotational shear force is applied to PA solution to circumferentially align the nanofibers within a tubular mold. The central rod is then retracted to allow influx of CaCl₂ solution, gelling the PA as shown in (e), maintaining nanostructure orientation. Covalent polymer chains are grafted from nanofibers with atom-transfer radical polymerization in a polymerization bath. (f) The resulting hybrid contains covalent chains grafted radially from the nanofiber surface and shows a distinct opacity change from the unpolymerized state (photographic insets, scale bars are 1 cm), while maintaining fibrous morphology (scanning electron microscopy insets, scale bars are 10 μm).
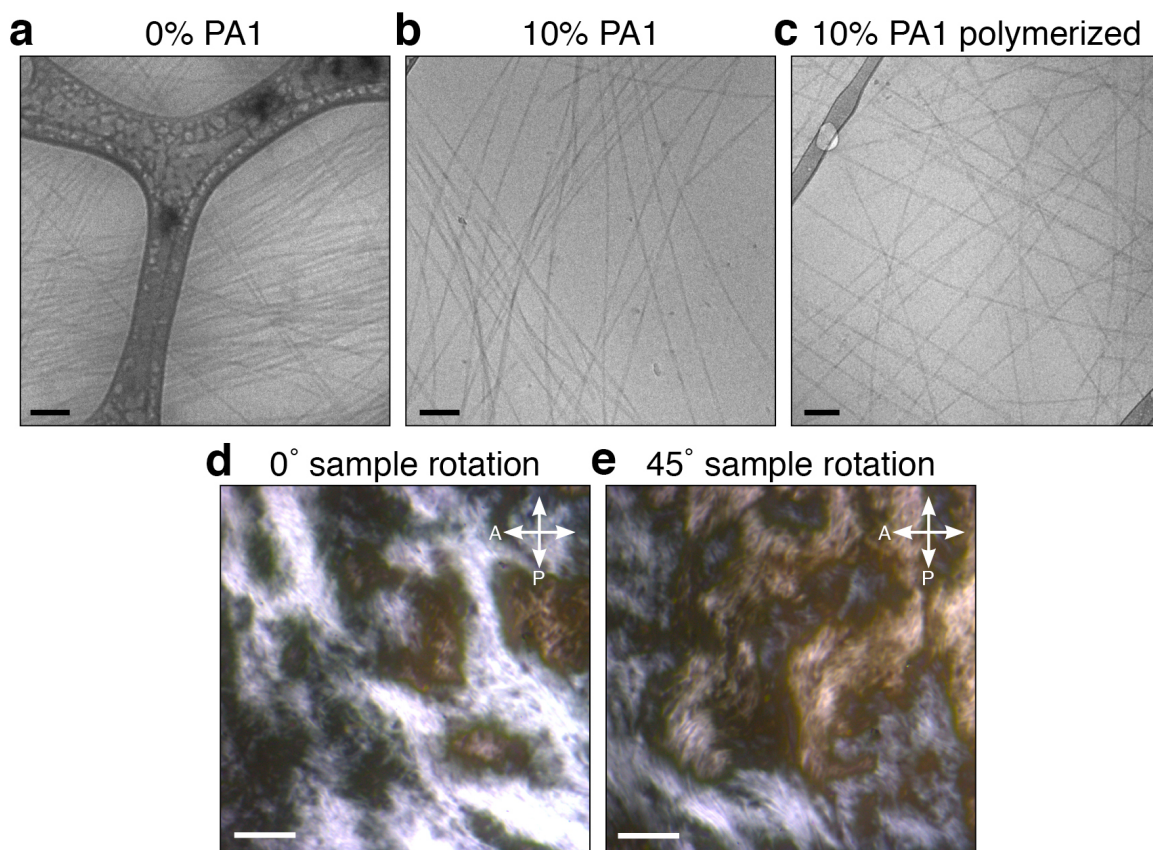
Figure 2.2: Cryo-TEM of (a), 0 mol% PA1 + 100 mol% PA2; (b) 10 mol% PA1 + 90 mol% PA2; (c) 10 mol% PA1 + 90 mol% PA2 after polymerization of thermoresponsive covalent polymer. Note that due to the similar density of the OEGMA copolymer to water, there is no distinct contrast from water within the polymer phase. (Scale bars are 100 nm). Polarized optical microscopy showing birefringence of a 1 wt% solution of 10 mol% PA1 + 90 mol% PA2 (same as panel b) after annealing; (d) 0°sample rotation, (e) 45°sample rotation. (Scale bars are 200 μm)

The random copolymer exhibits the expected lower critical solution temperature (LCST) of 35 °C by dynamic light scattering (DLS, Fig. 2.3).[111] We monitored the consumption of monomer using nuclear magnetic resonance (NMR, Fig. 2.3). We estimate the molecular weight of tethered chains by gel permeation chromatography of non-tethered chains grown from soluble initiator (ethyl α-bromoisobutyrate), which has been shown to be in good agreement with those grown from surfaces.[112]

While the tube dimensions and fibrous morphology (Fig. 2.4) remain the same before and after polymerization, distinct differences in the material opacity are observed due to the crosslinking
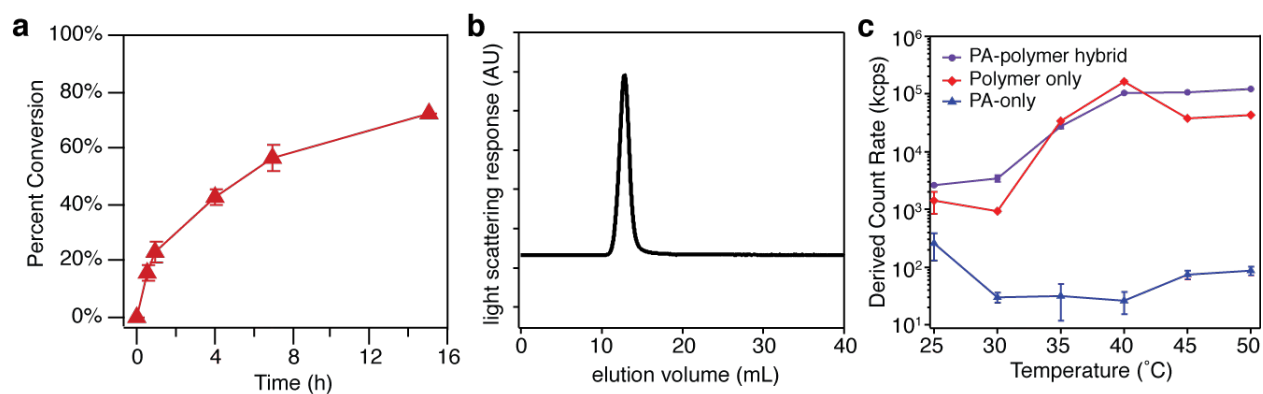
Figure 2.3: (a) Polymer conversion is monitored by following the decrease in signal intensity of vinyl peaks by ^{1}H NMR. (b) Representative GPC In THF of polymer after 15 hours shows a monomodal peak on light scattering detector. M_n = 9.8x10^4, PDI = 1.36. (c) Light-scattering behavior at increasing temperature, showing increased scattering above LCST for samples containing PEGMA polymers. Error bars represent one standard deviation.
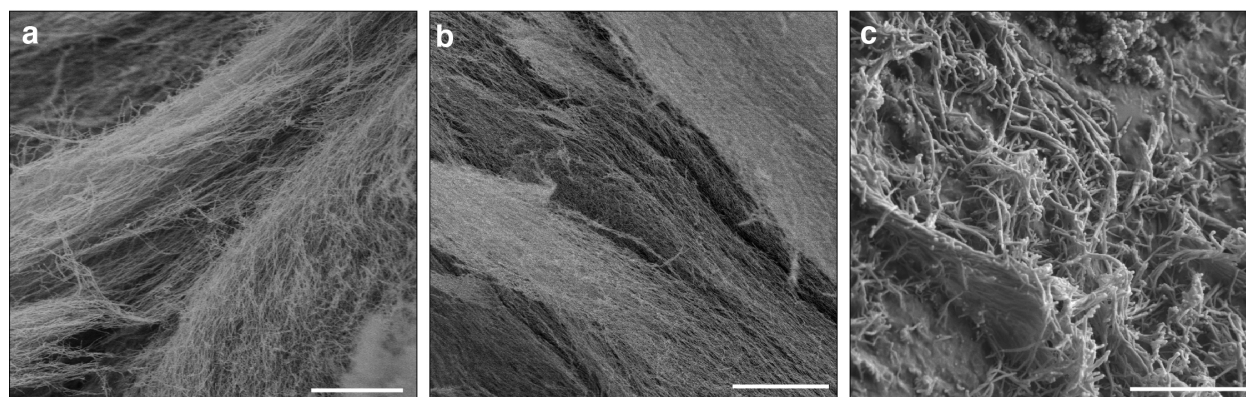
Figure 2.4: (a) After gelation with 0.1M CaCl$_2$ solution (scale bar is 5 μm). (b) After polymerization and dialysis (scale bar is 10 μm). (c) SEM image of polymer-only hydrogel (scale bar is 2 μm). Note that the polymer hydrogel also has a fibrous structure on small length scales, but does not contain long-range order. Images were taken from within a cross-section of the tube wall.

density (photographic insets, Fig. 2.1e, f). Further discussion of the material opacity can be found in the Methods (Section 2.5). The hybrid material was stable in a hydrated state at ambient temperature for more than one year. Furthermore, mass calculations show a decrease of the water content from approximately 98% to 94% after polymerization, as well as an increase of overall dry mass, indicating successful polymerization of the covalent polymer. The hybrid tubes can be easily handled and are mechanically much more robust than tubes formed only by the supramolecular scaffold.

Microindentation experiments indicate a fourfold increase in radial compressive modulus for the hybrid tubes relative to their supramolecular counterparts (4.2 ± 1.5 vs. 16.7 ± 2.8 kPa, mean $\pm$ s.d., n = 3 – 5).

We examined the distribution of covalent polymer throughout the tubular structure using confocal microscopy and fluorescently labeled materials. In both the tube cross-section and
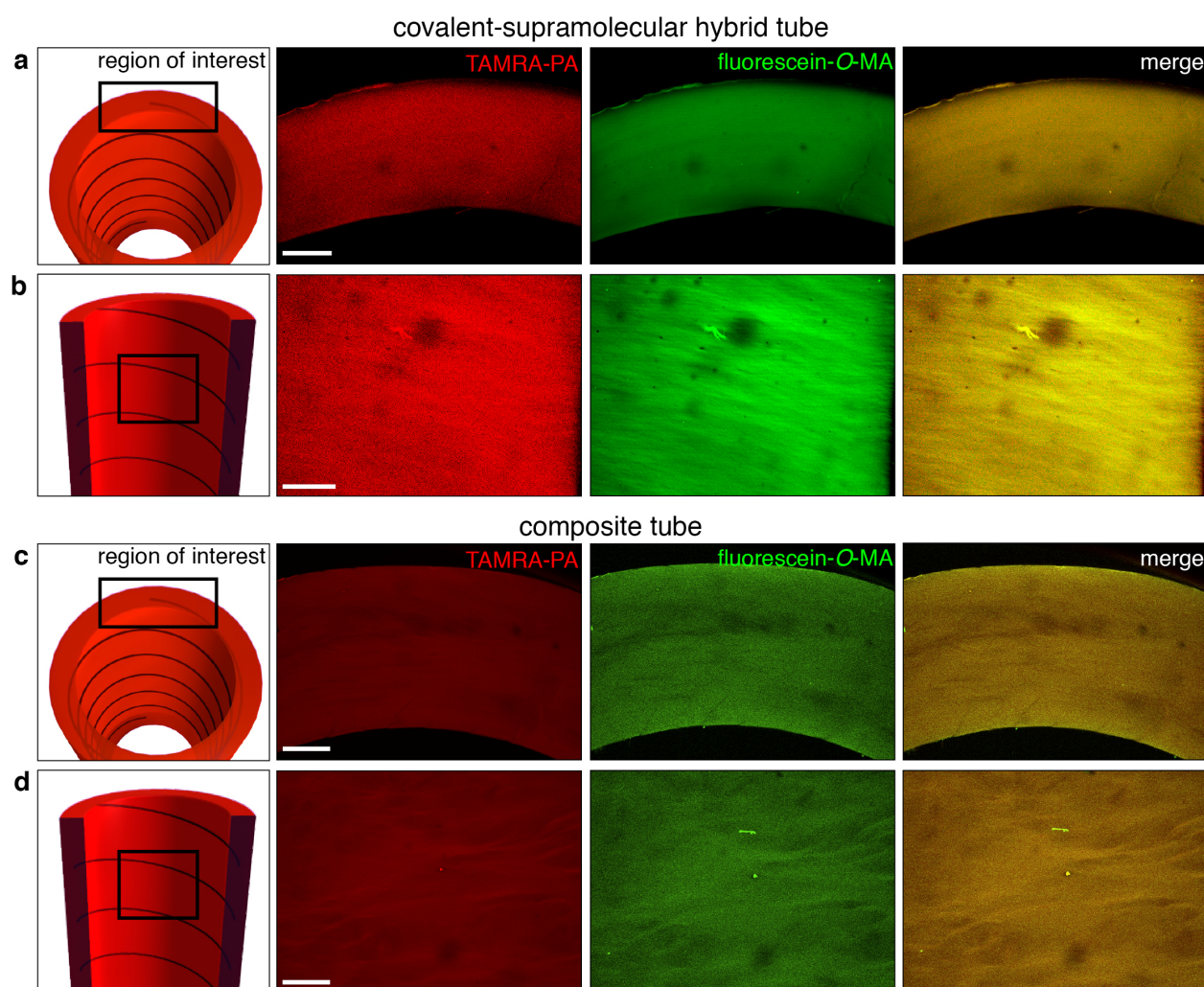
Figure 2.5: (a) Confocal microscopy of fluorescently tagged circumferentially aligned hybrid tube in tube cross-section. (b) Confocal microscopy of fluorescently tagged circumferentially aligned hybrid along tube wall. (c) Confocal microscopy of fluorescently tagged composite tube in tube cross-section. (d) Confocal microscopy of fluorescently tagged composite along tube wall. Fluorescently tagged hybrids and composites contain 1 mol% of PA3 in the supramolecular phase and 1 monomer wt% of fluorescein-O-methacrylate in the covalent phase. Scale bars are 200 μm.

the tube wall we observed a homogeneous distribution of fluorophores and a high degree of colocalization (Fig. 2.5). This indicates that during polymerization, monomer can freely diffuse within the supramolecular scaffold, allowing polymer chains to be initiated throughout the entire volume of the tube.

2.3.2 *Anisotropic thermoresponse*

Next, we investigated the actuation behavior of the hybrid tubes by immersing them in water and heating from 25 °C to 70 °C over a period of 30 minutes. Above the LCST of the copolymer, we observed a significant contraction of hybrid tubes (Fig. 2.6a, d). The contraction is reversible and upon cooling, the polymer re-swells to its original dimensions.

The hybrids can be actuated for multiple cycles and with similar dimensional changes (Fig. 2.7). The actuation of these materials is sufficiently strong to perform work (Fig. 2.8), with samples able to lift up to 380 times their dry weight with a work capacity of 0.629 kJ kg^{-1} and volumetric energy density of 5.656 kJ m^{-3}.

Hybrid tubes containing circumferentially aligned supramolecular scaffold exhibited anisotropic actuation, contracting more strongly along their length relative to their width (62% versus 79% of original dimensions, see Fig. 2.6a). This behavior is not observed in tubes containing only covalent polymer or only supramolecular scaffold (Fig. 2.6b, c). Tubular hydrogels containing only covalent polymer contract isotropically to 77% of their original length and width, while supramolecular PA tubes, as expected, have no observable contraction. When we aligned the supramolecular scaffold axially (parallel to the tube long axis) instead of circumferentially (Fig. 2.6d), the anisotropy reverses to 79% of original width versus 88% of original length. These observations suggest that anisotropic actuation is linked to the alignment of the supramolecular scaffold containing covalently grafted thermoresponsive polymer.
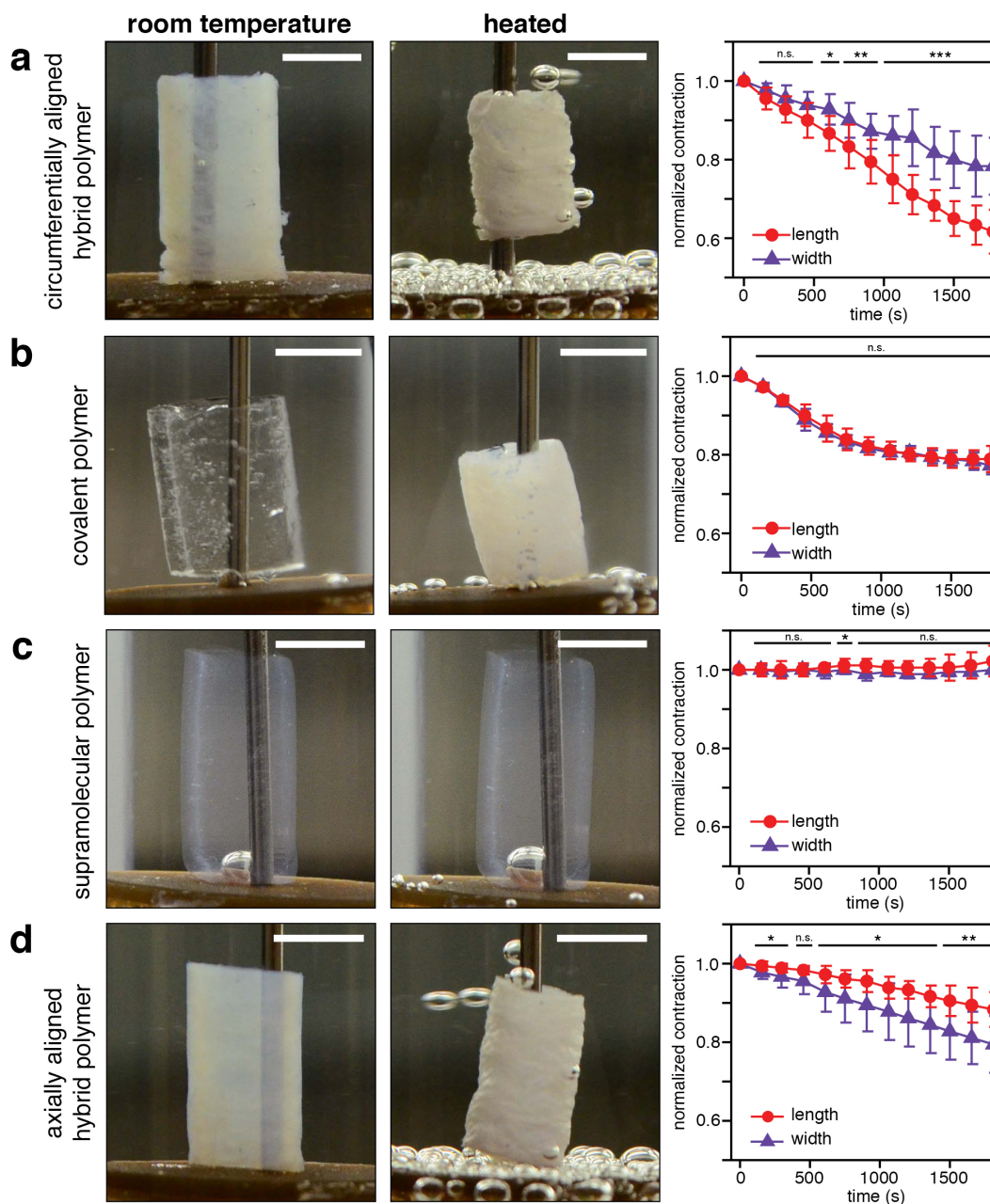
Figure 2.6: (a) Circumferentially aligned hybrid polymer (left) shows anisotropic contraction along the length of the tube upon heating (center), as normalized to original tube dimensions (right) over the course of 1800 seconds. (b) Covalent polymer tube. (c) Supramolecular polymer tube. (d) Axially aligned hybrid polymer. (scale bars are 3mm). A representative heating curve is depicted in Figure 2.19. Statistical analysis was performed using an unpaired two samples Student's t-test; * $p<0.05$, ** $p<0.01$, *** $p<0.001$; (Data are presented as mean $\pm$ s.d., n = 3).
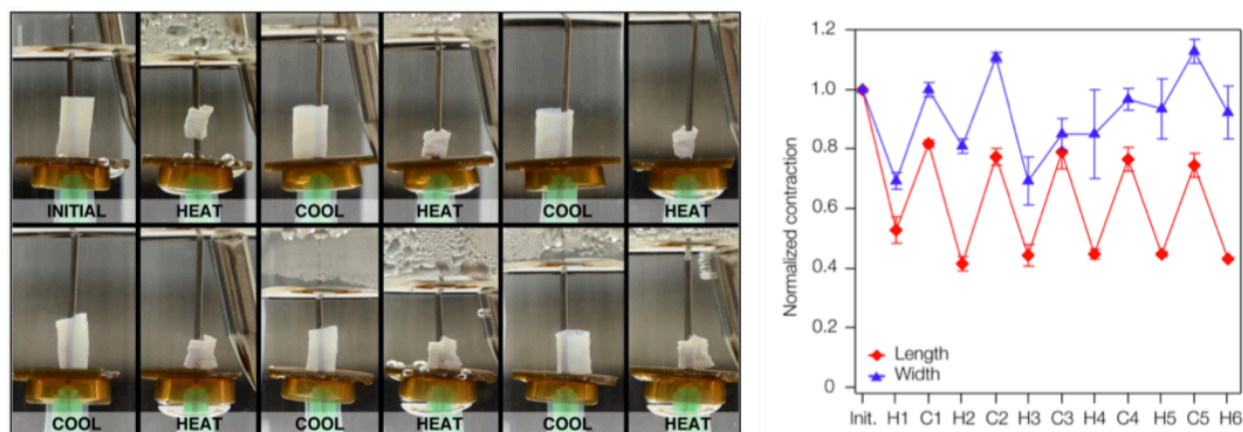
Figure 2.7: Circumferentially aligned PA-polymer hybrid is able to retain shape and ability to contract across six heating-cooling cycles (data represented as mean $\pm$ s.d. of 3 measurements). After repeated handling, width contraction of the hybrids tends to become somewhat ellipsoidal (for example, from touching the central post in the contraction chamber), causing deviations in tube measurement.
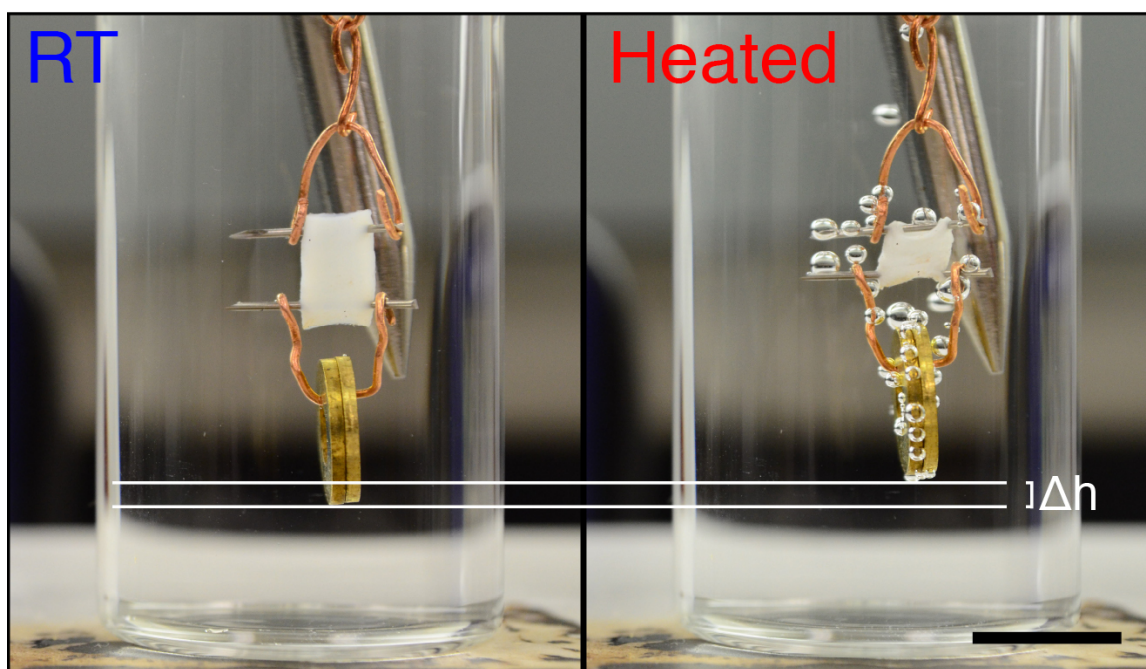
Figure 2.8: PA-polymer hybrid is able to perform work upon heating. 760 mg weights were attached to a hybrid material (2.0 mg dry weight) and lifted 1.67 mm against gravity (scale bar is 1 cm). This corresponds to a work capacity of 0.629 kJ kg^{-1} and volumetric energy density of 5.656 kJ m^{-3}.

2.3.3 *Alignment of the supramolecular scaffold in hybrid materials*

The data presented in Fig. 2.6 indicates that anisotropic actuation originates from the combination of covalent polymer and supramolecular phases in the hybrid material. The difference in response between circumferentially and axially aligned polymers indicates that the direction of alignment in the supramolecular phase determines the nature of the anisotropy.

To investigate the importance of this alignment, we analyzed samples with polarized optical microscopy (Fig. 2.10). The circumferentially aligned hybrid material shows strong birefringence in both the cross-section and the tube wall, indicating the presence of highly aligned structures (Fig. 2.9a, d). In contrast, the axially aligned sample only shows strong birefringence in the tube wall but little in the tube cross-section, which is expected for a material with this orientation (Fig. 2.9b, e). The cross-section and wall of a tube fabricated from covalent polymer hydrogel show negligible birefringence, thus revealing no net orientation (Fig. 2.9c, f).

We also characterized orientation in the tubular samples using small-angle X-ray scattering (SAXS) (see Fig. 2.9g-i, Fig. 2.11). The 2D scattering of aligned samples reveals ellipsoidal patterns consistent with long-range order, whereas unoriented ones have no angular dependence of the observed scattering. The plot of integrated radial intensity as a function of azimuthal angle (Fig. 2.9g, h insets) in the circumferentially and axially aligned hybrid material show maximum intensities around 180° and 90°, respectively, confirming the proposed alignment of supramolecular nanofibers within tubular samples. Finally, the SAXS data reveals that tubes composed of the covalent polymer contain randomly oriented chains (Fig. 2.9i). It is therefore clear that the strongest contraction of the tube is observed perpendicular to the orientation of supramolecular nanofibers. In the case of circumferentially aligned nanofibers, the tubes shrink preferentially along the length, whereas those with axial alignment reveal preferential shrinkage along the width. We therefore have strong evidence that anisotropic contraction of the tubes is directly linked to the macroscopic orientational order provided by the supramolecular phase.
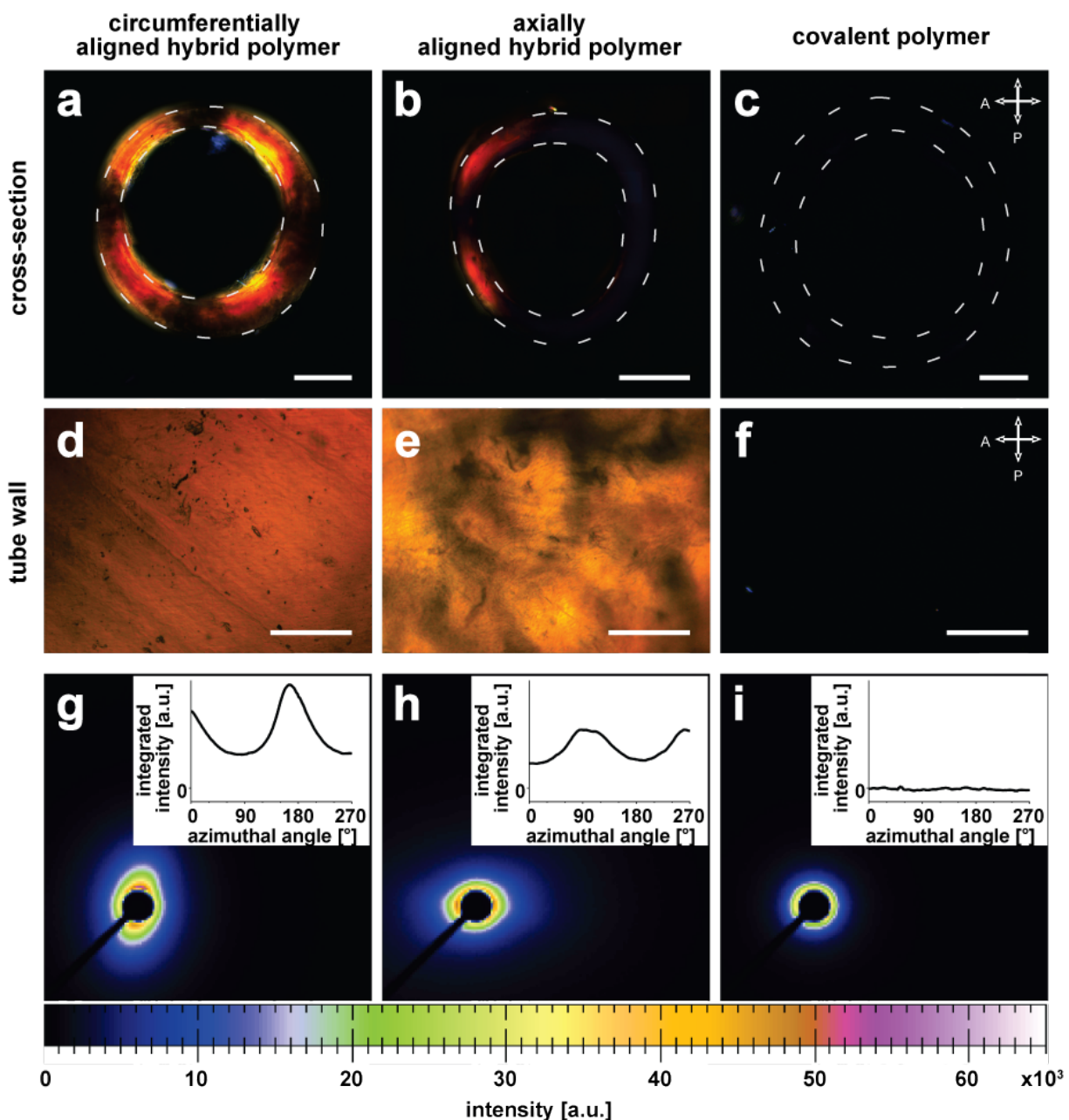
Figure 2.9: Circumferentially aligned hybrid polymer shows birefringence in cross-sectional slices (a) as well as along the tube wall (d) under cross-polarized light. Axially aligned hybrid polymer shows birefringence only in the tube wall (b, e). Covalent polymer shows negligible birefringence (c, f). 2D small-angle X-ray scattering patterns show angle dependent intensity maxima in the aligned hybrids but not in the covalent polymer (g-i). Insets show integrated radial intensity versus azimuthal angle. Scale bars in images of cross-sectional slices (a, b, c) are 1 mm and 400 µm in images of the tube walls (d, e, f).
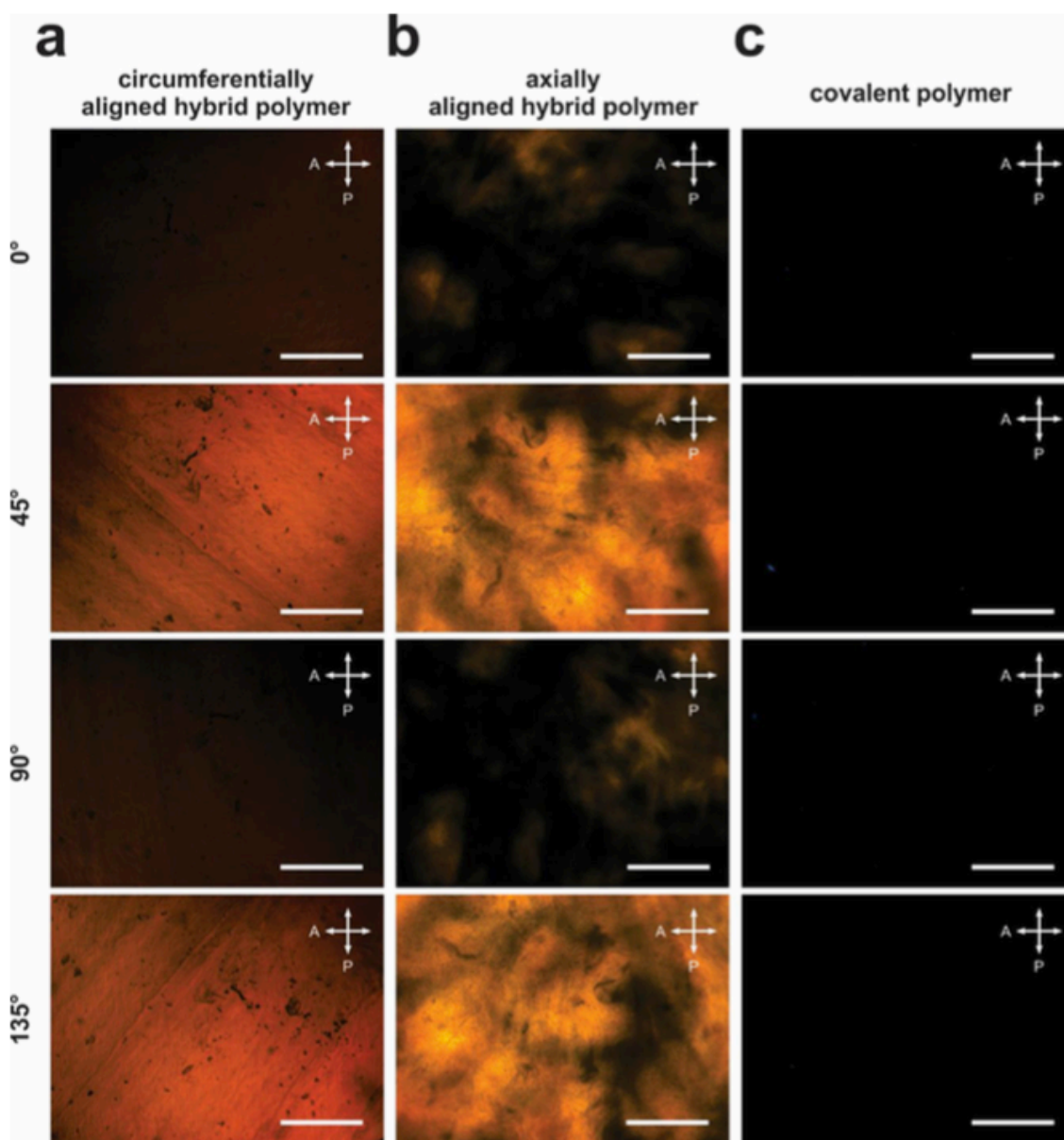
Figure 2.10: Microscopy images of sections of the tube wall of tubular hydrogels from (a) circumferentially aligned hybrid, (b) axially aligned hybrid, and (c) covalent polymer under cross-polarized light. A sample stage was used to rotate the samples by 0, 45, 90, and 135 degrees, respectively. As expected, the highly circumferentially aligned tube shows strong birefringence at 45 and 135 degrees of sample rotation and minimal birefringence at 0 and 90 degrees. The axially aligned hybrid exhibits the same trend as the circumferentially aligned hybrid, however, domains with different alignment are present. In contrast, the covalent polymer tube shows no birefringence at any sample orientation. Scale bars are 400 μm.
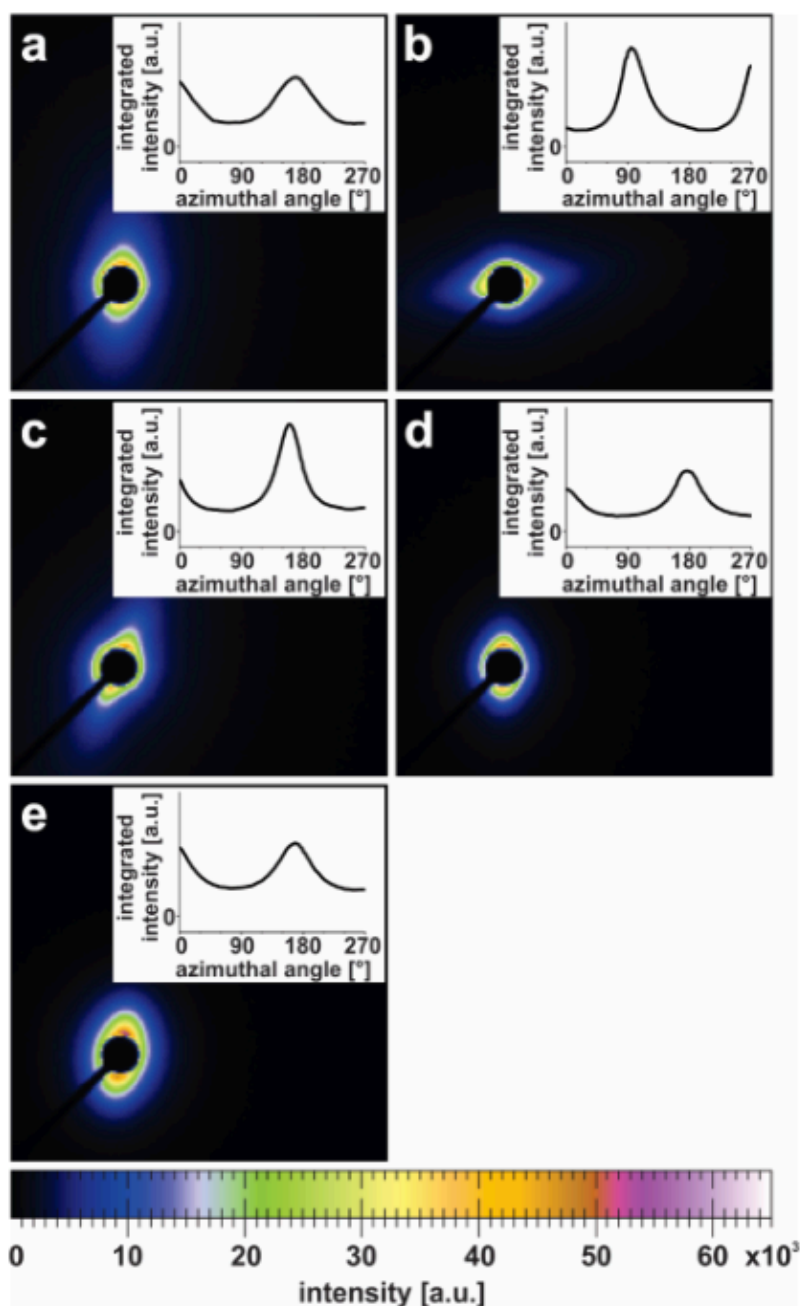
Figure 2.11: 2D small angle X-ray scattering patterns show angle dependent intensity maxima in the tubular hydrogels. Insets show integrated radial intensity versus azimuthal angle. (a) circumferentially aligned and (b) axially aligned PA tubes before grafting of covalent polymer. Composite tubular hydrogel (c) before and (d) after grafting of covalent polymer. e) The alignment of the PA nanostructures is maintained within the circumferentially aligned hybrid structures after multiple contraction and expansion cycles (n > 3). All measurements were taken at room temperature.
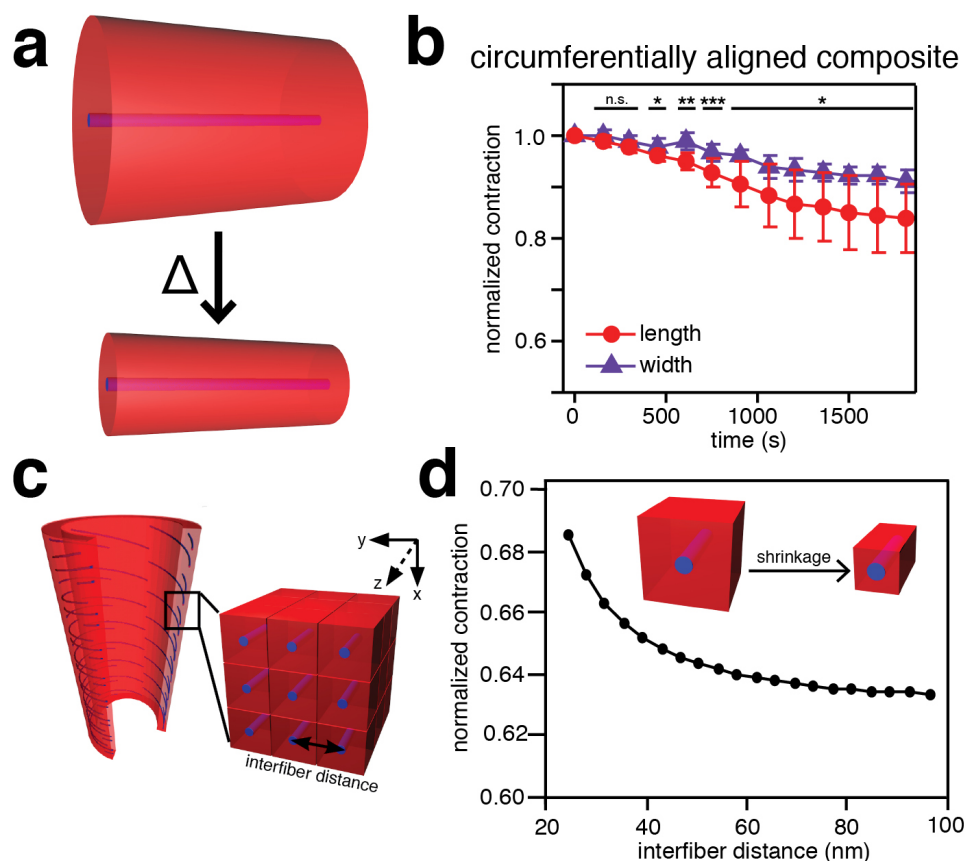
Figure 2.12: (a) PA nanofibers with high persistence length provide mechanical reinforcement along the PA axis, preventing contraction in the direction of alignment. (b) Experimental results of heating a circumferentially aligned composite material. Statistical analysis was performed using an unpaired two samples Student's t-test; * p<0.05, ** p<0.01, *** p<0.001; (Data are presented as mean ± s.d., n = 3). (c) Schematic of finite element analysis model of covalent-noncovalent system. (d) Finite element analysis results of shrinkage due to mechanical reinforcement with varying interfiber distance.

We considered possible mechanisms that link the observed correlation between anisotropic actuation and orientation of the supramolecular phase. One possibility is that high-persistence length structures mechanically restrict contraction of the covalent polymer. In this case, the oriented, rigid structures would diminish contraction preferentially in the direction of alignment and lead to macroscopic anisotropic actuation (Fig. 2.12a).

Tensile experiments show a difference in the Young's modulus perpendicular and parallel to the nanofiber alignment axis (50.3 ± 39 kPa vs. 263.3 ± 179 kPa, mean ± s.d., n = 6 – 12), indicating
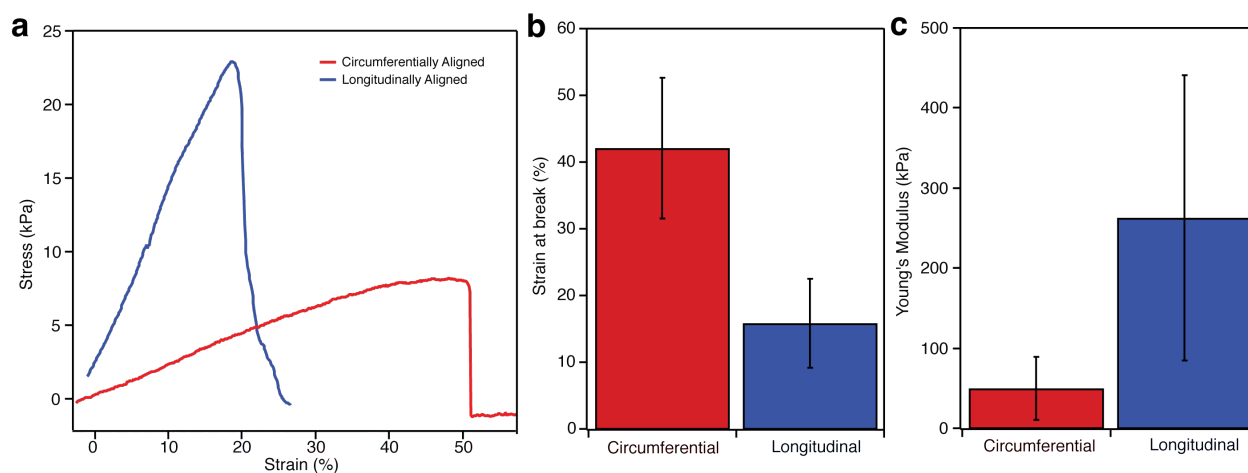
Figure 2.13: Tensile experiments of circumferentially (red) and longitudinally aligned (blue) hybrid tubes. (a) Representative examples of tensile tests. (b) Mean engineering strain at break (%) and (c) mean Young's modulus (kPa). Experiments show the circumferentially aligned hybrids (where the tensile force is applied perpendicular to nanofiber alignment) have higher strain at break than longitudinally aligned hybrids where tensile force is applied parallel to the direction of nanofiber alignment (42.1 ± 10.6 % vs 15.8 ± 6.7 %). Conversely, the circumferentially aligned samples show lower modulus (50.3 ± 39 kPa vs 263.3 ± 179 kPa). Data is represented as mean $\pm$ s.d. of 6 – 12 samples.

the nanofiber orientation does affect the material mechanics (Fig. 2.13). We hypothesize that if the anisotropic response were solely due to mechanical restriction from the rigid nanofibers, a composite material – where the polymer is not covalently connected to the supramolecular nanofibers – should match that of the hybrid materials. We therefore synthesized composite samples containing circumferentially aligned PA2 nanofibers embedded in a covalent polymer matrix (Fig. 2.12b), in contrast to the previously described hybrid materials. These composite samples show similar integration of the covalent polymer component throughout the material (Fig. 2.5). We found that composite samples do exhibit anisotropic actuation, shrinking to 85% of their original length and 92% of their original width. However, this actuation is of considerably lower magnitude than that of the previously described circumferentially aligned hybrid samples (Fig. 2.6a). This indicates that while mechanical restriction contributes, it cannot be the sole cause of the observed hybrid anisotropy.

In addition to the preparation of a composite control, we also constructed a computational model using finite element analysis. However, it is challenging to directly model this system due to

the vast differences in length scale between supramolecular nanofibers and the macroscopic tube. Therefore, we treat the bulk hybrid tube as a periodic array of rigid, non-deformable PA nanofibers embedded in a soft matrix so that the behavior of the system can be captured using a unit cell with periodic boundary conditions. Specifically, each unit cell contains one PA nanofiber, which is modeled as a cylindrical rod strongly adhered to the surrounding polymer in order to prevent slippage at the PA-polymer interface and therefore constraining the matrix during contraction (Fig. 2.12c). In this model, the size of the unit cell represents the distance between fibers, and the PA nanofiber is considered an infinitely long object given the periodic boundary conditions. This assumption is a reasonable approximation given the very high aspect ratio and relative stiffness of PA nanofibers (see Section 2.5). Below, we describe this finite element model of a soft matrix containing dispersed, rigid nanofibers, which has successfully been used to describe deformed hybrid hydrogels.[113,114]

The free energy, F, of the covalent polymer in the hybrid structure is described using the Flory-Rehner theory,[115] which incorporates the elastic energy of the polymer gel into the free energy of mixing of the solvent and the polymer gel,

$$F = \frac{1}{2} NkT[\lambda_x^2 + \lambda_y^2 + \lambda_z^2 - 3 - ln(\lambda_x \lambda_y \lambda_z)] + kT \frac{V_m}{v}[(\frac{1}{\phi} - 1)ln(1 - \phi) + \chi(1 - \phi)] \quad (1)$$

where N is the total number of polymer chains (defined as segments between crosslinking junctions), λ_x, λ_y, and λ_z are the stretching ratios along the principal axes (final length after deformation/initial length), V_m is the volume of the polymer in the absence of solvent, v is the volume of each solvent molecule, phi is the volume fraction of monomers, and chi is the Flory interaction parameter between the solvent and the polymer. For a polymer gel with LCST behavior, chi becomes larger when the temperature increases. For simplicity, we assume here that chi only depends on temperature. In an isotropic gel, the stretching ratios are the same along all principal axes and therefore $\lambda_x = \lambda_y = \lambda_z = \phi^{-\frac{1}{3}}$. In the case of an anisotropic gel, where the gel is constrained uniaxially along

the z direction (fiber direction) and free to swell in the x and y directions, $\lambda = \lambda_x = \lambda_y = (\phi\lambda_z)^{-\frac{1}{2}}$. By varying χ, a change in ϕ and consequently λ is directly obtained from the equilibrium equations, and therefore, the relation between $\chi(T_i)$ and $\chi(T_f)$ and the resulting change in the stretching ratios λ can be derived (see Section 2.5.10),

$$\frac{\chi}{\lambda^2\lambda_z} = \frac{1}{2}\frac{N_v}{V_m}\left(1 - 2\lambda^2\right) - \lambda^2\lambda_z ln(1 - \frac{1}{\lambda^2\lambda_z} - 1) \tag{2}$$

Estimates of the interfiber distances range from approximately 30 nm in a two-dimensional crystalline state previously observed[116] to 80 nm in a hydrated gel (see Supplementary Note 3). The finite element analysis indicates that the hybrid material should have significantly larger contraction perpendicular to the fiber axis within the range of interfiber distances modeled from 24 to 96 nm (Fig. 2.12d). Within this range of interfiber distances, the analysis predicts a contraction ranging from 69% to 63% of its original length. This model likely overestimates the contraction, as it does not reflect all aspects of the hybrid system. In particular, the thermal response of the polymer as well as the chemical structure and unique molecular architecture of the hybrid is not properly represented in the finite element analysis. To complement the finite element analysis and investigate other mechanisms that would aid in the occurrence of anisotropy, we extended an existing molecular theory that describes the chemistry and molecular architecture of the hybrid more accurately.

It is known that end-grafting of chains into polymer brushes greatly affects the resulting physical properties. At high densities, the grafting of polymer chains to a surface leads to polymer chain confinement resulting in more extended conformations compared to those in solution.[117] We expect that, due to the grafting, the more extended conformations of chains perpendicular to the nanofiber lead to a more pronounced radial collapse of polymer chains above the LCST (Fig. 2.14a). Since the previously described finite element model does not take this molecular picture into account, we used theory to model a single PA nanofiber with end-grafted polymer chains.

The molecular approach used in this work is based on a theory that has successfully been applied to study structural and thermodynamic properties of a variety of end-tethered polymer systems.[118]
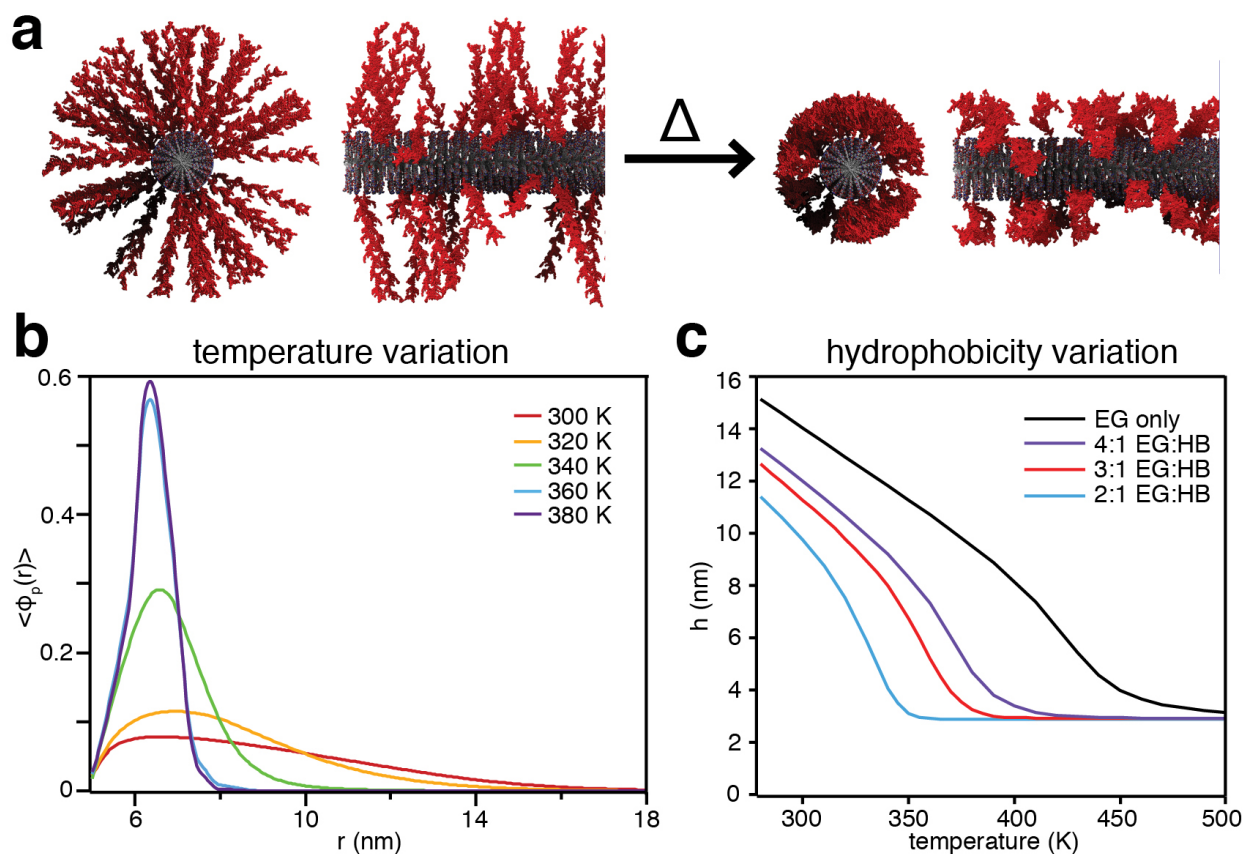
Figure 2.14: (a) Schematic representation of confinement effect in grafted polymer chains below (extended) and above (collapsed) the transition temperature leading to pronounced volume changes in the material perpendicular to the supramolecular nanofiber. (b) Polymer volume fraction versus radial distance away from the PA nanofiber. Polymer is a linear alternating copolymer (EG_2-a-HB) $_{66}$-EG_2. (c) Height of end-tethered polymer as function of temperature for different copolymers with increasing amounts of hydrophobic monomers. The polymer is a linear alternating copolymer (EG_n-a-HB_1) $_m$. Number of segments is N_p=200, the surface coverage is 0.07 chains nm^{-2}, and radius of nanofiber equals 5 nm.

The theory explicitly includes conformations of polymer chains, as well as size, shape, and volume of every molecular species in the system. For simplicity, the model represents the thermoresponsive DEGMA/OEGMA$_{500}$ copolymer as a linear poly(ethylene glycol) (PEG)-like copolymer of ethylene glycol and hydrophobic monomers. This allows us to investigate the effect of end-grafting and molecular chemistry on the structure and thermal response of the system. We assume the polymer chains to be evenly distributed and irreversibly end-tethered to the cylindrical nanofiber surface.

Previous work has explored PEG chains end-tethered to planar surfaces[119] as well as the behavior of PEG solutions.[120] It was found that in order to accurately represent the LCST behavior of PEG polymers, hydrogen bonding between water and monomer, as well as between water molecules, must be included. Here, we go well beyond the Flory-Rehner approach employed in the finite element analysis described above. These specific hydrogen bond interactions, in addition to the typical polymer-water and polymer-polymer interactions, are necessary to obtain the correct thermal response. In fact, the hydrogen bonding is explicitly included into the free energy expression of the PA nanofibers (see Section 2.5.23).

For a given grafting density, the model allowed us to calculate the polymer volume fraction, $\langle \phi_p(r) \rangle$, at a given distance from the surface, r. Upon increasing the temperature above the transition temperature, a rapid collapse of the polymer chains is predicted, accurately replicating the experimentally observed LCST behavior (Fig. 2.14b). The average height, h, of the polymer brush is defined as twice the normalized first moment of the volume fraction, $\langle r \rangle$, minus the radius of the nanofiber, R,

$$h = 2(\langle r \rangle - R) \; with \; \langle r \rangle = \int_R^\infty r \langle \phi_p(r) \rangle dr / \int_R^\infty \langle \phi_p(r) \rangle dr \qquad (3)$$

Assuming that every tenth PA molecule grows a polymer chain, we estimate a grafting density of 0.07 chains nm^{-2} on the nanofiber surface.[121] For a copolymer of 200 segments, we observe a drastic change in the average height of the brush. In our model, the height of the brush decreases from approximately 12 nm to 2.75 nm (23% of original height) when the temperature is increased from room temperature to 375 K, and variations in grafting density in the range of that used experimentally result in only minor changes in contraction (Fig. 2.16a, Fig. 2.17). This collapse is induced by the relative reduction of polymer-water hydrogen bonds in favor of water-water hydrogen bonds (Fig. 2.15). The extent of the collapse predicted by the model is more extreme than what is observed in the experimental system. This is due to the fact that in this calculation the chains are linear and not crosslinked, and are likely more strongly affected by confinement effects. A qualitatively similar
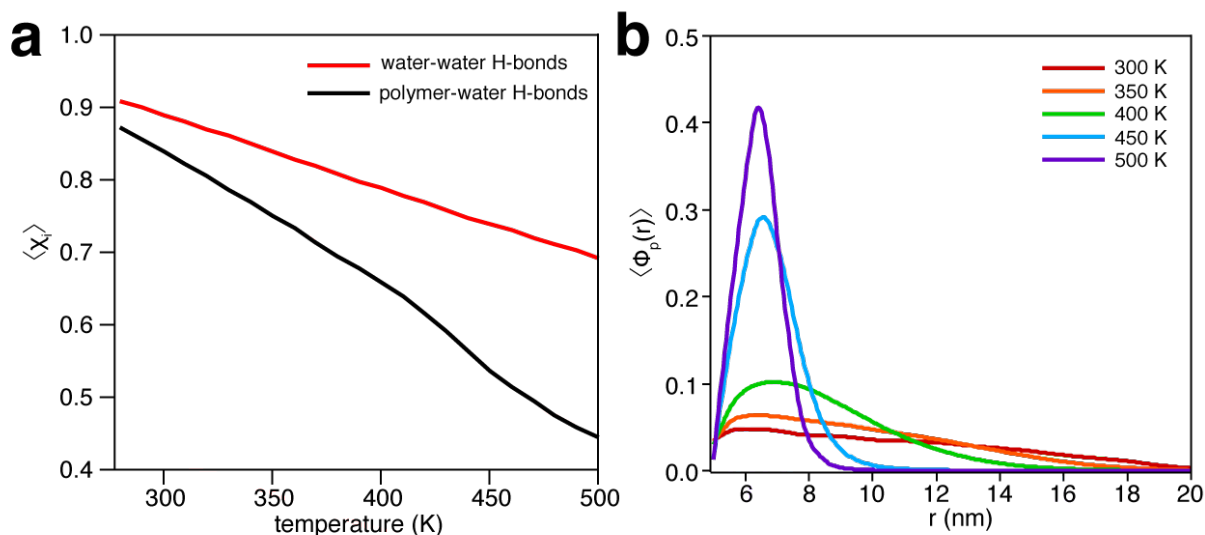
Figure 2.15: (a) Spatial average fraction of polymer-water hydrogen bonds and water-water hydrogen bonds as function of temperature for the PA nanofiber end-tethered with PEG. (b) The polymer volume fraction versus radial distance away from the PA nanofiber for different temperatures. Radius of the nanofiber is 5 nm, N_p=200, and the surface coverage is 0.07 chains nm^{-2}.
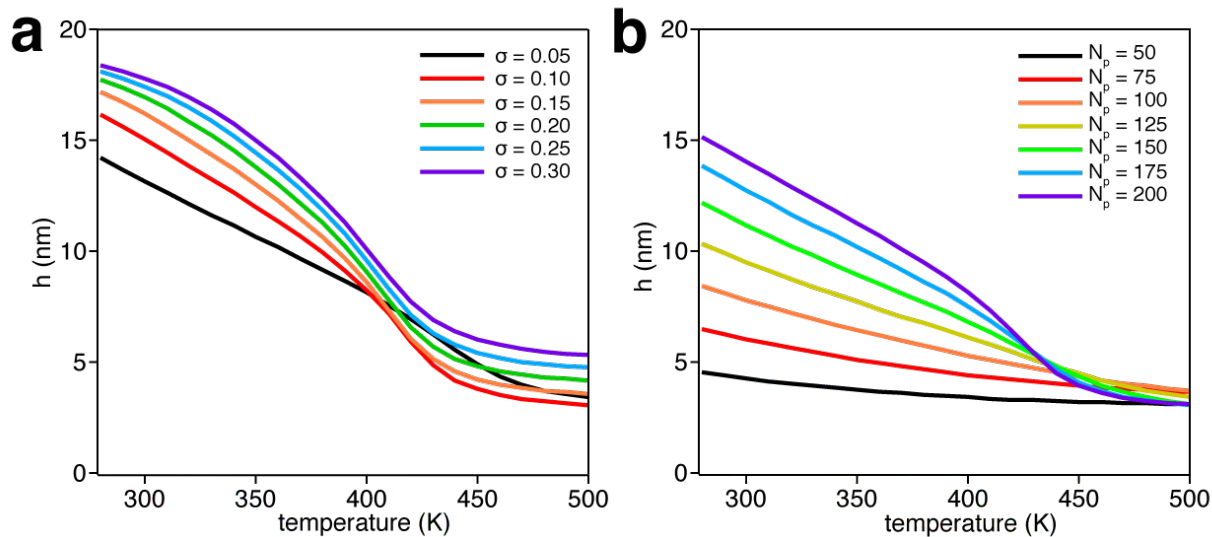
Figure 2.16: (a) Height of end-tethered PEG polymers as function of temperature for different grafting densities for fixed number of segments (N_p=200). (b) Height of end-tethered PEG polymers as function of temperature for different polymer chain lengths for fixed surface coverage of 0.07 chains^{-2}. Radius of the nanofiber is 5 nm.
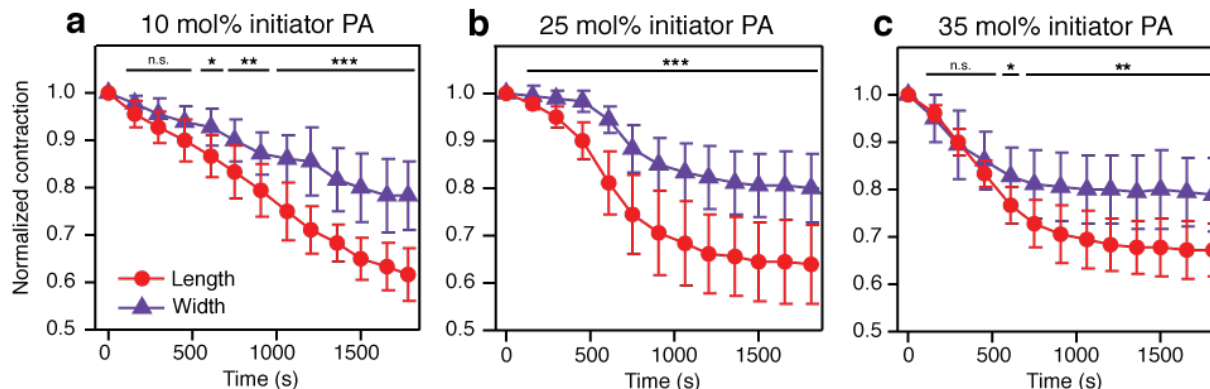
Figure 2.17: The effects of modifying grafting density on actuation at (a) 10 mol% PA1, (b) 25 mol% PA1, (c) 35 mol% PA1. Statistical analysis was performed using an unpaired two samples Student's t-test; * p<0.05, ** p<0.01, *** p<0.001; (Data are presented as mean $\pm$ s.d., n = 3).

thermal response was predicted by the model when we vary grafting density, molecular weight, and chemical composition (Fig. 2.14, Fig. 2.16). Increasing differences in brush height between the extended and collapsed states were found to occur when grafting densities and molecular weights were increased. We found that the strategy to control the thermal response is to vary the hydrophobic component of the polymer, which can drastically change the transition temperatures (Fig. 2.14c). This could be and important handle for the design of further actuating materials. In summary, the molecular approach indeed predicts the LCST behavior of the polymer and the connection between anisotropic actuation and the radial collapse of chains in a brush configuration on the nanofiber surface. We conclude that end-grafting of chains on the supramolecular fibers and mechanical reinforcement of the hydrogel by the fibers both contribute to the anisotropic actuation observed in the experimental system.

2.4 CONCLUSIONS

We have demonstrated the bottom-up molecular design of a soft anisotropic actuator based on conjugation between a supramolecular and a covalent polymer. Directed by the facile alignment and internal stability of mesogenic supramolecular polymers, it was possible to induce anisotropic

actuation in an extremely flexible, thermoresponsive covalent polymer on macroscopic scale. In the future, dynamic rearrangement of the supramolecular building blocks will add an additional level of control not possible with conventional materials, and may allow for the creation of actuators that adapt to specific applications on demand, for example by changing the direction of anisotropic actuation. We anticipate that hybrid materials based on the design principles outlined here will drive the development of superior soft actuators responsive to external stimuli and capable of performing complex mechanical tasks. The grand challenge moving forward is to explore the design of such active matter encoded molecularly to create complex forms of actuation.

2.5 MATERIALS & METHODS

Materials

Acetonitrile, ammonium hydroxide (NH$_4$OH), 2,2'-bipyridine (Bpy), a-bromoisobutyryl bromide, calcium chloride (CaCl$_2$), copper(I) bromide (CuBr), dichloromethane (DCM), di(ethylene glycol) methyl ether methacrylate (DEGMA), diisopropylethylamine (DIEA), *N,N*-dimethylformamide (DMF), diethylether, ethanol, ethyl α-bromoisobutyrate, fluorescein-*O*-methacrylate, 1,1,1,3,3,3-hexafluoro-2-propanol (HFIP), *N,N'*-methylenebis(acrylamide), methanol, 4-methylpiperidine, poly(ethylene glycol) methyl ether methacrylate of M$_n$ 500 (OEGMA$_{500}$), sodium chloride (NaCl), sodium hydroxide (NaOH), sodium persulfate (NaPS), trifluoroacetic acid (TFA), and deuterium oxide (D$_2$O), trifluoroacetic acid-*d$_1$*, and 4,4-dimethyl-4-silapentane-1-sulfonic acid were purchased from Sigma-Aldrich. Diethanolamine was received from TCI America. All fluorenylmethyloxycarbonyl (Fmoc) protected amino acids were delivered from P3 Biosystems except for Fmoc-ϵ-Ahx-OH which was obtained from aappTEC. P3 Biosystems also provided the coupling agents 2-(1H-benzotriazol-1-yl)-1,1,3,3-tetramethyluronium hexafluorophosphate (HBTU) and benzotriazol-1-yl-oxytripyrrolidinophosphonium hexafluorophosphate (PyBOP). Carboxytetramethylrhodamine (TAMRA) acid and palmitic acid were obtained from Click Chemistry Tools and Acros Organics, respectively. Triisopropylsilane (TIPS) was purchased from Chem-Impex Int'l INC. DEGMA and OEGMA$_{500}$ were passed over basic alumina to remove inhibitors immediately prior to use. All other chemicals were used as received unless specifically stated otherwise.

Peptide amphiphile synthesis and purification

PA molecules were synthesized using standard Fmoc-solid-phase peptide chemistry. Molecules PA1-3 were synthesized on Rink amide MBHA resin (aappTEC). Fmoc deprotection was performed using 20% 4-methylpiperidine in DMF for 20 minutes. The resin was then washed with DMF

and swollen with DCM. Amino acid couplings were performed with 4 equivalents of protected amino acid, 4 equivalents of HBTU, and 6 equivalents of DIEA in 50% DMF/50% DCM for 2 hours. Palmitic acid was coupled to the peptide N-terminus with 8 equivalents of palmitic acid, 8 equivalents of HBTU, 12 equivalents of DIEA in 50% DMF/50% DCM for 4 hours. Deprotection and couplings were verified through ninhydrin colorimetric assays (Kaiser test). Initiator-containing PA1 was synthesized with a Fmoc-Lys(Mtt)-OH coupled first to the Rink Amide MBHA resin. Deprotection of the 4-methyltrityl (Mtt) group on the lysine e-amine was performed by swelling the resin in DCM and adding solution of 4% TFA, 5% TIPS and 91% DCM for multiple 5 minute washes until yellow color was no longer seen in solution. α-bromoisobutyryl bromide was coupled to the free ϵ-amine with 4 equivalents a-bromoisobutyryl bromide, 1.1 equivalents PyBOP, and 6 equivalents DIEA in DCM for 4 hours. Synthesis of the peptide then continued as described above.

PAs were cleaved from resin by shaking in a solution of 95% TFA, 4% TIPS, 1% water. After cleavage, the solvent was concentrated under reduced pressure and the remaining 1 mL of solution was precipitated into an excess of cold diethyl ether. The crude product was redissolved at 10 mg mL^{-1} in water with 0.1% NH4OH. This solution was purified using standard preparatory reverse-phase high-performance liquid chromatography (HPLC) techniques on a Shimadzu Prominence instrument equipped with a Phenomenex Gemini NX-C18, 30 x 150 mm column. A mixture of water/acetonitrile containing 0.1% NH4OH was used as eluent. Pure fractions were selected based on the corresponding product signals in electrospray ionization mass spectrometry using direct injection on an Agilent 6520 Q-TOF LC-MS. Organic solvent was removed from selected fractions under reduced pressure before being frozen, lyophilized, and stored at -20°C until further use.

The purity of the PA materials used in this work was determined to be >95% from integrating the absorption signals at 220 nm in analytical liquid chromatography-mass spectrometry (LC-MS) using a Agilent 1200 system equipped with a Phenomenex Gemini C18, 1 x 100 mm column with the same Agilent 6520 Q-TOF detector (Fig. 2.18, left column). The two peaks in the analytical LC trace of PA3 (Fig. 2.18c) at an elution time of 16 and 16.3 minutes correspond to two isomers

of the TAMRA dye. The mass spectra shown in the right column of Fig. 2.18 were obtained from the whole peak region of the respective LC trace. Supplementary Tables 1-3 list the species with a minimum ion count signal of 2% of the highest intensity in the spectrum. The majority of the identified signals correspond to the expected masses of PA1-3 or their clusters, with proton-, sodium-, or ammonia adducts or combinations thereof. In the case of PA1 and PA2, a trace amount of contamination was observed with a species that had acquired an additional alanine, termed as PA4 and PA5, respectively. The addition of an amino acid such as alanine is a common occurrence in solid phase peptide synthesis and such impurities are very difficult to completely remove through HPLC purification. In our experience, the self-assembled structures of PA1 and PA2 were not affected by the presence of trace amounts of PA4 and PA5. PA structures were also confirmed through NMR spectroscopy.
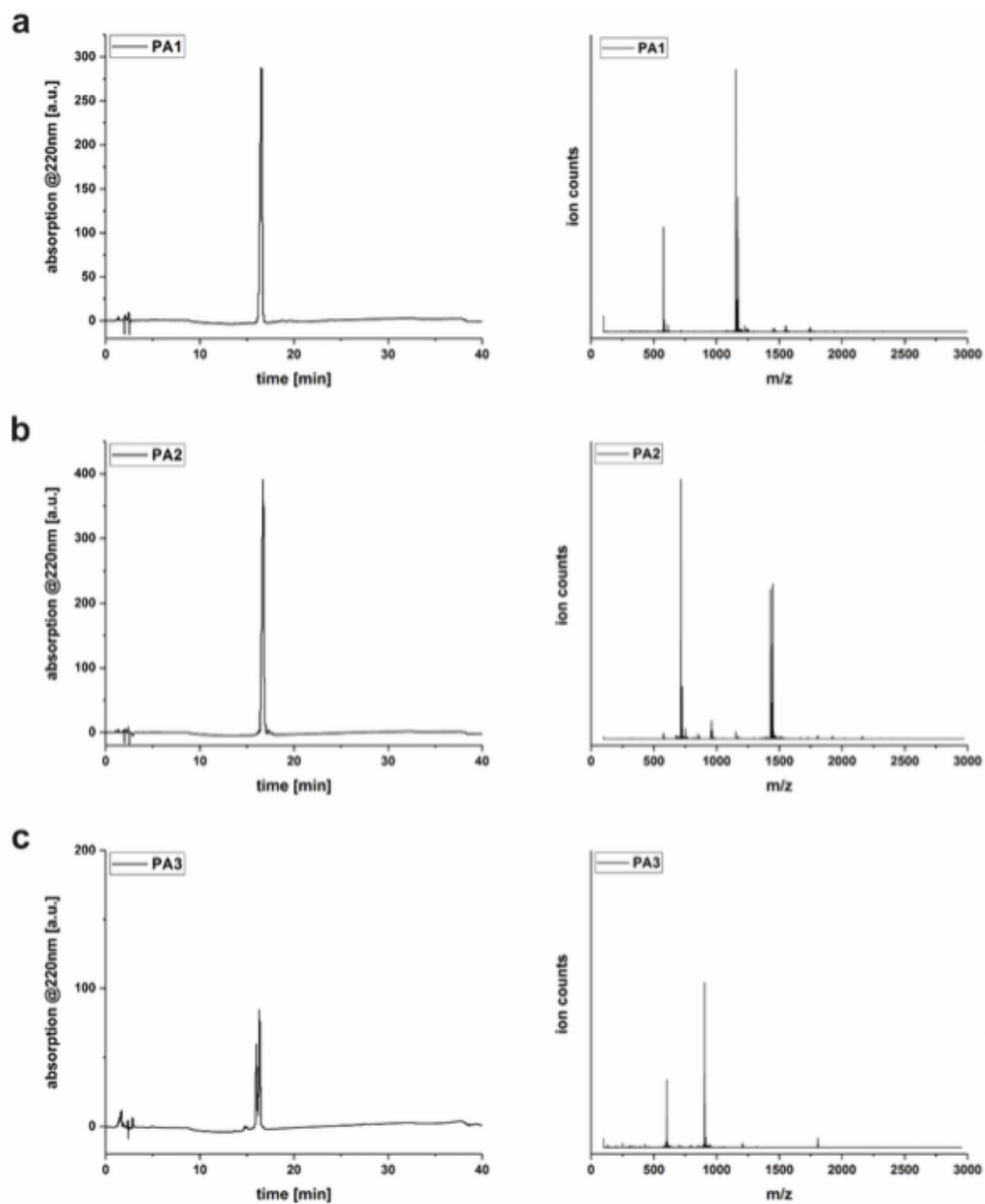
Figure 2.18: LC-MS traces (left) of (a) PA1, (b) PA2, and (c) PA3 from purity analysis. The mass spectra (right) are obtained by integrating the ion counts from the full peak region in the LC-MS trace.

Table 2.1: Mass spectral identification of HPLC purified PA1

m/z$_{expt.}$	Ion Assignment	Formula	m/z$_{theor.}$	Δ m/z
577.2859	$[\mathbf{PA1} + 2\ H]^{2+}$	$[C_{55}H_{98}N_{10}O_{16}]^{2+}$	577.3576	0.0717
585.7971	$[\mathbf{PA1} + NH_4 + H]^{2+}$	$[C_{55}H_{101}N_{11}O_{16}]^{2+}$	585.8708	0.0737
612.8002	$[\mathbf{PA4} + 2\ H]^{2+}$	$[C_{58}H_{103}N_{11}O_{17}]^{2+}$	612.8761	0.0759
1153.5993	$[\mathbf{PA1} + H]^{+}$	$[C_{55}H_{97}N_{10}O_{16}]^{+}$	1153.7079	0.1086
1159.2657	$[3\ \mathbf{PA1} + NH_4 + 2H]^{3+}$	$[C_{165}H_{294}N_{31}O_{48}]^{3+}$	1159.3834	0.1177
1162.1066	$[2\ \mathbf{PA1} + NH_4 + H]^{2+}$	$[C_{110}H_{197}N_{21}O_{32}]^{2+}$	1162.2210	0.1144
1164.5879	$[2\ \mathbf{PA1} + Na + H]^{2+}$	$[C_{110}H_{193}N_{20}NaO_{32}]^{2+}$	1164.6988	0.1109
1170.6220	$[\mathbf{PA1} + NH_4]^{+}$	$[C_{55}H_{100}N_{11}O_{16}]^{+}$	1170.7344	0.1124
1175.5756	$[\mathbf{PA1} + Na]^{+}$	$[C_{55}H_{96}N_{10}NaO_{16}]^{+}$	1175.6898	0.1142
1224.6253	$[\mathbf{PA4} + H]^{+}$	$[C_{58}H_{102}N_{11}O_{17}]^{+}$	1224.7450	0.1197
1549.1489	$[4\ \mathbf{PA1} + 2\ NH_4 + H]^{3+}$	$[C_{220}H_{393}N_{42}O_{64}]^{3+}$	1549.2924	0.1435
1554.8224	$[4\ \mathbf{PA1} + 3\ NH_4]^{3+}$	$[C_{220}H_{393}N_{43}O_{64}]^{3+}$	1554.9679	0.1455

Table 2.2: Mass spectral identification of HPLC purified PA2

m/z$_{expt.}$	Ion Assignment	Formula	m/z$_{theor.}$	Δ (m/z)
577.2850	$[\mathbf{PA1} + 2\ H]^{2+}$	$[C_{55}H_{98}N_{10}O_{16}]^{2+}$	577.3576	0.0726
715.3001	$[\mathbf{PA2} + 2H]^{2+}$	$[C_{65}H_{115}BrN_{12}O_{18}]^{2+}$	715.3812	0.0811
723.8114	$[\mathbf{PA2} + NH_4 + H]^{2+}$	$[C_{65}H_{118}BrN_{13}O_{18}]^{2+}$	723.8945	0.0831
750.8145	$[\mathbf{PA5} + 2\ H]^{2+}$	$[C_{68}H_{120}BrN_{13}O_{19}]^{2+}$	750.8998	0.0853
853.3498	unknown double charged	-	-	-
953.4043	$[2\ \mathbf{PA2} + 3\ H]^{3+}$	$[C_{130}H_{229}Br_2N_{24}O_{36}]^{3+}$	953.5059	0.1016
959.0796	$[2\ \mathbf{PA2} + NH_4 + 2\ H]^{3+}$	$[C_{130}H_{232}Br_2N_{25}O_{36}]^{3+}$	959.1814	0.1018
964.7538	$[2\ \mathbf{PA2} + 2\ NH_4 + H]^{3+}$	$[C_{130}H_{235}Br_2N_{26}O_{36}]^{3+}$	964.8569	0.1031
1153.5943	$[\mathbf{PA1} + H]^{+}$	$[C_{55}H_{97}N_{10}O_{16}]^{+}$	1153.7079	0.1136
1429.6266	$[\mathbf{PA2} + H]^{+}$	$[C_{65}H_{114}BrN_{12}O_{18}]^{+}$	1429.7552	0.1286
1435.2900	$[3\ \mathbf{PA2} + NH_4 + 2\ H]^{3+}$	$[C_{195}H_{345}Br_3N_{37}O_{54}]^{3+}$	1435.4307	0.1407
1437.6231	unknown double charged	-	-	-
1442.6340	unknown triple charged	-	-	-
1446.6519	$[\mathbf{PA2} + NH_4]^{+}$	$[C_{65}H_{117}BrN_{13}O_{18}]^{+}$	1446.7817	0.1298

Table 2.3: Mass spectral identification of HPLC purified PA3

m/z$_{expt.}$	Ion Assignment	Formula	m/z$_{theor.}$	Δ (m/z)
597.3403	unknown triple charged	-	-	-
603.0170	[**PA3** + 3 H]$^{3+}$	[$C_{92}H_{142}N_{15}O_{22}$]$^{3+}$	603.0146	0.0024
610.3430	[**PA3** + Na + 2 H]$^{3+}$	[$C_{92}H_{141}N_{15}NaO_{22}$]$^{3+}$	610.3419	0.0011
897.0110	unknown double charged	-	-	-
904.0224	[**PA3** + 2 H]$^{2+}$	[$C_{92}H_{141}N_{15}O_{22}$]$^{2+}$	904.0183	0.0041
915.0104	[**PA3** + Na + H]$^{2+}$	[$C_{92}H_{140}N_{15}NaO_{22}$]$^{2+}$	915.0092	0.0012
1205.0218	[2 **PA3** + 3 H]$^{3+}$	[$C_{184}H_{281}N_{30}O_{44}$]$^{3+}$	1205.0219	0.0001
1807.0271	[**PA3** + H]$^{+}$	[$C_{92}H_{140}N_{15}O_{22}$]$^{+}$	1807.0292	0.0021

<u>**PA1**</u> ^{13}C NMR (125 MHz, TFA-d$_1$): δ 13.5 (Pal-CH$_3$), 16.8 – 17.1 (3x Ala-$\underline{C}_{(\beta)}$H$_3$), 17.9 (2x Val-$\underline{C}_{(\gamma)}$H$_3$), 18.2 (Val-$\underline{C}_{(\gamma)}$H$_3$), 18.6 (Val-$\underline{C}_{(\gamma)}$H$_3$), 18.7 (Val-$\underline{C}_{(\gamma)}$H$_3$), 18.8 (Val-$\underline{C}_{(\gamma)}$H$_3$), 23.2 (several Pal-$\underline{C}$H$_2$), 23.4 (Lys-$\underline{C}_{(\gamma)}$H$_2$), 27.1 (Pal-$\underline{C}_{(\beta)}$H$_2$), 27.5 (2x Glu-$\underline{C}_{(\beta)}$H$_2$), 27.6 (Glu-$\underline{C}_{(\beta)}$H$_2$), 28.8 (Lys-C(d)H$_2$), 29.7 – 30.4 (3x Glu-$\underline{C}_{(\gamma)}$H$_2$, several Pal-$\underline{C}$H$_2$), 31.8 (2x Bib-CH$_3$), 31.9 (Val-$\underline{C}_{(\beta)}$H), 32.0 (Val-$\underline{C}_{(\beta)}$H), 32.1 (Lys-$\underline{C}_{(\beta)}$H$_2$), 32.3 (Val-$\underline{C}_{(\beta)}$H), 32.7 (several Pal-$\underline{C}$H$_2$), 35.7 (Pal-$\underline{C}_{(\alpha)}$H), 41.3 (Lys-$\underline{C}_{(\epsilon)}H_2$), 51.1 (2x Ala-$\underline{C}_{(\alpha)}$H), 51.4 (Ala-$\underline{C}_{(\alpha)}$H), 54.4 (2x Glu-$\underline{C}_{(\alpha)}$H), 54.6 (Glu-$\underline{C}_{(\alpha)}$H), 55.1 (Lys-$\underline{C}_{(\alpha)}$H), 60.4 ($\underline{C}$(CH$_3$)$_2$Br), 60.9 (Val-$\underline{C}_{(\alpha)}$H), 61.5 (Val-$\underline{C}_{(\alpha)}$H), 62.1 (Val-$\underline{C}_{(\alpha)}$H), 173.6 (Val-$\underline{C}$O), 174.2 ($\underline{C}$O), 174.3 ($\underline{C}$O), 174.5 ($\underline{C}$O), 174.7 ($\underline{C}$O), 175.5 ($\underline{C}$O), 175.8 ($\underline{C}$O), 176.0 ($\underline{C}$O), 176.4 ($\underline{C}$O), 177.5 (Bib-$\underline{C}$O), 178.8 (Lys-$\underline{C}$O), 180.5 (Glu-$\underline{C}_{(\delta)}$O), 180.6 (2x Glu-$\underline{C}_{(\delta)}$O), 181.6 (Pal-$\underline{C}$O).

^{1}H NMR (600 MHz, TFA-d_1): δ 0.80 (t, 3H, J = 6.5 Hz, Pal-$\underline{C}$H$_3$), 0.92 – 0.99 (m, 18H, 6x Val-$\underline{C}_{(\gamma)}$H$_3$), 1.21 – 1.37 (m, 24H, several Pal-$\underline{C}$H$_2$), 1.44 – 1.54 (m, 11H, 3x Ala-$\underline{C}_{(\beta)}$H$_3$, Lys-$\underline{C}_{(\gamma)}$H$_2$), 1.63 – 1.73 (m, 4H, Lys-$\underline{C}_{(\delta)}$H$_2$, Pal-$\underline{C}_{(\beta)}$H$_2$), 1.84 – 1.99 (m, 8H, 2x Bib-$\underline{C}$H$_3$, Lys-$\underline{C}_{(\beta)}$H$_2$), 2.04 – 2.21 (m, 5H, Glu-$\underline{C}_{(\beta)}$H$_2$, 3x Val-$\underline{C}_{(\beta)}$H), 2.25 – 2.34 (m, 4H, 2x Glu-$\underline{C}_{(\beta)}$H$_2$), 2.58 – 2.64 (m, 8H, 3x Glu-$\underline{C}_{(\gamma)}$H$_2$, Pal-$\underline{C}_{(\alpha)}$H$_2$), 3.36 (t, 2H, J = 6.60 Hz, Lys-$\underline{C}_{(\epsilon)}H_2$), 4.38 (d, 1H, J = 8.24 Hz, Val-$\underline{C}_{(\alpha)}$H), 4.43 (d, 1H, J = 7.85 Hz, Val-$\underline{C}_{(\alpha)}$H), 4.52 (d, 1H, J = 7.73 Hz, Val-$\underline{C}_{(\alpha)}$H), 4.59 – 4.65 (m, 4H, 3x Ala-$\underline{C}_{(\alpha)}$H, Lys-$\underline{C}_{(\alpha)}$H), 4.77 – 4.82 (m, 3H, 3x Glu-$\underline{C}_{(\alpha)}$H).

PA2 ^{13}C NMR (125 MHz, TFA-$\underline{d}_1$): δ 13.5 (Pal-$\underline{C}$H$_3$), 16.8 (Ala-$\underline{C}_{(\beta)}$H$_3$), 16.9 (Ala-$\underline{C}_{(\beta)}$H$_3$), 17.1 (Ala-$\underline{C}_{(\beta)}$H$_3$), 17.9 (2x Val-$\underline{C}_{(\gamma)}$H$_3$), 18.2 (Val-$\underline{C}_{(\gamma)}$H$_3$), 18.6 (Val-$\underline{C}_{(\gamma)}$H$_3$), 18.7 (Val-$\underline{C}_{(\gamma)}$H$_3$), 18.8 (Val-$\underline{C}_{(\gamma)}$H$_3$), 23.2 (several Pal-$\underline{C}$H$_2$), 27.1 (Pal-$\underline{C}_{(\beta)}$H$_2$), 27.3 (Glu-$\underline{C}_{(\beta)}$H$_2$), 27.6 (Glu-$\underline{C}_{(\beta)}$H$_2$), 27.7 (Glu-$\underline{C}_{(\beta)}$H$_2$), 29.7 – 30.4 (3x Glu-$\underline{C}_{(\gamma)}$H$_2$, several Pal-$\underline{C}$H$_2$), 31.9 (Val-$\underline{C}_{(\beta)}$H), 32.0 (Val-$\underline{C}_{(\beta)}$H), 32.3 (Val-$\underline{C}_{(\beta)}$H), 32.7 (several Pal-$\underline{C}$H$_2$), 35.7 (Pal-$\underline{C}_{(\alpha)}$H$_2$), 51.1 (Ala$_{(\alpha)}$-$\underline{C}$H), 51.2 (Ala$_{(\alpha)}$-$\underline{C}$H), 51.4 (Ala$_{(\alpha)}$-$\underline{C}$H), 53.9 (Glu$_{(\alpha)}$-$\underline{C}$H), 54.4 (Glu$_{(\alpha)}$-$\underline{C}$H), 54.7 (Glu$_{(\alpha)}$-$\underline{C}$H), 60.9 (Val$_{(\alpha)}$-$\underline{C}$H), 61.6 (Val$_{(\alpha)}$-$\underline{C}$H), 62.2 (Val$_{(\alpha)}$-$\underline{C}$H), 173.6 (Val-$\underline{C}$O), 174.3 ($\underline{C}$O), 174.4 ($\underline{C}$O), 174.5 ($\underline{C}$O), 174.7 ($\underline{C}$O), 175.5 (Ala-$\underline{C}$O), 176.0 (Ala-$\underline{C}$O), 176.5 (Ala-$\underline{C}$O), 177.7 (Glu-$\underline{C}$O), 180.6 (Glu-$\underline{C}_{(\delta)}$O), 180.6 (Glu-$\underline{C}_{(\delta)}$O), 180.7 (Glu-$\underline{C}_{(\delta)}$O), 181.6 (Pal-$\underline{C}$O);

^{1}H NMR (600 MHz, TFA-d_1): δ 0.81 (t, 3H, J = 6.6 Hz, Pal-$\underline{C}$H$_3$), 0.93 – 1.00 (m, 18H, 6x Val-$\underline{C}_{(\gamma)}$H$_3$), 1.20 – 1.37 (m, 24H, 12x Pal-$\underline{C}$H$_2$), 1.44 – 1.47 (m, 9H, 3x Ala-$\underline{C}_{(\beta)}$H$_3$), 1.70 – 1.75 (m, 2H, Pal-$\underline{C}_{(\beta)}$H$_2$), 2.06 – 2.19 (m, 5H, Glu-$\underline{C}_{(\beta)}$H$_2$, 3x Val-$\underline{C}_{(\beta)}$H), 2.27 – 2.37 (m, 4H, 2x Glu-$\underline{C}_{(\beta)}$H$_2$), 2.59 – 2.66 (m, 8H, 3x Glu-$\underline{C}_{(\gamma)}$H$_2$, Pal-$\underline{C}_{(\alpha)}$H$_2$), 4.39 (d, 1H, J = 8.4 Hz, Val-$\underline{C}_{(\alpha)}$H), 4.44 (d, 1H, J = 8.0 Hz, Val-$\underline{C}_{(\alpha)}$H), 4.53 (d, 1H, J = 7.7 Hz, Val-$\underline{C}_{(\alpha)}$H), 4.60 – 4.66 (m, 3H, 3x Ala-$\underline{C}_{(\alpha)}$H), 4.78 – 4.85 (m, 3H, 3x Glu-$\underline{C}_{(\alpha)}$H).

Tube fabrication

PA solutions were prepared by dissolving PAs 1 and 2 in a 1:9 molar ratio in HFIP and sonicating for 1 minute. The solvent was removed and the resulting film dissolved at 10 mg/mL in a solution of 50 mM Tris buffer and 150 mM NaCl. The solution was pH-adjusted to pH 7.4 with 1M NaOH and sonicated for 2 minutes. The solutions were annealed at 80°C for 30 minutes and slowly cooled to room temperature over the course of several hours to create a LC solution of PA nanofiber bundles.

Tubes were fabricated using a method adapted from a previously described protocol.[70] Briefly, PA solution was injected via a 25-gauge needle into the annular gap of a 4 mm inner diameter shearing chamber. A 3 mm diameter steel rod was inserted and the chamber fitted onto a 50-mL falcon tube filled with 100 mM CaCl$_2$. The device was loaded onto a modified metal lathe and ro-

tated for 308 ± 5 RPM for 120 seconds, exerting an estimated rotational shear strain of 97 s^{-1}. The translational stage was then retracted slowly, causing CaCl$_2$ solution to flow into the glass tube, immediately gelling the PA suspension. The inner rod was completely removed and the resulting tube was carefully extracted. Laterally aligned samples were prepared in a similar manner but without rotational shear applied; the strain applied in this case is 5-10 s^{-1}.

Hybrid tube polymers

In a 20-mL scintillation vial, 0.1153 g DEGMA (0.613 mmol, 2850 equiv) and 0.0161g OEGMA$_{500}$ (0.032 mmol, 150 equiv) were mixed with 1.3 mg NBAA (8.43 µmol, 1 wt% of total monomer) and 1.51 mg ascorbic acid (8.6 µmol, 40 equiv) in 1.5:1 water:methanol (5 mL total). Trace amounts of 4,4-dimethyl-4-silapentane-1-sulfonic acid were added as an internal NMR standard. The solution was mixed and a circumferentially aligned PA tube gel (0.31 mg PA1, 2.19 mg PA2), made as described above, was added to the solution. The vial was sealed with a rubber septum and degassed with N$_2$ for 15 minutes. Separately, 3.3 mg CuBr and 8.0 mg Bpy was dissolved in 10 mL methanol in a 50-mL Schlenk flask and degassed with N$_2$. The reaction was initiated by injecting 0.1 mL CuBr/Bpy stock into the reaction vial and placing within a 45 °C oil bath for 16 h. 40 µL aliquots were removed at t = 0 h and 16 h, and diluted in D$_2$O for ^{1}H NMR analysis of monomer conversion. After 16h, tubes were removed from monomer solution and rinsed repeatedly with Milli-Q water to remove residual monomer. Samples were stored in Milli-Q water until further analysis.

Covalent tube polymer

0.2273 g DEGMA (1.2 mmol), 0.0315 g OEGMA$_{500}$ (0.063 mmol), 2.4 mg NBAA (15.57 µmol, 1 wt% of total monomer), and 2.4 mg NaPS (1.01 µmol, 1 wt% of total monomer) were dissolved in 90 µL Milli-Q water and 60 µL ethanol. The mixture was degassed with N$_2$ for 15 minutes, then placed in a 4 mm diameter cylindrical Teflon mold with a 3 mm central steel post. The mold was sealed

and placed in a 67 °C water bath for 19 hours. The covalent polymer hydrogel was then carefully removed from the Teflon mold, rinsed with Milli-Q water, and stored in Milli-Q water until further analysis.

Composite tube polymer

Water-soluble ATRP initiator 2-bromanyl-*N,N*-bis(2-hydroxyethyl)-2-methyl propanamide was synthesized by the addition of α-bromoisobutyryl bromide dropwise to a stirred solution of dry diethanolamine in DCM under nitrogen atmosphere overnight. The resulting mixture was extracted with 0.5 M HCl and the organic phase dried under reduced pressure. The initiator was dissolved in a 1:9 molar ratio with PA2 in HFIP with sonication, then the solvent was removed and the resulting film redissolved at 1 w/v% PA2 in a solution of 50 mM Tris buffer and 150 mM NaCl. The solution was pH-adjusted to pH 7.4 with 1 M NaOH and sonicated for 2 minutes. The solutions were annealed at 80 °C for 30 minutes and slowly cooled to room temperature over the course of several hours. Tubes of the annealed solution were prepared as described above, and the tubes subsequently polymerized using the procedure for the hybrid polymers immediately after fabrication.

NMR spectroscopy

Structural analysis of PA1 and PA2 was performed with deuterated trifluoroacetic acid-d_1 as the solvent on an Agilent DD 600 MHz w/HCN cryoprobe (^{1}H) and a Bruker Avance III 500 MHz w/direct cryoprobe (^{13}C). Chemical shifts are relative to the solvent signal. Structural assignments were performed using ^{1}H-^{1}H-gCOSY, ^{1}H-^{13}C-gHSCQAD, and ^{1}H-^{13}C-gHMBCAD.

Anisotropy measurements

Tubes were sectioned into 7-10 mm segments and placed within a 20 mL glass scintillation vial on a polypropylene base centered on a 21-gauge needle to prevent translational motion upon

heating. The scintillation vial equipped with a temperature probe was filled with sonicated Milli-Q water and heated for 30-40 minutes with a hotplate. A representative temperature ramp is shown below. Images were taken every 30 seconds with a Nikon D5100 camera equipped with a Nikon AF-S DX 18-55 mm lens. Images from every 2.5 minutes were analyzed by measuring length and width at three different tube positions per direction in each image. Distances were normalized to length at t=0. Three independent tubes were measured for each sample condition and averaged. Error bars represent one standard deviation.
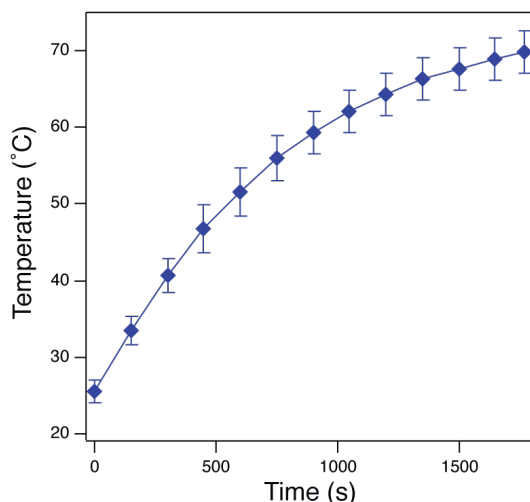
Figure 2.19: Average heating curve of samples heated in Fig. 2.6and Fig. 2.12b. (mean ± s.d., n = 20)

Polarized optical microscopy

For cross-sectional images the tubes were sectioned into thin segments of approximately 1mm thickness cut perpendicular to the tube's long axis. The images of the tube's walls were obtained after sectioning along the tube's long axis. The samples were placed in glass bottom 35mm-dishes (MatTek Corporation, P35G-1.5-14-C) filled with Milli-Q water. The samples were then imaged in between two perpendicular light polarizers using a Leica DM750 P instrument in reflection mode with a 4x magnification using Leica Application Suite V4.2 software. A sample stage allowed for

the precise rotation and x, y-positioning of the samples. Cross-sectional images were stitched using the ImageJ plugin tools "MosaicJ" and Grid/Collection Stitching by Preibisch *et al.*[122] Bright-field images were recorded using the same instrument without the light polarizers.

Small-angle X-ray scattering

SAXS measurements were performed at beamline 5-ID-D of the DuPont-Northwestern-Dow Collaborative Access Team (DND-CAT) Synchrotron Research Center at the Advanced Photon Source, Argonne National Laboratory. Liquid samples were prepared at 1 w/v% in 1.5 mm quartz capillaries (Charles Supper), while gel samples were sectioned from tube samples and placed with aqueous solution in an aluminum three-well sample holder with Kapton sides. Data was collected using an energy of 17 keV using a CCD detector positioned 245 cm behind the sample. Scattering intensities were recorded within a q range of $0.0024 < q < 0.40$ Å^{-1}, where the wave vector q is defined as $q = (4\pi/\lambda)sin(\theta/2)$ where θ is the scattering angle.

For the plot of integrated intensity vs. azimuthal angle "Fit2D" software[123] was used to average the 2D SAXS images of the tubes from at least two separate measurements and the background from a solvent-containing well was subtracted to obtain a 2D image. A radial integration in the q range of $0.0024 < q < 0.0135$ Å^{-1} with an azimuthal angle range of 270 degrees to exclude the beamstop was performed.

Confocal laser-scanning microscopy

Fluorescently labeled hybrid tubes were prepared analogue to the procedure described above. Fluorescent PA scaffold was prepared by coassembling TAMRA functionalized PA3 (Fig. 2.20) with PA1 and PA2 at a molar ratio of 0.01/0.1/0.89. Fluorescein-*O*-methacrylate was added to the monomer solution at 1 wt% of the monomer fraction to fluorescently label the covalent polymer through copolymerization. For confocal imaging, the tubes were cut along the tubes long axis (tube wall) or sectioned into thin segments of approximately 1 mm thickness cut perpendicular to

the tube's long axis (cross-section). The samples were then placed in glass bottom 35 mm-dishes (MatTek Corporation, P35G-1.5-14-C) filled with Milli-Q water and visualized using a Nikon A1R confocal laser-scanning microscope equipped with GaAsP detectors.
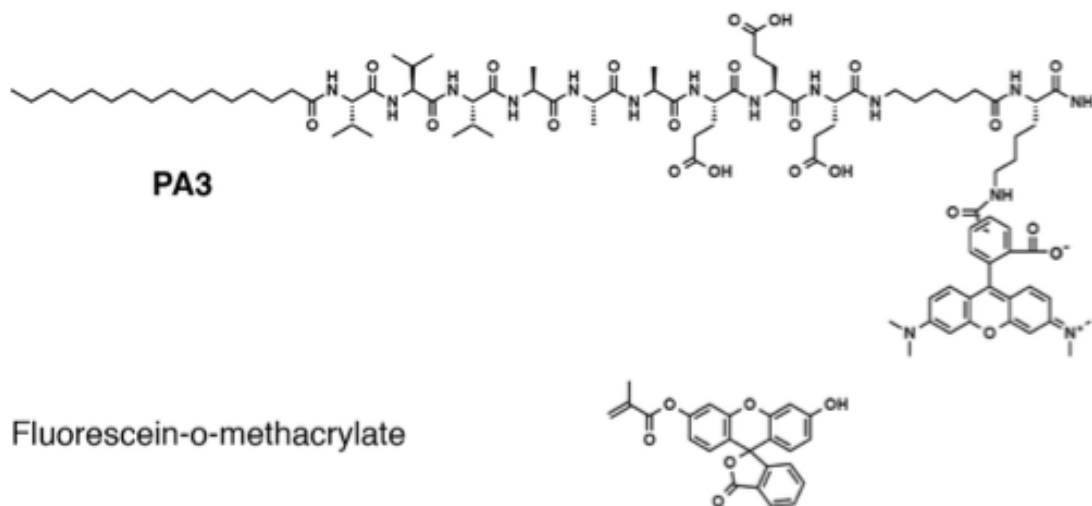
Figure 2.20: Structures of fluorescent molecules used in characterization experiments.

Scanning electron microscopy

Hybrid tubes were dehydrated by incubation in a series of ethanol solutions of increasing concentration. Ethanol was subsequently removed by critical point drying (Tousimis Samdri-795). Extra caution was taken to ensure the samples were not heated above the lower critical solution temperature of the polymer material during the exchange. Dehydrated hybrid tubes were mounted on stubs using carbon glue and coated with 21 nm of osmium (Filgen, OPC-60A) to create a conductive sample surface. All SEM images were taken using a Hitachi SU8030 or LEO 1525 instrument operating at an accelerating voltage of 2 kV.

Liquid chromotography-Mass spectrometry

The purity of the PAs after HPLC purification was determined by analytical LC-MS using an Agilent 1200 system equipped with a Phenomenex Gemini C18, 1 x 100 mm column, detector

Agilent 6520 Q-TOF LC-MS. Gradient: acetonitrile 5% for 5 min at 50 µL min^{-1}, 5 – 95% over 25 min at 50 µL min^{-1} followed by 95% for 5 min at µL min^{-1}. Peaks were detected at 220 nm.

Gel permeation chromatography

Samples were taken by polymerizing hybrids as described above with additional soluble ethyl a-bromoisobutyrate, and aliquots were taken from the aqueous solution. Aliquots were dialyzed against Milli-Q water, lyophilized, and reconstituted in tetrahydrofuran (THF). Molecular weights and molecular weight distributions were determined by size exclusion chromatography in THF at 25°C using two Varian PolyPore 300x7.5mm columns (flow rate 1 mL min^{-1}). Detection was performed with multi-angle light scattering (18-angle Dawn Heleos II), viscometer (ViscoStar-II), and differential refractive index (OptiLab T-rex) detectors.

Cryogenic-transmission electron microscopy

Cryo-TEM was performed using a JEOL 1230 TEM working at 100 kV accelerating voltage. Samples were plunge frozen using a Vitrobot Mark IV (FEI) vitrification robot at room temperature at 95-100% humidity. 7.5 µL of sample solution (0.1 w/v%, diluted from 1 w/v% immediately before grid preparation) were placed on 300-mesh copper grids with lacey carbon support, blotted, and plunge frozen into liquid ethane. Samples were transferred into a liquid nitrogen bath, and placed into a Gatan 626 cryo-holder through a cryo-transfer stage. Images were acquired using a Gatan 831 CCD camera.

Microindentation

Indentation tests were carried out using an axisymmetric probe tack device, consisting of a piezoelectric stepping motor connected in parallel to a load transducer attached to a flat cylindrical indenter with a radius (R) of 0.59 mm. Displacement was monitored using an optical sensor with submicrometer sensitivity. All samples with thickness (h) of 0.5 mm were fixed on a glass plate

with a camera underneath providing optional imaging. The indenter approached the sample with a constant velocity of 10 μm s⁻¹ until a specified load, ranging from 10 to 25 mN, was reached. The resulting load (P) and displacement (d) data were used to calculate the modulus of the sample. The Young's modulus (E) of the sample was calculated by using the relation between the compliance ($C = d/P$) and the modulus at a specified contact radius (a) assuming Poisson's ratio of the sample equals 0.5.[124]

$$E = \frac{3P}{8\delta a}\left(1 + \frac{1.33a}{h} + 1.33\left(\frac{a}{h}\right)^3\right)^{-1} \qquad (4)$$

An average value of E from the above equation from 10 – 40% strain was used as the modulus. Moduli from multiple indents (3 – 5 per sample) were averaged to give the reported modulus.

Tensile testing

Force-displacement measurements were taken on a Sintech 20G apparatus with a 2.5N load cell. Tube samples were removed from water, cut in half longitudinally using a razor blade, and flattened immediately before loading into the apparatus. Gage length and sample dimensions were measured and samples were approximated as a rectangular cross-section. Samples were extended at 5 mm min⁻¹ until failure was observed. Data was analyzed using Testworks software to determine modulus and strain at break. Moduli and strain were averaged across multiple samples (n = 6 – 12) to give reported values.

Calculation of mechanical properties

The work capacity of the circumferentially aligned tube was calculated using established methods in the actuator field,[125] dividing the work of contraction (kJ) by the mass (kg) of the hybrid material, using the equation below:

$$Work\ capacity\ (kJ/kg) = m_w g \Delta h / m_h \qquad (5)$$

where m_w is mass of the weights hung from the actuator (kg), g is gravitational acceleration (9.8 m s^{-2}), Δh is the displacement of the weight (m), and m_h is the mass of the hybrid (not including water).

The volumetric energy density is calculated as the work during contraction (kJ) divided by the volume of the actuator (m^3) using the equation below:

$$Volumetric\ energy\ density\ (kJ/m^3) = m_w g \Delta h/V \qquad (6)$$

where V is the volume of the actuator tube (m^3), calculated by multiplying the surface area of the ring by the initial height of the sample.

Statistical analysis

Using OriginPro 2017 software, a Welch corrected two sample t-test was performed to determine if the normalized width and length of a tube at a given timepoint show statistically significant differences. Statistically significant differences are indicated by p < 0.05 (*), p < 0.01 (**), and p < 0.001 (***).

Finite element analysis: isotropic and anisotropic swelling of hydrogel

For an isotropic swelling hydrogel, the polymer network deforms homogeneously, and $\lambda = \lambda_x = \lambda_y = \lambda_z = \phi^{-1/3}$. Following the notation in the main text we can rewrite Eq. 1 as

$$F(\phi, T) = \frac{1}{2} NkT \left(\frac{3}{\phi^{2/3}} - 3 + ln\phi \right) + kT \frac{V_m}{v} \left[\left(\frac{1}{\phi} - 1 \right) ln(1 - \phi) + \chi(1 - \phi) \right] \qquad (7)$$

When the free swelling gel is in equilibrium with the external solvent, its osmotic pressure Π must be zero, i.e.,

$$\Pi = -\frac{\delta F(\phi,T)}{\delta V} = \frac{\phi^2}{V_m}\frac{\delta F(\phi,T)}{\delta \phi} = 0 \tag{8}$$

where the number of monomers is assumed to be constant. Inserting Equation 7 in Equation 8 and substituting ϕ with λ^{-3} gives

$$\frac{\chi}{\lambda^3} = \frac{1}{2}\frac{N_v}{V_m}(1 - 2\lambda^2) - \lambda^3 ln\left(1 - \frac{1}{\lambda^3}\right) - 1 \tag{9}$$

For an anisotropic gel constrained along the z direction, $\lambda = \lambda_x = \lambda_y = (\phi\lambda_z)^{-1/2}$. The equilibrium is reached when the stress in the free directions (i.e., x and y directions) equals to zero, which gives

$$\frac{\chi}{\lambda^2\lambda_z} = \frac{1}{2}\frac{N_v}{V_m}(1 - 2\lambda^2) - \lambda^2\lambda_z ln\left(1 - \frac{1}{\lambda^2\lambda_z}\right) - 1 \tag{10}$$

When $\lambda = \lambda_z$, the stretching ratios in all directions are equal, thus Equation 10 reduces to Equation 9, indicating that the anisotropic gel reaches an isotropic swollen state. The corresponding χ given by Equation 10 at $\lambda = \lambda_z$ is denoted by χ_C in the following texts.

For an anisotropic gel constrained by rigid fibers oriented to the z-axis, λ is homogeneous if the fibers are assumed to be infinitely long, while λ_x and λ_y are inhomogeneous due to the constraint from the fibers. As such, it is challenging to achieve an analytical solution of the $(\lambda_x, \lambda_y, \lambda_z)$ distribution at equilibrium, and we therefore follow a finite element approach to numerically solve λ_x and λ_y with a fixed value of λ_z under periodic boundary conditions.

Finite element analysis simulations

The finite element simulations are performed in the commercial software ABAQUS. The constitutive model of the hydrogel (Equation 1 in the main text) is implemented using the UHYPER

subroutine. The hydrogel matrix is meshed with C3D8R elements. In all the simulations, the mesh density is validated in mesh convergence studies. The periodic boundary conditions are imposed as follows: Let S^+ and S^- be a pair of opposite boundaries defined by the lattice vector l; for an arbitrary point located at r on S^+ and its duplicate point located at $r - l$ on S^-, their displacements $u(r)$ and $u(r - l)$ must satisfy

$$u(r) - u(r - l) = l' - l \tag{11}$$

where l' is the deformed lattice vector. Because $l' - l$ is the same for all pairs of duplicate points on S^+ and S^-, Equation 11 can be easily implemented using constraint equations in ABAQUS.

Consistent with the contraction experiments described in the main text, the dimensional change of a constrained gel is induced in the simulation when $\chi(T)$ varies. Specifically, the initial and final χ (denoted by $\chi(T_i)$ and $\chi(T_f)$, respectively) are defined by the given initial volume fraction and shrinkage for an isotropic shrinking gel. At χ_C, a constrained gel unit cell with a PA nanofiber embedded is in equilibrium and stress-free; when its χ varies from χ_C to $\chi(T_i)$ and $\chi(T_f)$, the constrained gel contracts correspondingly and we can then measure the contraction ratio from $\chi(T_i)$ to $\chi(T_f)$.

In the simulations, the pre-defined isotropic contraction of the swelling gel is 77%. The initial stretching ratio of the covalent polymer gel at room temperature is estimated to be 1.77. Using Equation 9, we can calculate the corresponding $\chi(T_i)$ and $\chi(T_f)$ and use them for the anisotropic gel contraction simulations. The parameter χ_C is calculated from Equation 10, using $\lambda = \lambda_z = 3.54$. The dimensionless quantity Nv/V_m is estimated as followed. Let N_{CL}, m_{CL}, M_{CL} denote the number, mass and molar mass of the crosslinkers respectively, $\rho_m \approx 10^6 g/m^3$ be the density of the DEGMA/OEGMA polymer, and $v = 3 \times 10^{-29} m^3$ be the volume of a single water molecule. The weight percentage of the crosslinkers with respect to the weight of the polymer is $w_{CL} = 1\%$. The number of chains between the adjacent crosslinking junctions is given by $N = \frac{1}{2}(4N_{CL}) = $

$2N_A m_C L/M_{CL}$ assuming that 4 subchains are attached to each crosslinker. $V_m = m_m/\rho_m$ where m_m is the mass of the polymer. $M_{CL} = 154 g/mol$ Therefore,

$$\frac{N_v}{V_m} = \frac{2N_A m_{CL} v \rho_m}{M_{CL} m_m} = \frac{2N_A w_{CL} v \rho_m}{M_{CL}} \approx 2 \times 10^{-3} \tag{12}$$

It is noteworthy that the PA nanofibers are modeled as rigid rods in our simulations due to the remarkable difference between the moduli of the gel matrix and the PA nanofiber. Per Equation 1, the initial shear modulus (when $\lambda = \lambda_y = \lambda_z = 1$) of the gel matrix is given by NkT/V_m. Assuming a Poisson ratio of 0.5, the Young's modulus of the gel matrix $E_{matrix} \approx 3NkT/V_m$. On the other hand, the Young's modulus of the PA nanofiber can be related to its persistence length l_p via $E_{fiber} \approx l_p kT/l$,[126,127] where $l = \pi r^4/4$ is the geometrical moment of inertia of a cylindrical rod with a radius of r.[127] Thus,

$$\frac{E_{fiber}}{E_{matrix}} = -\frac{4}{3}\pi l_p V_m/Nr^4 \tag{13}$$

In our system, we assume r = 5 nm, l_p = 50 μm based on persistence lengths in the micrometer range[128] previously determined for other PA nanofibers; by substituting Equation 12 in Equation 13 we have E_{fiber}/E_{matrix} = 434. As such, using a deformable fiber instead of a rigid one only results in a negligible change (<0.1%) of the contraction ratio in our simulations. Therefore, it is adequate to calculate the contraction of the polymer hybrid without considering the deformation of the PA nanofibers.

Estimating interfiber distances

We used the dimensions of the mold (outer diameter = 4 mm, inner diameter = 3 mm, and length = 32 mm to calculate a tube volume of $V_{tube} = 175.23 mm^3$) and the known mass concentration (10 mg mL⁻¹) of the PA solution filling the mold prior to gelation, to calculate the amount of PA per tube (1.75 mg). From atomistic simulations of similar PA nanofibers,[121] we obtained an

approximate density of 0.778 mg mm^{-3} for the PA within the tubes. We assume a fiber diameter of 10 nm, which is consistent with data obtained from small angle X-ray scattering. From these parameters, we calculate a volume of $V_{fiber} = 2.249 mm^3$ to be occupied by the PA nanofibers within the tube. Assuming the PA nanofibers to be arranged in a 2D square lattice as used in the finite element analysis, we can calculate the interfiber distance by solving the following equation for the width of the lattice, a:

$$\frac{\pi \times r^2}{a^2} = \frac{V_{fiber}}{V_{tube}} \tag{14}$$

Therefore, the interfiber distance can be estimated to be:

$$a = \sqrt{\frac{\pi r^2 V_{tube}}{V_{fiber}}} = 78 \; nm \tag{15}$$

Molecular theory: free energy model

One PA polymer hybrid nanofiber is modeled as a cylinder of radius R that is end-tethered with N_p polymers chains covalently end-tethered to a cylindrical surface of area $A(R)$. Each copolymer contains temperature-responsive ethylene glycol monomers (denoted as A) and hydrophobic monomers (denoted as B). Here, we present a description of the theory outlining its most important features. A complementary description of the theory for planar surfaces was previously described.[119] The total Helmholtz free energy of the system has the following contributions:

$$F = -TS_{conf} - TS_{mix} + E_{VdW} + F_{assoc} \tag{16}$$

where T is the temperature; S_{conf} is the conformational entropy of the polymers chains; S_{mix} is the translational entropy of the water; E_{VdW} corresponds to the Van der Waals attraction between the monomers; F_{assoc} is the free energy of hydrogen bond formation, i.e., the enthalpic and entropic cost associated with forming water-water and water-monomer hydrogen bonds. In the following a

description of each of the terms of the free energy is presented. The conformational entropy of the polymer chains,[118] which per unit area, is given by

$$-\frac{S_{conf}}{k_B A(R)} = \sigma \sum_{\alpha} P(\alpha) ln P(\alpha) \tag{17}$$

Here, $\sigma = N_p/A(R)$ is the grafting density or surface coverage, i.e., the number of chains per unit area. $P(\alpha)$ corresponds to the probability to find a chain in conformation α. This probability distribution function (pdf) is essential in describing various thermodynamic and structural quantities related to the polymers. For instance, the average polymer number density, $\langle \rho_i(r) \rangle$, for monomers of type i at position r is given by

$$\langle \rho_i(z) \rangle = \frac{\sigma}{G(r)} \sum_{\alpha} n_i(\alpha; r) \tag{18}$$

Here $n_i(\alpha; r)$ is the number of polymer segments of monomer type i found within a volume element $[r, r + dr]$ that belong to polymer conformation α. The variable $n_i(\alpha; r)$ is input and dependent on the molecular architecture and chemistry of the polymer. The variable r is the radial coordinate in cylindrical coordinates. The system is assumed to be laterally homogeneous and only explicitly anisotropic in the radial cylindrical direction. The function $G(r) = A(r)/A(R) = r/R$ is the Jacobian determinant divided by the area of the cylindrical surface of the hybrid. It describes the change in volume as function of distance away from the nanofiber. The total polymer volume fraction is the sum of the volume fractions of the individual monomer of type A and B and is given by

$$\langle \phi(r) \rangle = \langle \phi_A(r) \rangle + \langle \phi_B(r) \rangle = \langle \rho_A(r) \rangle v_A + \langle \rho_B(r) \rangle v_B \tag{19}$$

where v_A and v_B is the volume of monomer of type A and B respectively. The second term in the free energy of Equation 16 is the mixing entropy of the water molecules and it is given by

$$-\frac{S_{mix}}{k_B A(R)} = \int dr \rho_w(r)[ln(\rho_w(r)v_w) - 1] \tag{20}$$

Here, $\rho_w(r)$ is the number density of water and v_w is the volume of water. The third term in the free energy describes the attractive Van der Waals interaction energy between monomers,

$$\frac{\beta E_{VdW}}{A(R)} = -\frac{\chi_A}{2v_w}\int dr G(r)\langle\phi_A(r)\rangle^2 - \frac{\chi_B}{2v_w}\int dr G(r)\langle\phi_B(r)\rangle^2 \tag{21}$$

where χ_i is the interaction parameter that measures the strength of attraction between like-monomers, being either temperature responsive (A) or hydrophobic $_{(\beta)}$ monomers. In our calculations, we take $\chi_i = B_i/T$. Considering only the above Van der Waals interaction energy would result in a phase behavior and thermal response characteristic of UCST (upper critical solution temperature) systems. Hydrophobic monomers, which have a UCST phase behavior, are appropriately described by above interaction energy. However, PEG polymers have LCST behavior, which has its origins in hydrogen bond formation between PEG monomers and water molecules. Thus we include an additional term in the free energy, the fourth term in Equation 16, which describes the free energy contribution of hydrogen bond formation between monomer and water and water-water molecules.[119,120] This contribution is represented by:

$$\frac{\beta F_{assoc}}{A(R)} = \int dr G(r) 2\langle\rho_A(r)\rangle[x_p(r)ln\, x_p(r) + (1 - x_p(r))ln(1 - x_p(r)) - x_p(r)\beta\Delta F_p]$$

$$+ \int dr G(r) 2\rho_w(r)[x_w(r)ln\, x_w(r) + (1 + x_w(r))ln(1 - x_w(r)) - x_w(r)\beta\Delta F_w]$$

$$+ \int dr G(r) 2\rho_A(r)\rangle\left[1 - x_w(r) - x_p(r)\frac{\langle\rho_A(r)\rangle}{\rho_w(r)}\right]ln\left[1 - x_w(r) - x_p(z)\frac{\langle\rho_A(r)\rangle}{\rho_w(r)}\right]$$

$$- \int dr 2\rho_w(r)\left[x_w(r) + x_p(r)\frac{\langle\rho_A(r)\rangle}{\rho_w(r)}\right]ln\frac{2\rho_w(r)v_w}{e} \tag{22}$$

where $\chi_p(r)$ is the local fraction of polymer-water hydrogen bonds for A monomers and $x_w(r)$ is the local fraction of water-water hydrogen bonds. Only hydrogen bonds formation between the A (PEG) monomers and water molecules and between water-water molecules are considered. The B monomers do not form hydrogen bonds with water. In Equation 23, the free energy contribution $\beta\Delta F_i = \beta\Delta E_i - \Delta S_i/k_B$ is the sum of the energetic gain (ΔE_i) of forming one hydrogen bond and the corresponding entropic loss (ΔS_i) of forming the hydrogen bond for either $i = p$ (polymer-water) or $i = w$ (water-water) hydrogen bond pair. They have the following values:

$$\beta\Delta F_p = \frac{2000K}{T} - 3.35 \; and \; \beta\Delta F_w = \frac{1800K}{T} - 2.25 \tag{23}$$

These values, obtained from experiments and simulation results, are specific for PEG and water.[120] A derivation of this free energy contribution was described previously.[119,120] The repulsive interactions in the theory are modeled as excluded volume interactions. The intrachain interactions are explicitly considered during generation of the polymer conformations. The intermolecular excluded volume interactions are accounted for by assuming that the system is incompressible at every position,

$$\langle\phi_p(r)\rangle + \rho_w(z)v_w = 1 \tag{24}$$

These volume constraints are enforced through introduction of the Lagrange multipliers $\pi(r)$. The free energy expression is minimized with respect to $P(\alpha)$, $\rho_w(r)$, $x_w(r)$, and $x_p(r)$, under the constraint of incompressibility. Minimization with respect to yields $P(\alpha)$,

$$P(\alpha) =$$

$$\frac{1}{q}exp\left[-\beta \int dr\pi(r)n_A(\alpha;r)v_A + \frac{\chi_A}{v_w}\int dr\langle\chi_A(r)\rangle n_A(\alpha;r)v_A - 2\int dr n_A(\alpha;r)ln(1-x_p(r))\right]$$

$$\times exp\left[-\beta \int dr\pi(r)n_B(\alpha;r)v_B + \frac{\chi_B}{v_w}\int dr\langle\phi_B(r)\rangle n_B(\alpha;r)v_B\right] \quad (25)$$

where q ensures normalization of $P(\alpha)$ and $\pi(r)$ is the Lagrange multiplier or lateral pressure field that enforces the incompressibility constraint. Minimizing with respect to the water number density or volume fraction gives

$$\phi_w(r) = exp\left[-\beta\pi(r)v_w - 2ln(1-x_w(r)) - 2ln\left(1 - x_w(r) - x_p(r)\frac{\langle\rho_A(r)\rangle}{\rho_w(r)}\right)\right] \quad (26)$$

Finally, minimizing the free energy expression with respect to the local fraction of polymer-water $x_p(r)$ and water-water hydrogen bonds $x_w(r)$ gives

$$x_p(r) = 2exp(\beta\Delta F_p)\phi_w(r)(1-x_p(r))\left(1 - x_w(r) - x_p(r)\frac{\langle\rho_A(r)\rangle}{\rho_w(r)}\right) \quad (27)$$

and

$$x_w(r) = 2exp(\beta\Delta F_w)\phi_w(r)(1-x_w(r))\left(1 - x_w(r) - x_p(r)\frac{\langle\rho_A(r)\rangle}{\rho_w(r)}\right) \quad (28)$$

The unknowns in Equation 19, and Equation 25, through Equation 28, are the Lagrange multipliers or lateral pressures, $\pi(r)$, the local fraction of polymer-water $x_p(r)$ and water-water hydrogen bonds $x_w(r)$. Once solutions for these variables are found all equilibrium thermodynamic and structural properties of the system are known. Solutions of these variables can be obtained numerically. This is accomplished by substituting expressions of the polymer and water volume fractions into the

incompressibility constraint Equation 24, and the 'chemical reaction equations' of Equation 27 and Equation 28, which results in a set of non-linear integro differential equations. By discretizing space these differential equations can be converted into a set of coupled non-linear algebraic equations that can be solved with standard numerical techniques.[129] Details on the discretization procedure and numerical methods can be found in the literature.[119,130]

Finally, we employ a three-state RIS model to generate the chain conformations.[131] In this model, each bond has three different isoenergetic states. The conformations are generated by a simple sampling method and all are self-avoiding and cannot penetrate into the nanofiber. We generated a set of independent conformations for each different molecular weight. The same set of conformations was used in all calculations for a given molecular weight. Each segment of the polymers had a length $l = 0.30$ nm, and a volume $v_a = v_b = 0.065$ nm³ which corresponds to the partial molar volume of PEG in water. The volume of a water molecule was $v = 0.03$ nm³. The interaction parameter for the ethylene glycol monomers is fixed at $\chi = 100/T$. The hydrophobic monomer is not allowed to form hydrogen bond between monomer and water. The discretization thickness was $\delta = 0.35$-0.5 nm, which is sufficient to obtain accurate solutions for the given set of equations.

Thermal response of PEG

To understand in more detail the role of hydrogen bonding on the thermal response of the PEG-like cylindrical brush we present in Fig. 2.15 the average fraction of water-water hydrogen bonds and polymer-water hydrogen bond as function of temperature for a PA nanofiber end-tethered with PEG polymers. Adjacent to that the polymer volume fraction as function of distance away of the nanofiber is shown. The number of water-water and polymer-water hydrogen bond is like the polymer volume fraction position dependent. Therefore, in order to be able to compare different temperatures we introduce the spatial average fraction of PEG-water hydrogen bonds, $\langle x_p \rangle = \int dr G(r) x_p(r) \langle \rho_A \rangle / \int dr G(r) \langle \rho_A(r) \rangle$ and the average fraction of water-water hydrogen bonds, $\langle x_w \rangle = \int dr G(r) x_w(r) \langle \rho_A \rangle / \int dr G(r) \langle \rho_w(r) \rangle$. The integration is restricted to the region where

there are polymers, otherwise if the integration is extended to infinity $\langle x_w \rangle$ would become equal to the average fraction of water-water hydrogen bonds of pure water. Observe that the formation of hydrogen bonds is always accompanied by a gain in free energy, that is, both $-\Delta F_p$ and $-\Delta F_w$ are negative (see Equation 24,). However, the free energy gain to form water-water hydrogen bonds is larger than the free energy gain to form polymer – water hydrogen bonds ($\Delta F_p < \Delta F_w$). Consequently, when temperature increases the free energy gain to form polymer-water hydrogen bonds decreases quicker than the decreases in free energy gain to form water-water hydrogen bonds. This effect is demonstrated in Fig. 2.15.

Hence water increasingly prefers to have hydrogen bonds with other water molecules instead of having hydrogen bonds with polymer segments. This effectively leads to a decrease in the solvent quality. With increasing temperature, the solvent quality decreases and is able to overcome the conformational entropy of the tethered polymer, which favors extended conformations. Therefore, the polymer layer shrinks, and at elevated temperatures the layer eventually collapses (Fig. 2.15b).

Thermal response of PEG-like copolymer

The LCST of pure PEG polymers is above 400K.[120] Therefore, we considered a very large and experimentally unrealistic temperature range. By introducing hydrophobic monomers into the copolymer, a drastic reduction of the transition temperature can be accomplished as displayed in Fig. 2.14c. Whereas a PEG polymer has a transition temperature of around 425 K, a linear alternating copolymer (EG_2-a-HB)$_{66}$-EG_2 (blue curve of Fig. 2.14c) transitions around 325 K from a swollen, extended state to a collapsed state. These predictions are consistent with the experimental observations by Lutz *et al.* showing that the fraction of hydrophobic monomers controls the LCST behavior for PEG copolymers similar to one considered in this paper.[132]

The drastic reduction is observed because the hydrophobic monomers are not allowed to form hydrogen bonds between monomer and water. Consequently, a water-hydrophobic monomer contact is energetically very unfavorable. There is no energetic gain, unlike forming hydrogen bonds

with other water molecules and with ethylene glycol monomers. This effectively causes the copolymer to experience very poor solvent quality, and the brushes collapse at a much lower temperature than the pure PEG polymer.

Note, the effect of varying the interaction parameter for the hydrophobic monomers is very small because the effective repulsions between the hydrophobic monomer and water molecules are mostly mediated indirectly by the hydrogen bond formation between water molecules, and not by the effective Van der Waals interaction. The height of polymer layer for the end-tethered copolymers, presented in Fig. 2.14c, has only a very limited dependence on χ_B. The interaction parameter was arbitrarily set to $\chi_B = 0.15/T$.

Thermal Response effect of surface density and molecular weight

In Fig. 2.16 we explore the effect of surface coverage and molecular weight or degree of polymerization on the thermal response of end-tethered PEG. We observe that with increasing surface coverage the height of the swollen state increases. This is due to the increased excluded volume interaction resulting from the increased polymer density near the nanofiber surface. Likewise, due to the increase in the number of monomers the collapsed state is also larger. A similar but much more pronounced trend can be observed with increases in chain length. Longer chains can stretch further away from the surface and form more energetically favorable hydrogen bond pairs with water molecules. Consequently, longer chains form a relatively more extended state. Effects of the variation of the density of initiators on the structure of the polymers are obtained via molecular modeling (shown in Fig. 2.16). We expect some increase in actuation with increased grafting above the experimental grafting density of 0.07 chains nm^{-2}; however, at high grafting densities the changes are minimal due to increased sterics preventing polymer mobility close to the nanofiber surface. This is corroborated experimentally in Fig. 2.17, where increasing the grafting density by increasing the mol% of initiator in the supramolecular coassembly. The overall degree of contraction remains sim-

ilar across three cases; however, the kinetics of the contraction appear to change. These kinetics will be explored in future work.

Effect of crosslinking on material opacity and thermoresponse

The continuum model shows that an important parameter for the degree of anisotropy is related to the degree of crosslinking within the gel as well as the response of the gel to temperature variations via $\chi(T)$, which is provided by the molecular theory in the absence of crosslinking (Fig. 2.15). However, the gel degree of collapse is restricted by the constraint imposed by crosslinking, which are similar to the constraints imposed by grafting chains on a surface. In this case heterogeneities develop, as evident in the lateral pressure as a function of area per grafted chain with increasing temperature (Fig. 2.21). The collapse at high temperature leads to a coexistence of two-phase composition due to the constraints in the grafted case vertical and lateral collapsed state. These constraints are similar to those in a crosslinked gel, which always have polydispersity in the number of monomers per crosslink causing regions with different monomer densities, providing an opaque color to the collapsed gels. We note that the number of monomers per crosslink is directly related to the number density of accessible chains for polymer growth from the fiber surface.
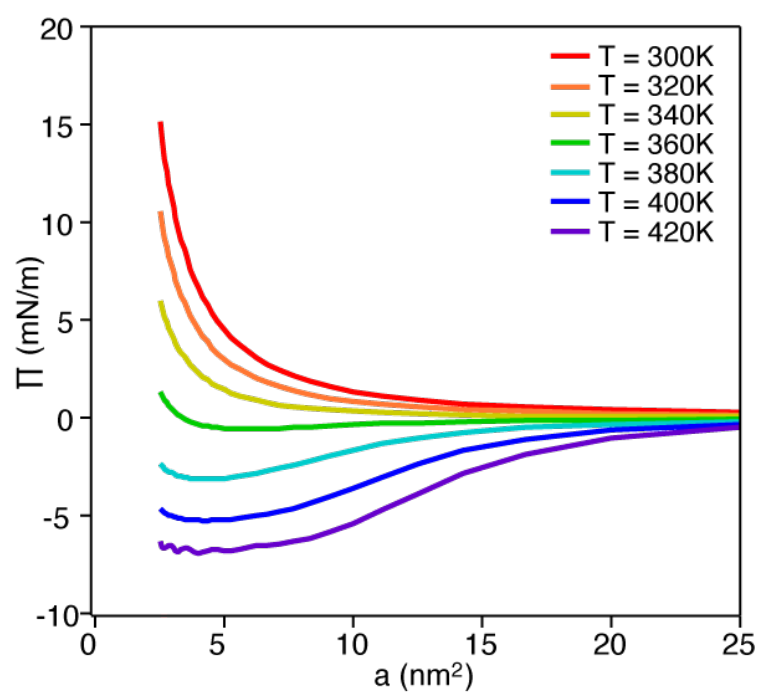
Figure 2.21: Lateral pressure as a function of the area per molecule, $\alpha = A(R)/N_p$. The polymer is a linear alternating copolymer of PEG and hydrophobic monomers, with a ratio of 4:1. The number of monomers is $N_p = 150$, and the radius of the nanofiber is 5 nm.

3 Macroscopic Control of Alignment and Hierarchy

3.1 objectives and significance

Hierarchical order and control of alignment is key in developing responsive materials, in order to transduce nanoscale actions to macroscopic motions. Peptide amphiphile materials are useful in the development of such hierarchical structure, due to their ability to be aligned through the application of weak shear forces. Using extrusion-based direct ink writing method of 3D printing, we are able to macroscopically control the fabrication of arbitrary alignment patterns that allow for additional complexity within the materials. In a PA-polymer hybrid printed system, this resulted in observed curling behavior due to gradients of alignment within the printed material. The macroscopic control of alignment was aided by further materials development, using the incorporation of cellulose nanocrystals or host-guest supramolecular interactions into the PA ink. These systems allowed for more versatile printing of these inks without the need for immediate addition of calcium counterions in order to maintain alignment after extrusion.

3.2 background

Thermoresponsive covalent-supramolecular hybrid polymers show extreme promise as artificial actuators for soft robotics due to their inherently anisotropic nature derived from the 1D peptide amphiphile nanofiber scaffold. However, the fabrication method used previously, application of rotational shear inside of a glass mold, inherently limits the geometries that can be created with these hybrid materials.[68] To fully take advantage of these hybrids as artificial actuators, it is imperative to develop new fabrication methods that allow for the design of arbitrary shapes with controlled alignment, which can direct anisotropy during the actuation process.

PA assemblies are of high interest due to their formation of extremely high aspect ratio ($\sim$10 nm $\times$ >5 µm) anisotropic nanostructures.[133] These nanostructures form liquid crystalline domains

in aqueous solution that can be aligned into monodomain gels via shear force while pipetting into media with divalent counterions.[69] These liquid crystalline solutions require very weak shear forces, as little as 1-4 s^{-1}.[70] The resulting gels exhibit bulk anisotropic properties, such as directionally enhanced mechanics or directional cell response due to the alignment of the nanoscale assemblies.[134,135] In most examples, however, these gels are drawn manually, and we therefore cannot reproducibly build these materials into complex patterns or 3D objects with consistent and programmable nanoscale alignment. In order to design advanced patterns and anisotropy within these hybrid materials, we must investigate alternative methods of fabrication.

Direct ink writing (DIW) has emerged as an attractive candidate for the fabrication of aligned hydrogel materials.[136,137] A type of 3D printing, direct ink writing is an extrusion-based technique that can precisely deposit viscous 'inks' in a predetermined pattern, and quickly solidify after extrusion, maintaining the desired morphology. During the extrusion process, DIW can also apply significant shear forces on the inks being printed, which can allow for the alignment of components, such as PA nanofibers, within the printed structure.

Using DIW to align anisotropic objects within the ink has been demonstrated in a number of systems, incorporating materials such as nanocrystalline cellulose,[138,139] carbon fibers,[140] and polymeric microfilaments within an overall cross-linked polymer network. These materials typically act as rheological fillers, and can impart directional mechanical properties into the composite ink. These incorporated materials can be used to bolster the anisotropic nature of the material as well as enable the creation of more complex structures.[141] Mechanically more robust inks are beneficial in making large, multilayered structures that are strong enough to support themselves, and still allow for diffusion and hydration throughout the printed hydrogel network, similar to vascularization of tissues or within plants.[142,143]

We describe here the use of DIW methods to 3D print covalent-supramolecular hybrid materials with pre-programmed alignment patterns. Depending on the pattern of alignment, these materials show advanced anisotropic actuation behavior. We investigate the nature of this curling

behavior, and attribute it to local gradients of alignment throughout the cross-section of the printed sheets. We extend the system through the inclusion of cellulose nanocrystals as a rheological filler within the PA ink in order to create more mechanically robust structures that are free-standing even before the addition of additional ionic crosslinking. We also introduce a method of adding mechanical strength to the PA inks through supramolecular crosslinks, which are able to create printable inks without the need for non-peptide additives within the materials.

3.3 RESULTS & DISCUSSION

3.3.1 *3D printing of supramolecular-covalent hybrid materials*

Since the supramolecular peptide amphiphile nanofibers can be aligned with weak shear forces, we are able to use other fabrication techniques such as extrusion printing in order to produce aligned PA hydrogel materials. 3D printing methods can produce more intricate PA architectures than the previously described tube. Recent studies in the Stupp group have developed procedures for the general 3D printing of PA-based inks, tuning printing parameters to allow for a high degree of alignment in the subsequent printed fibrils (Fig. 3.1).

We proceeded with the fabrication of thermoresponsive supramolecular-covalent hybrid sheets from extruded PA filaments as shown in Figure 3.2a, which are subsequently polymerized in the
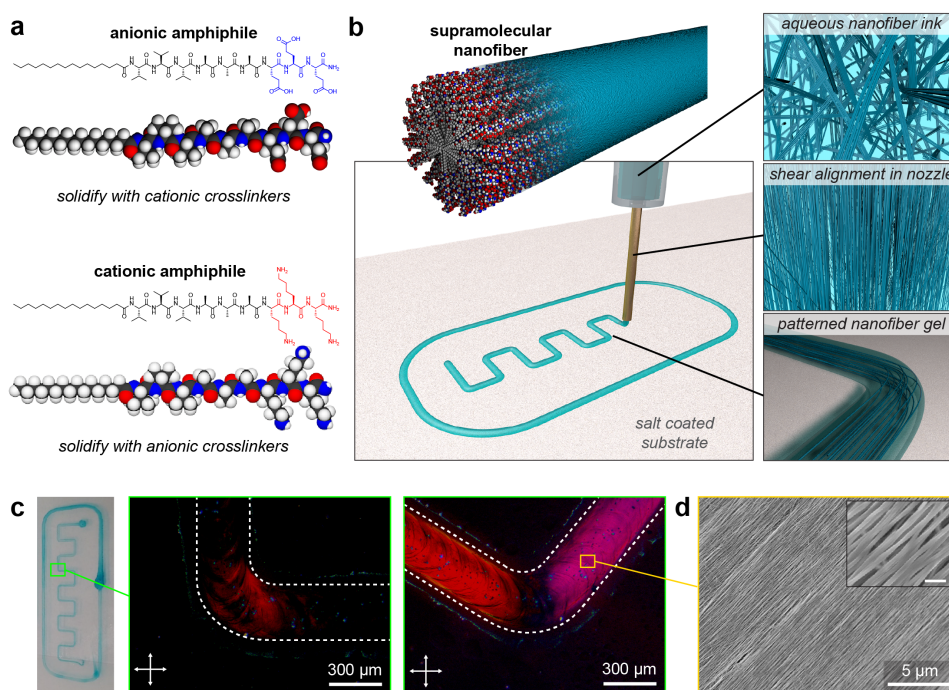
Figure 3.1: Extrusion printing supramolecular liquid crystalline hydrogels. (a) Molecular structures of peptide amphiphiles used in anionic and cationic nanofiber inks. (b) Assembled nanofibers are extruded through a thin nozzle onto a salt coated substrate to gel the shear-aligned nanofibers in place. (c) Photo and POM images of printed E3 nanofiber gel on $CaCl_2$ coated substrate and (d) SEM image of printed E3 nanofiber gel filament (inset scale bar: 100 nm). Reproduced from Sather *et al.*[144]

same manner as the tubes described in Chapter 2. Because the hybrid sheets contain the same mechanical reinforcement and end-grafting as the tubes, we expect to observe similar anisotropic actuation perpendicular to the direction of supramolecular alignment. Interestingly, sheets that have a net alignment bend in a distinct orientation upon heating (Fig. 3.2b, e). In contrast, sheets lacking a net alignment, either through the printing of concentric spirals or with a cross-hatch pattern do not show similar bending, but rather non-uniform wrinkling (Fig. 3.2c, d, f, g).

The aligned hybrid sheets bend unidirectionally, towards the printing substrate and perpendicular to the aligned fiber axis, upon increase in the surrounding temperature above the transition temperature of the covalent polymer. This bending is highly reversible and repeatable over multiple cycles. Similar bending and even rolling behavior of polymer sheets has been observed in the case of bilayers.[22,23] However, these materials typically bend due to the mismatch in moduli or expansion coefficients between the two components of the bilayer. In contrast, the hybrid sheets presented here have a homogeneous dispersion of supramolecular nanofibers within the polymer matrix, as shown in the cross-sectional confocal microscopy image (Fig. 3.3).

In polarized microscopy images, we find increased birefringence of the layers closest to the substrate, indicating stronger alignment, compared to the upper layers of the sheets (Fig. 3.4). SEM
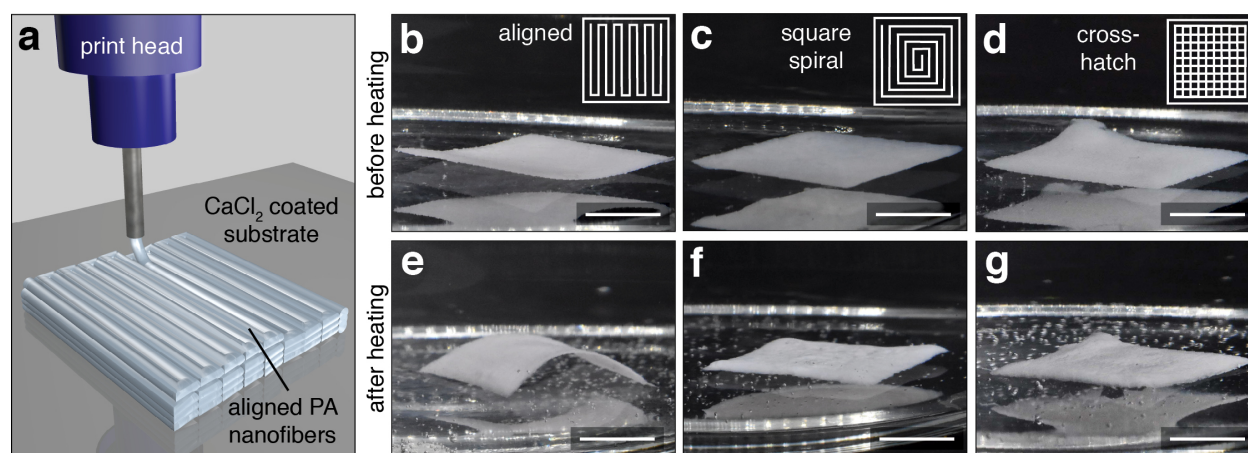
Figure 3.2: (a) Schematic of 3D printing process. Aligned sheets before (b) and after (e) heating. Square spiral printed sheets before (c) and after (f) heating. Cross-hatched sheets before (d) and after (g) heating. Insets show printing patterns of each sheet. (scale bars are 5 mm).
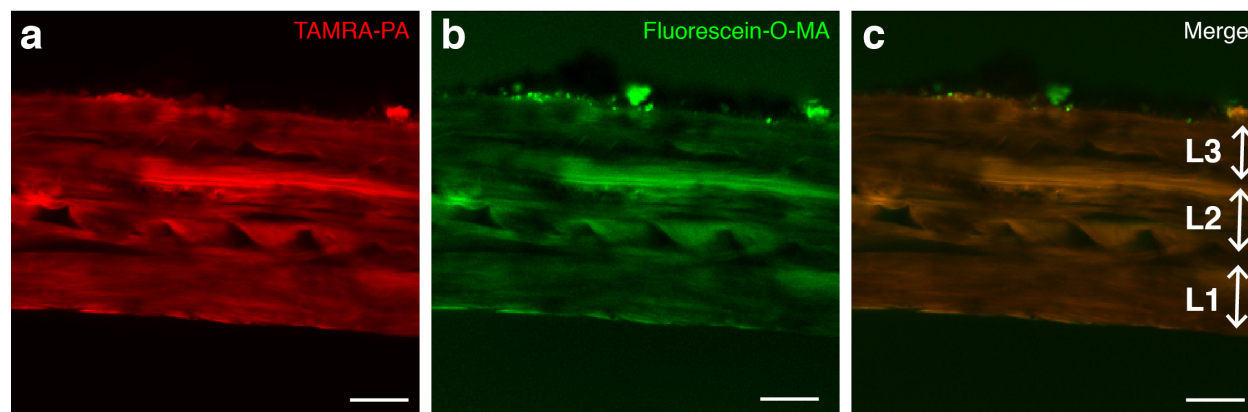
Figure 3.3: Confocal microscopy of the cross-section of a 3D printed three layer aligned sheet. (a) TAMRA-labelled supramolecular nanofiber component. (b) Fluorescein-labeled covalent polymer component. (c) Merged channels showing colocalization of components. L1 represents the first layer printed on the glass substrate and L2 and L3 are the subsequent printed layers. Scale bar are 100 µm.
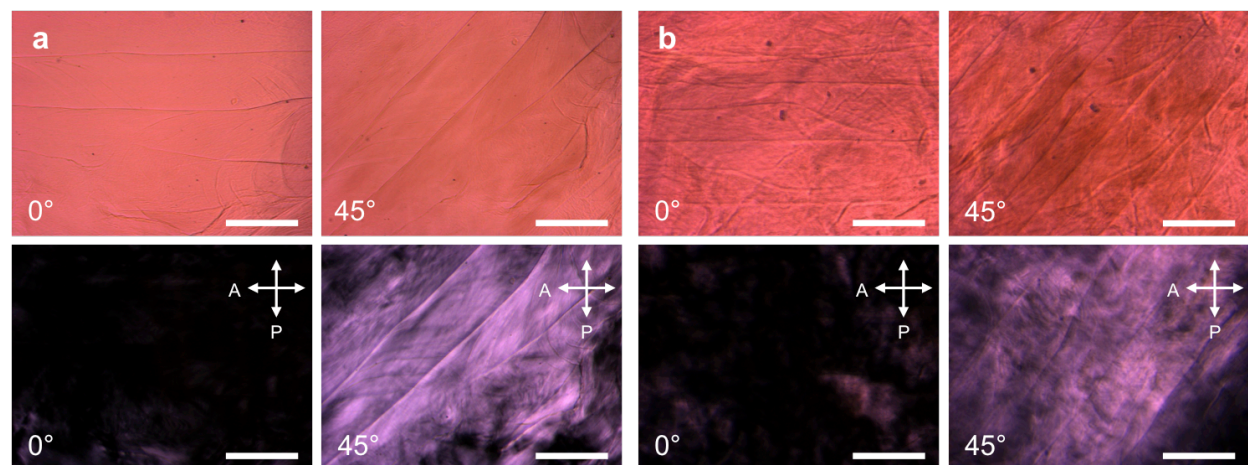
Figure 3.4: Optical microscopy of (a) one layer and (b) three layer aligned 3D printed sheets. When the sample is aligned 45° to the polarizer, a more uniform and stronger birefringence is observed for one layer sheets than for three layer sheets. Scale bars are 400 µm.

imaging also suggests that there is better alignment on the bottom surface of the sheets than on the top surface (Fig. 3.5).

We hypothesize that the first layer may have a higher drag shear force during extrusion onto a hard glass substrate than the drag shear force experienced by the upper layers when extruded onto the soft hydrogel surface of the initial previous layer. The differences in alignment between layers
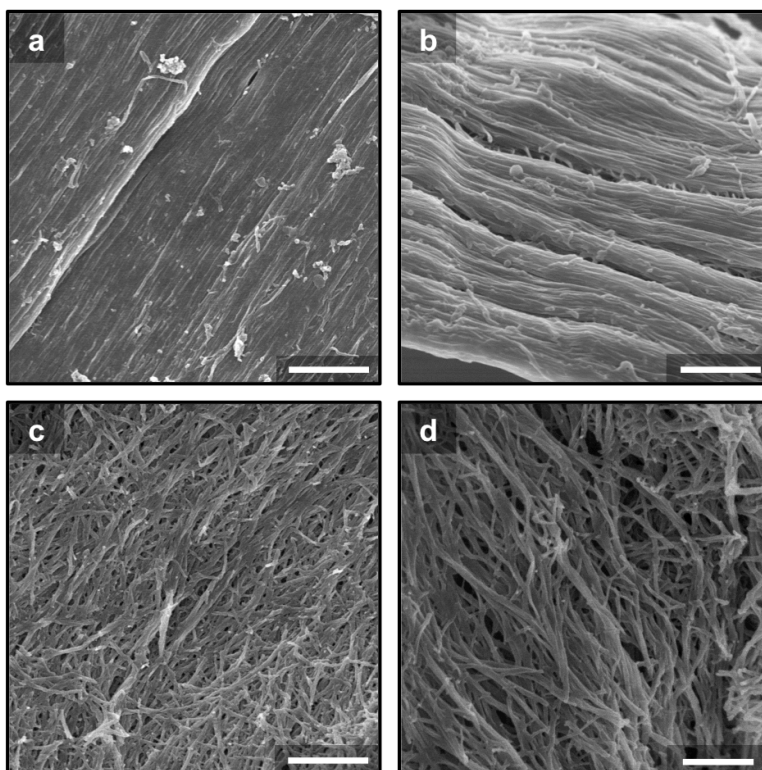
Figure 3.5: Representative SEM images from the bottom (a, b) and top (c, d) surfaces of a 3D printed three layer aligned sheet. Scale bars are 1 μm in (a, b, c) and 500 nm in (d).

may be responsible for the preferential direction of bending in the hybrid sheets, where the more aligned bottom layer contracts more along the direction perpendicular to fiber alignment than the top layers, resulting in a net bending motion towards the bottom of the gel.

Interestingly, hybrid sheets that have a cross-hatch or square spiral pattern and do not feature net alignment, show a buckling behavior instead of a bending motion (Fig. 3.2). This indicates that the stresses generated by the transition of the thermo-responsive polymer cannot be released in a directed motion as is the case for sheets having a net alignment.

Our results demonstrate that these aligned hybrid materials are a general platform for programmable actuation, and we anticipate this feature to be useful in designing more complex macroscopic responses of our material by using pre-programmed patterns of the 3D printed material, inspired by the work of the Lewis group.[94]

3.3.2 *Incorporation of cellulose nanocrystals into PA-polymer hybrids for 3D printing*

As the 3D printing and subsequent polymerization of the covalent-supramolecular hybrids showed excellent promise as a new fabrication method for aligned hierarchical materials, we worked to further develop the printed hybrid system. While the sheet-like structures from above were easily printed with PA-only inks, the relatively weak (<10 kPa) modulus does not lend itself to the printing of large, robust structures. In addition, the aerosol spray method of delivering cross-linking calcium ions used in the previous prints significantly slows down the printing process, as it means only one layer can be printed at a time before human intervention is needed. Increasing the rheological properties of the extruded PA ink would prove to be very advantageous to this hybrid polymer system and allow for printed structures of increased size. The printed structures can then subsequently be placed in a $CaCl_2$ solution in order to further crosslink and strengthen the material.
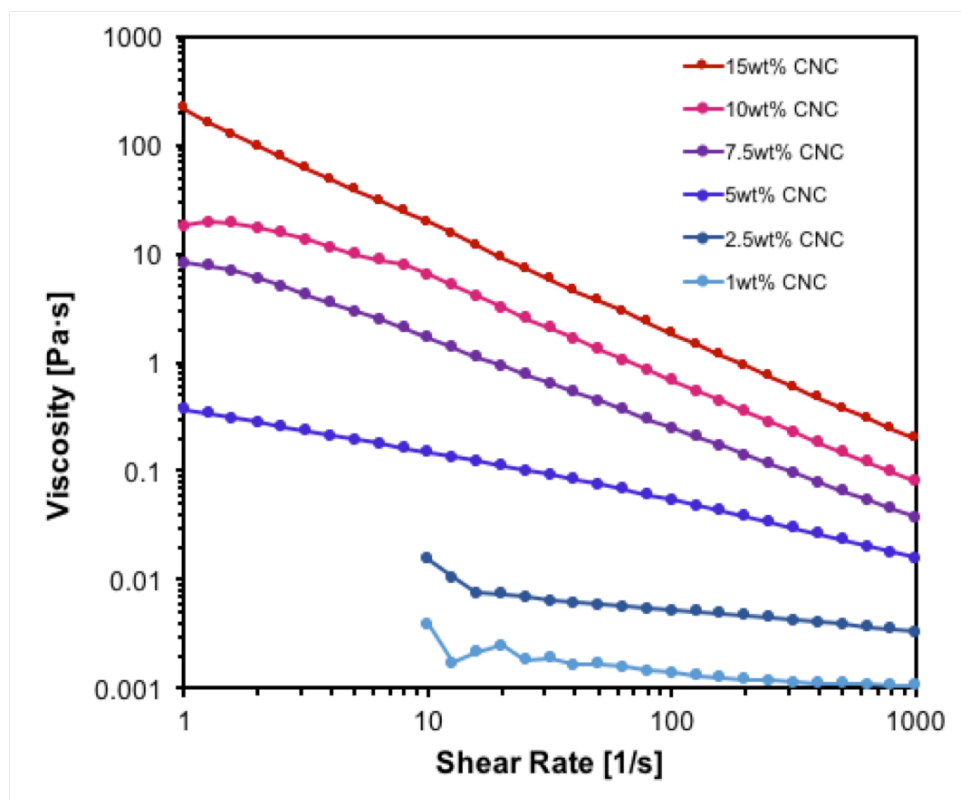
Figure 3.6: Shear-thinning behavior of CNC suspensions between 1-15 wt/v%.
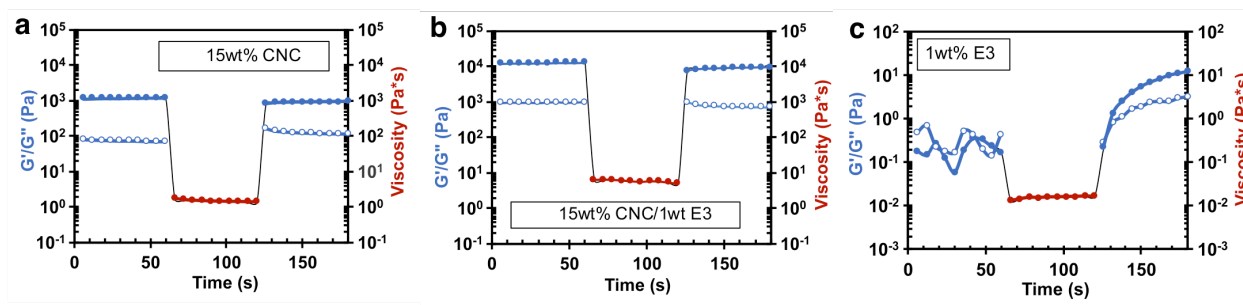
Figure 3.7: Rheological tests examining the behavior of (a) 15 w/w% CNC-only, (b) 15 wt% CNC with 1 wt% PA, and (c) 1 wt% PA-only inks under 3D printing conditions (steady state-high shear-steady state).

To this end, we investigated the incorporation of cellulose nanocrystals (CNCs) into the PA inks. CNCs are anisotropic particles composed of the crystalline portions of cellulose microfibrils; they are typically extracted from the amorphous regions through acid digestion. CNCs are ~20 nm in diameter and ~200 nm or more in length, depending on processing conditions, and have been investigated extensively in direct ink writing applications.[139,145] Cellulose nanocrystal dispersions are observed to have shear-thinning properties across a wide range of concentrations,[79] allowing for the opportunity to tune the rheological properties. (Fig. 3.6). Incorporation of CNCs into the PA ink at 10-15 wt/v% with 1-1.5 wt/v% PA produced inks with superior mechanical properties, with a storage modulus (G') of 10^4 Pa (Fig. 3.7b), over a magnitude higher than CNCs or PA alone (Fig. 3.7a, c). The inks were then exposed to high rotational strain (100 s^{-1} to mimic the shear forces that would be experienced during the extrusion process). After the high strain is released, CNC-containing inks immediately return to their original viscoelastic state, indicating that their structure would be maintained during the printing process (Fig. 3.7a, b). In comparison, the PA-only sample (Fig. 3.7c) shows a modest increase in G' and G", likely due to alignment of the PA nanofibers, but is nonlinear, indicating that the ink would relax over time, resulting in loss of fine printed features if not crosslinked with calcium ions immediately.

These CNC-PA materials were self-supporting once printed, unlike the previously described PA inks. This allowed for the printing of not only fully infilled sheets (Fig. 3.8a, b), but also the
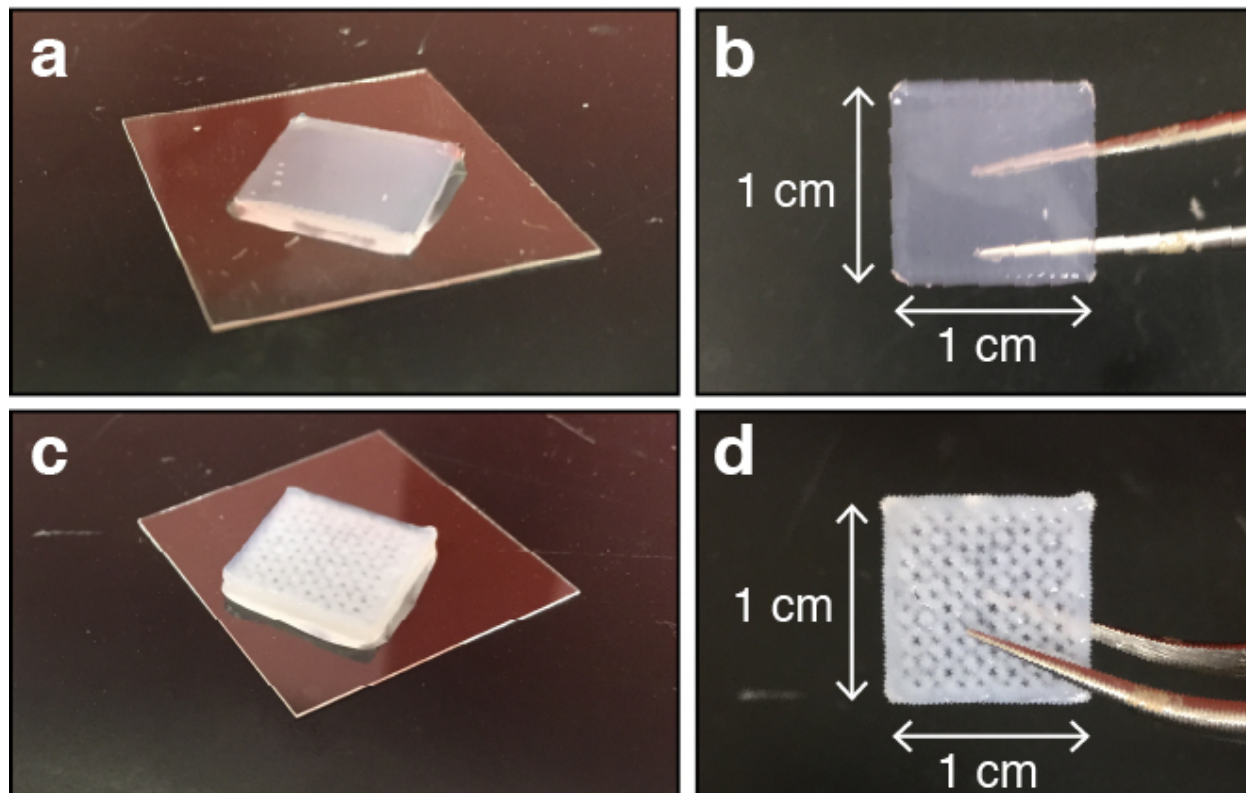
Figure 3.8: (a) Photograph of fully infilled CNC-PA hybrid sheet. (b) Photograph of previous free-standing material being easily handled with tweezers. (c) Photograph of a lattice-like printed CNC-PA hybrid sheet. (d) Photograph of previous freestanding material being easily handled with tweezers.

printing of sheets with a lattice-like pattern (Fig. 3.8c, d), where the printed filaments could span millimeter-sized gaps while maintaining the integrity of the print pattern. Further incubation with 0.1 M CaCl$_2$ solution produced an extremely robust CNC-PA composite hydrogel that could easily be manipulated.

These CNC/PA prints can be polymerized in the same manner as the previous materials (described in the Methods section 3.5). These materials show excellent mechanical properties, with a compressive modulus of 45.9 ± 17.1 kPa as measured by microindentation, a 2.75-fold increase over hybrid polymers without CNCs incorporated (16.7 ± 2.8 kPa). The CNC/PA hybrids show colocalization of polymer and PA throughout the printed structure, as shown in confocal microscopy of cross-sectional slices of the prints. (Fig. 3.9). It should be noted that the CNC materials do appear to
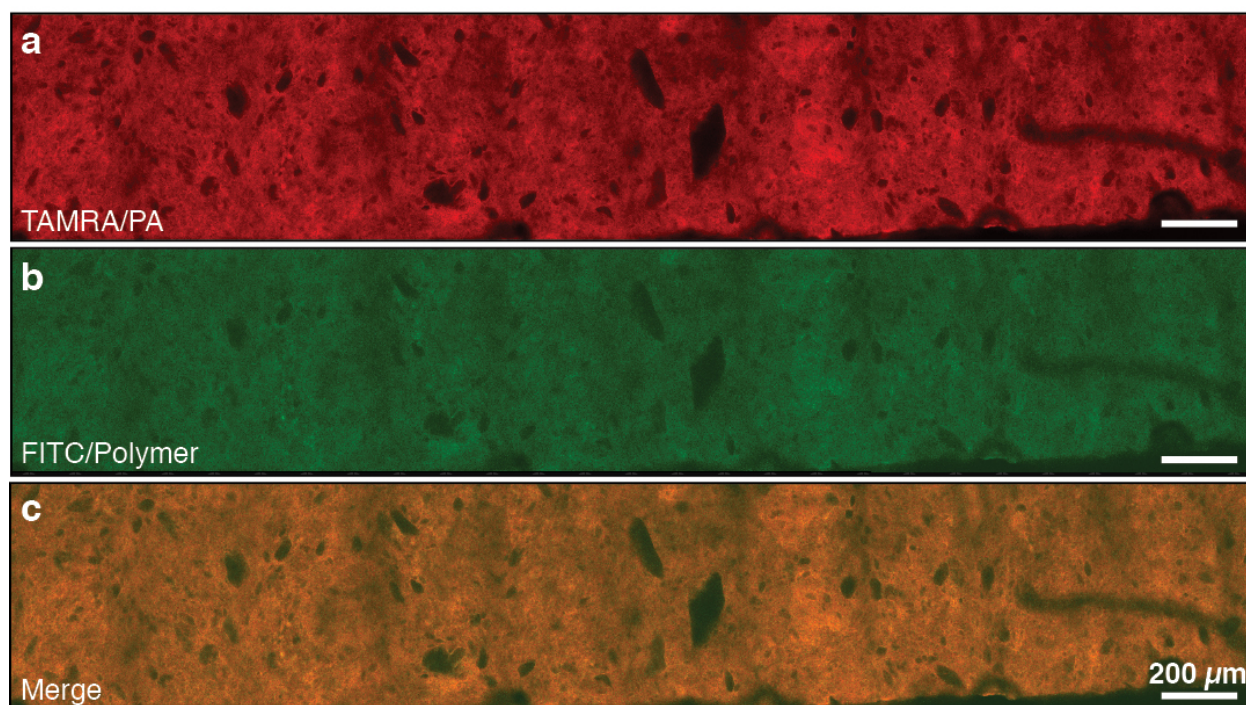
Figure 3.9: Confocal microscopy of a CNC-PA hybrid cross section showing (a) TAMRA-labeled PA, (b) FITC-labeled polymer, and (c) merged channels showing colocalization. Scale bars are 200 μm.

have some phase separation between the cellulose and peptide components of the material, shown as voids without fluorescent labeling of the CNCs.

Despite the phase segregation, these printed materials still show a high level of birefringence in POM (Fig. 3.10). These materials appear to have multiple smaller domains of alignment, as opposed to the previously printed materials, which have a singular monodomain of aligned nanofiber samples. This indicates that the phase separation of the cellulose nanocrystals may be preventing some of the alignment of the nanofibers at the current printing parameters. However, despite the lack of monodomain alignment, analysis of fluorescently labeled CNC/PA prints before polymerization show a high degree of alignment within the CNC portion and modest alignment of the PAs, which could still contribute to mechanical and actuation anisotropy (Fig. 3.11).

When heated, these CNC-containing hybrid materials show the expected increase in turbidity associated with the LCST transition (Fig. 3.12). However, the materials undergo modest overall con-
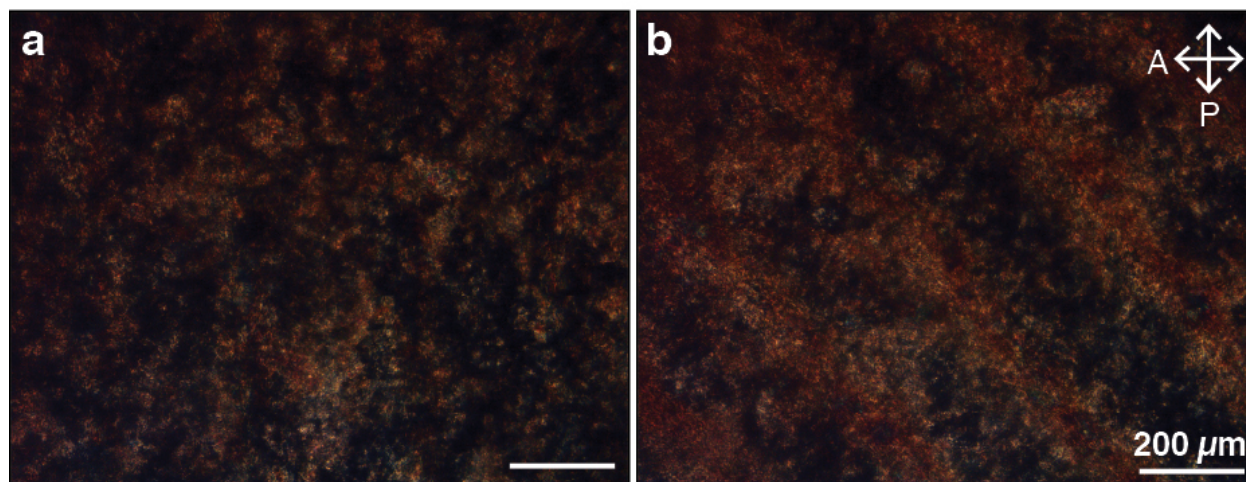
Figure 3.10: Polarized optical microscopy showing birefringence of CNC-PA hybrid oriented at (a) 0°and (b) 45°with respect to the polarizer. Scale bars are 200 μm.
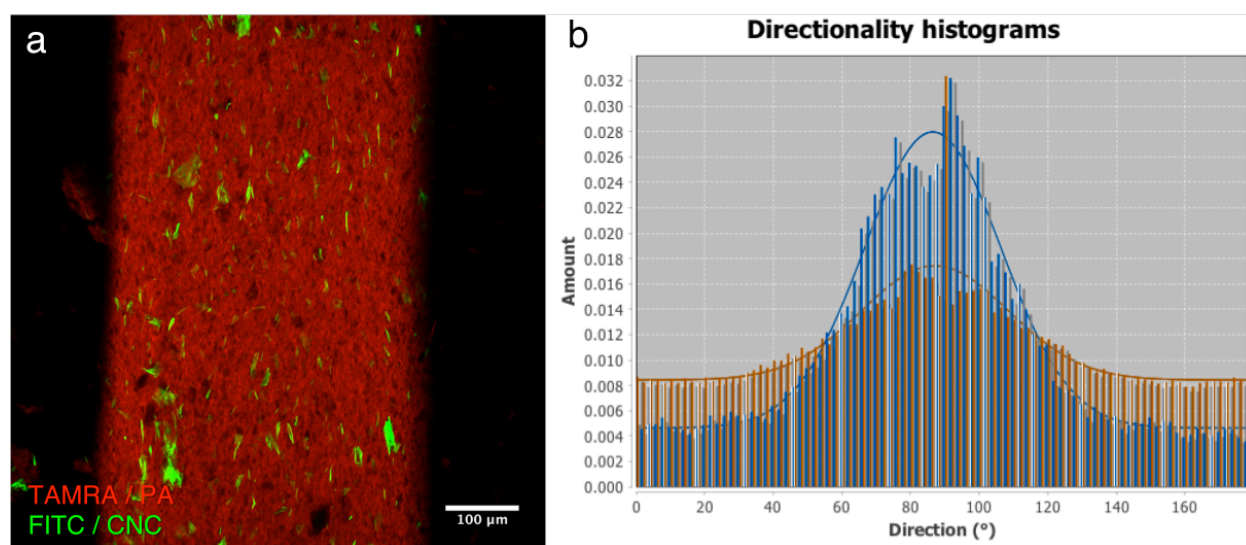
Figure 3.11: (a) Confocal microscopy of a CNC-PA printed material without polymerization. Scale bar is 100 μm. (b) Directionality histogram of image shown in (a) based off of Fourier analysis (blue are CNCs, red are PA)

traction, resulting in a reduction of surface area to 80% of the initial state. However, as the material is heated, the individual printed filaments seem to increase in polymer density, creating pronounced striping patterns (Fig. 3.12, insets); this could indicate that the filament-filament crosslinking needs to be increased during the polymerization process to improve the macroscopic contraction. These prints seem to show little to no bending behavior, unlike the PA-polymer only hybrids. This could
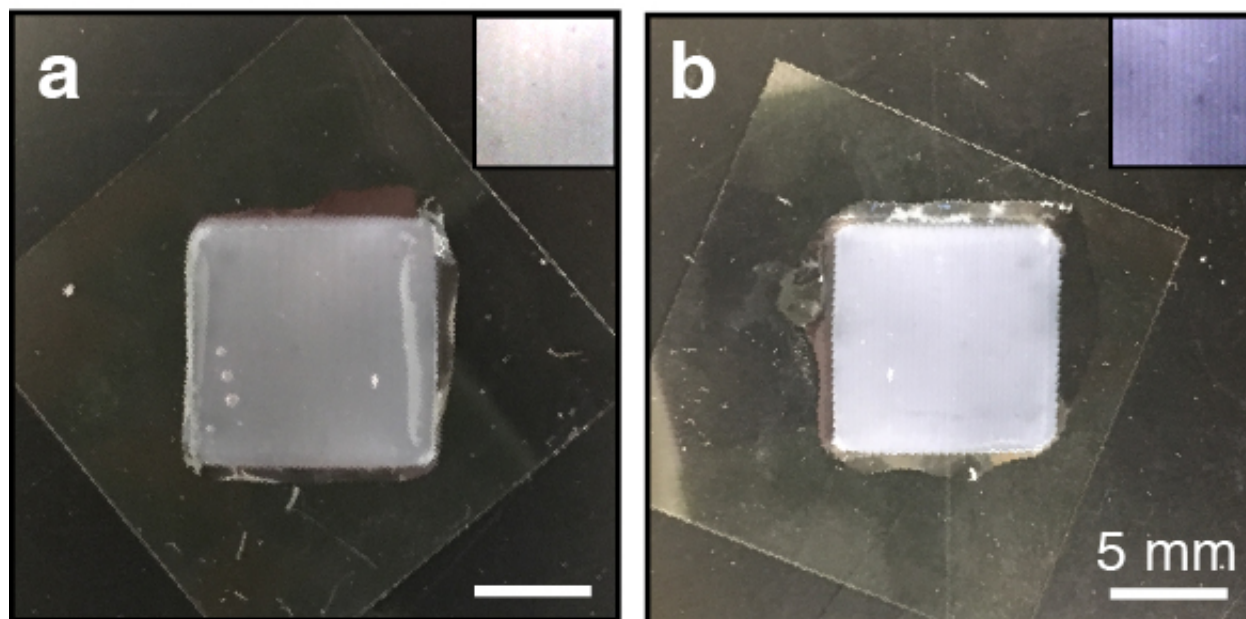
Figure 3.12: (a) Photograph of fully infilled CNC-PA hybrid print at room temperature. Inset: contrast enhancement of printed filaments. (b) Photograph of fully infilled CNC-PA hybrid print after heating for 20 minutes. Inset: contrast enhancement of printed filaments, showing distinct striations.

be due to the fact that the CNC-containing ink undergoes significantly less drag shear force when being printed, as it does not need to be printed on a $CaCl_2$-coated substrate in order to maintain its printed shape. This could lead to fewer differences in alignment between the top and bottom faces of the sheets, reducing the modulus mismatch that occurs upon shrinking. This alignment variation could be more intentionally built in the material by changing the printing parameters for different layers to build in differences in the alignment from the top down.

Our results demonstrate a significantly more rheologically robust material that is able to create complex, free-standing structures before the addition of calcium crosslinker. This robust material is easily handled, and can be subsequently polymerized to grow thermoresponsive polymer chains from the nanofiber surfaces. These materials show modest actuation that can be further developed by controlling additional printing parameters that control shear force for alignment.

3.3.3 *Host-guest supramolecular crosslinking for 3D printing*

The phase segregation of the CNCs within the hybrid materials indicates that inhomogeneous dispersion of the rheological additive component is not ideal for all desired applications. Ideally, a printable material would be a homogeneous mixture containing sufficient mechanical strength and viscoelastic properties to be printed on its own, but without the need for addition of calcium cross-linking at every printed layer. Therefore, we designed an entirely peptide amphiphile-based system using additional host-guest interactions as the basis for additional cross-linking and strengthening of the PA material. Host-guest based systems have been shown as an effective cross-linking mechanism to improve the rheological properties of macromolecular systems such as hyaluronic acid.[146,147]
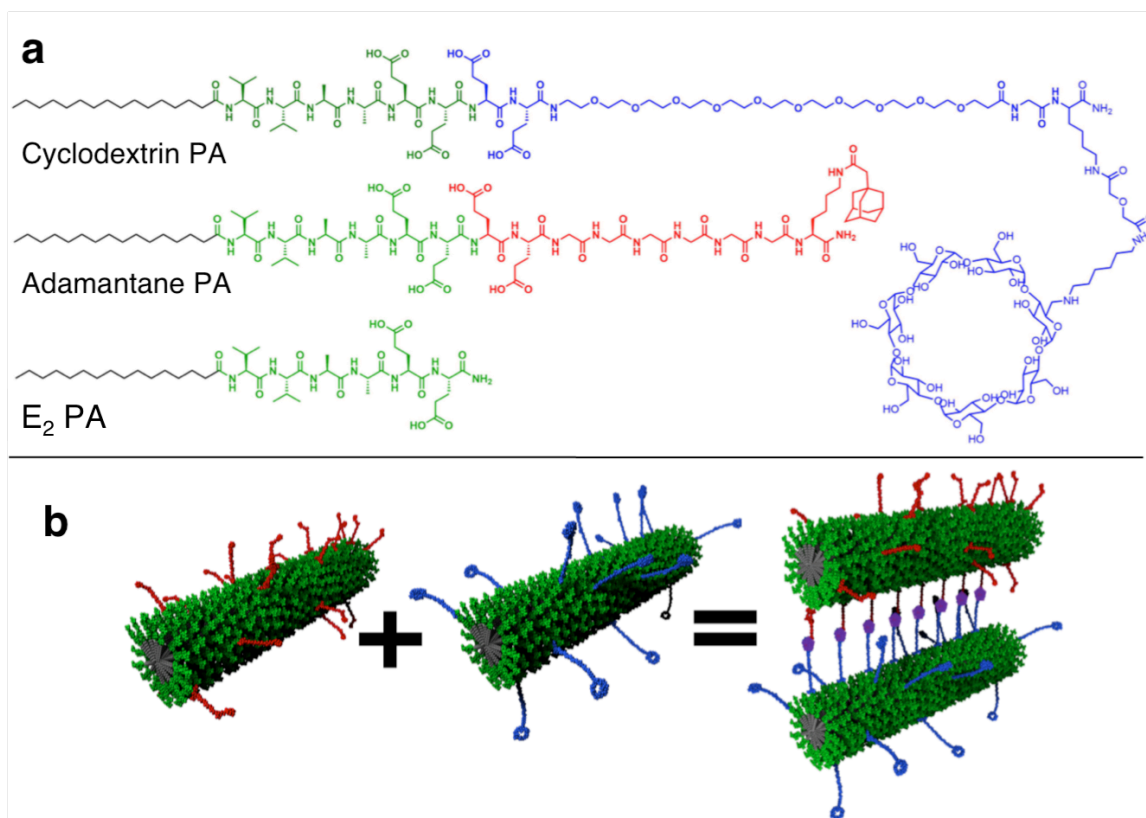
Figure 3.13: (a) Chemical structures of β-cyclodextrin containing host PA, adamantane-containing guest PA, and $C_{16}V_2A_2E_2$ filler PA. (b) Schematic illustration of host-guest interactions along assembled PA nanofibers.

The molecular design of this system is shown in (Fig. 3.13). This system utilizes the strong noncovalent interactions between β-cyclodextrin and adamantane as a supramolecular crosslinker between nanofibers. β-Cyclodextrin is known to strongly bind adamantane derivatives (K=10^3 − 10^4)[148] and has been extensively used in the hydrogel literature, particularly as a mechanism for self-healing.[149,150] The molecules were designed with long PEG_{10} or G_6 linkers in order to increase the availability of these host and guest groups in solution.[151] We envision mixing nanofibers that contain the adamantane-PA with nanofibers that have been separately prepared containing the cyclodextrin-PA after annealing; in solution, the host-guest complex will form, leading to a supramolecular crosslinked structure that can form a gel even without calcium.
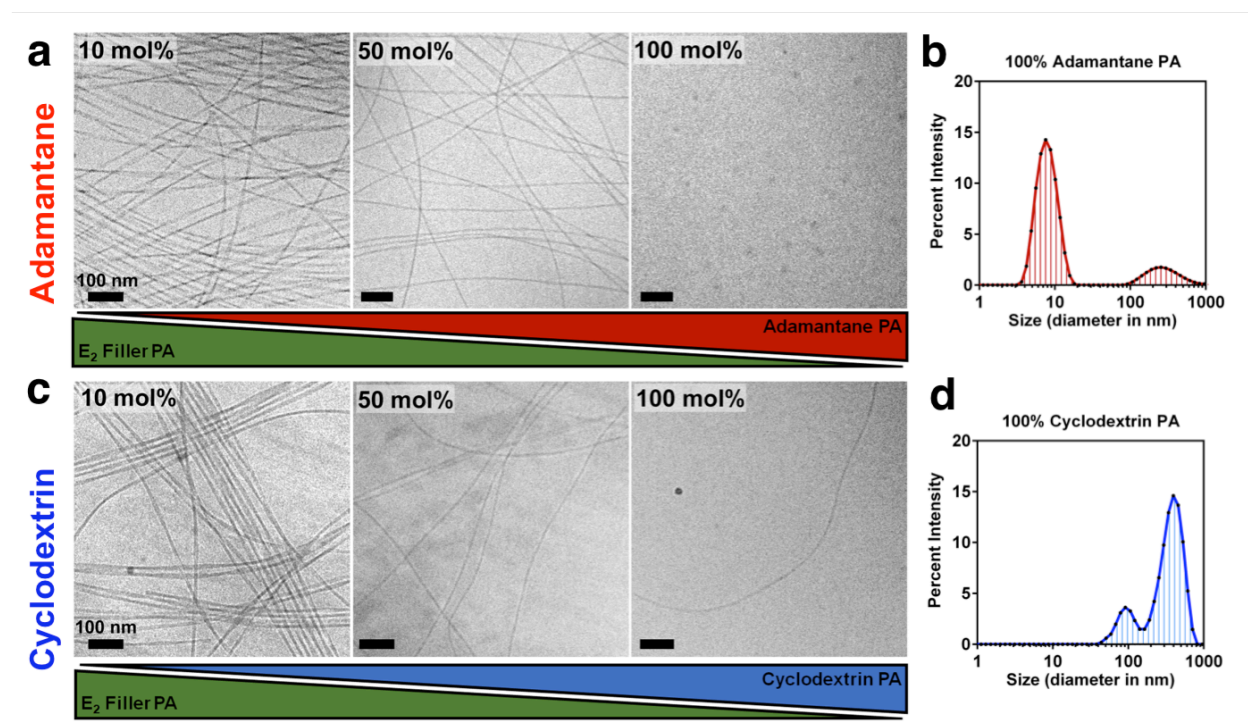
Figure 3.14: (a) Cryo-TEM of adamantane-containing PA coassembled at various mole percentages (10%, 50%, 100%) with E2 filler PA. (b) DLS trace of 100% adamantane PA showing high proportion of micelles. (c) Cryo-TEM of cyclodextrin-containing PA coassembled at various mole percentages (10%, 50%, 100%) with E2 filler PA. (b) DLS trace of 100% cyclodextrin PA showing mostly larger aggregates. Scale bars are 100 nm.

Incorporating these molecules into assemblies of $C_{16}V_2A_2E_2$ 'filler' peptide, we see that at low mole percentages of the host or guest PAs do not affect the overall nanofiber assembly Fig. 3.14. At higher mole percentages, the structures appear to shorten considerably, and at 100 mol% of the cyclodextrin or adamantane containing PAs, 1D assemblies no longer seem to present, with the majority of structures converting to micelles. This is likely due to the destabilization of the nanostructures due to the steric interference of the large cyclodextrin groups at the PA surface, resulting in poor packing when in the nanofiber state. Thus, a coassembly ratio of 10 mol% of each host and guest PA within the $C_{16}V_2A_2E_2$ backbone was used for all further studies to ensure assembly and incorporation of the host and guest moieties within the nanofibers.

When mixing the two annealed host-containing and guest-containing nanofibers together, we see a significant increase in the nanofiber width, becoming more ribbon-like (Fig. 3.15b, c). This indicates that there must be some interaction that are occurring between the host and guest moieties that are causing elongation of the nanofiber width. Mixing these two solutions also immediately causes turbidity in the sample (Fig. 3.7a), indicating that there must be some interactions occurring and formation of structures on the optical length scale in order to cause light scattering of the solution.

Looking more closely at these mixed solutions using scanning electron microscopy (SEM, Fig. 3.16), we observe micron-scale bundled structures that could be indicative of the cyclodextrin-adamantane interactions. These bundled features are not observed in any of the singular PA components within the host-guest system. This bundling interaction has also been observed in other PA systems with programmable attractive interactions, such as DNA or electrostatic interactions.[73]

The mixed host-guest system shows significant increase in the rheological properties of the material without the addition of calcium crosslinking (Fig. 3.17a). The mixed host-guest material at 3 w/v% showed significant increase in storage and loss modulus over unmixed or filler samples, with a 210x increase in G' over the E_2 PA alone, and between 4-20× increase in G' over each of the host
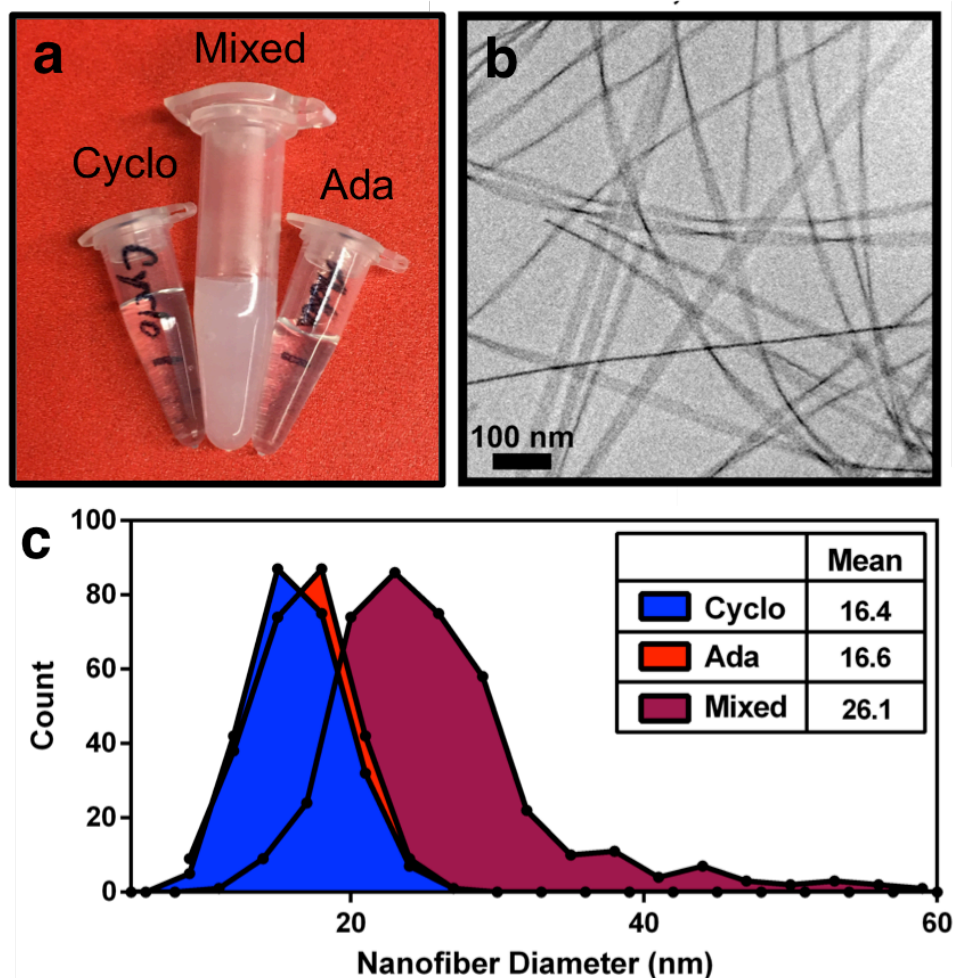
Figure 3.15: (a) Photograph of clear cyclodextrin-only (left) and adamantane-only (right) PA solutions, which turn immediately turbid (center) upon mixing. (b) Cryo-TEM of mixed host-guest PA solution. (c) Quantification of nanofiber width, showing significant increase in nanofiber diameter after mixing.

or guest components alone. Host-guest interaction are dynamic, meaning these materials are able to re-form the supramolecular cross-links if they are broken during the shearing process. During oscillatory strain tests alternating between low and high strain, the host-guest PA system recovers to its original modulus, whereas the backbone PA alone shows a distinct drop in modulus as high strain is applied (Fig. 3.17b). This shows that at high strain, the ionic cross-links in the backbone PA (gelled with $CaCl_2$) are irreversibly broken, and cannot re-form once the strain is lifted. In contrast,
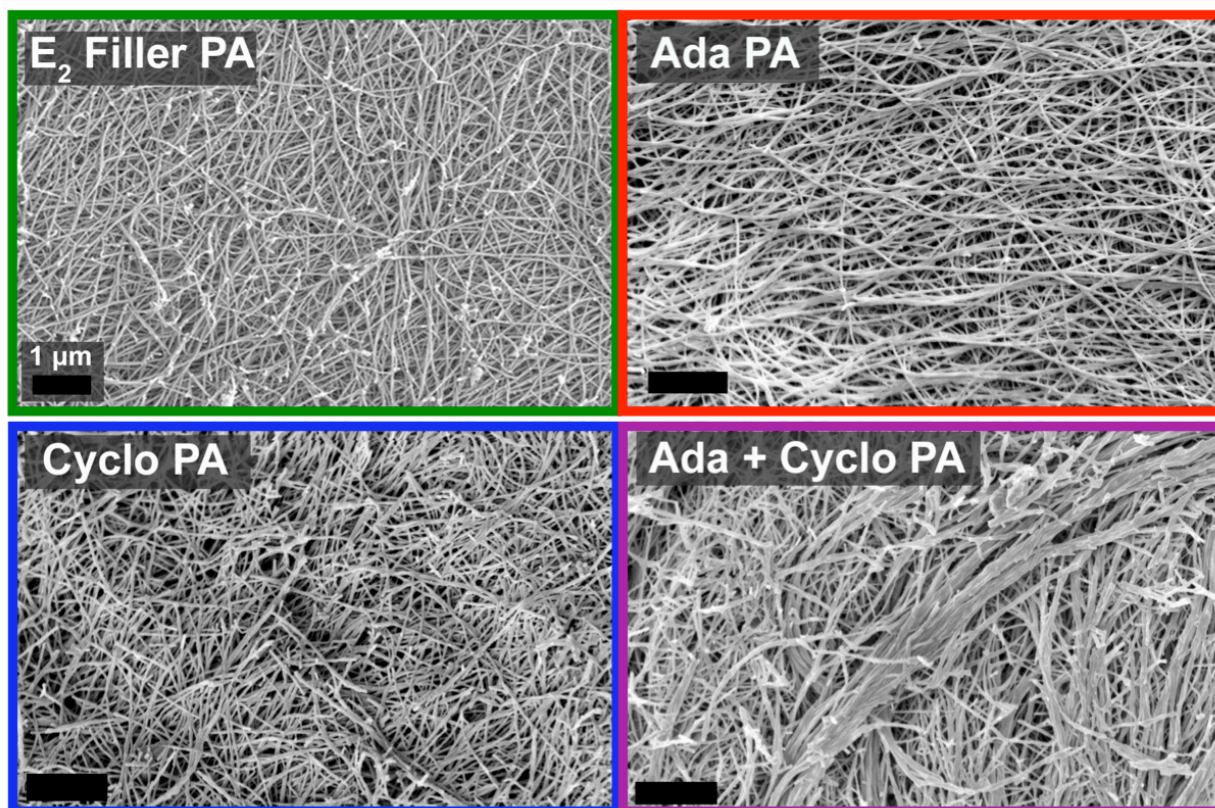
Figure 3.16: SEM images of mixed adamantane-cyclodextrin PAs (purple, bottom right) showing bundled behavior. Individual components alone (E2, adamantane PA, cyclodextrin PA) do not show the same bundling behavior. Scale bars are 1 μm.
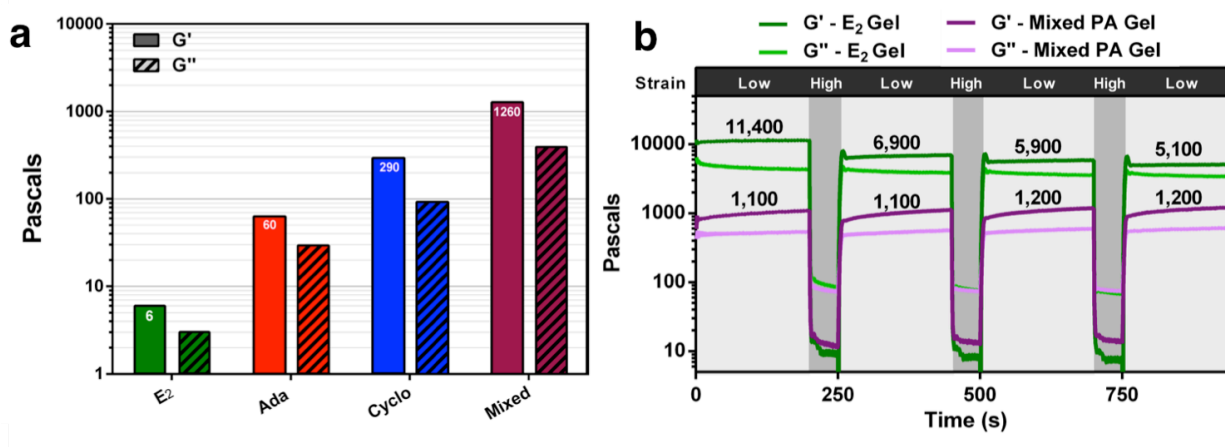
Figure 3.17: (a) Storage (G') and loss (G") modulus of host-guest PA components separately and together with no added $CaCl_2$ gelator. (b) Rheological behavior of mixed host-guest PAs compared to E2 filler gelled with $CaCl_2$ at alternating low and high strain.

the supramolecular cross-links in the host-guest system can be re-formed, resulting in complete recovery of the mechanical properties once the strain is lifted.
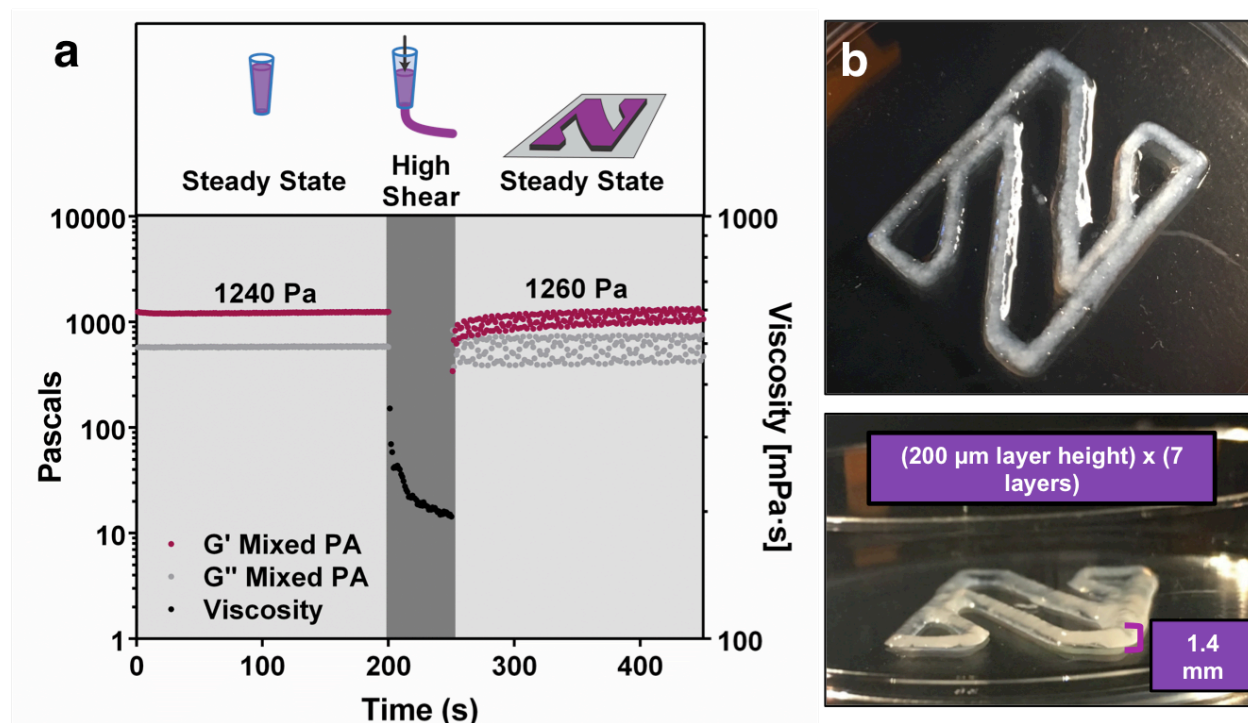
Figure 3.18: (a) Rheological assay showing shear thinning and recovery behavior of mixed host-guest PA, similar to conditions expected during the extrusion process. (b) Extrusion-printed free-standing host-guest peptide amphiphile hydrogel. Print is 7 layers tall, with no CaCl$_2$ on the substrate surface or added in between layers.

The excellent rheological properties of the host-guest PA system indicated this material would be a promising candidate for 3D printing, as it showed significant shear-thinning and recovery behavior (Fig. 3.18a). Pilot printing studies showed that this material could be printed into free-standing shapes without the addition of CaCl$_2$ crosslinking or other additives. These host-guest materials were able to be printed up to 7 layers, or 1.4 mm in height, without significant degradation of the print fidelity (Fig. 3.18b, c).

Our results demonstrate that this host-guest system shows promise for a new type of PA-based ink that can be used for 3D printing. This all-PA system requires no rheological composite additives, and can be used for printing biologically relevant scaffolds, such as regenerative tissue matrices.

3.4 CONCLUSIONS

In conclusion, we have demonstrated the development of PA-based inks for direct ink writing 3D printing applications. The applied shear force during the extrusion process is able to align PA nanofibers, creating arbitrary patterns of alignment within the material. When polymerized with thermoresponsive polymers, these sheets show a bending-based actuation behavior due to differences in alignment between the top and bottom layers of the material. We also demonstrate that the mechanical properties of the PA ink can be modulated through the incorporation of cellulose nanocrystals, which act as a rheological additive and allow for the printing of more complex architectures, including those with increased porosity. We also develop a new, host-guest PA system whose supramolecular crosslinks enhance the mechanical properties of PA inks before gelation, allowing for printing of a homogenous peptide-based system without the addition of calcium counterions. Taken together, these systems allow for the control over many different parameters in the PA 3D printing space. These materials can be used for the printing of complex hydrogel patterns as well as controlled alignment within the printed materials, which can control properties such as direction of actuation as well as provide physical cues in biological systems such as tissue regeneration.

3.5 MATERIALS & METHODS

Materials

All fluorenylmethyloxycarbonyl (Fmoc)-protected amino acids were ordered from P3 BioSystems. P3 BioSystems also provided the coupling agents 2-(1H-benzotriazol-1-yl)-1,1,3,3-tetramethyluronium hexafluorophosphate (HBTU) and benzotriazol-1-yl-oxytripyrrolidino-phosphonium hexafluorophosphate (PyBOP). 1-adamantaneacetic acid, β-cyclodextrin, and 1,6-hexanediamine were purchased from Sigma-Aldrich. Acetonitrile, ammonium hydroxide (NH_4OH), calcium chloride ($CaCl_2$), diisopropylethylamine (DIEA), *N,N*-dimethylformamide (DMF), diethylether, dichloromethane (DCM), 1,1,1,3,3,3-hexafluoro-2-propanol (HFIP), sodium

chloride (NaCl), sodium hydroxide (NaOH), and trifluoroacetic acid (TFA) were purchased from Fisher Scientific. Sulfuric acid-extracted, freeze-dried cellulose nanocrystals (CNCs) were sourced from the U.S. Department of Agriculture Forest Products Laboratories (FPL) through the University of Maine. Full processing details of these CNCs are given by Reid *et al.*[152] All chemicals were used as received unless specifically stated otherwise.

PA synthesis

PAs used in sections 3.3 and 3.4 were synthesized and purified as described in 2. PAs used in section 3.4 were synthesized using standard fluorenylmethyloxycarbonyl (Fmoc)-solid phase peptide chemistry. The peptide was synthesized on a 1 mmol scale on Rink amide MBHA resin (1.92g, 0.52 meq g^{-1}, 100-200 mesh) in the Peptide Synthesis Core at the Simpson Querrey Institute. The $C_{16}V_2A_2E_2$ filler PA, $C_{16}V_2A_2E_4G_6K(Mtt)$, and $C_{16}V_2A_2E_4PEG_{10}GK(Mtt)$ PAs were synthesized using a CEM Liberty microwave-assisted peptide synthesizer. The E2 filler PA was cleaved and HPLC-purified using standard methods, whereas the other two sequences were stored uncleaved on resin in a solution of 1:1 DMF:DCM until further chemical modification.

Adamantane PA synthesis

Resin-bound $C_{16}V_2A_2E_4G_6K(Mtt)$ was transferred to a fritted peptide synthesis vessel and swollen in DCM for 30 minutes. The ϵ-amine of the lysine residue was selectively deprotected using a solution of 4% TFA and 5% TIPS in 91% DCM. The resin was incubated with the Mtt deprotection solution for 5 min increments, washing thoroughly with DCM in between until no yellow color remained in solution. 1-adamantaneacetic acid was coupled to the free amine using 1.1 equivalents 1-adamantaneacetic acid, 1.1 equivalents PyBOP, and 6 equivalents DIEA in a 1:1 mixture of DCM and DMF for two hours. Coupling was verified through a ninhydrin colorimetric assay.

The PA was cleaved from resin and purified using standard preparatory reverse-phase HPLC techniques. Organic solvent was removed from selected fractions under reduced pressure before

being frozen, lyophilized, and stored at -20 °C until further use. Purity of the PA was determined through analytical LC-MS (Calculated M⁺: 1759.08, observed: 1758.90).
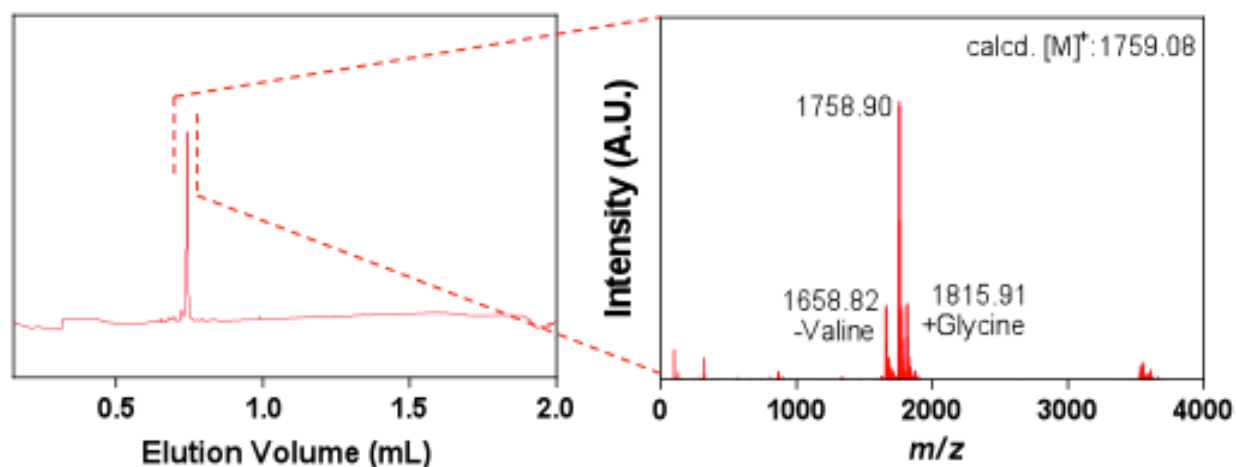
Figure 3.19: Analytical LC trace of adamantane PA with MS (inset) of primary peak.

Cyclodextrin PA synthesis

Synthesis of the cyclodextrin amine (CD-amine) was performed as described in Loebel *et al.*[153] Briefly, in a 250-mL round bottom flask, β-cyclodextrin (20 g, 17.62 mmol) was suspended in water (125 mL) and cooled to 0 °C over ice. *p*-Toluenesulfonyl chloride (4.2 g, 22 mmol) was dissolved in 10 mL acetonitrile and added dropwise to the suspension. The reaction was stirred at room temperature for 2 hours. The reaction was then basified to pH ~8.5 with addition of solid ammonium chloride. The crude produced was purified by multiple precipitations from water and acetone and dried under vacuum to give the intermediate 6-*o*-monotosyl-6-deoxy-β-cyclodextrin as a white powder.

The intermediate 6-*o*-monotosyl-6-deoxy-β-cyclodextrin (5g, 3.88 mmol) and DMF (25 mL) was added to a three-necked flask equipped with a condenser and sealed under nitrogen. 1,6-hexanediamine (20g, 172 mmol) was heated until liquid and added immediately to the reaction flask via syringe. The reaction was carried out under nitrogen at 80°C for 18 hours. The produced

was precipitated 3× from acetone and washed with diethyl ether to afford the final product as a white powder.

Resin-bound $C_{16}V_2A_2E_4PEG_{10}GK(Mtt)$ was transferred to a fritted peptide synthesis vessel and swollen in DCM for 30 minutes. The ϵ-amine of the lysine residue was selectively deprotected using a solution of 4% TFA and 5% TIPS in 91% DCM. The resin was incubated with the Mtt deprotection solution for 5 min increments, washing thoroughly with DCM in between until no yellow color remained in solution. Diglycolic acid was coupled to the free amine using 1.1 equivalents diglycolic acid, 1.1 equivalents PyBOP, and 6 equivalents DIEA in a 1:1 mixture of DCM and DMF for one hour. Coupling was verified through a ninhydrin colorimetric assay. Then, CD-amine was coupled to the free carboxylic acid using 1.1 equivalents CD-amine, 1.1 equivalents PyBOP, and 6 equivalents DIEA in DMF overnight. Coupling was verified by microcleavage of a small amount of resin and analysis by ESI-MS.

The PA was cleaved from resin and purified using standard preparatory reverse-phase HPLC techniques. Organic solvent was removed from selected fractions under reduced pressure before being frozen, lyophilized, and stored at -20°C until further use. Purity of the PA was determined through analytical LC-MS. (Calculated M^+: 3138.54, observed: 3156.76).
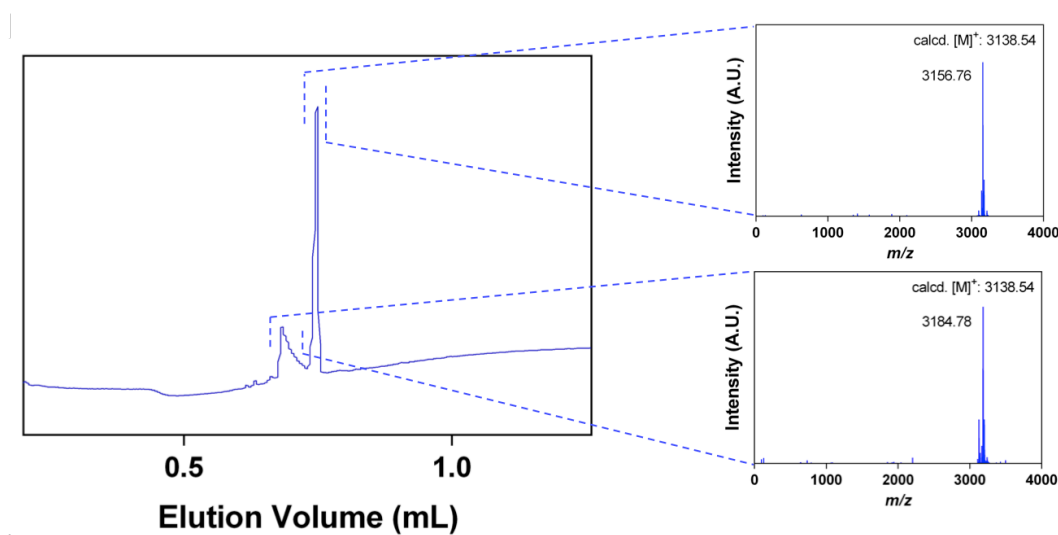
Figure 3.20: Analytical LC trace of cyclodextrin PA with MS (inset) of primary peak..

Mixing of host-guest PAs

PAs were co-assembled at different percentages with E2 filler PA by dissolving the lyophilized powder in HFIP and mixing for 15 min. Samples were frozen in liquid N_2, and HFIP was removed *in vacuo* for 2 h. Samples were then re-dissolved using several microliters of 1N NaOH in distilled deionized water. These solutions were frozen in liquid N_2 and lyophilized to remove any residual HFIP. The co-assembled peptide amphiphile powder was reconstituted in 125mM NaCl and 3mM KCl solution to a final concentration of 30 mg/mL (3 w/v%). It was then adjusted to a pH of 7.4 using 1 μL additions of 1N NaOH. Samples were annealed at 80 °C for 30 min, then slowly cooled at 1°C per minute to reach a final temperature of 27 °C. To mix, equal volumes of cyclodextrin PA and adamantane PAs were added to an eppendorf tube and vigorously pipetted together until mixed.

Fluorescent labeling of CNCs

Based on the protocol from Way *et al.*,[154] the CNCs were TEMPO oxidized utilizing a 4 wt% solution of CNCs to which 0.1 mmol/g of TEMPO and 1 mmol/g of NaBr were added. 10 mmol/g of NaOCl was added dropwise to the solution. 0.5 M NaOH was added to adjust the pH to around 10. This was left for an hour on a shaker plate before being centrifuged down at 4500 rpm for 10 min and then decanted. This was washed in ethanol 3x and then in water 3x before being left in water overnight. The CNC-COOH product was centrifuged (4500 rpm for 10 min) and decanted then lyophilized and stored as a powder before labeling with fluorescenamine.

0.3 mmol of EDC (1-(3-Dimethylaminopropyl)-3-ethylcarbodiimide hydrochloride, 99%) was combined with a solution of 1.6 wt% CNC-COOH. 0.15 mmol of fluoresceinamine was then dissolved in milliQ water and added to the CNC-COOH/EDC solution. This was placed on a shaker plate for 24 hours. The solution was then added to methanol and vortexed and centrifuged down (4500 rpm for 10 min). This was then rotovapped down and placed into 3500 kDa dialysis tubes and dialyzed for a week. This was then lyophilized, leaving a yellow product.

3D printing of covalent-supramolecular hybrid polymers

PA1 and PA2 were coassembled in a 1:9 molar ratio as described in Chapter 2, but redissolved at a final concentration of 15 mg mL^{-1} before annealing. The annealed PA fibers were printed into 1 cm × 1 cm squares on CaCl$_2$-coated glass substrates using a Hyrel 3D System 30M printer. Substrates were prepared by first washing glass coverslips with milliQ water and drying on a hot plate at 70 °C. The clean and dry coverslips were then aerosol spray coated with 0.1 M CaCl$_2$ while still heated at 70 °C, resulting in dispersed 10-50 μm CaCl$_2$ crystals at a surface density of 0.5 μmol cm^{-2}. The PA solution was extruded through a 0.41 mm inner diameter nozzle (Nordson EFD) and gelled immediately upon contact with CaCl2, allowing for string hydrogels to be patterned into squares with varying print paths designed in Slic3r (Fig. 3.21- 3.23). The tip-to-substrate distance was approximately 200 μm, with a print speed of 10 mm s^{-1} and a flow rate of 0.42 μL s^{-1}. Typical gels were 1 mm thick and consisted of 3 or 4 printed layers, with salt introduced via aerosol spray between each subsequent layer. Following printing, the square gels were stored in a hydrated environment to prevent drying before polymerization.

The printed PA hydrogels were polymerized using the procedure for the hybrid polymers described in Chapter 2 with molar ratios of DEGMA:OEGMA$_{500}$:PA1:CuBr:Bpy:ascorbic acid of 14250:750:1:2:5:100. 1 monomer wt% of NBAA crosslinker and 0.5 monomer wt% fluorescein-*O*-methacrylate were also included in the polymerization solution.
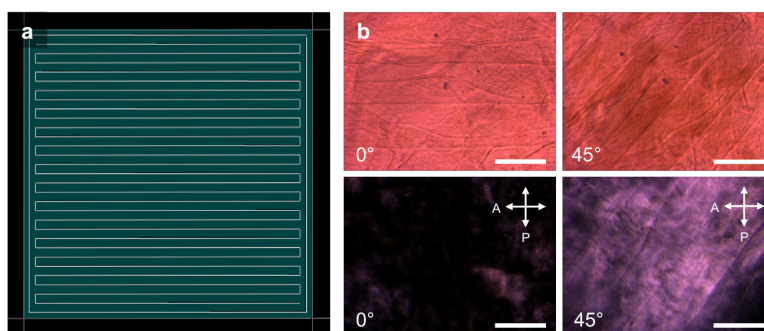
Figure 3.21: (a) Print path for a uniaxially aligned three-layer sheet. (b) Optical microscopy of an aligned three-layer sheet, demonstrating strong birefringence when the sample is rotated 45°to the polarizer. Scale bars are 400 μm.
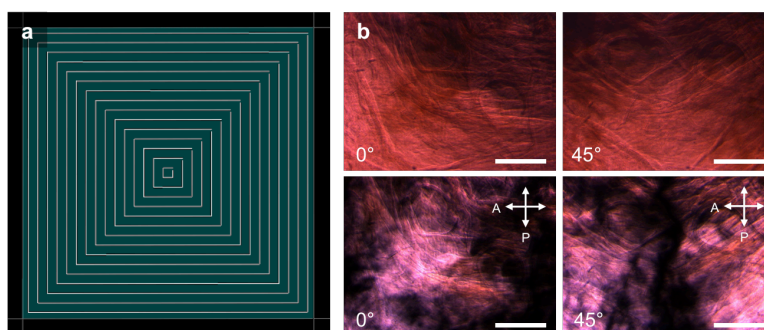
Figure 3.22: (a) Print path for a square spiral three-layer sheet. (b) Optical microscopy on a corner of a square spiral three-layer sheet, showing bright birefringence at the point of the corner when the sample is at 0°, but a dark region at the corner point when the sample is rotated 45°to the polarizer. At the corner point, the fibers bend at ∼45°to connect one edge of the square to the adjacent edge. Scale bars are 400 μm.
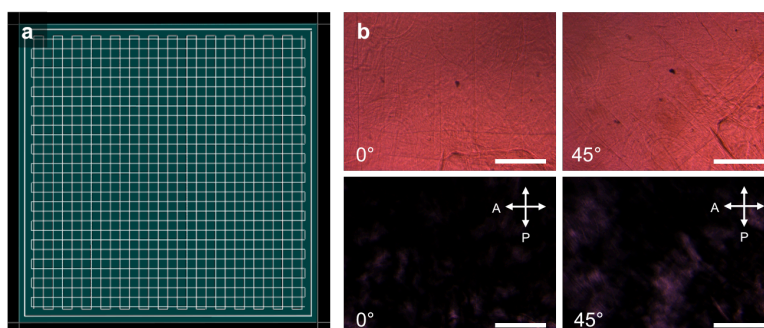
Figure 3.23: (a) Print path for a cross-hatched four-layer sheet. (b) Optical microscopy of a cross-hatch four-layer sheet, with birefringence extinguished at both 0°and 45°because the layers are oriented 90°to each other. Scale bars are 400 μm.

3D printing of CNC-PA hybrid polymers

The CNC/PA inks were prepared at a composition of 12.5 w/v% CNC and 1.5 w/v% PA (90 mol% $C_{16}V_3A_3E_3$ with 10 mol% EATRP PA and trace TAMRA). The CNCs were dispersed in milliQ water at 20 w/w% (25 w/v%) concentration through alternated stirring for 5 min and vortexing for 30 sec until the resulting material was visibly smooth. The ink was then centrifuged down at 4500 rpm for 5 min and horn sonicated in an ice bath at 20% amplification (Fisher Scientific Model 120 Sonic Dismembrator with 0.3 cm diameter probe). The ink was pulsed 30× for 10 seconds on/off intervals while moving the probe to different locations within the sample to optimize the processing due to its high viscosity. After each 10 cycles, the ink was stirred to get a homogenous product. After the horn sonication, the ink was centrifuged down for 5 min at 4500 rpm and transferred to a syringe and extruded into a solution of 3 wt% PA. This was then hand stirred with a spatula until combined (~10 min) and then transferred to a printing cartridge and centrifuged down at 4500 rpm for 1 min.

CNC/PA composite prints were made using an EnvisionTEC 3D Bio-plotter (Manufacturer Series) with a low temp cartridge head. The ink was printed with either a 27G (0.2 mm diameter), conical (tapered) plastic nozzle or a 12.7 mm long 27G (0.2 mm diameter) straight nozzle). The prints were 10 mm × 10 mm × 540 µm (3 layers) with an aligned inner structure with center-center strand distances of 0.3 mm. With the 27G conical nozzle, the printing parameters were 0.4 bar and 20 mm/s. The structures were printed onto either glass coverslips or wetted dialysis membranes. After printing, the structures were ionically crosslinked with ~500 µL of 0.1 M $CaCl_2$ pipetted onto the print surface and held for at least 10 minutes. The prints were kept in humid conditions until further polymerized as described above.

3D printing of host-guest PAs

3 wt% solutions of adamantane PA and cyclodextrin PA were mixed in a 1:1 ratio via manual pipetting and loaded into 3 mL pneumatic piston syringe barrels (Nordson EFD). Constructs were printed onto untreated plastic petri dishes using a Cellink BioX 3D bioprinter to minimize spread.

The optimal printing parameters used a 0.41 mm inner diameter conical nozzle (Nordson EFD) with 5 kPa extrusion pressure, 5 mm/s print speed and 0.2 mm layer height. Both the ink and the build platform were kept at 25 °C throughout the printing process.

Polarized optical microscopy

Samples were placed in glass bottom 35mm-dishes (MatTek Corporation, P35G-1.5-14-C) filled with milliQ water. The samples were then imaged in between two perpendicular light polarizers using a Leica DM750 P instrument in reflection mode using Leica Application Suite V4.2 software. A sample stage allowed for the precise rotation and x, y-positioning of the samples. Bright-field images were recorded using the same instrument without the light polarizers.

Confocal laser-scanning microscopy

Cross-sectional samples were created by thinly slicing printed and polymerized hybrid materials into ~1 mm sections using a razor blade. These sections were placed on glass coverslips and kept hydrated during the course of imaging. Samples were visualized using a Nikon A1R confocal laser-scanning microscope equipped with GaAsP detectors.

Scanning electron microscopy

Printed hybrids were dehydrated by incubation in a series of ethanol solutions of increasing concentration. Ethanol was subsequently removed by critical point drying (Tousimis Samdri-795). Extra caution was taken to ensure the samples were not heated above the lower critical solution temperature of the polymer material during the exchange. Dehydrated hybrid prints were mounted on stubs using carbon glue and coated with 21 nm of osmium (Filgen, OPC-60A) to create a conductive sample surface. All SEM images were taken using a Hitachi SU8030 or LEO 1525 instrument operating at an accelerating voltage of 2 kV.

Cryogenic transmission electron microscopy

PA samples were prepared as described in section 3.5. Cryo-TEM was performed using a JEOL 1230 TEM working at 100 kV accelerating voltage. Samples were plunge frozen using a Vitrobot Mark IV (FEI) vitrification robot at room temperature at 95-100% humidity. 7.5 µL of sample solution (0.1 w/v%, diluted from 1 w/v% immediately before grid preparation) were placed on 300-mesh copper grids with lacey carbon support, blotted, and plunge frozen into liquid ethane. Samples were transferred into a liquid nitrogen bath, and placed into a Gatan 626 cryo-holder through a cryo-transfer stage. Images were acquired using a Gatan 831 CCD camera.

Nanofiber diameter was measured manually in ImageJ, using the widest part of the ribbon-like assembly. Multiple nanofibers were measured per image, and at least five representative images were analyzed per sample.

Rheological measurements of CNC-PA inks

To mimic the 3D printing extrusion process, rheological assays based on Schaffner *et al.* were done using an Anton Paar MCR302 rheometer with a CP25-2 fixture.[155] The ink was first oscillated for 60 seconds at 0.1% strain and 10 rad/s angular frequency to determine the resting modulus before printing. Then, a standard flow test with constant rotation at a shear rate of 100 s^{-1} was performed for 60 seconds, which mimics the extrusion process. Then, the resting modulus after flow was measured for 60 seconds using the same 0.1% strain and 10 rad/s angular frequency.

Shear thinning properties of PA inks with various CNC content was measured using a standard flow test on an Anton Paar MCR302 rheometer with a CP50-1 fixture. Shear rate was varied between 1 s^{-1} and 1000 s^{-1} and viscosity was measured at various shear rates.

Rheological measurements of host-guest PAs

PA materials were prepared using methods described above. An Anton Paar MCR302 Rheometer with a 25 mm cone plate was used for all rheological studies. 150 µL of PA liquid was placed on

the sample stage. Divalent gelling solution was only used for the "E2 PA Gel" sample in which 30 μL of 150 mM CaCl$_2$ solution (final concentration 25 mM) was placed on the plunger positioned above the material. The plunger was lowered to the measuring position and a humidity collar was added to prevent sample evaporation. For the experiments used to determine storage and loss modulus, the sample was equilibrated for 30 minutes with a constant angular frequency of 10 rad/s and 0.1% strain. The storage and loss modulus were recorded at the end of the 30-minute interval. For the recovery experiments, the sample underwent cyclical loading. The sample was exposed to 0.5% shear strain for 200 seconds, followed by 50% shear strain for 50 seconds all at 10 Hz over a course of 4 cycles. The storage and loss modulus were recorded and plotted against time.

Microindentation

Indentation tests were carried out using an axisymmetric probe tack device, consisting of a piezoelectric stepping motor connected in parallel to a load transducer attached to a flat cylindrical indenter with a radius (R) of 0.59 mm. Displacement was monitored using an optical sensor with submicrometer sensitivity. All samples with thickness (h) of 0.5 mm were fixed on a glass plate with a camera underneath providing optional imaging. The indenter approached the sample with a constant velocity of 10 μm s^{-1} until a specified load, ranging from 10 to 25 mN, was reached. The resulting load (P) and displacement (d) data were used to calculate the modulus of the sample. The Young's modulus (E) of the sample was calculated by using the relation between the compliance ($C = d/P$) and the modulus at a specified contact radius (a) assuming Poisson's ratio of the sample equals 0.5.[124]

$$E = \frac{3P}{8\delta a}\left(1 + \frac{1.33a}{h} + 1.33\left(\frac{a}{h}\right)^3\right)^{-1} \tag{1}$$

An average value of E from the above equation at low strain (displacement between 0.01 and 0.03 mm) was used as the modulus. Moduli from multiple indents were averaged to give the reported modulus.

4 Microscale Thermoresponse of Liquid Crystalline Assemblies

4.1 OBJECTIVES AND SIGNIFICANCE

Developing complex, responsive materials requires the hierarchical ordering of smaller building blocks into precise structures that can translate responses or motions that occur on the nanoscale to a bulk, macroscopic response. Taking inspiration from nature, we use innately anisotropic self-assembled peptide amphiphiles to direct their assembly into higher ordered superstructures during an annealing process. When heated in aqueous solution, these supramolecular nanofibers exhibit lower critical solution temperature (LCST) behavior, which causes the fibers to reversibly pack into a hexagonal lyotropic liquid crystalline lattice and further aggregate into micron-scale bundles containing thousands of ordered fibers. This crystallization into a hexagonal lattice is highly dependent on the ionicity of the peptide amphiphile nanofibers and the strength of electrostatic interactions and charge screening between fibers. Using molecular dynamics simulations, we conclude that this crystallization behavior and bundling is entropically driven by the changing strength of water-PA hydrogen bonding interactions at elevated temperatures, similar to the LCST behavior that is seen in thermoresponsive polymers. This is the first observation of LCST behavior in a fully supramolecular assembly, and is shown to be generalizable to peptide amphiphile molecules with different peptide sequences. This work reported suggests strategies to control superstructure formation and alignment within a liquid crystalline peptide amphiphile solution, which could be used for development of optical properties or macroscopic pattern generation.

4.2 BACKGROUND

Over the millenia, nature has developed extraordinarily complex responsive materials that are able to take chemical input signals and turn them into physical output, such as the motion of muscles,[11] the color-changing abilities of melanocytes,[156] or the drooping defense response of *Mimosa pudica* plants.[157] Natural systems are able to devise these responsive materials through structural hierarchy, where smaller building blocks are precisely ordered into larger and larger structures. Key to this behavior is anisotropy within these building blocks, where having one axis that is different (typically longer) than the others can direct the responsive properties of the material along a certain direction.

This structural hierarchy often lends itself to increased mechanical strength, such as the collagen fibrils that guide bone growth,[9] or help turn small nanoscale motions into large macroscopic ones, such as the actin and myosin proteins that make up muscles.[14,15] While nanoscale building blocks such as peptides, oligonucleotides, and saccharides are abundant, extending their structures to a larger length scale in an ordered manner is much more challenging than nature would make it seem.

Researchers have put significant efforts into designing synthetic macromolecules that display some of this responsive behavior. Typically, in synthetic macromolecular systems, responsive behavior occurs through a change in the interaction energy of the molecules with the surrounding environment when certain stimuli, such as change in temperature, electric field, or light are applied. One such class of polymers are lower critical solution temperature (LCST) polymers. These polymers are soluble at low temperatures due to a high degree of hydrogen bonding interactions with the solvent. If the temperature is increased above a critical temperature, more of the hydrophobic portion of the polymers becomes exposed, and it becomes entropically unfavorable for the surrounding water molecules to hydrogen bond with the polymer molecules. This causes a collapse of the polymer chains and precipitation from the solution, leading to increased turbidity and volumetric contraction of the sample. However, the molecular requirements for these responsive behaviors mean that the chemistries are limited to certain monomers that have hydrophilic-hydrophobic com-

ponents such as NIPAM,[158] DMAEMA,[159] OEGMA,[111,160] and elastin-like peptides,[34,161] which are all highly studied systems within this field. However, the difficulty with macromolecular systems is that it is difficult to achieve the structural control needed for building hierarchical order. Most polymers intrinsically have low persistence length and often form globular structures in solution, meaning anisotropic structures that would be able to direct properties along one axis are difficult to achieve. In order to achieve anisotropy and subsequent ordering, very specific structural considerations, such as the formation and phase separation of block copolymers, or application of strong forces such as high shear, must be devised, which is very limiting.

Liquid crystalline assemblies are promising for the development of hierarchically structured materials. Lyotropic liquid crystals consist of a suspension of mesogen molecules in a solvent, the morphology of which can be tuned by their concentration.[162] Molecules that form liquid crystalline solutions are often structurally anisotropic, causing them to align along their long axis in order to maximize translational entropy.[74] This typically results in microdomains of structural anisotropy, however, due to the nucleation of many aligned domains simultaneously, it is difficult to achieve global alignment within a sample or bulk material. Lyotropic liquid crystals can be aligned by placing the sample within external fields such as an electric field, magnetic field, or by applying mechanical forces.[163] Similarly, these external fields can also be used to induce a specific response within a liquid crystalline material. However, these fields typically need to be fairly strong in order to induce alignment or change in alignment. In addition, the chemistry of the mesogen molecules must be fairly specific in order to exhibit the desired response; changing the chemistry of a mesogen molecule without changing the responsive properties is not trivial.

Peptide amphiphiles are a class of molecules that contain an oligopeptide sequence covalently conjugated to a lipid tail.[58] This creates a molecule with distinctly hydrophobic and hydrophilic ends that can subsequently pack into very high-aspect ratio anisotropic nanostructures, where the length of the structure is on the micron length scale while the height and width remain on the nanometers length scale. The oligopeptide sequence, created through solid-phase peptide synthesis,

is easily modifiable to contain not only groups for assembly, but can also have additional active sequences attached, such as bioactive epitopes for cell signaling. Our group has studied this class of materials extensively for applications in tissue regeneration, where the peptide amphiphiles can act as structural scaffolds for cells to grow on.[164–166] More recently, our group has also investigated these nanostructures as a scaffold that directs the reversible thermally driven anisotropic actuation of a macroscopic thermoresponsive material.[68]

These peptide amphiphiles have been shown to form lyotropic liquid crystals in aqueous solutions at high concentration. These liquid crystalline solutions can be easily aligned into macroscopic domains using shear force, which can be applied easily in a variety of processing conditions.[69] It is known that in order to form these liquid crystalline solutions, thermal annealing is necessary. This annealing changes the nanoscale features, such as fiber length, driving them to their thermodynamically favored state.[45] However, the effects of annealing on micro- or macro-scale features, such as the molecular ordering that causes the formation of the lyotropic liquid crystal, have not been studied.

Here, we investigate the behavior of peptide amphiphile assemblies during annealing processes. We show the formation of the lyotropic liquid crystalline phase and the formation of μm-scale superstructures upon heating, attributing this behavior to a reversible lower critical solution temperature (LCST) behavior. We employ variable temperature confocal laser-scanning microscopy (VT-CLSM) and variable temperature X-ray scattering experiments to observe the LCST behavior, as well as additional calorimetric and spectroscopic techniques. These experiments, along with full atomistic molecular dynamics simulations, suggest that the molecular mechanisms is similar to the entropically driven LCST behavior seen in thermoresponsive macromolecular systems. This LCST behavior is observed for multiple PA molecules with varying peptide sequence, and is the first demonstration of such behavior in a fully supramolecular assembly.

4.3 RESULTS & DISCUSSION

4.3.1 *Observation of LCST behavior in PA assemblies*

We used an amide terminated palmitoyl-Val-Val-Val-Ala-Ala-Ala-Glu-Glu-Glu ($C_{16}V_3A_3E_3$) as the model peptide amphiphile sequence for our studies due to its strong propensity to form beta-sheet hydrogen bonds and assemble into robust, long nanostructures. We use this structure as the basis for our studies. We prepare the fresh PA solutions at 2 w/v% in milliQ water, with 1.5 equivalents of base (NaOH or CsOH) to solubilize the PA molecules. No additional salt was added to the solution, and solutions were well-sonicated to ensure full dissolution and removal of any micron-sized anisotropic features, as confirmed by polarized optical microscopy (full preparation details in the Methods Section 4.5).

Variable-temperature small-angle X-ray scattering (VT-SAXS) profiles of sample solutions within sealed quartz capillaries reveal an interesting temperature-dependent change in translational order of these assemblies (Fig. 4.1a). At room temperature, we observe the scattering form factor that is typical of PA nanofiber assemblies, with no sharp Bragg peaks that would be indicative of any crystallinity in the system. As the assemblies are heated between 65-75 °C, we see the appearance of sharp Bragg peaks attributed to the formation of a hexagonal lyotropic liquid crystalline phase. As the heating continues to 95 °C, these Bragg peaks shift outward to higher q-values, representing smaller interfiber spacings. Upon cooling, the interfiber spacings shift back to lower q-values and the intensity of the Bragg peaks diminish, but the hexagonal packing pattern remains, even at 35 °C.

Seeing this nanoscale order, we investigated the presence of higher order structures at the micron scale using variable-temperature confocal laser-scanning microscopy (VT-CLSM) and polarized optical microscopy (VT-POM). Most typical commercial VT stages for confocal microscopy are not designed for the high temperatures needed in the annealing process (80-95 °C) with short working distances required for CLSM, and thus we designed and machined a custom aluminum
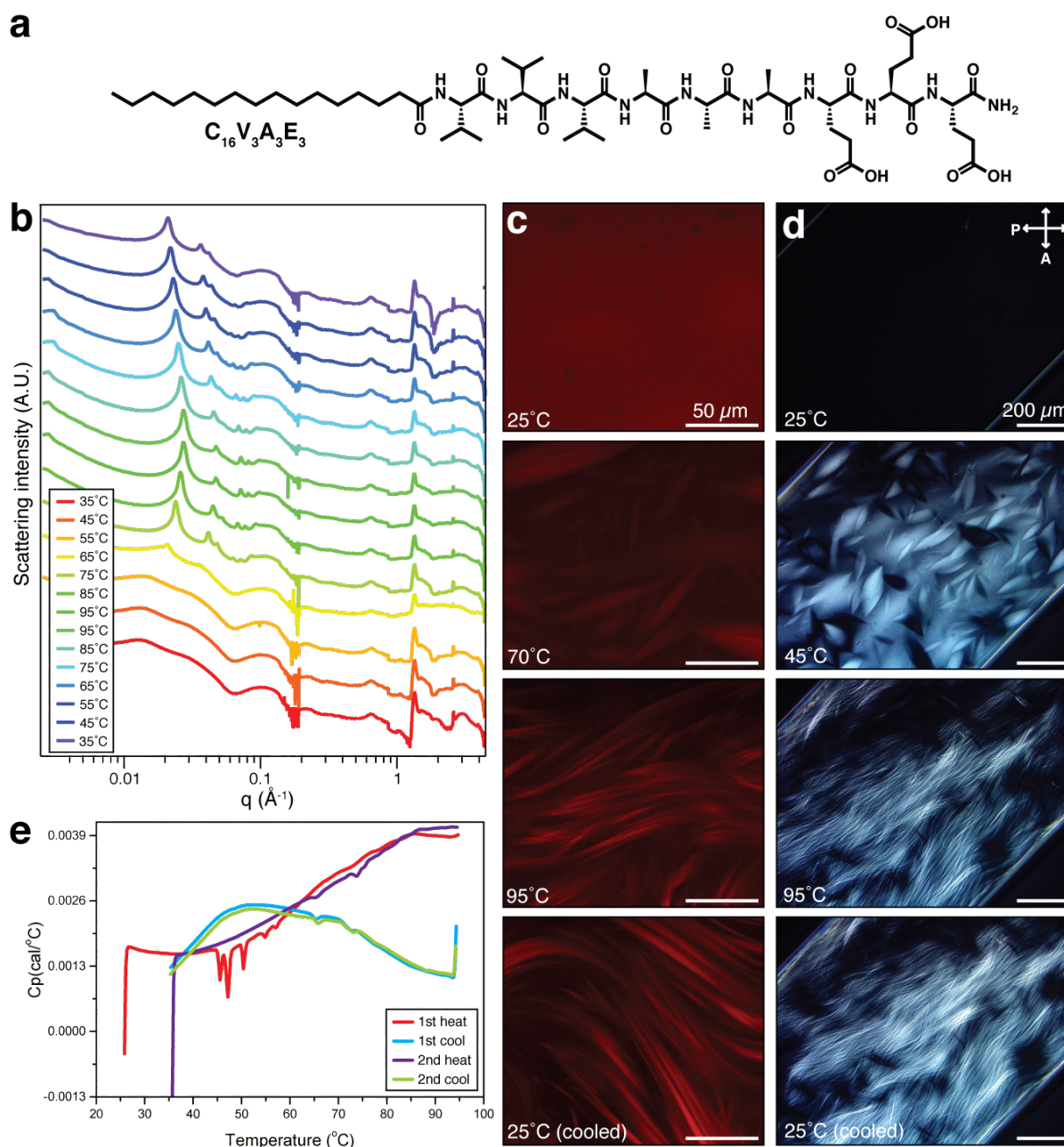
Figure 4.1: (a) Chemical structure of $C_{16}V_3A_3E_3$ PA. (b) Variable-temperature X-ray scattering experiments showing growth of hexagonal liquid crystalline peaks upon heating. (c) Variable-temperature confocal laser-scanning microscopy. (d) Variable temperature polarized optical microscopy. (e) Differential scanning calorimetry.
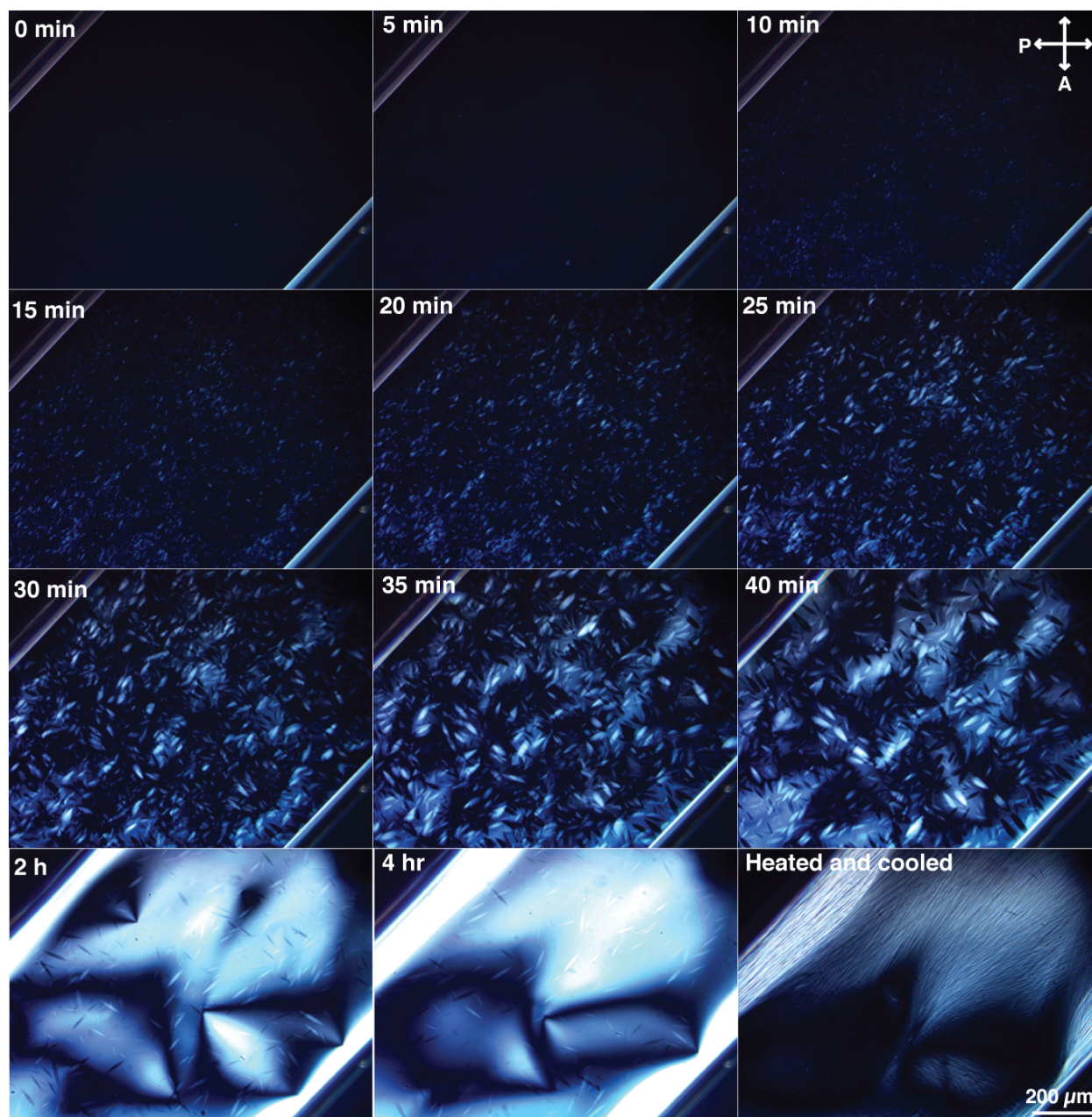
Figure 4.2: VT-polarized optical microscopy showing growth of tactoids over time at 25 °C. Tactoids grow and coalesce over time, but do not bundle until heated. Scale bar = 200 μm.

heating stage that could easily and evenly heat sealed glass capillaries for these experiments (Methods Section 4.5).

PA samples immediately showed aggregation into spindle-like structures within 5-10 minutes of sample preparation at room temperature in both CLSM and POM (Fig. 4.1). These highly bire-

fringent spindle-like structures are known in the liquid crystal literature as tactoids, which can form within a solution of liquid crystalline mesogens.[83,167] Due to local microphase separation, the tactoids are nematic domains within isotropic matrix of the mesogens. These domains are metastable in nature, and can grow or coalesce to approach a single domain of nematic liquid crystal.[168,169] These tactoids also have some degree of rotational freedom, which allows them to align over time. Once two proximal tactoids are at the same angle of orientation, they can coalesce into one larger tactoid domain (Fig. 4.2). This tactoid growth and coalescence corresponds with PA nanofiber growth over time, which can be observed using transmission electron microscopy (TEM). Qualitatively, the PA nanofibers are shown to significantly elongate over the course of 60 minutes as well as increase in contour length (Fig. 4.3)

These PA tactoids grow and elongate as the samples are heated. At high temperatures (~80-95 °C), the tactoids abruptly transition into extremely long bundles (Fig. 4.1). These bundles are fairly regular, between 4-5 μm in diameter, and do not occur upon aging, only upon heating of the sample (Fig. 4.2). In some samples, precipitation can be seen at this high temperature, implying a high degree of crystallinity within the sample. Upon cooling, these bundled features become less regular, and the entire lattice redissolves and re-swells (Fig. 4.1). This bundling/unbundling
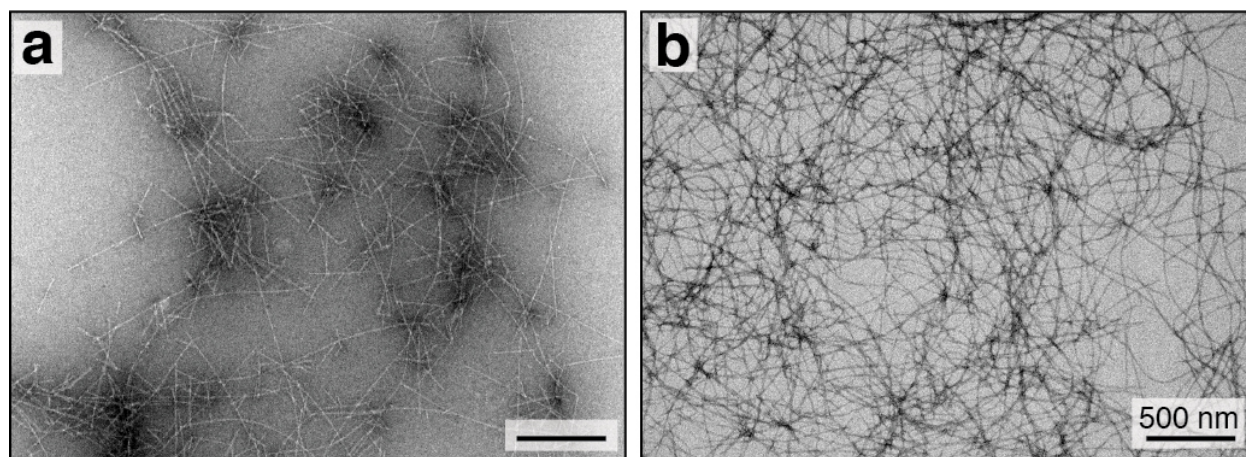
Figure 4.3: Conventional TEM of PA samples when (a) freshly dissolved at 2 wt/v% and (b) after 60 minutes of aging at room temperature. Samples stained with 1 w/v% uranyl acetate solution. Scale bar = 500 nm.
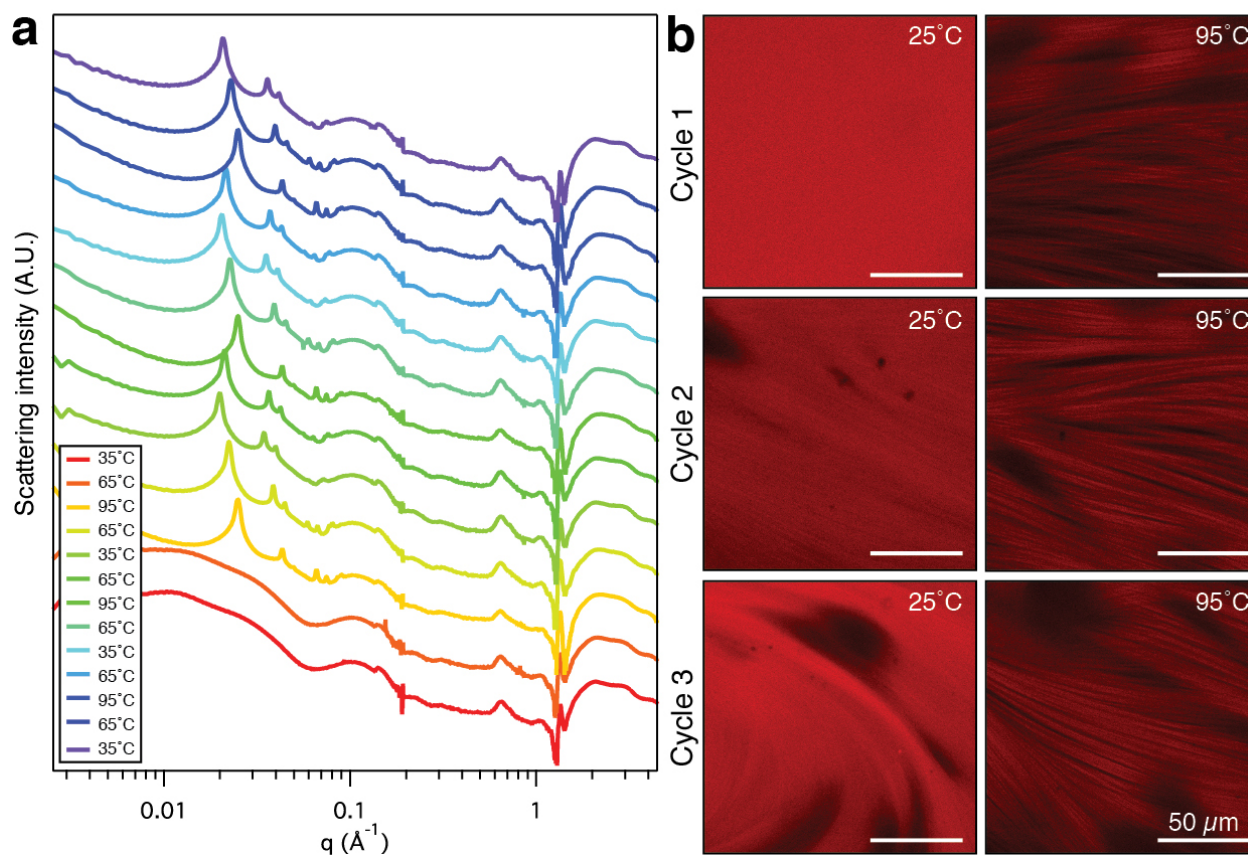
Figure 4.4: (a) VT-SAXS showing three heating-cooling cycles. Once formed, the primary peak position of the hexagonal lattice shifts reversibly between low and high q range. (b) VT-CLSM showing PA microstructures during three heating and cooling cycles. Scale bar = 50 μm.

behavior must be indicative of a significant reversible volume change within the PA-rich regions of the superstructure. This bundling-unbundling behavior, with corresponding shifts of the hexagonal packing peaks, can be observed upon multiple heating-cooling cycles; though tactoid structures do not reform-upon cooling. (Fig. 4.4)

Taken together with the X-ray scattering data, we propose that the bundles are highly ordered domains of hexagonally packed PA nanofibers, with each bundle comprised of hundreds of individual nanofibers. Upon cooling, the interfiber spacing increases, causing re-swelling of the super-structure and some loss of superstructure order. This behavior is similar to the LCST behavior observed in thermoresponsive polymers. In LCST polymers, this contraction-expansion behavior

is an entropically driven aggregation process due to the entropic penalty of having water bound to the surface of a hydrophobic polymer at elevated temperatures.

We investigated the thermodynamic nature of the observed phase transitions using differential scanning calorimetry (DSC, Fig 4.1e). Upon initial heating, we see several sharp exothermic transitions between 40-60 °C that are likely related to the formation and growth of the tactoids. At higher temperatures, around 65 °C and 75 °C, we also see small inflection points that seem to match up with the onset of the hexagonal crystalline packing peaks in VT-SAXS. Upon cooling, these transitions are more prominent, meaning these are reversible, entropically driven transitions. In addition, upon second heating, the sharp exothermic transitions attributed to the tactoids are no longer present, consistent with the observations from microscopy. The reversible entropically driven transitions seen at 65 °C and 75 °C are consistent with the LCST behavior seen in thermoresponsive polymers, and correspond to the release of bound water molecules,[170,171] and further corroborate the observed LCST behavior in this fully supramolecular system.
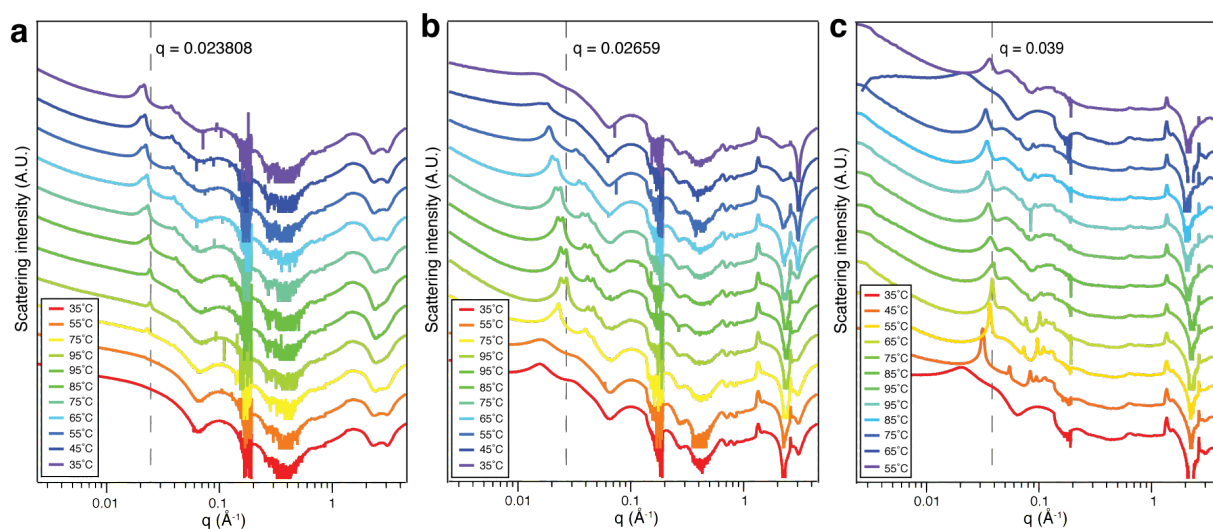
Figure 4.5: VT-X-ray scattering experiments at different PA concentrations. (a) 1 wt% PA, showing primary peak at q = 0.023808 Å at 95 °C. (b) 2 wt% PA, showing primary peak at q = 0.02659 Å at 95 °C. (c) 5 wt% PA, showing primary peak at q = 0.039 Å at 95 °C.

Typical of a lyotropic liquid crystalline solution, the interfiber distance is concentration dependent, ranging from 16.1-26.4 nm center-to-center distance between 1-5 wt% PA (Fig. 4.5). The maintenance of hexagonal packing at low temperatures is also concentration dependent (Fig. 4.5); at lower concentrations, the Bragg peaks disappear upon cooling, with only the fiber form factor remaining. This is likely due to the ability for larger volumetric expansion and more disorder at lower concentrations. Looking at the wide-angle X-ray scattering (WAXS) patterns, we observe that the peak at $q \simeq 1.5$ Å^{-1}, attributed to the beta-sheet hydrogen-bonding, is maintained throughout the heating-cooling cycle. This implies that there is a reversible change in interfiber spacing at 65 – 95 °C; however, the overall hexagonal translational order is fixed once it is formed.

4.3.2 *Effect of ionicity on LCST behavior*

With this observation of LCST behavior in a supramolecular system for the first time, we further investigated the factors that control the LCST behavior. Previous work in the Stupp group has shown that fibrillar supramolecular systems in water can pack into hexagonal liquid crystal phases; however, the interfiber packing distances in these systems were static once the hexagonal phase was formed.[116,172] The formation of these hexagonal assemblies were shown to be strongly dependent on buildup of repulsive charges between molecular assemblies. As such, we then varied environment conditions such as amount of base, added salt, and concentration within our system.

The formation of the hexagonally packed phase shows a strong dependence on PA ionicity within the sample (Fig. 4.6). We see that with a lower amount of base (Fig. 4.6a), and therefore lower net charge per PA molecule, the onset of Bragg peaks is suppressed, with only broad peaks that suggest a loose, less regular interfiber correlation occuring. Conversely, with higher amounts of base (2 equivalents CsOH/PA molecule, Fig. 4.6b) we see even an immediate onset of crystallization to the hexagonal phase, with sharp Bragg peaks observed as low as 35 °C. The hexagonal packing is maintained throughout the entire heating and cooling profile. By VT-CLSM and VT-
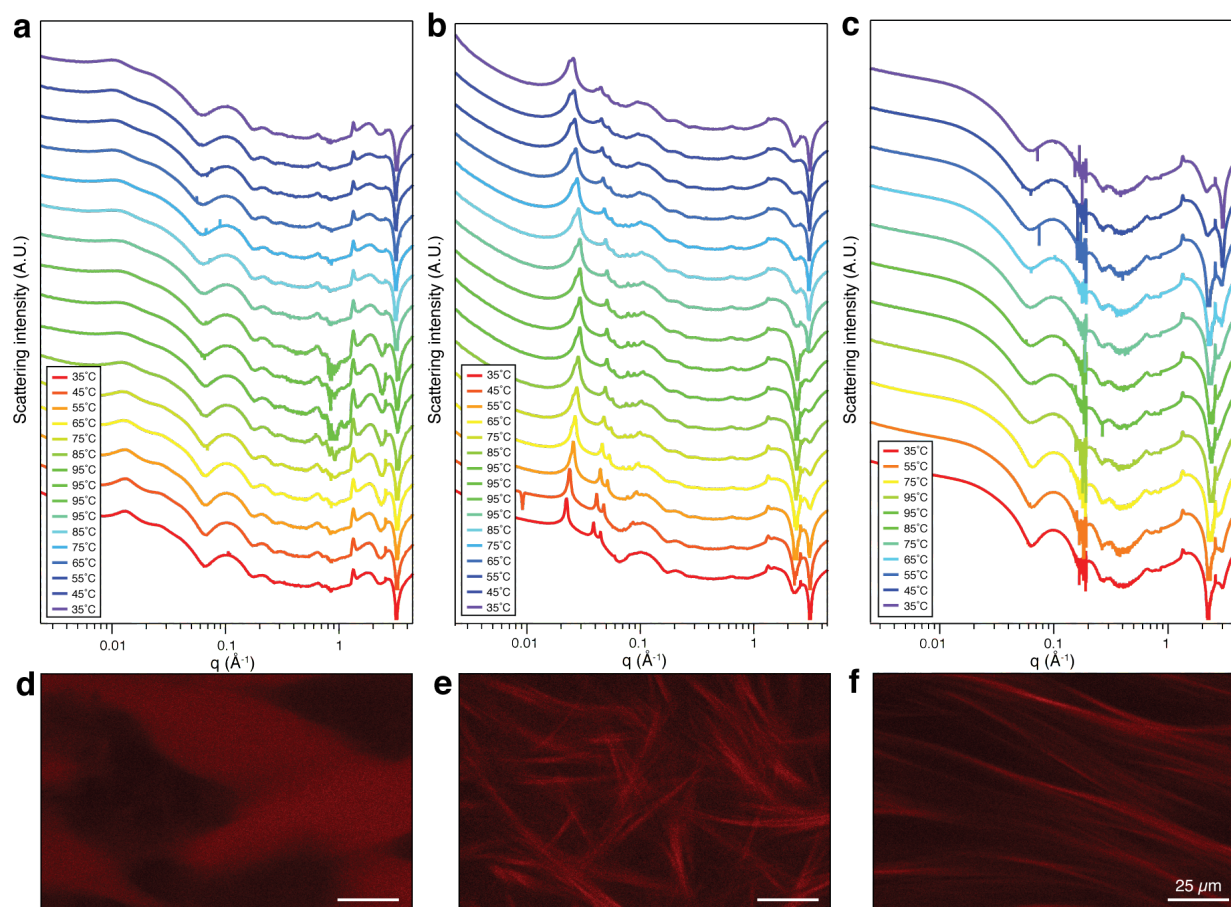
Figure 4.6: (a) VT-SAXS showing annealing behavior of $C_{16}V_3A_3E_3$ with 1 equivalent CsOH/PA. (b) VT-SAXS showing annealing behavior of $C_{16}V_3A_3E_3$ with 2 equivalents CsOH/PA. (c) VT-SAXS showing annealing behavior of $C_{16}V_3A_3E_3$ with 1.5 equivalents CsOH/PA + 0.5 equivalents CsCl/PA. (d-f) Corresponding CLSM images of samples at 95 °C. Scale bars are 25 μm.

POM, both samples show bundling behavior at high temperatures with the presence of hexagonal packing peaks.

Since the formation of the hexagonal lyotropic liquid crystal phase is so highly dependent on charge, adding additional salt to charge screen the system should suppress this peak formation. This is indeed what we see when an additional 0.5 equivalents of CsCl was added to a sample with 1.5 equivalents CsOH per PA molecule (Fig. 4.6c). While the total ionic strength of the solution is identical to the sample in Figure 4.6b, the peaks corresponding to the lyotropic liquid crystal are completely lost at all temperatures. However, in VT-CLSM, we still see the formation of bundles at

high temperatures. This implies that the PA molecules are able to form higher ordered superstructures even without crystalline translational order. These results indicate that while the formation of the lyotropic hexagonal lattice formation is highly affected by the ionic environment, such as the degree of deprotonation of the PA molecules and the existence of screening salt species, the bundling behavior is a more robust phenomenon. While the latter result is somewhat surprising given the well-known "salting-in/salting-out" effect of the macromolecular LCST transition,[173–175] we believe the addition of salt affects the translational order more severely than the LCST behavior itself.

4.3.3 *Molecular dynamics simulations of the PA LCST behavior*

In order to further probe the interactions that lead to the observed LCST behavior, we used full atomistic molecular dynamics (MD) simulations to look more closely at the changes of attractive and repulsive forces at elevated temperatures. In previous reports, MD simulations have been implemented on PA nanofibers to understand assembly states, energy profiles, solvent and ion interactions, and more.[176,177] Here, we carry out MD simulations looking at PA assembly behavior at different temperatures. We compare the final structures at 298K and 353K to see differences in ion condensation, ion distribution, and water distribution to understand the nature of the experimentally observed LCST behavior.

As described in section 4.5, a $18 \times 18 \times 9$ nm³ simulation box was constructed with 18 PA molecules per cross-section, with 144 PA molecules in total. 72 PA molecules had a single glutamic acid deprotonated and 72 PAs had two glutamic acids deprotonated. These PA molecules were placed in an alternating fashion around the cross-section; each cross-section was rotated 20 °with respect to the one below. Water and sodium counterions are placed surrounding the fiber and after a short equilibration, 8 cycles of periodic annealing are done 50 ns/temp, alternating 298K and 353K. Production simulations are done after 740 ns for the 353K simulation and 790ns for the 298K simulation. Figure 4.7a shows the final conformation of the nanostructure cross-section at 298K after the simulation procedure.
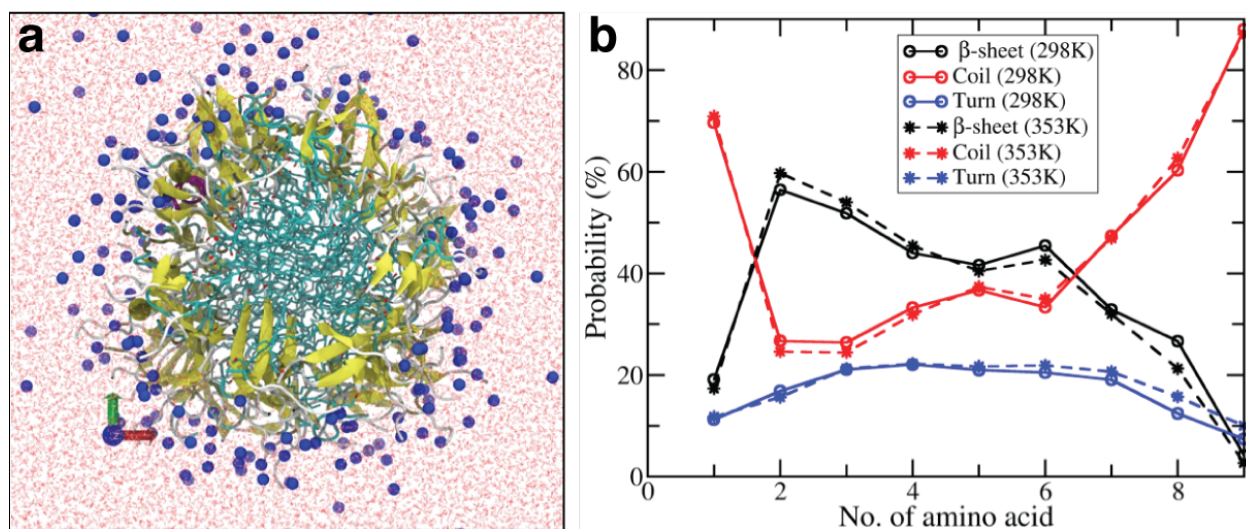
Figure 4.7: (a) Top view of simulation snapshot (outlined in black) at 298K, after 800 ns of periodic annealing. Sodium counterions are shown in blue and the peptides in light green. β-sheets are shown in yellow. (b) Secondary structures of amino acids at each residue position, where 0 represents the lipid tail. Solid lines show probabilities at 298K, while dashed lines are at 353K.

The overall PA nanofiber secondary structure remains very similar at low and high temperatures, with a high degree of beta-sheet hydrogen bonds within the valines and alanines residues (Fig. 4.7b). This is consistent with the WAXS data, which showed minimal change in the beta-sheet hydrogen bonding peak over the course of heating and cooling (Fig. 4.1a). In addition, the nanofiber cross-section changes only slightly (3.17 ± 0.02 nm at 298K vs 3.22 ± 0.02 nm at 353K). This implies that the changes in aggregation we see at the nano- and micro-scale are not due to overall changes in the nanostructure morphology when heated, but due to changes in other interactions.

Looking at the electrostatic interactions, it is evident that there is a much higher degree of charge screening due to increased ion condensation at higher temperatures (Fig. 4.8). Figure 4.8a shows the radial distribution function (RDF) of the carboxylate groups of the glutamic acid residues with the sodium counterions. At 353K, the sodium-nanofiber interactions are significantly stronger than at room temperature. This corresponds with a higher degree of carboxylate neutralization (defined as sodium atoms present within 4 Åof the carboxylate groups) at elevated temperatures Fig. 4.8b),
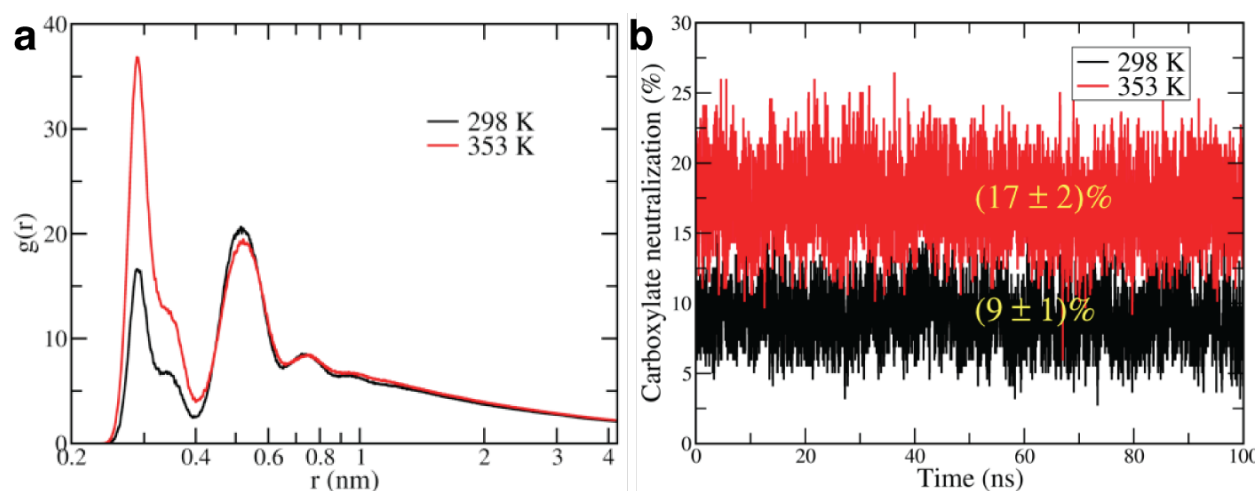
Figure 4.8: (a) Radial distribution function of glutamic acid carboxylate-sodium ion interactions at 298 and 353K (b) Percentage of carboxylates neutralized at 298K (black) and 353K (red). Carboxylate neutralization is defined as sodium within 4 Åof the carboxylate group.

where roughly twice as many carboxylate groups are neutralized at 353K than at room temperature ($17 \pm 2\%$ vs $9 \pm 1\%$).

This increase in condensed ions around the PA nanofibers implies a higher degree of charge screening and therefore a decrease in repulsive interactions between carboxylate groups. These changing interactions should also be reflected in the PA-water interactions. Figure 4.9 shows the RDF between the carboxylates and water. In contrast to the PA-sodium interactions, PA-water shows the opposite trend, where the interactions are decreased at high temperature. This is in agreement with the LCST mechanism, as it becomes entropically unfavorable for PA-water hydrogen bonding interactions to occur as the PA molecules become more charge-screened.

The MD simulations can also give us insight into the long-range ordering of the nanofibers. The larger interfiber spacings ($\sim$25-30 nm) are unusually large compared to the typical short range of repulsive electrostatic interactions ($\propto 1/r^2$). Therefore, changes in the repulsive forces due to the carboxylate neutralization cannot be the only factor contributing to the LCST and bundling behavior. Figure 4.10 examines long-range water orientation as a function of temperature. In this simulation, water displays a long-range correlation up to the simulation box boundary of 10 nm; in

a typical protein system, it would not be expected to see significant water correlation past 1-2 nm of the protein surface. More extensive simulations using larger box sizes will be done in the future.
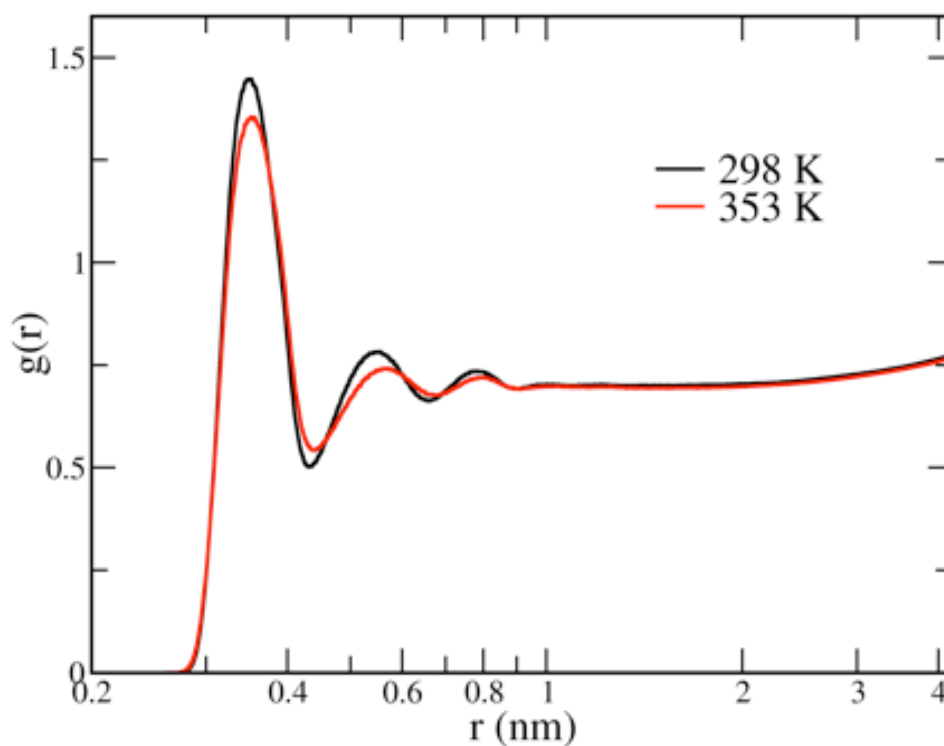
Figure 4.9: Radial distribution function of glutamic acid carboxylate-water interactions at 298K and 353K.
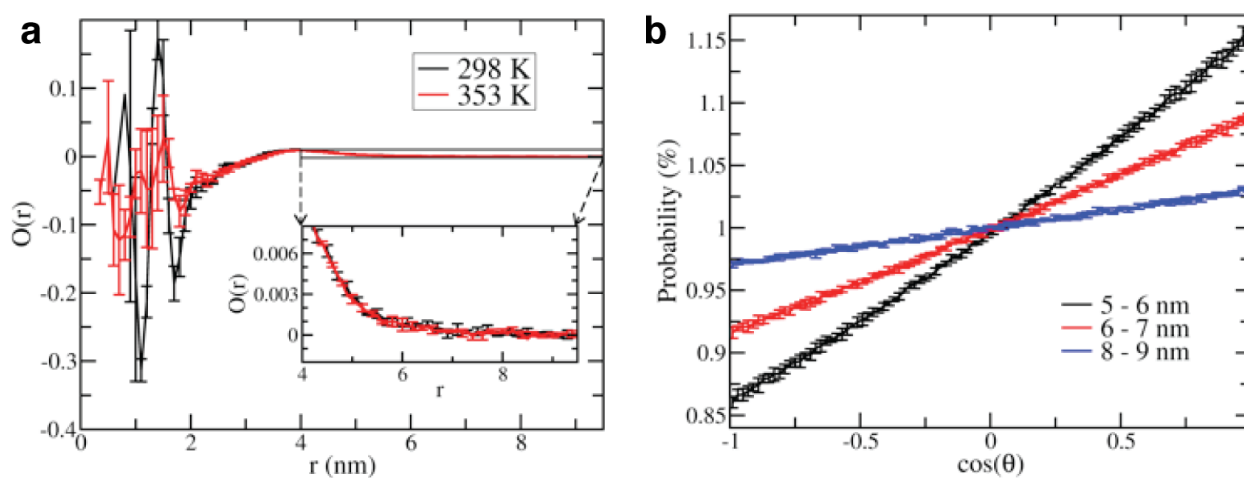
Figure 4.10: (a) Second order water orientation of waters at different temperatures. (b) Distribution of water orientation in different distance ranges from the nanofiber central axis.
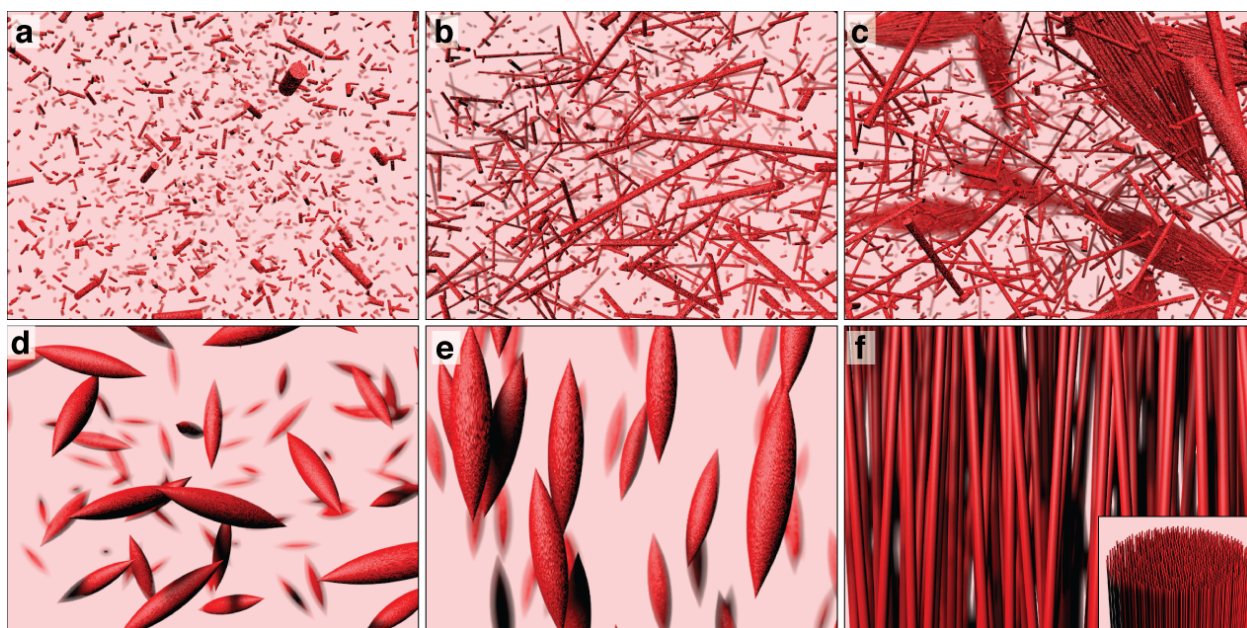
Figure 4.11: (a) PAs initially dissolved in solution as monomeric species or short nanofiber aggregates. (b) Within minutes, PA nanofibers begin to elongate and aggregate in solution. (c) PA aggregates form tactoids in solution due to microphase separation between the elongated nanofibers and the free molecules in solution. (d) tactoids begin to rotate in solution in order to merge with tactoids with a similar direction of alignment. (e) Tactoids coalesce and align in solution. (f) At high temperatures, tactoids elongate and form regular, micron-sized bundles consisting of hundreds of hexagonally packed nanofibers (inset).

With information from experiments and simulations, we propose the following mechanism for PA LCST behavior (Fig. 4.11). When freshly dissolved, the PA molecules form small aggregates or short nanofibers that are dispersed isotropically in solution (Fig. 4.11a). Very quickly, the nanofibers elongate and start to align with each other to maximize the translational degrees of freedom (Fig. 4.11b). As the PAs align, tactoids form due to the local density differences and microphase separation (Fig. 4.11c). These tactoids still have rotational freedom, which allows them to align and coalesce with nearby tactoids that have the same alignment (Fig. 4.11d, e). As the temperature is elevated, these tactoids elongate and eventually transition into long, highly ordered bundles each containing hundreds of hexagonally ordered PA nanofibers (Fig. 4.11f). This hexagonal packing and bundling is attributed to the higher degree of charge screening at high temperatures, and the concurrent decrease in PA-water interactions leading to long-range ordering across tens of nanome-

ters. Upon cooling, the PA-water interactions re-form, and the bundles re-swell and lose some of the crystalline order, though some ordered fiber-fiber interactions remain (Fig. 4.11g). These heated and cooled states are can be repeatedly attained upon subsequent heating and cooling samples.

4.3.4 *Behavior of other PA sequences*

Given the proposed mechanism for the behavior of $C_{16}V_3A_3E_3$, we wanted to explore if this LCST behavior is universal to other peptide amphiphile sequences. To this end, we investigated the annealing behavior for PAs with different beta-sheet sequences ($C_{16}V_2A_4E_3$ and $C_{16}A_6E_3$), charge ($C_{16}V_3A_3K_3$), and nanostructure morphologies ($C_{16}VEVE$) (Fig. 4.12, Fig. 4.13).

Changing the sequence of beta-sheet forming residues within the PA molecule has been shown to drastically change the properties of the resulting nanostructures and materials.[46,178] Recent unpublished studies in our group have shown that varying the valine:alanine ratio can change the supramolecular chirality, transitioning from left-handed to flat to right-handed assemblies with increasing valine content (Fig. 4.14).
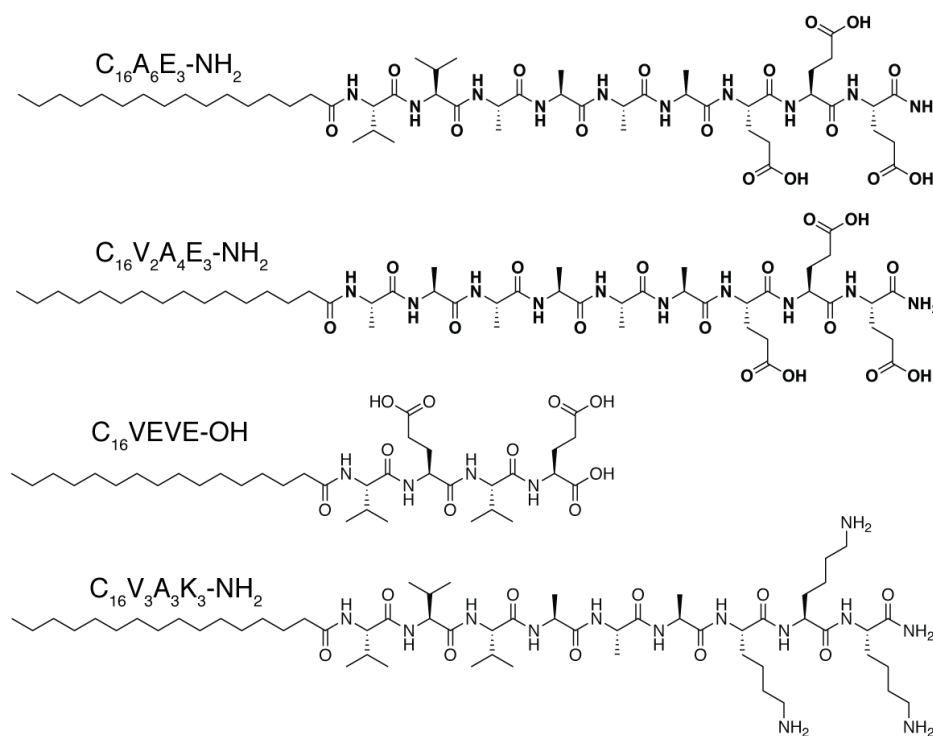
Figure 4.12: Other peptide sequences explored in this work: $C_{16}A_6E_3$, $C_{16}V_2A_4E_3$, $C_{16}V_3A_3K_3$, and $C_{16}VEVE$.
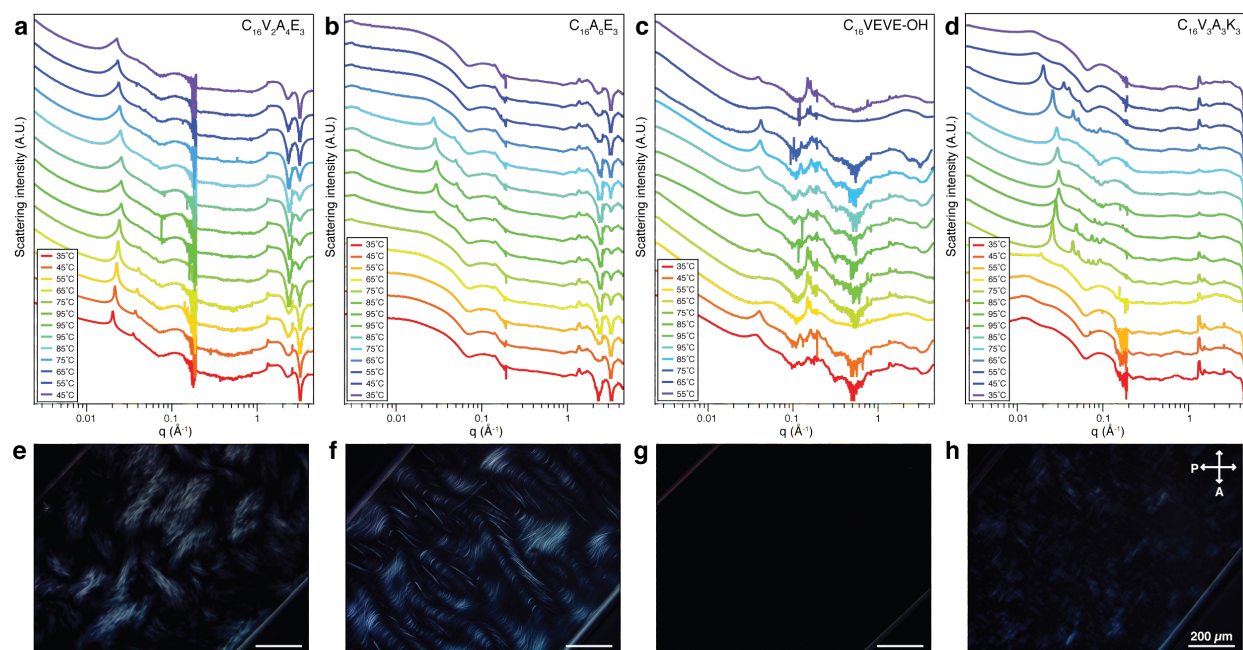
Figure 4.13: (a) VT-SAXS of $C_{16}V_2A_4E_3$. (b) VT-SAXS of $C_{16}A_6E_3$. (c) VT-SAXS of $C_{16}V_3A_3K_3$. (d) VT-SAXS of $C_{16}VEVE$.(e-h) Corresponding POM images of PA sequences at 95 °C. Scale bars are 200 μm.
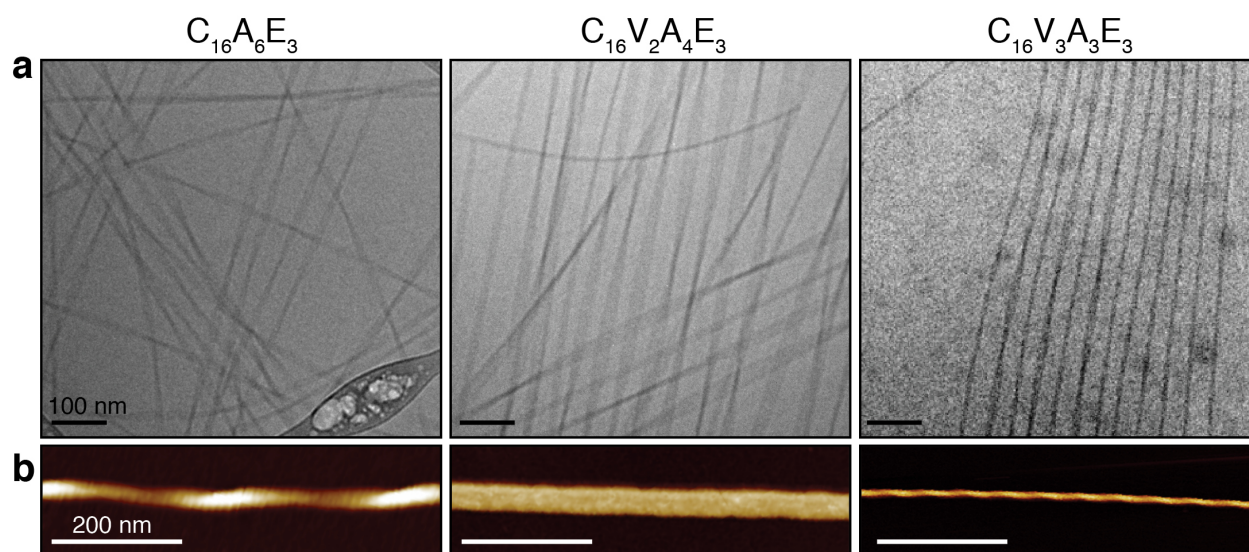
Figure 4.14: (a) Cryo-TEM and (b) AFM images of nanostructures with different supramolecular chiralities created by (left) $C_{16}A_6E_3$, (center) $C_{16}V_2A_4E_3$, and (right) $C_{16}V_3A_3E_3$. Cryo-TEM scale bars are 100 nm, AFM scale bars are 200 nm.

Looking at $C_{16}A_6E_3$, which forms left-handed nanostructures, we see significant suppression in the suppression of the hexagonal packing peaks, with small peaks appearing only at 95 °C (Fig. 4.13a). Nevertheless, in VT-POM, bundling is still apparent upon heating (Fig. 4.13b). Alanine is known to have less beta-sheet forming ability than valine, so it is possible that the reduction in cohesive forces in the nanofiber assembly make it more difficult to form the hexagonally ordered structure than in the $C_{16}V_3A_3E_3$ case.

Looking at $C_{16}V_2A_4E_3$, which forms predominantly flat ribbons in solution, no hexagonal packing peaks can be seen at any temperature; only the nanostructure form factor can be identified (Fig. 4.13c). However, in VT-POM, tactoid and subsequent superstructure formation still occurs (Fig. 4.13d). This indicates that these flat ribbons are unable to pack into the same hexagonal phase as the other two sequences, whose twisting affords a more cylindrical cross-section. However, there are still enough associative forces to form bundled structures on the micro-scale.

Carboxylate-terminated $C_{16}VEVE$ is also known to form wide nanoribbon or nanobelt-like structures.[60] These assemblies, which approach 2D assemblies instead of 1D, are also unable to pack in a hexagonal manner. Due to the large surface area of the ribbon face, these PA molecules exhibit a Bragg peak that is attributed to lamellar packing (Fig. 4.13c). However, in VT-POM, these samples show no significant birefringence over time, suggesting that higher order superstructures with alignment are absent in $C_{16}VEVE$.

Looking at the nature of the ionic component is also important. All work described above has used carboxylate-containing glutamic acid residues, resulting in a negatively charged PA species. By replacing the glutamic acid residues with amine-containing lysine residues, we can investigate the generality of the PA LCST behavior to other ionic systems (Fig. 4.13). When heated, $C_{16}V_3A_3K_3$ shows similar LCST behavior, with Bragg peaks due to hexagonal packing appearing around 75 °C and reversibly shifting to higher q upon heating. Notably, at 2 wt% the Bragg peaks become significantly wider upon cooling, indicating a significant loss of translational order upon cooling, unlike the glutamic acid-based molecules. In addition, the WAXS region of the lysine-based system

displays a disappearance of the beta-sheet peak at higher temperatures, suggesting a loss of some internal interactions at high temperature even as nanoscale order is gained. We hypothesize that the degree of dehydration at elevated temperatures becomes too large for the charges to keep the translational order between fibers, which leads to ion condensation onto the fibers and loss of Bragg peaks. VT-CLSM shows similar bundling behavior as the $C_{16}V_3A_3E_3$ molecules.

4.3.5 *PA superstructures at high ionicity*

Similar to what was seen in the $C_{16}V_3A_3E_3$ case (Fig. 4.6), it is possible to induce crystalline order through the introduction of additional charge in the system (Fig. 4.15). With the addition of 2 equivalents CsOH/PA instead of 1.5, both systems show strong crystalline hexagonal packing peaks at all temperatures, with the same shift of interfiber spacings that is indicative of LCST behavior. This indicates that the fine balance of attractive and repulsive behaviors that causes the LCST behavior is
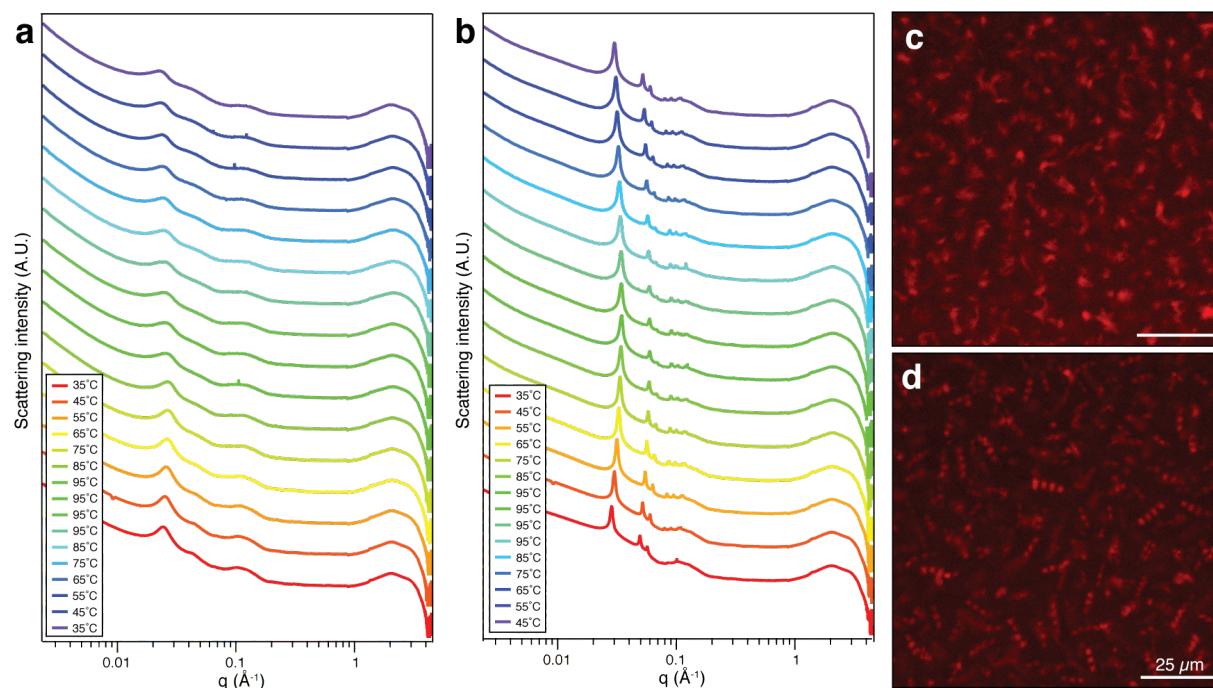
Figure 4.15: VT-SAXS patterns of (a) $C_{16}V_2A_4E_3$, and (b) $C_{16}A_6E_3$ with 2 equivalents CsOH/PA. Corresponding CLSM images of (c) $C_{16}V_2A_4E_3$, and (d) $C_{16}A_6E_3$ at room temperature. Scale bars are 25 μm.
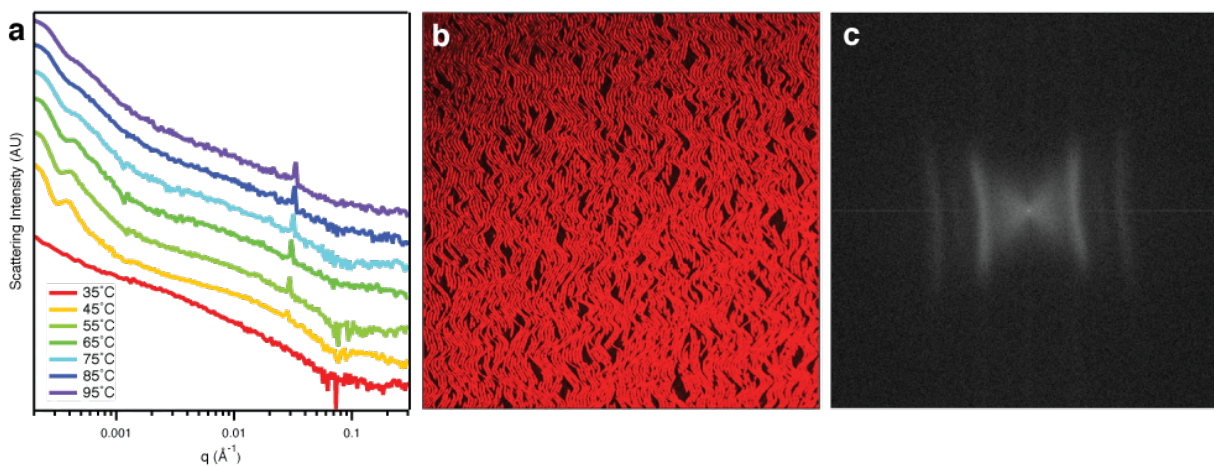
Figure 4.16: (a) VT-USAXS profile of $C_{16}A_6E_3$ with 2 equivalents CsOH/PA. (b) Thresholded CLSM image of initial $C_{16}A_6E_3$ structures at glass surface. (c) Corresponding Fourier transform of image shown in (b), indicating highly regular spacings.

slightly shifted with different beta sheet sequences. Interestingly, looking at the VT-CLSM of these highly ionized samples shows a suprising initial state of assembly. Instead of nucleating into tactoid formations, these structures appear to assemble into micron-size corkscrew-like superstructures. In the $C_{16}A_6E_3$ case, these structures seem extremely regular, showing a consistent 2.17 μm diameter by Fourier analysis of the CLSM images as well as ultrasmall X-ray scattering (Fig. 4.3.5).

Further investigation using CLSM shows that these corkscrew superstructures require some addition of thermal energy to nucleate (Fig. 4.17). Observing the growth of these isothermally at 25 °C, only tactoid structures form, even after several hours. At 40 °C, however, these spiral structures form very quickly, within minutes. These spirals seem to be nucleated on the glass surface, where they form very regular stripes that appear to delaminate from the glass surface to form the spirals in solution. Isothermally at 40 °C, these spirals seem to stay fairly static after about 30 minutes.

When heated, these spirals still elongate and form bundles at higher temperatures (Fig. 4.18). These bundles seem finer than bundles for other PA sequences, with each bundle of fibers only XX μm in diameter. This spiraled superstructure and subsequent bundling seems to inhibit the alignment within the sample, resulting in an overall less uniformly oriented sample.
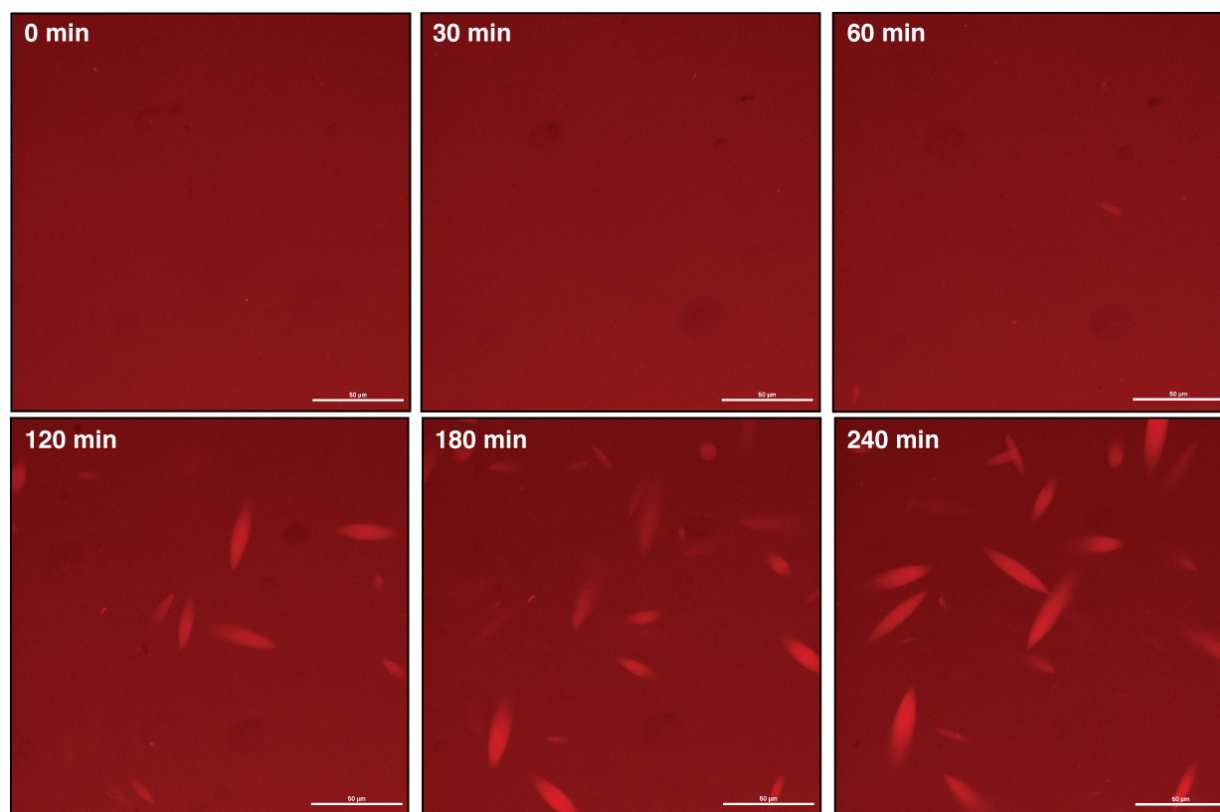
Figure 4.17: CLSM images of $C_16A_6E_3$ dissolved with 2 equivalents CsOH/PA over 4 hours at 25 °C. Scale bars are 50 μm.
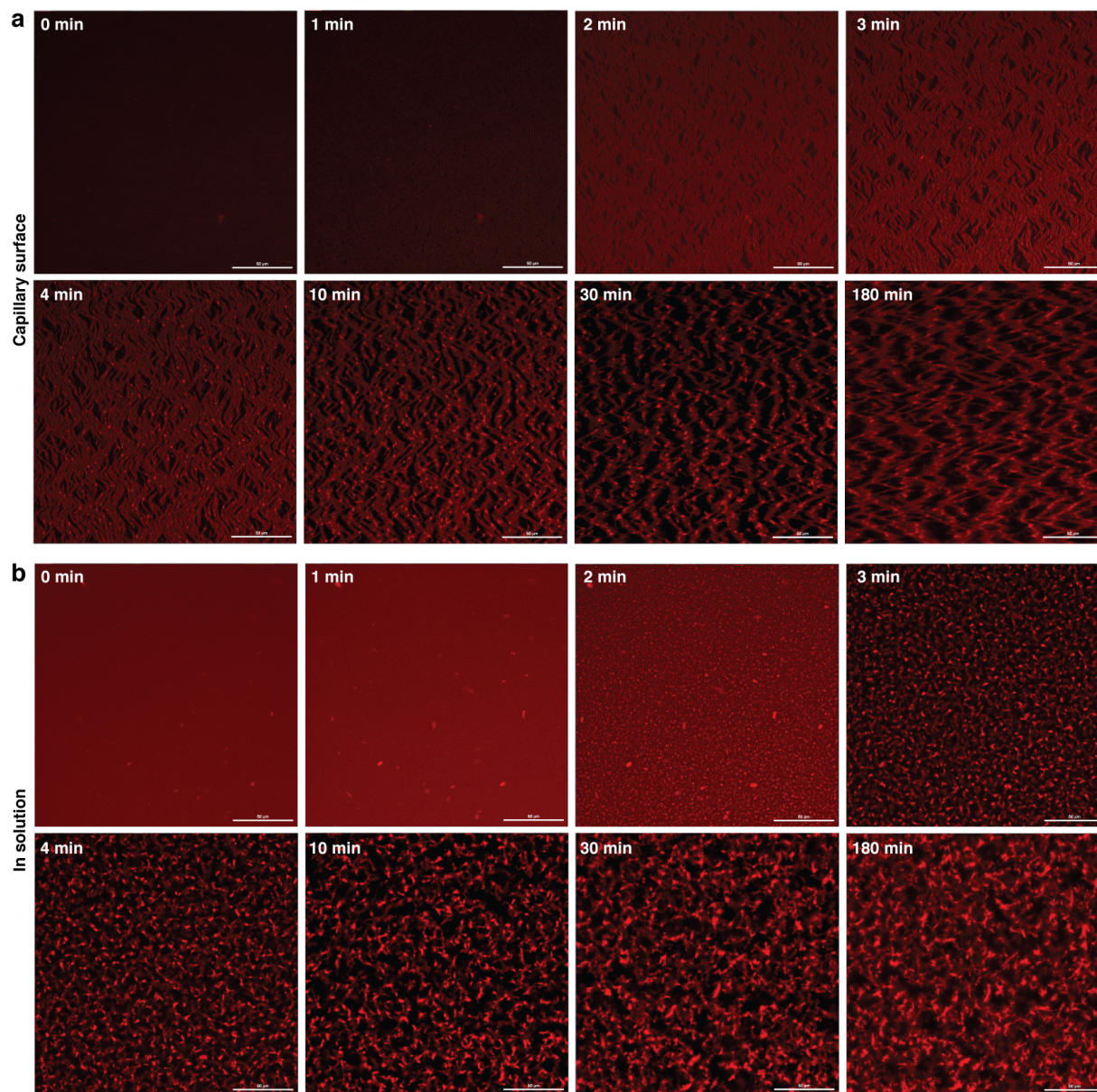
Figure 4.18: CLSM images over 3 hours at 40 °C of $C_{16}A_6E_3$ dissolved with 2 equivalents CsOH/PA at (a) the capillary surface and (b) 30 μm into solution. Scale bars are 50 μm.

4.4 CONCLUSIONS

We have investigated the alignment and liquid crystalline phase behavior during annealing within a confined environment using microscopy, spectroscopic, and calorimetric techniques. We demonstrate the entropically driven LCST behavior within a peptide-based completely supramolecular system during an annealing process. All-atom molecular dynamics simulations indicate that this behavior is due to increased charged screening and related increase in effective hydrophobicity at elevated temperatures, resulting in decreased PA-water interactions. This is also associated with an increase in water correlation distance, which could result in the large experimentally observed interfiber spacings. We anticipate that this LCST effect can be used to direct the alignment and assembly of functional hierarchical soft materials.

4.5 MATERIALS & METHODS

Materials

All Fmoc-protected amino acids were purchased from P3 Biosystems, as well as coupling agents 2-(1H-benzotriazol-1-yl)-1,1,3,3-tetramethyluronium hexafluorophosphate (HBTU) and benzotriazol-1-yl-oxytripyrrolidinophosphonium hexafluorophosphate (PyBOP). Palmitic acid was purchased from Chem-Impex Int'l Inc. Carboxytetramethylrhodamine (TAMRA) acid was obtained from Click Chemistry Tools. 4-methylpiperidine was purchased from Acros Organics. Acetonitrile, ammonium hydroxide (NH_4OH), dimethylformamide (DMF), dichloromethane (DCM), diisopropylethylamine (DIEA), diethyl ether, 1,1,1,3,3,3-hexafluoro-2-propanol (HFIP), sodium chloride (NaCl), sodium hydroxide (NaOH), cesium chloride (CsCl), and cesium hydroxide (CsOH) were purchased from Fisher Scientific. All chemicals were used as received unless stated otherwise.

Peptide amphiphile synthesis and purification

PA molecules were synthesized using standard Fmoc-solid-phase peptide chemistry. All peptides were synthesized on Rink amide MBHA resin (aappTEC) at 1-2 mmol scale. Fmoc deprotection was performed using 20 v/v% 4-methylpiperidine in DMF for 20 minutes. The resin was then washed with DMF and swollen with DCM. Amino acid couplings were performed with 4 equivalents of protected amino acid, 4 equivalents of HBTU, and 6 equivalents of DIEA in 50% DMF/50% DCM for 2 hours. Palmitic acid was coupled to the peptide N-terminus with 8 equivalents of palmitic acid, 8 equivalents of HBTU, 12 equivalents of DIEA in 50% DMF/50% DCM for 4 hours. Deprotection and couplings were verified through ninhydrin colorimetric assays (Kaiser test).

TAMRA-labeled PAs were synthesized by the addition of a Fmoc-Lys(Mtt)-OH residue. While on resin as the final step before cleavage, the Mtt group of the lysine e-amine was performed by swelling the resin in DCM and adding solution of 4% TFA, 5% TIPS and 91% DCM for multiple 5 minute washes until yellow color was no longer seen in solution. TAMRA acid was them coupled to the free amine with 1.1 equivalents. TAMRA acid, 1.1 equivalents PyBOP, and 6 equivalents DIEA in DCM for 4 hours.

PAs were cleaved from resin by shaking in a solution of 95% TFA, 4% TIPS, 1% water. After cleavage, the solvent was concentrated under reduced pressure and the remaining 1 mL of solution was precipitated into an excess of cold diethyl ether. The crude product was redissolved at 10 mg mL^{-1} in water with 0.1% NH4OH. This solution was purified using standard preparatory reverse-phase high-performance liquid chromatography (HPLC) techniques on a Shimadzu Prominence instrument equipped with a Phenomenex Gemini NX-C18, 30 x 150 mm column. A mixture of water/acetonitrile containing 0.1% NH4OH was used as eluent. Pure fractions were selected based on the corresponding product signals in electrospray ionization mass spectrometry using direct injection on an Agilent 6520 Q-TOF LC-MS. Organic solvent was removed from selected fractions under reduced pressure before being frozen, lyophilized, and stored at -20 °C until further use.

Preparation of PA solutions

PA solutions were prepared by dissolving lyophilized PA material in HFIP and sonicating for 3-5 minutes, until fully dissolved. The HFIP was removed under vacuum for at least 3 hours until a dry film remained. The films was re-dissolved in milliQ water with specific equivalents of base added from a stock solution (either 0.5M CsOH or 1M NaOH) to a final concentration of 20 mg/mL (2 w/v%). The solutions were probe sonicated in a water bath to prevent sample heating for 30 seconds using a Fisher Scientific Model 120 sonic dismembrator (25% amplitude, 2 sec on/5 sec off pulse). Samples were then immediately used for experiments described below.

Variable temperature stage for high-resolution optical imaging

The variable temperature stage consists of commercial thermoelectric modules mounted between a 0.25 inch thick aluminum heat distribution plate and aluminum water blocks with room temperature circulated water (Fig. refCh4Fig19). An aluminum sample holder plate with a channel machined to accommodate square cross-section sealed glass capillaries is screwed to the bottom of the heat distribution plate. Due to the short working distance typically employed for high-resolution optical imaging, we designed the holder plate such that the aluminum on the bottom of the sample channel possesses a thickness of 100 micrometers. A 2 mm diameter viewport is machined through the center of both the heat distribution plate as well as the sample holder to allow for bright-field imaging in addition to fluorescence imaging on an inverted microscope. Full description, as well as testing for the thermal and temporal stability of the stage is described in Sai *et al.*[179]
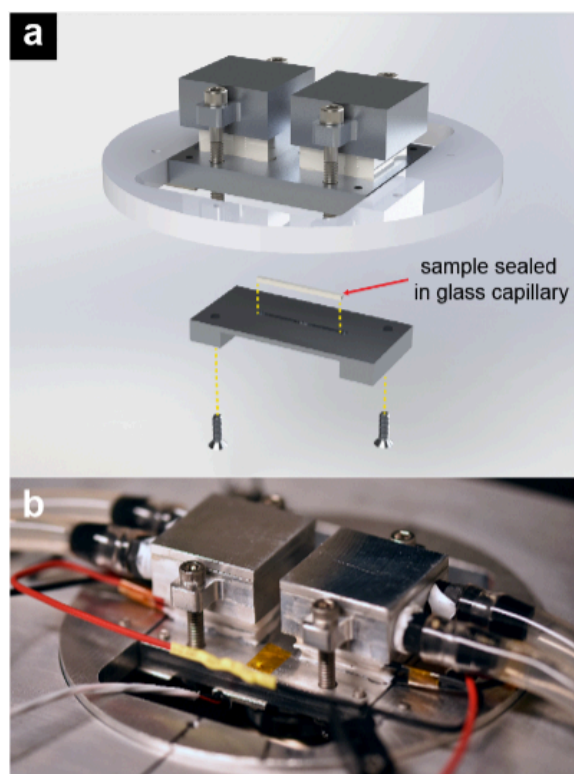
Figure 4.19: (a) CAD-rendered schematic. (b) Photograph of stage assembly mounted on an interved confocal laser scanning microscope.

Confocal laser-scanning microscopy.

A stock solution of TAMRA-labeled PA in HFIP (0.5 mg/mL) was used to add TAMRA-PA at 0.5% of the unlabelled PA mass to the PA solution during the initial HFIP mixing stage. Samples were then dried and re-dissolved as described above. Freshly-dissolved samples were placed into borosilicate glass capillaries (1mm x 1mm or 1mm x 0.1mm, VitroCom) and sealed using UV-curable epoxy (UV Clear Fly Finish, Loon Outdoors) under long-wave UV light (365 nm). Samples were placed within a variable-temperature stage and visualized using a 20x air objective on a Nikon A1R confocal laser-scanning microscope equipped with GaAsP detectors. Samples were heated at 5 °C/min from 25 °C to 95 °C, held at 95 °C for 30 minutes, and cooled at 2 °C/min until 25 °C. Samples were imaged every 30 seconds at multiple z-positions.
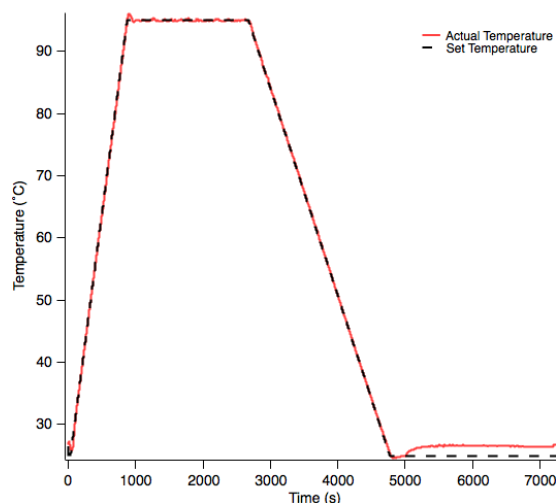
Figure 4.20: Representative heating trace for VT-CLSM and VT-POM experiments. Black dashed trace: Temperature set point. Red trace: Actual temperature.

Polarized optical microscopy

Freshly-dissolved samples were placed into borosilicate glass capillaries (1mm × 1mm or 1mm × 0.1mm, VitroCom) and sealed using UV-curable epoxy (UV Clear Fly Finish, Loon Outdoors) under long-wave UV light (365 nm). Samples were placed within a variable-temperature within a Nikon A1R confocal laser-scanning microscope between two perpendicular light polarizers, with the capillary oriented 45 °with respect to the axis of cross-polarization. Samples were heated at 5 °C/min from 25 °C to 95 °C, held at 95 °C for 30 minutes, and cooled at 2 °C/min until 25 °C (as shown in Fig 4.20). Samples were visualized every 30 seconds using an AmScope MU1000 Digital Microscope Camera.

Small-angle X-ray scattering

SAXS measurements were performed at beamline 5-ID-D of the DuPont-Northwestern-Dow Collaborative Access Team (DND-CAT) Synchrotron Research Center at the Advanced Photon Source, Argonne National Laboratory. PA solutions were placed in 1.5 mm quartz capillaries (Charles Supper) and sealed using UV-curable epoxy under UV light for 2 min. Samples were

placed in an aluminum multicapillary heating stage and measured every 10 °C from 35 °C to 95 °C, held at 95 °C for 30 minutes while measuring, and every 10 °C upon cooling from 95 °C to 35 °C. Data was collected using an energy of 17 keV using a CCD detector positioned 245 cm behind the sample. Scattering intensities were recorded within a q range of 0.0024 < q < 0.40 Å^{-1}, where the wave vector q is defined as $q = (4\pi/\lambda)sin(\theta/2)$ where θ is the scattering angle.

Aging studies using transmission electron microscopy

Samples of $C_{16}V_3A_3E_3$ were dissolved in 2 w/v% as described above, and 5 uL of the samples were aliquoted for TEM sample preparation at 0 min, 10 min, 20 min, 30 min and 60 min after horn sonication. The samples were applied on glow-discharged carbon coated copper grids (CF300-Cu, Electron Microscopy Sciences) for 30 seconds and blotted from the side of the grids using filter paper. The grids were then subjected to two cycles of addition of 10 μL DI water droplets, 10 second wait and blotting, followed by one cycle of addition of 1 w/v % uranyl acetate solution (22400, Electron Microscopy Sciences), 30 second wait and blotting. The transmission electron microscopy images of the negatively stained samples were obtained using a JEOL ARM300F microscopy operated at 300 keV, equipped with a Gatan OneView CCD camera.

Ultrasmall-angle X-ray scattering

USAXS measurements were performed at beamline 9-ID-C at the Advanced Photon Source, Argonne National Laboratory with a Bonse-Hart camera setup at the beam energy of 21 keV, along with pinhole cameras for SAXS and WAXS detection. The details of the beamline configuration is described in Ilavsky *et al.*[180] PA solutions were placed in 4 mm inner diameter glass NMR tubes (Wilmad-LabGlass) and sealed using UV-curable epoxy under UV light for 2 min. The NMR tubes were loaded on a sample heater at the beamline and the temperature was changed in a stepwise manner every 10 degrees, followed by data acquisition. Data was analyzed using Igor Pro software with Indra and Nika packages for data reduction.[181]

Data was analyzed using Igor Pro software with Indra and Nika packages for data reduction.[181]

Differential scanning calorimetry

Differential scanning calorimetry of PA solution samples, prepared as described above, were obtained using a Microcal VP-DSC instrument. Two cycles of heating to 95 °C and cooling to 35 °C were performed at 1 °C/min scan rate.

Molecular dynamics simulations

Classical molecular dynamics (MD) simulations were performed at the all-atom resolution. The GROMOS 54a7 force field was employed for the PA molecules and counterions. The simple point charge (SPC) 3-point water model was employed with the structure constrained using the SETTLE algorithm.

The initial configuration of the PA system was created in Packmol. The simulation box was set at $18 \times 18 \times 9$ nm^3, containing 144 PA molecules, 216 Na$^+$, and 90,000 water molecules. Each cross-section, containing 9 PA molecules processes a thickness of 0.5 nm along the nanofiber normal axis, congruent with intermolecular hydrogen bond distance. PAs are radially distributed in layers stacked along the z-axis. Each cross-section is equivalent but rotated 360°/2n, where n is the number of PA molecules per cross-section.

In the MD simulations, periodic boundary conditions were imposed on each dimension. At the beginning of each simulation, energy minimization was employed using the steepest descent algorithm. The system then underwent periodic annealing for 800 ns (8 cycles). Each cycle consisted of 50 ns at 353K followed by 50 ns at 298K. In the annealing simulations and the following productions, the isothermal-isobaric ensemble (constant temperature, temperature and pressure, NTP) was employed, where the box lengths in all dimensions were allowed to fluctuate over the course of the simulation.

Production simulations began at 740 ns for 353K simulations and at 790 ns for the 298K simulations. The simulation parameters in the annealing simulations were the same as those employed in the production simulations.

Cryogenic transmission electron microscopy

Cryo-TEM was performed using a JEOL 1230 TEM working at 100 kV accelerating voltage. Samples were plunge frozen using a Vitrobot Mark IV (FEI) vitrification robot at room temperature at 95-100% humidity. 7.5 μL of sample solution (0.1 w/v%, diluted from 1 w/v% immediately before grid preparation) were placed on 300-mesh copper grids with lacey carbon support, blotted, and plunge frozen into liquid ethane. Samples were transferred into a liquid nitrogen bath, and placed into a Gatan 626 cryo-holder through a cryo-transfer stage. Images were acquired using a Gatan 831 CCD camera.

Atomic force microscopy

10 mM solutions of annealed PA nanofibers were diluted by 10-20× in 150 mM NaCl, and dropcast on to freshly cleaved mica surfaces. After 1 min the excess solution was removed and the substrate was rinsed three times. The substrate was then immersed in a bath of 150 mM NaCl and 20 mM $CaCl_2$ to immobilize the nanofibers on the mica surface, and rinsed once to remove large aggregates. Samples were imaged in the $CaCl_2$ bath in PeakForce tapping mode on a Dimension Icon Atomic Force Microscope (Bruker) with SNL10-A (Bruker) cantilevers.

5 Summary and Future Outlook

The work presented in this thesis uses a combination of bottom-up molecular design and self-assembly with top-down patterning and directed alignment in order to develop structural and functional hierarchy across multiple length scales, from the nanoscopic to the macroscopic. Inspired by the functional, responsive materials found in nature, these studies used supramolecular peptide amphiphiles as a basis for generating anisotropic structures that were further arranged into higher-order, thermally responsive assemblies that can be used as artificial actuators. These studies give insight into the mechanisms behind anisotropic actuation and templation of alignment, and lay the foundation for future work on the rational design of soft materials that display complex responsive behavior based on their hierarchical structure.

5.1 COVALENT-SUPRAMOLECULAR HYBRID POLYMERS AS ARTIFICIAL ACTUATORS

The covalent-supramolecular hybrid polymers developed in Chapter 2 integrated the structural anisotropy of peptide amphiphiles with the thermoresponsive behavior of LCST macromolecules. When fabricated as an aligned, tubular hydrogel, these hybrid materials were able to reversibly actuate in an anisotropic fashion, more strongly perpendicular to the direction of nanofiber alignment. Finite element analysis simulations and molecular modeling attributed this anisotropy to a combination of microscale fiber reinforcement and nanoscale steric repulsion due to the tethered polymer chains. We can use this knowledge of the mechanisms of anisotropic motion to design more advanced behaviors than just shrinking or contracting. The 3D printed materials in Chapter 3.3.1 were the first step in that direction, showing a more complex bending behavior due to differences in alignment between layers, similar to materials such as bigels. Work done by those in the 3D printing field, such as the group of Jennifer Lewis,[94] has put significant efforts into the computer-aided design of motion that could be utilized in the PA systems as well.

From a chemical standpoint, the ATRP initiator that is used to grow the polymeric component gives significant versatility to the stimuli-responsive system. ATRP methods have been developed for a large number of monomers, including other thermoresponsive and pH responsive polymers (NIPAM, DMAEMA). By compatibilizing these established ATRP methods with the PA chemistry and solvents, the stimuli for the system could be altered or added to create a multi-responsive system.

From a device standpoint, there is more that can be done with the tube hydrogel geometry. As demonstrated in Fig. 2.8, they are able to perform significant work, lifting many times their own mass. By reconfiguring the load-bearing design, the work performance of the hybrids could be significantly enhanced, and could potentially be used for tensile contraction, similar to the skeletal muscles these materials are inspired by. The tubular geometry also lends itself for pump-type applications, to restrict or promote flow through the channel depending on the state of contraction or expansion.

To improve the function of these devices, improvements upon the actuation speed are necessary. By its nature, LCST behavior is dependent on the expulsion and re-swelling of water into a hydrophobic material. These slow kinetics limit the possible material thickness and thus the overall size of the actuators. This could be overcome by programming vasculature into the material design. By having water-filled channels throughout the structure, the diffusion path length is shortened, which should increase the contraction speed and allow for the creation of larger structures. In order to do this, void space could be integrated during the printing process, or templation of the vasculature through a degradable component could be done. In order to print the vasculature directly, the rheological properties of the PA ink would need to be improved to prevent collapse of the channels. This could be done using some of the CNC or host-guest chemistry described in Chapter 3. The vasculature could also be done through templation, such as through ice crystal nucleation or UV-degradable PA components that have been previously developed in our group.[182]

5.2 3D PRINTING WITH CNC-CONTAINING PA MATERIALS

As described in Chapter 3.3.2, the incorporation of nanocrystalline cellulose into the covalent-supramolecular hybrid materials significantly improved the mechanical properties of the hybrids. The materials were able to be printed continuously, without the need for calcium chloride addition between layers, and were able to be easily handled both pre- and post-polymerization. These materials were also able to be stably printed spanning gaps of up to 1 mm without significant sagging or compromise of the print structure. Despite, or potentially due to, their robust mechanical properties, these CNC-PA hybrids showed only modest thermoresponsive behavior. Improving dispersion of the CNCs within the PA matrix and reducing the phase-segregated domains of CNC could improve the actuation behavior by reducing the amount of noncontractile volume and providing more ability for PA entanglement and crosslinking to increase contraction. Solving these problems would allow these materials to be used for the vascularization of the supramolecular-covalent hybrid materials.

The excellent mechanical properties could prove to be useful in other applications as well. Highly crystalline cellulose is biocompatible and not immunogenic towards human tissues,[183] thus the mechanical stability would be useful in tissue regeneration and implantation applications. It is known that certain cell types prefer stiffer matrices for development and differentiation, such as fibroblasts.[184] These CNC-PA materials could also include bioactive epitope sequences to further promote desired biological activity.

5.3 SUPRAMOLECULARLY CROSS-LINKED HOST-GUEST MATERIALS

In chapter 3.3.3, we developed PA molecules containing β-cyclodextrin or adamantane moieties that are able to form host-guest interactions to cross-link PA nanofibers through supramolecular chemistry. These materials, through simple mixing of the two components, showed superior rheological properties to PA alone, and were able to print structures of high fidelity without divalent

counterions as additional cross-links. This all-PA ink will be especially attractive for the printing of biologically relevant scaffolds, where large biomolecules or inorganic rheological additives may not be desirable due to the sensitivity of cellular interactions.

Future studies will investigate the incorporation of bioactive epitope-containing PAs into this system, such as those containing a mimetic of brain-derived neurotrophic factor (BDNF), which is essential for neuronal cell survival. Using this host-guest system in combination with the BDNF-mimetic PA could give a more robust scaffold to promote tissue regeneration in the central nervous system. The supramolecular nature of the host-guest interaction also gives the possibility of self-healing within the hydrogel scaffold. Furthermore, due to the versatility and wide base of knowledge in the field of host-guest chemistry, this system could, in addition to the 3D printing applications, also be extended for the delivery of hydrophobic drugs or other moieties from a PA scaffold.

5.4 LCST BEHAVIOR OF PA ASSEMBLIES

In chapter 4, the formation of hierarchical structures and LCST behavior of an entirely supramolecular PA system was demonstrated due to annealing under a spatially confined environment. Within the model system of $C_{16}V_3A_3E_3$ peptide, we determined the LCST behavior results from changes in ion condensation and therefore hydrophobicity on the PA fiber surface. Since water interactions with the PA nanofiber are key to this process, future studies should more directly probe the water behavior. Initial MD simulations indicated there was long-range water orientation, up to the simulation box boundary of 10 nm. Simulations with larger box sizes could be done to determine the extent of the water orientation. Overhauser dynamic nuclear polarization relaxometry has also been previously used to measure water dynamics within a supramolecular structure.[185] With careful design and placement of TEMPO or other spin-labels, this technique could give insight to the water correlation at different sites within the PA structure with varying temperature.

We demonstrated that the LCST behavior and superstructure formation is not unique to the model PA system, and is observed among multiple PA sequences. This gives a rich phase space for further exploration, including other parameters such as concentration, ionicity, salt, annealing temperature, and ramp rate for each PA sequence. From these studies, we hope to develop a general set of rules for the control of PA hierarchical structures from the nanoscale to the microscale. One especially interesting behavior to explore further is the PA behavior at high ionicity, where 2/3 or more of the PA charged species are ionized. In C_{16} A_6E_3, this condition nucleated the growth of highly regular spiral structures, which have previously never been observed in PA materials. Experiments investigating the internal order of these spiral structures, including X-ray diffraction experiments and microscopy, would give insight to not only the translational order, but also any off-axis effects that must be occurring to give rise to the spiral pitch.

Varying the size of the PA bundles could also lead to interesting optical effects, such as structural color. This would require tight control and near monodispersity of bundle size; which could possibly be achieve through the spatial confinement or other patterning. Bundle size should also be affected by the heating rate during the annealing process, depending on the size of the tactoids within the solution. A more extensive study of heating and cooling rates would be informative for additional structural control.

REFERENCES

(1) Teeri, T. T.; Brumer, H.; Daniel, G.; Gatenholm, P. *Trends Biotechnol.* **2007**, *25*, 299–306.

(2) Palmer, L. C.; Newcomb, C. J.; Kaltz, S. R.; Spoerke, E. D.; Stupp, S. I. *Chem. Rev.* **2008**, *108*, 4754–4783.

(3) Mata, A.; Geng, Y.; Henrikson, K. J.; Aparicio, C.; Stock, S. R.; Satcher, R. L.; Stupp, S. I. *Biomaterials* **2010**, *31*, 6004–6012.

(4) Baughman, R. *Synth. Met.* **1996**, *78*, 339–353.

(5) Tondu, B.; Emirkhanian, R.; Mathé, S.; Ricard, A. *Sens. Actuators, A* **2009**, *150*, 124–130.

(6) Wegst, U. G. K.; Bai, H.; Saiz, E.; Tomsia, A. P.; Ritchie, R. O. *Nat. Mater.* **2015**, *14*, 23–36.

(7) Barbhuiya, S.; Qureshi, M., *Applications of Nanotechnology in Cement and Concrete Science*; Handbook of Research on Diverse Applications of Nanotechnology in Biomedicine, Chemistry, and Engineering; IGI Global: Pennsylvania, 2015.

(8) Gibson, L. J. *J. Royal Soc. Interface* **2012**, *9*, 2749–2766.

(9) Fratzl, P.; Gupta, H. S.; Paschalis, E. P.; Roschger, P. *J. Mater. Chem.* **2004**, *14*, 2115–2123.

(10) Lodish, H.; Berk, A.; Darnell, J. E.; Kaiser, C. A.; Krieger, M.; Scott, M. P.; Bretscher, A.; Ploegh, H.; Matsudaira, P., *Molecular Cell Biology*; WH Freeman: New York, 2008; Vol. 8.

(11) Peters, S. E. *Am. Zool.* **1989**, *29*, 221–234.

(12) Huxley, A. F.; Niedergerke, R. *Nature* **1954**, *173*, 971.

(13) Huxley, H. *Nature* **1954**, *173*, 149–152.

(14) Rayment, I.; Holden, H.; Whittaker, M.; Yohn, C.; Lorenz, M.; Holmes, K.; Milligan, R. *Science* **1993**, *261*, 58–65.

(15) Huxley, H. *Philos. Trans. Royal Soc. B* **2000**, *355*, 539–543.

(16) Cutts, A. *J. Anat.* **1988**, *160*, 79–88.

(17) Witus, L. S.; Hartlieb, K. J.; Wang, Y.; Prokofjevs, A.; Frasconi, M.; Barnes, J. C.; Dale, E. J.; Fahrenbach, A. C.; Stoddart, J. F. *Org. Biomol. Chem.* **2014**, *12*, 6089–6093.

(18) Balzani, V.; Credi, A.; Raymo, F. M.; Stoddart, J. F. *Angew. Chem., Int. Ed.* **2000**, *39*, 3348–3391.

(19) Bruns, C. J.; Stoddart, J. F. *Acc. Chem. Res.* **2014**, *47*, 2186–2199.

(20) Ionov, L. *Langmuir* **2015**, *31*, 5015–5024.

(21) Ionov, L. *Mater. Today* **2014**, *17*, 494–503.

(22) Jeon, S.-J.; Hauser, A. W.; Hayward, R. C. *Acc. Chem. Res.* **2017**, *50*, 161–169.

(23) Jiang, S.; Liu, F.; Lerch, A.; Ionov, L.; Agarwal, S. *Adv. Mater.* **2015**, *27*, 4865–4870.

(24) Yu, Y.; Nakano, M.; Ikeda, T. *Nature* **2003**, *425*, 145–145.

(25) Sumaru, K.; Takagi, T.; Sugiura, S.; Kanamori, T. In *Soft Actuators*; Springer: 2014, pp 219–229.

(26) Tanaka, T.; Nishio, I.; Sun, S.-T.; Ueno-Nishio, S. *Science* **1982**, *218*, 467–469.

(27) Yu, C.; Duan, Z.; Yuan, P.; Li, Y.; Su, Y.; Zhang, X.; Pan, Y.; Dai, L. L.; Nuzzo, R. G.; Huang, Y.; Jiang, H.; Rogers, J. A. *Adv. Mater.* **2013**, *25*, 1541–1546.

(28) Zarzar, L. D.; Kim, P.; Aizenberg, J. *Adv. Mater.* **2011**, *23*, 1442–1446.

(29) Ahn, S.-K.; Kasi, R. M.; Kim, S.-C.; Sharma, N.; Zhou, Y. *Soft Matter* **2008**, *4*, 1151–1157.

(30) Pennadam, S. S.; Firman, K.; Alexander, C.; Górecki, D. C. *J. Nanobiotechnology* **2004**, *2*, 8–15.

(31) Klouda, L.; Mikos, A. G. *Eur. J. Pharm. Bioparm.* **2008**, *68*, 34–45.

(32) Schild, H. G. *Prog. Polym. Sci.* **1992**, *17*, 163–249.

(33) Ashbaugh, H. S.; Paulaitis, M. E. *Ind. Eng. Chem. Res.* **2006**, *45*, 5531–5537.

(34) Li, N. K.; Quiroz, F. G.; Hall, C. K.; Chilkoti, A.; Yingling, Y. G. *Biomacromolecules* **2014**, *15*, 3522–3530.

(35) De, S. K.; Aluru, N. R.; Johnson, B.; Crone, W. C.; Beebe, D. J.; Moore, J. *J. Microelectromech. Syst.* **2002**, *11*, 544–555.

(36) Nistor, V.; Cannell, J.; Gregory, J.; Yeghiazarian, L. *Soft Matter* **2016**, *12*, 3582–3588.

(37) Yeghiazarian, L.; Mahajan, S.; Montemagno, C.; Cohen, C.; Wiesner, U. *Adv. Mater.* **2005**, *17*, 1869–1873.

(38) Hubbard, A. M.; Mailen, R. W.; Zikry, M. A.; Dickey, M. D.; Genzer, J. *Soft Matter* **2017**, *13*, 2299–2308.

(39) Xu, B.; Jiang, H.; Li, H.; Zhang, G.; Zhang, Q. *RSC Advances* **2015**, *5*, 13167–13170.

(40) Dong, C.; Chen, B. *Proc. Royal Soc. A* **2017**, *473*, 20170092.

(41) Stoychev, G.; Zakharchenko, S.; Turcaud, S. B.; Dunlop, J. W.; Ionov, L. *ACS Nano* **2012**, *6*, 3925–3934.

(42) Kim, Y. S.; Liu, M.; Ishida, Y.; Ebina, Y.; Osada, M.; Sasaki, T.; Hikima, T.; Takata, M.; Aida, T. *Nat Mater* **2015**, *14*, 1002–1007.

(43) Lehn, J. M. *Acc. Chem. Res.* **1978**, *11*, 49–57.

(44) Aida, T.; Meijer, E.; Stupp, S. *Science* **2012**, *335*, 813–817.

(45) Tantakitti, F.; Boekhoven, J.; Wang, X.; Kazantsev, R. V.; Yu, T.; Li, J.; Zhuang, E.; Zandi, R.; Ortony, J. H.; Newcomb, C. J. *Nat. Mater.* **2016**.

(46) Cui, H.; Cheetham, A. G.; Pashuck, E. T.; Stupp, S. I. *J. Am. Chem. Soc.* **2014**, *136*, 12461–12468.

(47) Lehn, J., *Nobel Lectures in Chemistry (1981 – 1990)*; Nobel Lectures; World Scientific Publishing Co.: Singapore, 1992.

(48) Richards, V. *Nat. Chem.* **2016**, *8*, 1090.

(49) Israelachvili, J. N.; Mitchell, D. J.; Ninham, B. W. *J. Chem. Soc., Faraday Trans. 2* **1976**, *72*, 1525–1568.

(50) Salim, M.; Minamikawa, H.; Sugimura, A.; Hashim, R. *MedChemComm* **2014**, *5*, 1602–1618.

(51) Cormier, A. R.; Pang, X.; Zimmerman, M. I.; Zhou, H.-X.; Paravastu, A. K. *ACS Nano* **2013**, *7*, 7562–7572.

(52) Krysmann, M. J.; Castelletto, V.; Kelarakis, A.; Hamley, I. W.; Hule, R. A.; Pochan, D. J. *Biochemistry* **2008**, *47*, 4597–4605.

(53) Marini, D. M.; Hwang, W.; Lauffenburger, D. A.; Zhang, S.; Kamm, R. D. *Nano Lett.* **2002**, *2*, 295–299.

(54) Yan, X.; Zhu, P.; Li, J. *Chem. Soc. Rev.* **2010**, *39*, 1877–1890.

(55) Kim, S.; Kim, J. H.; Lee, J. S.; Park, C. B. *Small* **2015**, *11*, 3623–3640.

(56) Berndt, P.; Fields, G. B.; Tirrell, M. *J. Am. Chem. Soc.* **1995**, *117*, 9515–9522.

(57) Hartgerink, J. D.; Beniash, E.; Stupp, S. I. *Science* **2001**, *294*, 1684–1688.

(58) Hendricks, M. P.; Sato, K.; Palmer, L. C.; Stupp, S. I. *Acc. Chem. Res.* **2017**, *50*, 2440–2448.

(59) Cheng, P.-N.; Pham, J. D.; Nowick, J. S. *J. Am. Chem. Soc.* **2013**, *135*, 5477–5492.

(60) Cui, H.; Muraoka, T.; Cheetham, A. G.; Stupp, S. I. *Nano Lett.* **2009**, *9*, 945–951.

(61) Pashuck, E. T.; Cui, H.; Stupp, S. I. *J. Am. Chem. Soc.* **2010**, *132*, 6041–6046.

(62) Webber, M. J.; Kessler, J.; Stupp, S. *J. Intern. Med.* **2010**, *267*, 71–88.

(63) Lee, S. S.; Huang, B. J.; Kaltz, S. R.; Sur, S.; Newcomb, C. J.; Stock, S. R.; Shah, R. N.; Stupp, S. I. *Biomaterials* **2013**, *34*, 452–459.

(64) Boekhoven, J.; Stupp, S. I. *Adv. Mater.* **2014**, *26*, 1642–1659.

(65) Conda-Sheridan, M.; Lee, S. S.; Preslar, A. T.; Stupp, S. I. *Chem. Commun.* **2014**, *50*, 13757–13760.

(66) Preslar, A. T.; Parigi, G.; McClendon, M. T.; Sefick, S. S.; Moyer, T. J.; Haney, C. R.; Waters, E. A.; MacRenaris, K. W.; Luchinat, C.; Stupp, S. I. *ACS Nano* **2014**, *8*.

(67) Edelbrock, A. N.; Álvarez, Z.; Simkin, D.; Fyrner, T.; Chin, S. M.; Sato, K.; Kiskinis, E.; Stupp, S. I. *Nano Lett.* **2018**, *18*, 6237–6247.

(68) Chin, S. M.; Synatschke, C. V.; Liu, S.; Nap, R. J.; Sather, N. A.; Wang, Q.; Álvarez, Z.; Edelbrock, A. N.; Fyrner, T.; Palmer, L. C.; Szleifer, I.; Olvera de la Cruz, M.; Stupp, S. I. *Nat. Commun.* **2018**, *9*, 2395.

(69) Zhang, S.; Greenfield, M. A.; Mata, A.; Palmer, L. C.; Bitton, R.; Mantei, J. R.; Aparicio, C.; de La Cruz, M. O.; Stupp, S. I. *Nat. Mater.* **2010**, *9*, 594–601.

(70) McClendon, M. T.; Stupp, S. I. *Biomaterials* **2012**, *33*, 5713–5722.

(71) Berns, E. J.; Sur, S.; Pan, L.; Goldberger, J. E.; Suresh, S.; Zhang, S.; Kessler, J. A.; Stupp, S. I. *Biomaterials* **2014**, *35*, 185–195.

(72) Rubert Pérez, C. M.; Álvarez, Z.; Chen, F.; Aytun, T.; Stupp, S. I. *ACS Biomater. Sci. Eng.* **2017**, *3*, 2166–2175.

(73) Freeman, R.; Han, M.; Álvarez, Z.; Lewis, J. A.; Wester, J. R.; Stephanopoulos, N.; McClendon, M. T.; Lynsky, C.; Godbe, J. M.; Sangji, H.; Luijten, E.; Stupp, S. I. *Science* **2018**, *362*, 808–813.

(74) Andrienko, D. *J. Mol. Liq.* **2018**, *267*, 520–541.

(75) O'Neill, M.; Kelly, S. M. *Adv. Mater.* **2003**, *15*, 1135–1146.

(76) Schiekel, M.; Fahrenschon, K. *Appl. Phys. Lett.* **1971**, *19*, 391–393.

(77) Meyer, R. B. *Mol. Cryst. Liq. Cryst.* **1977**, *40*, 33–48.

(78) Ikeda, T.; Tsutsumi, O. *Science* **1995**, *268*, 1873–1875.

(79) Ureña-Benavides, E. E.; Ao, G.; Davis, V. A.; Kitchens, C. L. *Macromolecules* **2011**, *44*, 8990–8998.

(80) Blackmore, E. S.; Tiddy, G. J. *J. Chem. Soc., Faraday Trans. 2* **1988**, *84*, 1115–1127.

(81) Saupe, A. *Mol. Cryst. Liq. Cryst.* **1969**, *7*, 59–74.

(82) Fowler, C. E.; Shenton, W.; Stubbs, G.; Mann, S. *Adv. Mater.* **2001**, *13*, 1266–1269.

(83) Zocher, H. *Z. Anorg. Allg. Chem.* **1925**, *147*, 91–110.

(84) Li, L.-S.; Walda, J.; Manna, L.; Alivisatos, A. P. *Nano Lett.* **2002**, *2*, 557–560.

(85) Goodby, J.; Görtz, V.; Cowling, S.; Mackenzie, G.; Martin, P.; Plusquellec, D.; Benvegnu, T.; Boullanger, P.; Lafont, D.; Queneau, Y. *Chem. Soc. Rev.* **2007**, *36*, 1971–2032.

(86) Kundler, I.; Finkelmann, H. *Macromol. Rapid Commun.* **1995**, *16*, 679–686.

(87) Jerome, B. *Rep. Prog. Phys.* **1991**, *54*, 391–451.

(88) Kempe, M. D.; Scruggs, N. R.; Verduzco, R.; Lal, J.; Kornfield, J. A. *Nat. Mater.* **2004**, *3*, 177–182.

(89) Schadt, M.; Seiberle, H.; Schuster, A. *Nature* **1996**, *381*, 212–215.

(90) Sato, S. *Jpn. J. Appl. Phys.* **1979**, *18*, 1679–1684.

(91) Lendlein, A.; Jiang, H.; Jünger, O.; Langer, R. *Nature* **2005**, *434*, 879–882.

(92) Van Oosten, C. L.; Bastiaansen, C. W.; Broer, D. J. *Nat. Mater.* **2009**, *8*, 677–682.

(93) Ahir, S. V.; Tajbakhsh, A. R.; Terentjev, E. M. *Adv. Funct. Mater.* **2006**, *16*, 556–560.

(94) Gladman, S. A.; Matsumoto, E. A.; Nuzzo, R. G.; Mahadevan, L.; Lewis, J. A. *Nat. Mater.* **2016**, *15*, 413–418.

(95) Yuan, C.; Roach, D. J.; Dunn, C. K.; Mu, Q.; Kuang, X.; Yakacki, C. M.; Wang, T.; Yu, K.; Qi, H. J. *Soft Matter* **2017**, *13*, 5558–5568.

(96) Hirokawa, Y.; Tanaka, T. *J. Chem. Phys.* **1984**, *81*, 6379–6380.

(97) Tanaka, T.; Fillmore, D.; Sun, S.-T.; Nishio, I.; Swislow, G.; Shah, A. *Phys. Rev. Lett.* **1980**, *45*, 1636–1639.

(98) Dong, L.; Agarwal, A. K.; Beebe, D. J.; Jiang, H. *Nature* **2006**, *442*, 551–554.

(99) Ionov, L. *Soft Matter* **2011**, *7*, 6786–6791.

(100) Kim, J.; Hanna, J. A.; Byun, M.; Santangelo, C. D.; Hayward, R. C. *Science* **2012**, *335*, 1201.

(101) Chen, J.; Leung, F. K.-C.; Stuart, M. C. A.; Kajitani, T.; Fukushima, T.; van der Giessen, E.; Feringa, B. L. *Nat. Chem.* **2018**, *10*, 132–138.

(102) Naciri, J.; Srinivasan, A.; Jeon, H.; Nikolov, N.; Keller, P.; Ratna, B. R. *Macromolecules* **2003**, *36*, 8499–8505.

(103) Ohm, C.; Brehmer, M.; Zentel, R. *Adv. Mater.* **2010**, *22*, 3366–3387.

(104) Zhou, J.; Sheiko, S. S. *J. Polym. Sci. A* **2016**, *54*, 1365–1380.

(105) Lendlein, A.; Kelch, S. *Angew. Chem., Int. Ed.* **2002**, *41*, 2034–2057.

(106) Erb, R. M.; Sander, J. S.; Grisch, R.; Studart, A. R. *Nat. Commun.* **2013**, *4*, 1712.

(107) Sano, K.; Ishida, Y.; Aida, T. *Angew. Chem., Int. Ed.* **2018**, *57*, 2532–2543.

(108) Ramakers, B. E. I.; van den Heuvel, M.; Tsichlis i Spithas, N.; Brinkhuis, R. P.; van Hest, J. C. M.; Löwik, D. W.P. M. *Langmuir* **2011**, *28*, 2049–2055.

(109) Wang, J.-S.; Matyjaszewski, K. *J. Am. Chem. Soc.* **1995**, *117*, 5614–5615.

(110) Matyjaszewski, K.; Xia, J. *Chem. Rev.* **2001**, *101*, 2921–2990.

(111) Lutz, J.-F.; Hoth, A. *Macromolecules* **2006**, *39*, 893–896.

(112) Couet, J.; Biesalski, M. *Macromolecules* **2006**, *39*, 7258–7268.

(113) Liu, S.; Yao, Z.; Chiou, K.; Stupp, S. I.; Olvera de la Cruz, M. *Proc. Natl. Acad. Sci. USA* **2016**, *113*, 7100–7105.

(114) Weiss, F.; Cai, S.; Hu, Y.; Kyoo Kang, M.; Huang, R.; Suo, Z. *J. Appl. Phys.* **2013**, *114*, 073507.

(115) Flory, P. J., *Principles of Polymer Chemistry*; Cornell University Press: New York, 1953.

(116) Cui, H.; Pashuck, E. T.; Velichko, Y. S.; Weigand, S. J.; Cheetham, A. G.; Newcomb, C. J.; Stupp, S. I. *Science* **2010**, *327*, 555–559.

(117) Advincula, R. C.; Brittain, W. J.; Caster, K. C.; Rühe, J., *Polymer Brushes*; Wiley Online Library: 2004.

(118) Szleifer, I.; Carignano, M. A. *Adv. Chem. Phys* **1996**, *94*, 165–260.

(119) Ren, C.-l.; Nap, R.; Szleifer, I. *J. Phys. Chem. B* **2008**, *112*, 16238–16248.

(120) Dormidontova, E. E. *Macromolecules* **2002**, *35*, 987–1001.

(121) Lee, O.-S.; Liu, Y.; Schatz, G. C. *J. Nanopart. Res.* **2012**, *14*, 936.

(122) Preibisch, S.; Saalfeld, S.; Tomancak, P. *Bioinformatics* **2009**, *25*, 1463–1465.

(123) Hammersley, A. The Fit2D Home Page., 2016.

(124) Shull, K. R.; Ahn, D.; Chen, W.-L.; Flanigan, C. M.; Crosby, A. J. *Macromol. Chem. Phys.* **1998**, *199*, 489–511.

(125) Kim, S. H.; Kwon, C. H.; Park, K.; Mun, T. J.; Lepro, X.; Baughman, R. H.; Spinks, G. M.; Kim, S. J. *Sci Rep* **2016**, *6*, 23016.

(126) Landau, L. D.; LIfshitz, E. M., *Statistical Physics, Part 1*, 3rd ed.; Statistical Physics, Part 1; Butterworth-Heinemann: Oxford, 1980.

(127) Landau, L. D.; Lifshitz, E. M.; Pitaevskii, L. P.; Kosevich, A. M., *Theory of Elasticity, Vol. 7*; Theory of Elasticity; Butterworth-Heinemann: Oxford, 1986.

(128) Hung, A. M.; Stupp, S. I. *Nano Lett.* **2007**, *7*, 1165–1171.

(129) Hindmarsh, A. C.; Brown, P. N.; Grant, K. E.; Lee, S. L.; Serban, R.; Shumaker, D. E.; Woodward, C. S. *ACM Trans. Math. Softw.* **2005**, *31*, 363–396.

(130) Nap, R.; Gong, P.; Szleifer, I. *J. Polym. Sci. A* **2006**, *44*, 2638–2662.

(131) Flory, P.; Volkenstein, M., *Statistical mechanics of chain molecules*; Wiley Online Library: 1969.

(132) Lutz, J.-F.; Akdemir, O.; Hoth, A. *J. Am. Chem. Soc.* **2006**, *128*, 13046–13047.

(133) Hartgerink, J. D.; Beniash, E.; Stupp, S. I. *Proc. Natl. Acad. Sci. USA* **2002**, *99*, 5133–5138.

(134) Li, A.; Hokugo, A.; Yalom, A.; Berns, E. J.; Stephanopoulos, N.; McClendon, M. T.; Segovia, L. A.; Spigelman, I.; Stupp, S. I.; Jarrahy, R. *Biomaterials* **2014**, *35*, 8780–8790.

(135) Motalleb, R.; Berns, E. J.; Patel, P.; Gold, J.; Stupp, S. I.; Kuhn, H. G. *J. Tissue Eng. Regen. Med.* **2018**, *12*, e2123–e2133.

(136) Lewis, J. A. *Adv. Funct. Mater.* **2006**, *16*, 2193–2204.

(137) Bhattacharjee, T.; Zehnder, S. M.; Rowe, K. G.; Jain, S.; Nixon, R. M.; Sawyer, W. G.; Angelini, T. E. *Sci. Adv.* **2015**, *1*, e1500655.

(138) Siqueira, G.; Kokkinis, D.; Libanori, R.; Hausmann, M. K.; Gladman, A. S.; Neels, A.; Tingaut, P.; Zimmermann, T.; Lewis, J. A.; Studart, A. R. *Adv. Funct. Mater.* **2017**, *27*, 1604619.

(139) Markstedt, K.; Mantas, A.; Tournier, I.; Martínez Ávila, H. c.; Hägg, D.; Gatenholm, P. *Biomacromolecules* **2015**, *16*, 1489–1496.

(140) Compton, B. G.; Lewis, J. A. *Adv. Mater.* **2014**, *26*, 5930–5935.

(141) Wehner, M.; Truby, R. L.; Fitzgerald, D. J.; Mosadegh, B.; Whitesides, G. M.; Lewis, J. A.; Wood, R. J. *Nature* **2016**, *536*, 451.

(142) Sazer, D.; Miller, J., *Vascular Networks Within 3D Printed and Engineered Tissues*; 3D Printing and Biofabrication, 2018.

(143) Malheiro, A.; Wieringa, P.; Mota, C.; Baker, M.; Moroni, L. *ACS Biomater. Sci. Eng.* **2016**, *2*, 1694–1709.

(144) Sather, N. A.; Sai, H.; Sato, K.; Ji, W.; Synatschke, C. V.; Ramos Sasselli, I.; Zambrotta, R. T.; Wallace, S. G.; Kohlmeyer, R. R.; Hardin, J. O.; Berrigan, J. D.; Hersam, M. C.; Durstock, M. F.; Mirau, P.; Stupp, S. I. *In Preparation*.

(145) Hausmann, M. K.; Rühs, P. A.; Siqueira, G.; Läuger, J. r.; Libanori, R.; Zimmermann, T.; Studart, A. R. *ACS Nano* **2018**, *12*, 6926–6937.

(146) Rodell, C. B.; Kaminski, A. L.; Burdick, J. A. *Biomacromolecules* **2013**, *14*, 4125–4134.

(147) Highley, C. B.; Rodell, C. B.; Burdick, J. A. *Adv. Mater.* **2015**, *27*, 5075–5079.

(148) Palepu, R.; Reinsborough, V. *Aust. J. Chem* **1990**, *43*, 2119–2123.

(149) Kakuta, T.; Takashima, Y.; Nakahata, M.; Otsubo, M.; Yamaguchi, H.; Harada, A. *Adv. Mater.* **2013**, *25*, 2849–2853.

(150) Miyamae, K.; Nakahata, M.; Takashima, Y.; Harada, A. *Angew. Chem., Int. Ed.* **2015**, *54*, 8984–8987.

(151) Sur, S.; Tantakitti, F.; Matson, J. B.; Stupp, S. I. *Biomater. Sci.* **2015**, *3*, 520–532.

(152) Reid, M.; Villalobos, M.; Cranston, E. In *Abstracts of Papers of the American Chemical Society*, American Chemical Society, CELL division: 2016; Vol. 251.

(153) Loebel, C.; Rodell, C. B.; Chen, M. H.; Burdick, J. A. *Nat. Protoc.* **2017**, *12*, 1521–1541.

(154) Way, A. E.; Hsu, L.; Shanmuganathan, K.; Weder, C.; Rowan, S. J. *ACS Macro Lett.* **2012**, *1*, 1001–1006.

(155) Schaffner, M.; Rühs, P. A.; Coulter, F.; Kilcher, S.; Studart, A. R. *Sci. Adv.* **2017**, *3*, eaao6804.

(156) Sköld, H. N.; Aspengren, S.; Wallin, M. *Pigment Cell Melanoma Res.* **2013**, *26*, 29–38.

(157) Allen, R. D. *Plant Physiol.* **1969**, *44*, 1101–1107.

(158) Djokpé, E.; Vogt, W. *Macromol. Chem. Phys.* **2001**, *202*, 750–757.

(159) Cotanda, P.; Wright, D. B.; Tyler, M.; O'Reilly, R. K. *J. Polym. Sci. A* **2013**, *51*, 3333–3338.

(160) Sun, S.; Wu, P. *Macromolecules* **2013**, *46*, 236–246.

(161) Li, N. K.; Roberts, S.; Quiroz, F. G.; Chilkoti, A.; Yingling, Y. G. *Biomacromolecules* **2018**.

(162) Pershan, P. S. *Phys. Today* **1982**, *35*, 34–39.

(163) Leferink op Reinink, A.; van den Pol, E.; Petukhov, A.; Vroege, G.; Lekkerkerker, H. *Eur. Phys. J. Spec. Top.* **2013**, *222*, 3053–3069.

(164) Shah, R. N.; Shah, N. A.; Lim, M. M.D. R.; Hsieh, C.; Nuber, G.; Stupp, S. I. *Proc. Natl. Acad. Sci. USA* **2010**, *107*, 3293–3298.

(165) Sur, S.; Newcomb, C. J.; Webber, M. J.; Stupp, S. I. *Biomaterials* **2013**, *34*, 4749–4757.

(166) Webber, M. J.; Berns, E. J.; Stupp, S. I. *Isr. J. Chem.* **2013**, *53*, 530–554.

(167) Modlińska, A.; Alsayed, A. M.; Gibaud, T. *Sci. Rep.* **2015**, *5*, 18432.

(168) Wang, P.-X.; MacLachlan, M. J. *Philos. Trans. A Math Phys. Eng. Sci.* **2018**, *376*, 20170042.

(169) Onsager, L. *Ann. N.Y. Acad. Sci.* **1949**, *51*, 627–659.

(170) Zhao, B.; Li, N. K.; Yingling, Y. G.; Hall, C. K. *Biomacromolecules* **2016**, *17*, 111–118.

(171) Dalgakiran, E.; Tatlipinar, H. *Phys. Chem. Chem. Phys.* **2018**, *20*, 15389–15399.

(172) Palmer, L. C.; Leung, C.-Y.; Kewalramani, S.; Kumthekar, R.; Newcomb, C. J.; Olvera de la Cruz, M.; Bedzyk, M. J.; Stupp, S. I. *J. Am. Chem. Soc.* **2014**, *136*, 14377–14380.

(173) Schild, H. G.; Tirrell, D. A. *J. Phys. Chem.* **1990**, *94*, 4352–4356.

(174) Florin, E.; Kjellander, R.; Eriksson, J. C. *J. Chem. Soc., Faraday Trans. 1* **1984**, *80*, 2889–2910.

(175) Park, T. G.; Hoffman, A. S. *Macromolecules* **1993**, *26*, 5045–5048.

(176) Deiss-Yehiely, E.; Ortony, J. H.; Qiao, B.; Stupp, S. I.; Olvera de la Cruz, M. *J. Polym. Sci. A* **2017**, *55*, 901–906.

(177) Iscen, A.; Schatz, G. C. *EPL* **2017**, *119*, 38002.

(178) Pashuck, E. T.; Stupp, S. I. *J. Am. Chem. Soc.* **2010**, *132*, 8819–8821.

(179) Sai, H.; Lau, G.; Dannenhoffer, A.; Chin, S. M.; Stupp, S. I. *In Preparation*.

(180) Ilavsky, J.; Zhang, F.; Andrews, R. N.; Kuzmenko, I.; Jemian, P. R.; Levine, L. E.; Allen, A. J. *J. Appl. Crystallogr.* **2018**, *51*, 867–882.

(181) Ilavsky, J.; Jemian, P. R. *J. Appl. Crystallogr.* **2009**, *42*, 347–353.

(182) Sur, S.; Matson, J. B.; Webber, M. J.; Newcomb, C. J.; Stupp, S. I. *ACS Nano* **2012**, *6*, 10776–10785.

(183) Miyamoto, T.; Takahashi, S. i.; Ito, H.; Inagaki, H.; Noishiki, Y. *J. Biomed. Mater. Res.* **1989**, *23*, 125–133.

(184) Wells, R. G. *Hepatology* **2008**, *47*, 1394–1400.

(185) Ortony, J. H.; Qiao, B.; Newcomb, C. J.; Keller, T. J.; Palmer, L. C.; Deiss-Yehiely, E.; Olvera de la Cruz, M.; Han, S.; Stupp, S. I. *J. Am. Chem. Soc.* **2017**, *139*, 8915–8921.

(186) Hayashi, Y. *Chem. Sci.* **2016**, *7*, 866–880.

(187) Robinson, R. *Journal of the Chemical Society, Transactions* **1917**, *111*, 762–768.

(188) Mukaiyama, T.; Ishikawa, H.; Koshino, H.; Hayashi, Y. *Chem. Eur. J.* **2013**, *19*, 17789–17800.

(189) Hayashi, Y.; Sakamoto, D.; Okamura, D. *Org. Lett.* **2015**, *18*, 4–7.

(190) Cohen, B. J.; Kraus, M. A.; Patchornik, A. *J. Am. Chem. Soc.* **1981**, *103*, 7620–7629.

(191) Voit, B. *Angew. Chem., Int. Ed.* **2006**, *45*, 4238–4240.

(192) Womble, C. T.; Kuepfert, M.; Weck, M. *Macromol. Rapid Commun.* **2019**, *40*, 1800580.

(193) Vriezema, D. M.; Garcia, P. M.; Sancho Oltra, N.; Hatzakis, N. S.; Kuiper, S. M.; Nolte, R. J.; Rowan, A. E.; van Hest, J. *Angew. Chem.* **2007**, *119*, 7522–7526.

(194) Tseng, Y.-C.; Darling, S. B. *Polymers* **2010**, *2*, 470–489.

(195) Matsen, M. W.; Bates, F. S. *Macromolecules* **1996**, *29*, 7641–7644.

(196) Bates, F. S.; Fredrickson, G. H. *Phys. Today* **1999**, *52*, 32–38.

(197) van Dongen, S. F. M.; Nallani, M.; Cornelissen, J. J.L. M.; Nolte, R. J. M.; van Hest, J. C. M. *Chem. Eur. J.* **2009**, *15*, 1107–1114.

(198) Lu, J.; Dimroth, J.; Weck, M. *J. Am. Chem. Soc.* **2015**, *137*, 12984–12989.

(199) Lee, L.-C.; Lu, J.; Weck, M.; Jones, C. W. *ACS Catal.* **2016**, *6*, 784–787.

(200) Hammer, D. A.; Kamat, N. P. *FEBS Lett.* **2012**, *586*, 2882–2890.

(201) Peters, R. J.; Louzao, I.; van Hest, J. C. *Chem. Sci.* **2012**, *3*, 335–342.

(202) Postupalenko, V.; Einfalt, T.; Lomora, M.; Dinu, I. A.; Palivan, C. G., *Bionanoreactors: From Confined Reaction Spaces to Artificial Organelles*; Organic Nanoreactors; Elsevier: 2016.

(203) Schoonen, L.; van Hest, J. C. M. *Adv. Mater.* **2016**, *28*, 1109–1128.

(204) Choudary, B.; Kantam, M. L.; Sreekanth, P.; Bandopadhyay, T.; Figueras, F.; Tuel, A. *J. Mol. Catal. A: Chem.* **1999**, *142*, 361–365.

(205) Motokura, K.; Fujita, N.; Mori, K.; Mizugaki, T.; Ebitani, K.; Kaneda, K. *J. Am. Chem. Soc.* **2005**, *127*, 9674–9675.

(206) Helms, B.; Guillaudeu, S. J.; Xie, Y.; McMurdo, M.; Hawker, C. J.; Fréchet, J. M. J. *Angew. Chem.* **2005**, *117*, 6542–6545.

(207) Sebren, L. J.; Devery, J. J.; Stephenson, C. R. J. *ACS Catal.* **2014**, *4*, 703–716.

(208) Liao, X.; Su, J.; Mrksich, M. *Chem. Eur. J.* **2009**, *15*, 12303–12309.

(209) Liao, X.; Petty, R. T.; Mrksich, M. *Angew. Chem., Int. Ed.* **2011**, *50*, 706–708.

(210) Li, J.; Nayak, S.; Mrksich, M. *J Phys Chem B* **2010**, *114*.

(211) Fornera, S.; Kuhn, P.; Lombardi, D.; Schlüter, A. D.; Dittrich, P. S.; Walde, P. *ChemPlusChem* **2012**, *77*, 98–101.

(212) Gruber, P.; Marques, M. P. C.; O'Sullivan, B.; Baganz, F.; Wohlgemuth, R.; Szita, N. *Biotechnol. J.* **2017**, *12*, 1700030.

(213) Yang, Y.; Liu, X.; Li, X.; Zhao, J.; Bai, S.; Liu, J.; Yang, Q. *Angew. Chem., Int. Ed.* **2012**, *51*, 9164–9168.

(214) Li, P.; Cao, C.-Y.; Chen, Z.; Liu, H.; Yu, Y.; Song, W.-G. *Chem. Commun.* **2012**, *48*, 10541–10543.

(215) Zhao, M.; Deng, K.; He, L.; Liu, Y.; Li, G.; Zhao, H.; Tang, Z. *J. Am. Chem. Soc.* **2014**, *136*, 1738–1741.

(216) Discher, B. M.; Won, Y.-Y.; Ege, D. S.; Lee, J. C.; Bates, F. S.; Discher, D. E.; Hammer, D. A. *Science* **1999**, *284*, 1143–1146.

(217) Discher, D. E.; Ahmed, F. *Annu. Rev. Biomed. Eng.* **2006**, *8*, 323–341.

(218) Wang, Z.; Yuan, X.; Cheng, Q. a.; Zhang, T.; Luo, J. *New J. of Chem.* **2018**.

(219) Schulz, M. F.; Khandpur, A. K.; Bates, F. S.; Almdal, K.; Mortensen, K.; Hajduk, D. A.; Gruner, S. M. *Macromolecules* **1996**, *29*, 2857–2867.

(220) Ishizu, K.; Bessho, K.; Fukutomi, T.; Kakurai, T. *Makromol. Chem. Rapid Comm.* **1983**, *4*, 163–167.

(221)   Bang, J.; Jain, S.; Li, Z.; Lodge, T. P.; Pedersen, J. S.; Kesselman, E.; Talmon, Y. *Macromolecules* **2006**, *39*, 1199–1208.

(222)   Bailey, T. S.; Pham, H. D.; Bates, F. S. *Macromolecules* **2001**, *34*, 6994–7008.

(223)   Sai, H.; Tan, K. W.; Hur, K.; Asenath-Smith, E.; Hovden, R.; Jiang, Y.; Riccio, M.; Muller, D. A.; Elser, V.; Estroff, L. A.; Gruner, S. M.; Wiesner, U. *Science* **2013**, *341*, 530–534.

(224)   Eichhorn, K.-J.; Fahmi, A.; Adam, G.; Stamm, M. *J. Mol. Struct.* **2003**, *661*, 161–170.

(225)   Kade, M. J.; Burke, D. J.; Hawker, C. J. *J. Polym. Sci. A* **2010**, *48*, 743–750.

(226)   Lo, C.-T.; Chou, P.-W. *J. Phys. Chem. B.* **2014**, *118*, 12763–12771.

Appendix I: Original Research Proposal: Cascade Reactions Within Catalytic Block Copolymer Mesophases

---

ABSTRACT

Cells are able to physically separate incompatible reactions and promote cascades of desired reactions through compartmentalization of reagents and processes within organelles. This spatial organization of reactants and catalysts is key to creating complex chemical products in an efficient manner. Replicating this behavior in synthetic processes by combining multiple reaction steps into a single reactor can significantly reduce costs by saving on reagents, solvents, and time. However, not all synthetic processes can be combined easily due to interfering interactions between catalysts or reaction conditions. The field has attempted to combine such incompatible reactions through the physical separation of catalysts onto different particles or through the site isolation of catalysts onto different parts of the same particle.

The objective of this proposal is to develop a new system of phase-segregated block copolymers that are able to facilitate multiple chemical reactions that would otherwise not be able to be performed in bulk solution. Using a model acidic and basic catalysts independently integrated to a poly(styrene-b-4-vinylpyridine) block copolymer, we will explore the cascade reaction behavior in different polymer self-assemblies, such as the bicontinuous gyroid phase. These phases should have significant higher interfacial surface area than the typically core-shell micellar systems, allowing for better diffusion of reagents between catalytic phases and therefore overall reactivity. The depth of research into polymer self-assembly gives rich opportunities for modifications to the system in order to tune the domain size, diffusion kinetics within the system, and catalyst chemistries, which allow us to address potential pitfalls as well as create variations of the system in order to look at other cascade reactions.

INTRODUCTION

Cells achieve remarkable feats of chemistry, facilitating hundreds of thousands of unique chemical reactions within only a few cubic microns of volume. Key to these processes is the spatial separation and compartmentalization of different types of reactions into organelles by lipid membranes. This allows for the segregation of processes that would interfere with others, such as the hydrolytic enzymes and acidic, oxidative environment found in the lysozyme that would quickly degrade other proteins if they were free in the cellular environment. The proximal spatial positioning of related reaction processes also allows for the fast diffusion and ability to create complex chemical structures through enzymatic cascades.

Replicating this behavior in traditional chemical synthesis has been more difficult. Typically, in order to undergo multiple chemical transformations, individual reaction setups are needed, as well as isolation and purification of intermediates in between each step. Not only is this time consuming, but it is more costly and uses additional reagents and solvents, which may be harmful to the environment. As such, researchers have developed a number of one-pot reactions,[187-189] where a substrate can undergo multiple transformations either sequentially or simultaneously, without a need for isolation or purification in between steps (Fig. 5.1). However, developing these reactions is not trivial.[186] Successful one-pot reactions require all components to be compatible and active in the same solvent, thermal, and atmospheric conditions, as well as being unaffected by other reagents
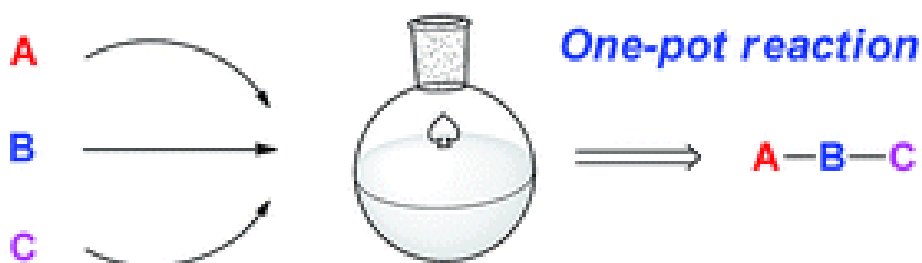
Figure 5.1: Schematic representation of a one-pot reaction and examples of the reductions in economy they can bring. Reproduced from Hayashi.[186]

in solution. Substrate selectivity may also have to be taken into consideration, if there are multiple possible sites or a specific order of transformation is desired.

Inherently, not all reactions are compatible with the one-pot process. Many compounds can catalyze complex transformations when used in sequence, such as Lewis acids and bases or oxidizing species and amines; however, they would be quenched and inactivated by the other reagents in solution. These types of incompatible reactions were dubbed "Wolf and Lamb" reactions by Cohen *et al.* in 1981, when they begun research on segregated polymer particle systems.[190] This allows for two incompatible catalysts to be placed in the same reaction vessel, but remain active because they are physically unable to interact. The wolf-lamb reaction system has led to the development of systems that spatially separate molecular or enzymatic catalysts in order to promote complex transformations in sequence, or "cascade reactions."[191–193]
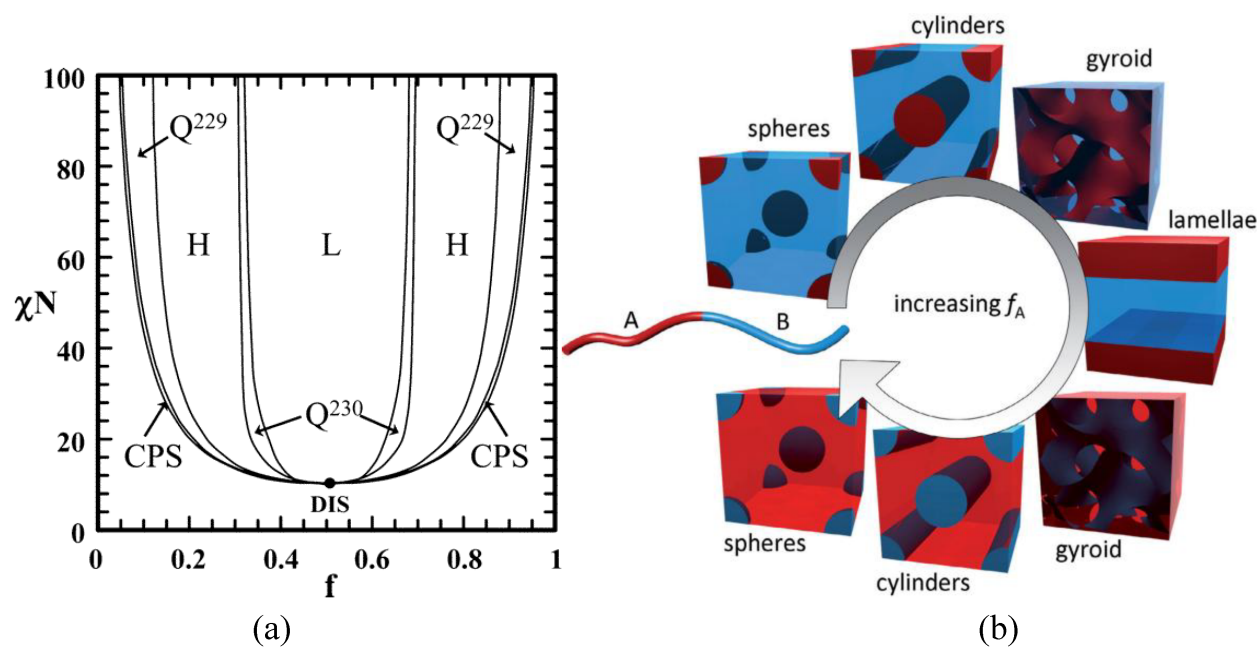
Figure 5.2: (a) Typical phase diagram of a coil-coil diblock copolymer. f: Volume fraction of one block. χ: Flory-Huggins interaction parameter. N: degree of polymerization. L: lamellae, H: hexagonally packed cylinders, Q^{230}: double-gyroid phase, Q^{229}: body-centered spheres, CPS: closed-packed spheres, DIS: disordered. (b) Structures of the different phases described in (a). f_A is the volume fraction of block A. Reproduced from Tseng *et al.*[194]

Phase separation of block copolymer systems has emerged as a promising technique for making complex, segregated systems. In 1996, Matsen and Bates described the principles of "complex self-assembly" of diblock copolymers and showed the relationship between block volume structure and the resulting structures (Fig. 5.2).[194,195] Since then, these principles have been extended to the assembly of triblock terpolymer systems.[196] Due to the advances in the synthesis and characterization of well-defined block copolymers and the wide number of monomer chemistries available, this has proved to be a very versatile for making spatially separated systems such as core-shell micelles and polymerosomes.[197–199]

As it progresses, the field ultimately works towards the development of "artificial organelles" and in the distant future "artificial cells," where complex molecules can be derived from simple precursors through multiple chemical transformations in the same reaction vessel due to the spatial positioning of catalysts.[200–203]

SPECIFIC AIMS

This work aims to develop block copolymer mesophase systems that covalently incorporate typically incompatible catalysts into separate blocks of the polymer chain. Due to the intimate contact and high interfacial surface area of the phase segregated polymer blocks, there will be fast and easy diffusion of the reagents between the different catalytic species. Careful design of the polymer blocks and catalytic substrate will promote the diffusion of intermediates into the other polymer phase, promoting the full reaction cascade. In order to achieve this, we will need to (1) synthesize diblock or triblock copolymers that can have organic catalysts incorporated either during the polymerization process or in a post-functionalization step. Then, it will be necessary to (2) investigate and characterize the phase space of assembly into different mesophases that can facilitate the desired cascade reactions. Finally, we will (3) investigate the reaction rates of the catalytic phases, both independently and within the cascade, and the effect the polymer mesophase has on the catalytic reactions.

PREVIOUS WORK

Initial studies on site-isolation focused on the spatial separation of incompatible reagents, such as strong acid and strong base. Cohen, Kraus, and Patchornik described a system of two insoluble polymeric reagents to undergo "wolf and lamb" reactions.[190] One polymer particle was modified with a strong base (trityllithium), and the other with an acylation reaction (benzoic acid), and together, this system was able to promote the benzoylation of phenylacetonitrile whereas the soluble analogues of these catalysts were not.

Since the description of the initial "wolf and lamb" system, scientists have investigated a number of other systems based on the spatial separation of catalysts on different particles. Similar to the wolf-and-lamb system, these works are based on the premise that the physically bound catalysts are unable to interact and therefore be quenched by each other. As supports a wide variety of materials have been used, such as modified MCM-41 zeolite,[204] layered montmorillonite and hydrotalcite clays (Fig. 5.3),[205] or core-confined catalysts within star polymers.[206] These systems rely on the reacting species to diffuse between the two different types of particle in order for the full cascade to occur, and particle size has been shown to have a strong effect on the rates of reaction. The diffusion requirements could also be problematic for certain cascade reactions with short-lived or reactive intermediates.[207]

In order to place the reactive sites more specifically, researchers have used patterning techniques, such as lithography or photomasking, in order to promote more intimate contact between desired reactive species. These approaches have been shown on self-assembled monolayers (SAMs),[208–210] as well as in microfluidic devices.[211,212] Through precise position of the catalytic species, reagents are able to efficiently undergo the entire cascade with minimally necessary diffusion. However, both SAMs and microfluidic systems are limited in their scalability, since these systems have limited surface area with which they can undergo reactions.

In order to bring the catalysts closer together in solution, researchers have turned to the confinement of catalysts on different parts of the same particle. Yolk-shell particles with a unique
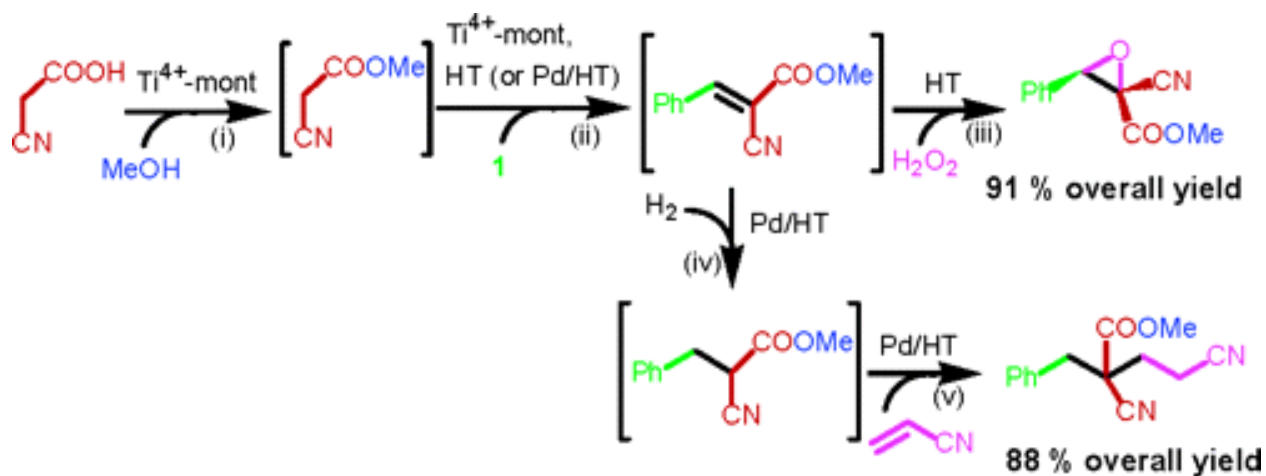
Figure 5.3: Epoxynitrile was successfully obtained using methanol, cyanoacetic acid, compound 1, and hydrogen peroxide in four sequential acid and base reactions, namely, esterification (i), deacetalization (ii), aldol reaction (ii), and epoxidation (iii), in a single reactor. A one-pot synthesis of glutaronitrile was also performed using the Ti^{4+}-mont and Pd/HT catalysts. Reproduced from Motokura *et al.*[205]

core@void@shell nanostructure were made by sol-gel processes and selective etching, and were able to catalyze a deacetalization-Henry cascade reaction.[213] Core-shell nanoparticles from structured mesoporous silica or nanoparticle@MOFs have similarly been used to perform cascade reactions.[214,215]

In addition to inorganic structures, researchers have also used the principles of polymer phase separation to create segregated catalytic systems. Using a block of hydrophilic polymer and hydrophobic polymer, Weck and coworkers were able to separate molecular inorganic catalysts in the core and shell of a polymeric micelle to promote a Co-catalyzed hydration followed by a Rh-catalyzed asymmetric transfer hydrogenation (Fig. 5.4).[198] Similarly, Jones *et al.* used a crosslinked core-shell micelle for a tandem deacetalization-nitroaldol reaction.[199] Importantly, results from Weck *et al.* noted that while the tandem reaction occurs when two catalysts are immobilized on different micellar particles, particles that contain both catalysts give significantly better results.[198]

More recently, using polymer assembly as a method for compartmentalization has been demonstrating using polymerosomes.[193,197] Assembled with hydrophilic and hydrophobic di- or tri-block copolymers, polymersomes form membranes with a hydrophobic wall, and often aqueous solution
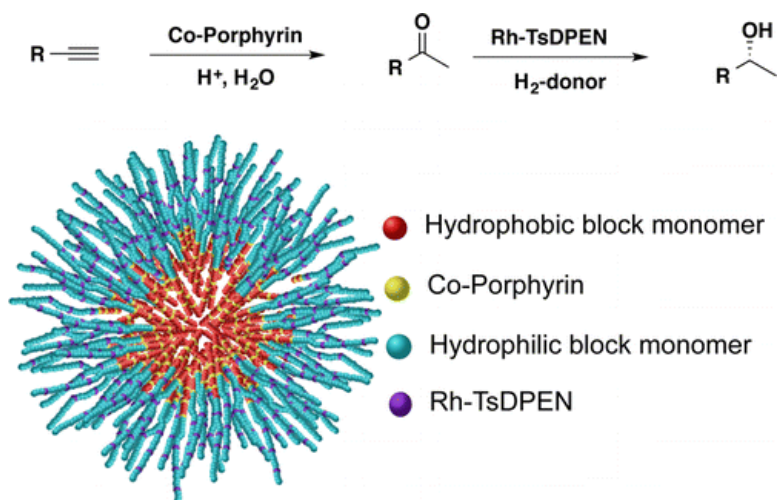
Figure 5.4: Schematic of cross-linked core-shell micelle for cascade reaction. The micelle core and shell provide different microenvironments for the transformations: Co-catalyzed hydration of an alkyne proceeds in the hydrophobic core, while the Rh-catalyzed asymmetric transfer hydrogenation of the intermediate ketone into a chiral alcohol occurs in the hydrophilic shell. Reproduced from Lu *et al.*[198]

at the core.[216,217] Polymersomes are attractive assembles due to their similarity to natural lipid vesicles and ability to encapsulate biologically relevant materials, such as enzymes. In a particularly elegant example, van Dongen *et al.* demonstrated a three-enzyme cascade reaction by spatially segregating enzymes to three different areas of a polymersome: the lumen, in the bilayer membrane, and coupled to the surface (Fig. 5.5).[197]

Despite the promise of these spatially separated systems, there are some drawbacks as well. In the polymersomes and core-shell micellar systems, diffusion of the substrate or the products through the membrane can limit the activity and overall turnover of the system. The necessary diffusivity between the two compartments also limits the lifetime of highly active intermediates. By increasing the interfacial surface area between the two catalytic functions, it would be easier for reactants to transfer between phases for reactions and therefore increase the percent yield of the cascade product.
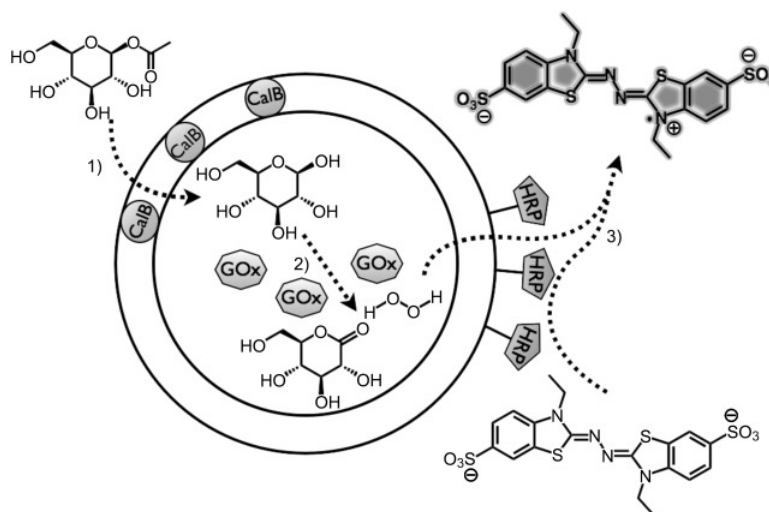
Figure 5.5: Schematic of porous polymersomes based on block copolymers of isocyanopeptides and styrene used to anchor enzymes at three different locations, namely, in their lumen (glucose oxidase, GOx), in their bilayer membrane (*Candida Antarctica* lipase B, CalB) and on their surface (horseradish peroxidase, HRP). Reproduced from van Dongen *et al.*[197]

PROPOSED RESEARCH

Synthesis

Of utmost importance is the choice of catalyst and block copolymer system. For the sake of ease in materials synthesis and reaction characterization, we use the prototypical acid and base "wolf and lamb" system. Together in solution, acidic and basic catalysts will neutralize each other, destroying the catalytic activity. Acid-catalyzed deacetalization of benzaldehyde dimethyl acetal is common as a first cascade step,[204,213,218] as the resulting aldehyde is susceptible to a number of nucleophilic attacks. Sulfonic acid catalysts such as *p*-toluenesulfonic acid are typically used, although free carboxylic acids have also been shown to perform the catalytic transformation.[199] From the reactive aldehyde species, a number of other transformations can be done using basic conditions, in particular, aldol-like reactions including the Henry condensation, Baylis-Hillman reaction, and the Knoevenagel condensation, depending on the other reactants present in solution (Fig. 5.6).[204,206,213] These basic reactions can be catalyzed by primary amine-containing species like tris(2-aminoethyl)amine (TREN), piperidines, or pyridine species. For ease of characterization, we will use the Knoevenagel
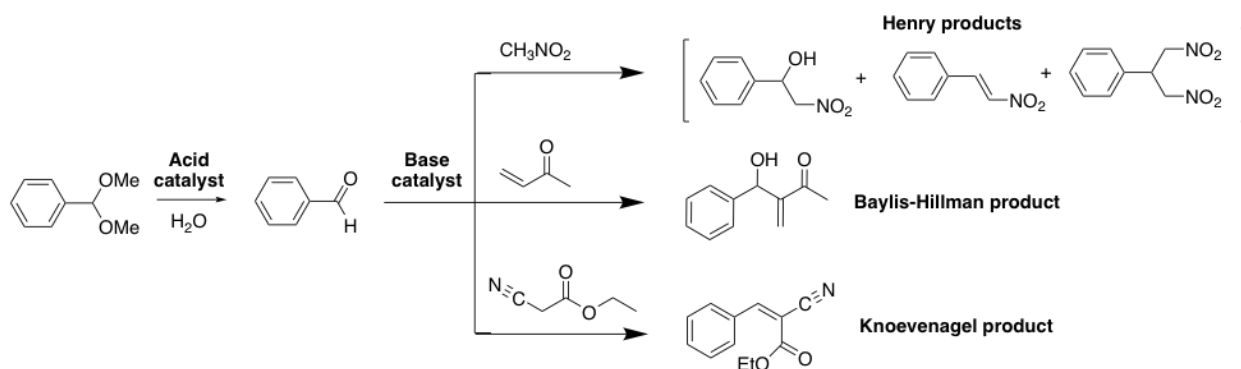
Figure 5.6: Schematic of possible acid-base cascade reactions starting with benzaldehyde demethyl acetal precursor.

condensation, as it produces a single product that has the potential for an extended pi conjugation system, both of which will make characterization of the reaction easier.

Poly(styrene) is one of the most extensively studied polymer systems, and its structural similarity to the acidic poly(styrenesulfonic acid) can be used for the facile incorporation of acidic sulfonic acid catalysts into this hydrophobic polymer block. In addition, the phase behavior in block copolymers with various other polymers have been studied. These include poly(2-vinylpyridine),[219] poly(4-vinylpyridine),[220] poly(isoprene),[221] and poly(ethylene oxide),[222,223] among others. Using a vinylpyridine polymer (either 2-vinylpyridine or 4-vinylpyridine) gives obvious benefits for our desired catalytic cascade, as the pendant pyridine moieties can be directly used as basic sites to facilitate the Knoevenagel condensation. In addition, the poly(styrene-b-2-vinylpyridine) creates a rational increase in polarity from the styrene block that will promote the transfer of the more hydrophilic aldehyde species into the hydrophilic pyridine phase.

Based on work by Schulz and Ishizu, it known that for both monomers, ordered microdomain structures such as lamellae, hexagonally perforated layers, bicontinuous cubic/gyroid, and hexagonally packed cylinders can be formed depending on the volume ratio of styrene to vinylpyridine.[219,220]

We propose the synthesis of a series of block copolymers using a two-step anionic polymerization with varying styrene content between 40-70% in 5-10 mol% increments (Fig. 5.7. These ratios
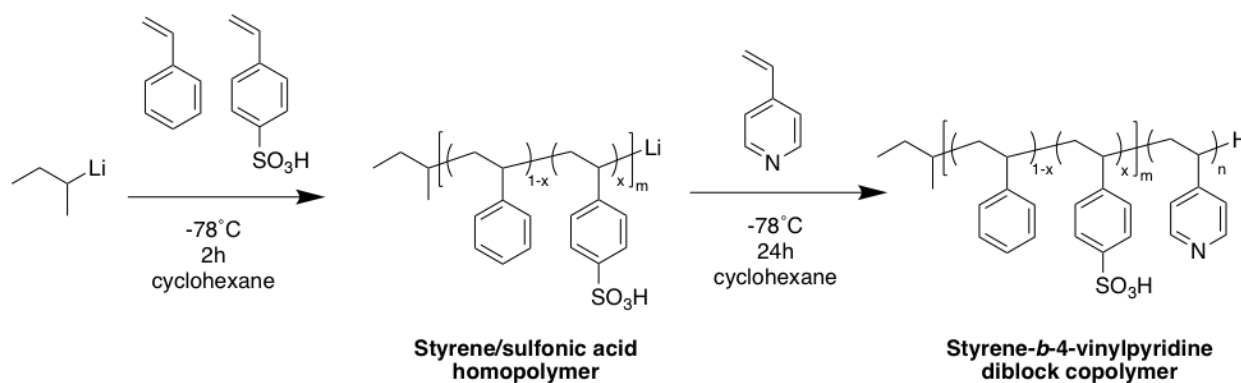
Figure 5.7: Scheme of synthetic route to the synthesis of poly(styrene-*b*-4-vinylpyridine) diblock copolymer incorporating styrene sulfonic acid as catalyst using anionic polymerization.

are in accordance with those found previously to form interesting mesophase separations.[219] In each case, a portion of the styrene monomer will be substituted for styrenesulfonic acid, which will statistically incorporate within the styrene block and act as the acidic catalyst for deacetalization reactions.

The reaction can be monitored by both GPC, NMR, and FTIR during the synthesis of each block. In GPC, we would expect to see a narrow, monomodal distribution at each step, with significantly increased molecular weight after addition of the 4-vinylpyridine block (Fig. 5.8a). The extent of conversion and quantification of the vinylpyridine incorporation can be done using ^{1}H NMR spectroscopy. Further quantification of the ratio of styrene to vinylpyridine can be done using FTIR spectroscopy, as the benzene ring of styrene will have distinct absorptions from the pyridine ring (1030 cm^{-1} vs 980 cm^{-1}).[220] Using these methods and by modifying the monomer ratios, we can create a series of well-characterized block copolymers with varying polymer compositions.

While a high catalyst loading is desired for a high activity, the nature of the PVP block means that the number of basic sites cannot be tuned. This could be changed by changing the second block of the polymer to a monomer that would not be catalytically active, but could have amine functionality doped in through random copolymerization of vinylpyridine or other amine-containing monomers. Another approach could be using a block such as poly(isoprene), which has as a pendant vinyl group. This would allow the attachment of any number of catalysts through facile thiol-ene
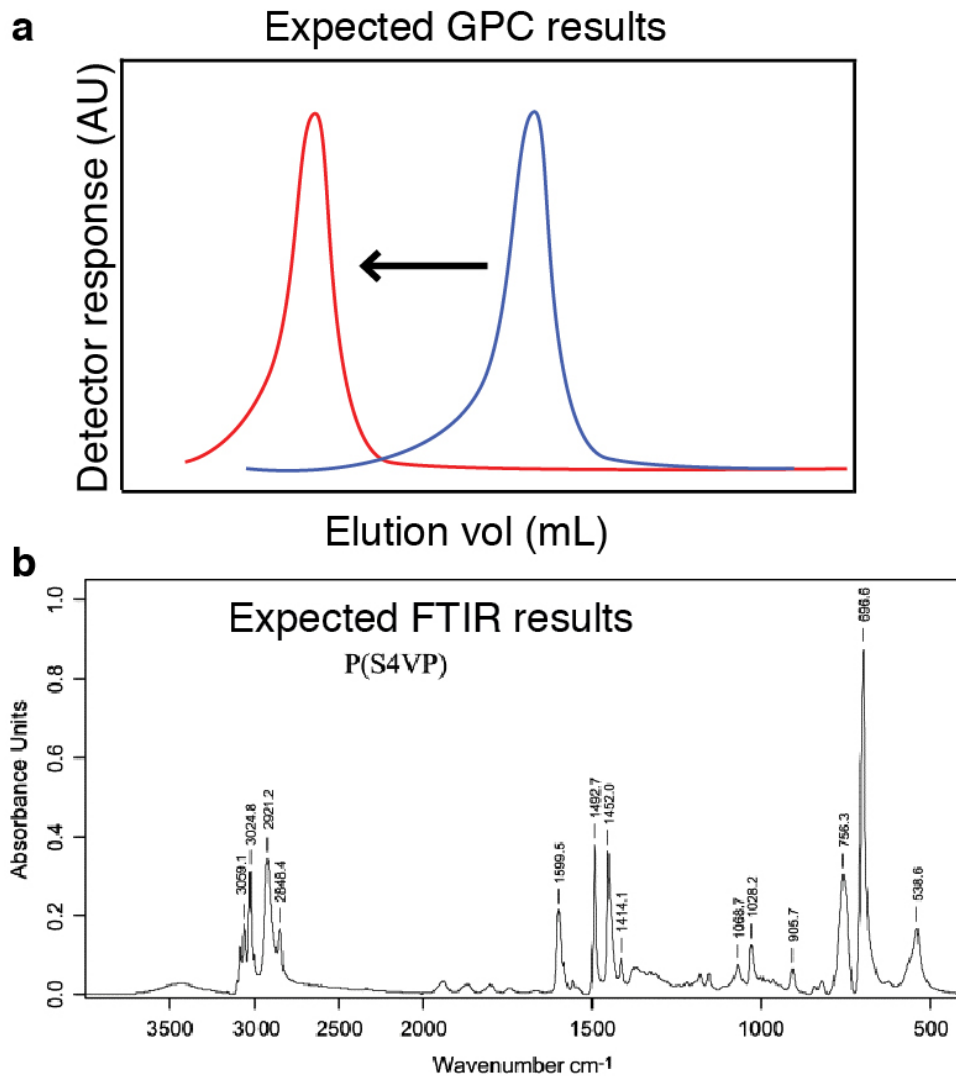
Figure 5.8: (a) Expected GPC traces for the styrene homopolymer and diblock copolymer. (b) Expected FTIR spectrum of poly(styrene-*b*-4-vinylpyridine) diblock copolymer. FTIR reproduced from Eichhorn *et al.*[224]

click chemistry.[225] However, this approach was not used for the initial design as the isoprene is quite hydrophobic, and we did not want its hydrophobicity to hinder diffusion within the system. The pendant vinyl groups may also pose the possibility of unwanted side reactions; those may need to be modified to be more inert after functionalization.

Block copolymer self-assembly

The next step is to look at the formation of block copolymer morphlogies. Block copolymer self-assembly is traditionally done through the slow concentration of polymer from a solvent that can dissolve both blocks (such as THF, chloroform, or trichloroethane) either through evaporation, or through the slow addition of a poor solvent (such as methanol). By screening solvent conditions as well as the library of different polymer compositions, it is likely that we will create multiple polymer phases to examine. The most interesting of these morphologies would be bicontinuous or gyroidal phases, as these would have the highest interfacial surface area to promote diffusion of the reactants to the next catalyst in the cascade. These can be characterized through microscopic techniques such as TEM and SEM, where one phase can be selectively stained for visualization purposes (Fig. 5.9). For packings that we expect to have a high degree of translational order, such as cubic or hexagonal cylinder phases, small-angle X-ray scattering can also give information about the molecular packing.

It is also important to confirm that the small molecule substrates do not affect the morphologies. Therefore, these phase segregation tests should take place with a catalytically relevant amount of
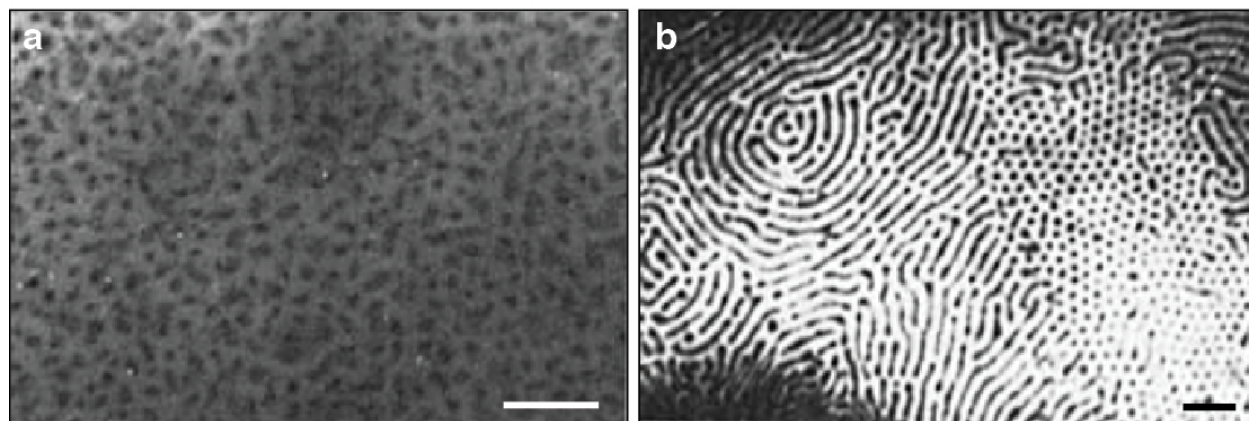
Figure 5.9: Expected TEM micrograph of (a) block copolymer morphology of polymer containing 30 mol% vinylpyridine cast from trichloroethane. (b) Block copolymer morphology of polymer containing 50 mol% vinylpyridine cast from trichloroethane. Scale bars are 2 μm. Modified from Ishizu *et al.*[220]

benzaldehyde dimethyl acetal and ethyl cyanoacetate. It is expected that with a small amount of reagent (as compared to the polymeric scaffold) the overall morphologies would not be affected. The small molecules may even have a beneficial effect, effectively acting as plasticizer in the system that could be beneficial for diffusion.

After examining the microphase separation of the block copolymer, it may be beneficial to increase the size of the polymerdomains. This could be done by adding a small amount of homopolymer for each of the desired polymer blocks, which, in small amounts will expand the domain size while maintaining the high interfacial surface area.[226] If this incorporation induces too much local curvature and therefore changes in phase, there are alternative options. This could also be done by increasing the overall block copolymer molecular weight while keeping the styrene to vinylpyridine ratio constant; this should result in larger domain but maintain the same overall morphology.

Monitoring the cascade reaction

After the block copolymer materials have been synthesized and well-characterized, their catalytic activity must be measured. As a comparison, the reactivity of this tandem system can be compared to control reactions of 1) Free molecular catalyst (*p*-toluenesulfonic acid and pyridine) dissolved in solution, 2) physically mixed, cross-linked particles of homopolymers, and 3) core-shell micelles of diblock copolymer.

The more difficult part of this process will be accurately sampling the reaction. The ideal method would be a non-destructive *in situ* sampling method, which can monitor each reaction species as they are formed. This could be done through the careful selection of reactive components; the Knoevenagel product ethyl benzylidenecyanoacetate is known to have an absorption maximum around 300 nm. If the UV-Vis methods do not work, we can also turn to more conventional, although sample destructive methods. At various reaction timepoints, parallel samples can be quenched by rapid immersion into a poor solvent for both polymer blocks. Then, one phase can be selectively swelled to release the reagents from that particular block. Aliquots from this sample can then be characterized
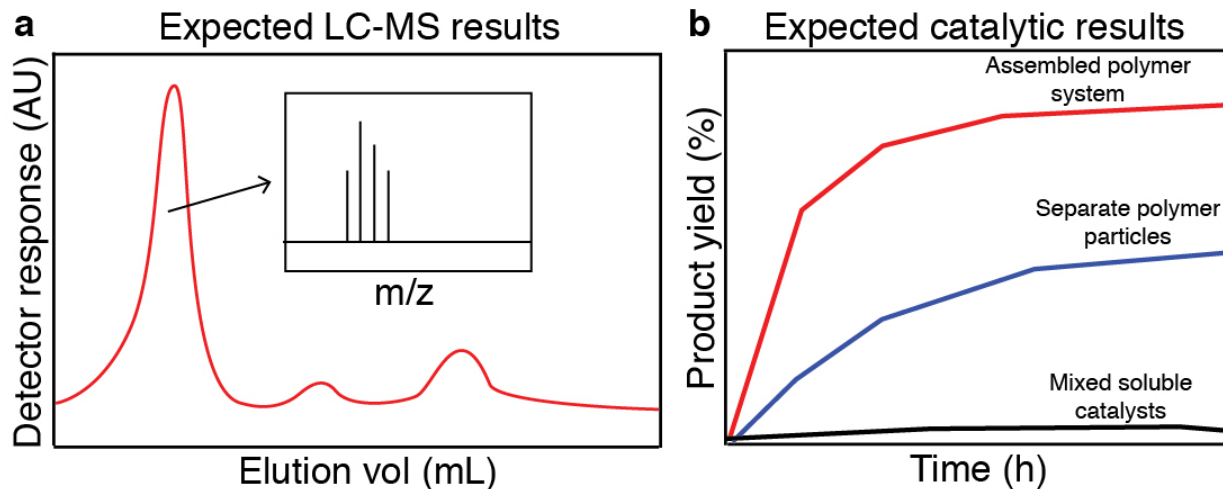
Figure 5.10: (a) Expected example LC-MS trace for a reaction aliquot. (b) Expected comparison of reaction yield between phase-separated copolymer system and control reactions of separate particles and soluble catalysts.

by liquid or gas-phase chromatography coupled with mass spectrometry (LC-MS or GC-MS). This method will give both identity and quantification of the concentrationw of reagents and products at any given time (Fig. 5.10a). From this information, we can determine the catalytic performance of our polymeric reactor as compared to the control reactions described above (Fig. 5.10b).

It is possible that selective swelling of the blocks is not enough to fully release the small molecule reactants and products, which would prove problematic for accurate sampling. If this is the case, instead of swelling, the entire system could be dissolved in a solvent such as THF, which would then require the sampling of the entire mixture at once. This could be more difficult to deconvolute, but because we are using established and well-known catalytic reactions, could be done with the use of proper standards.

One potential pitfall is that diffusion of the small molecules through the polymer mesophase may be too slow, due to the crowded nature of the bulk polymer phase. It is expected that the presence of the small molecules and solvent needed for the catalytic reaction will somewhat plasticize the polymers, allowing for better diffusion. However, this may not be enough. In that case, we could induce mesoscale porosity into the system while still maintaining the order within the poly-
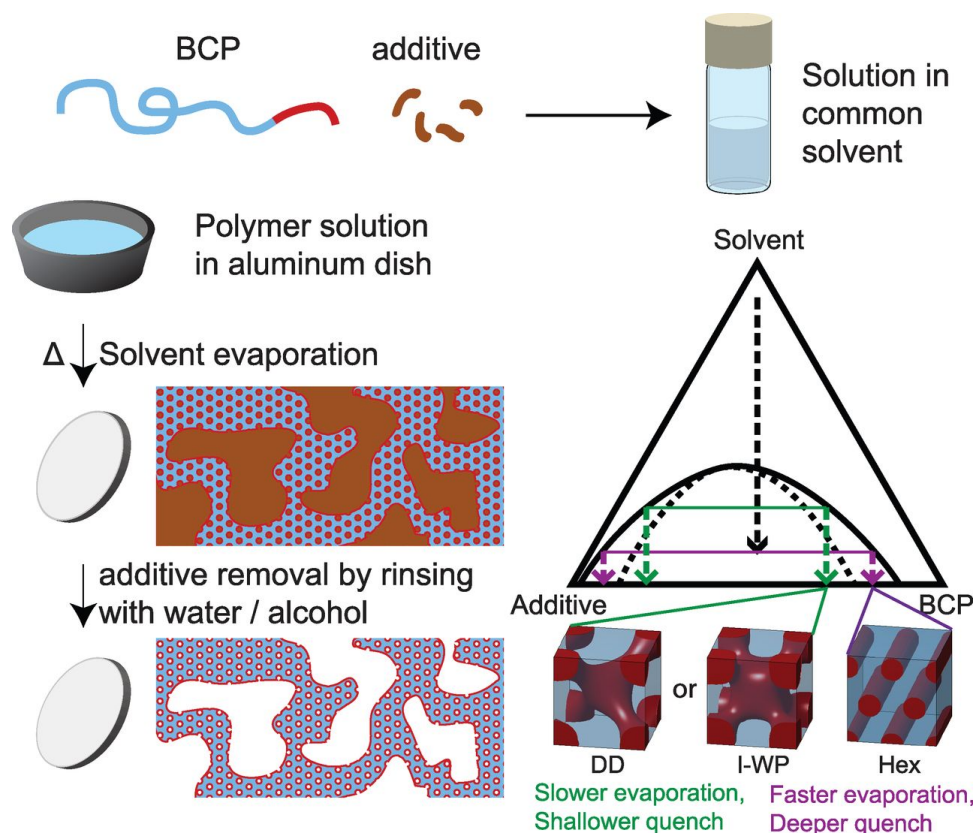
Figure 5.11: Synthesis of hierarchically porous polymer scaffolds with ordered mesostructure using removable additive to create pores. Reproduced from Sai *et al.*[223]

mer phase through the spinodal decomposition of the polymer blend with an additive that could be selectively washed out (Fig. 5.11).[223] This would maintain the high interfacial surface area for the intermediates to transfer between polymer phases, but also have mesoscale porosity for the reactants to diffuse more freely and thus increase reaction rates.

SUMMARY AND CONCLUSIONS

In this work, we propose the development of a catalytic cascade system based on the spatial confinement of two incompatible acid-base catalysts (a "wolf and lamb" system) onto to separate portions of a block copolymer system based on the phase separation of poly(styrene-*b*-4-vinylpyridine). While these cascade reactions have been demonstrated in dispersed core-shell micelles and polymer-

somes, no one has explored this behavior in more interesting and complex polymer phase assemblies. We believe using these bicontinuous phases will promote more efficient diffusion of reactants between the different catalysts due to their high interfacial surface area, and therefore an increase in reaction rate and bias towards the final cascade product. We detail the synthetic plan for the creation of the catalyst-modified polymers, block copolymer self-assembly, and reaction monitoring, as well as how to address potential pitfalls at each step.

STACEY CHIN

425.681.8024 | 1000 Main Street, Apt. 3F. Evanston, IL 60202 | stacey.chin@u.northwestern.edu

EDUCATION

Ph.D. in Chemistry | Northwestern University, Evanston IL   March 2019
  GPA: 3.81/4.0 | Adviser: Samuel I. Stupp
  Thesis: "Control of Hierarchical Order and Development of Stimuli-Responsive Self-Assembled
      Materials across Multiple Length Scales"
  National Science Foundation Graduate Research Fellow (2012–2015)

B.S. in Chemistry (Biology minor) **| Carnegie Mellon University**, Pittsburgh, PA   May 2013
  GPA: 3.68/4.0 | Dean's List (Fall 2009 – Spring 2013)

RESEARCH EXPERIENCE

Northwestern University Department of Chemistry, Evanston, IL   Sept. 2013 – Present
Ph.D. Candidate | Graduate Researcher | Teaching Assistant
- Completed advanced coursework and performed interdisciplinary research in the lab of Prof. Samuel I. Stupp.
- Led research project on developing hybrid peptide amphiphile-polymer materials as artificial actuators for soft robotics applications, including synthesis and materials characterization (TEM/SEM, SAXS, confocal microscopy, mechanical testing); resulted in first-author publication in *Nature Communications*.
- Investigated liquid crystalline behavior or self-assembled peptide under annealing conditions, including peptide synthesis and extensive variable temperature studies (confocal/polarized optical microscopy, SAXS, DSC).
- Synthesized, purified, and analyzed peptide-based materials for regenerative tissue scaffolds, including conjugation of fluorophores and small molecules for enhanced binding or controlled release properties.
- Fostered and maintained 5 collaborations within DOE-funded Center for Bio-Inspired Energy Science across multiple universities and national labs. Supervised and mentored two undergraduate students.
- Contributed writing to successfully funded grants and grant renewals from DOE and NIH.
- Attended ComSciCon Chicago, a workshop on improving scientific communication skills, particularly towards non-technical audiences (Aug. 2018)
- Teaching assistant for 5 undergraduate and graduate-level chemistry courses (90+ students).

Carnegie Mellon University Department of Chemistry, Pittsburgh, PA   Jan. 2011 – May 2013
Undergraduate Researcher | Teaching Assistant | Course Developer
- Synthesized and characterized stimuli-responsive multi-block copolymers using ATRP and RAFT polymerization in the lab of Prof. Krzysztof Matyjaszewski, resulting in first-author publication.
- Sole undergraduate TA in team of 10 graduate students for 200-level organic lab course (100+ students).
- One of two undergraduate students that aided in development of new bioorganic lab course (09-323), developing modular synthesis of caffeine analogues and writing course materials.

Virginia Tech Department of Chemistry, Blacksburg, VA   June 2012 – Aug. 2012
Undergraduate Researcher, Research Education for Undergraduates (REU) program
- Member of NSF-funded REU program, synthesized and characterized polymers with anti-HIV microbicide activity in the lab of Prof. Richard Turner, resulting in authorship in a peer-reviewed journal article.

AWARDS & HONORS

- 2nd place, Simpson-Querrey Institute Scientific Image Contest   October 2018
- Northwestern TGS Conference Travel Award   April 2018
- Center for Bio-Inspired Energy Science Conference Travel Award   December 2017, May 2018
- National Science Foundation Graduate Research Fellowship   June 2015 – June 2018
- Allen S. Hussey Award for Excellence in 200-Level Teaching   June 2013
- Carnegie Mellon University Dean's List   Fall 2009 – Spring 2013
- Carnegie Mellon University Chemistry Departmental Award for Seniors   Spring 2013
- ACS Undergraduate Analytic Chemistry Division Award   Spring 2012

STACEY CHIN

PROFESSIONAL EXPERIENCE & LEADERSHIP

Department of Energy Early Career Network, Evanston, IL   Jan. 2017 – Dec. 2018
Center for Bio-inspired Energy Science Representative
- Led group of 12 students and post-docs from multiple universities to plan Diversity in Energy Science panel at biannual Energy Frontiers Research Center meeting in Washington D.C. (August 2017).
- Co-led 2017 panel discussion of four academic and industry scientists on diversity topics (attendance: 200+).
- Planned June 2018 webinar on best practices and resources available to promote diversity and inclusion in energy sciences as member of Diversity and Inclusion Committee.

Research Safety Student Initiative, Evanston, IL   Dec. 2017 – June 2018
Communications Coordinator
- Led marketing campaign for first annual Safety Awareness Week (Feb. 2018), including developing promotional posters and print collateral for kickoff event (attendance: 100).
- Liaison for 6 STEM departments; coordinated event promotion through email, print, and social media.

The Tartan **Student Newspaper**, Pittsburgh, PA   Jan. 2010 – May 2012
Layout Manager | Contributing Editor
- Oversaw design and layout of 32-page weekly paper (Distribution: 6,000) using Adobe InDesign.
- Managed and delegated responsibilities among layout staff of 10 volunteers; collaborated with editorial staff to determine newspaper content, style, and governance.
- Copy-edited articles for content, clarity, and adherence to Associated Press and internal style guide.

Net Impact, San Francisco, CA   June 2011 – Aug. 2011
Program Fellow, Publications
- Managed editorial content, design, and print process of 350-page *Business as UNusual* guide (Distribution: 4,000) using Adobe InDesign. Led marketing campaign, creating media kit and emailing 2000+ contacts.

SKILLS & TECHNICAL PROFICIENCY

Techniques: **Synthesis:** small molecule, polymeric, solid-phase peptide synthesis, Schlenk technique.
Characterization: High-performance liquid chromatography (HPLC), gel permeation chromatography (GPC), X-ray scattering (USAXS, SAXS, MAXS, WAXS), dynamic/static light scattering (DLS/SLS), differential scanning calorimetry (DSC), tensile testing.
Spectroscopy: Nuclear magnetic resonance (NMR), mass spectrometry (MS), UV-visible, fluorescence, Fourier transform infrared spectroscopy (FT-IR), circular dichroism (CD)
Microscopy: Transmission electron microscopy (TEM), Cryogenic-TEM, laser-scanning confocal microscopy (CLSM), optical and polarized optical microscopy (POM).
Biological: Bacterial culture, phage display, ELISA assays

Software: Windows, Mac OS, Microsoft Office Suite, G Suite Applications, Adobe Creative Suite (Photoshop, Illustrator, InDesign), Cinema 4D, ChemBioDraw, IGOR, Mathematica, Fit2D, ImageJ/FIJI.

Other: Copy-editing, print production (newspaper, print collateral), photography.

OTHER INVOLVEMENT
- Carnegie Mellon Admission Council, Alumni volunteer interviewer   Aug. 2013 – Present
- Graduates Mentoring Undergraduates, Graduate Student mentor   Jan. 2018 – Present
- Volunteering Untapped, Volunteer Team Leader   Apr. 2017 – Nov. 2018
- Science in the Classroom Outreach Program, Team Leader   Sept. 2014 – June 2018
- CHEMUnity Mentorship Program, Mentor   Sept. 2017 – June 2018

STACEY CHIN

PUBLICATIONS (*Indicates equal contribution)

- Udumula, V.R.; **Chin, S.M.;** Picco, A.; Iriart, C.H.; Kirkpatrick, S.; Zaldivar, G. Tagliazucchi, M.; Stupp, S.I. Conda-Sheridan, M. When medicinal chemistry meets materials science: isostere replacements in peptide amphiphiles. *In preparation.*
- Edelbrock, A.N.; **Chin, S.M.;** Stupp, S.I. Host-guest interactions as a supramolecular cross-link between peptide amphiphile assemblies. *In preparation.*
- **Chin, S.M.*;** Wek, K.*; Stupp, S.I. Extrusion printing of a nanocrystalline cellulose composite within a thermoresponsive supramolecular-covalent hybrid material for mechanical stability. *In preparation.*
- **Chin, S.M.***; Sai, H.*; Qiao, B.; Olvera de la Cruz, M.; Stupp, S.I. Liquid crystalline phases of peptide amphiphile assemblies. *In preparation.*
- Sai, H.*; Lau, G.*; Dannenhoffer, A.; **Chin, S.M.;** Stupp, S.I. In-situ observation of supramolecular assembly dynamics through variable temperature confocal laser scanning microscopy. *In preparation.*
- Ifergan, I.; Xu, D.; Synatchke, C.V.; **Chin, S.M.;** Terry, R.; Stupp, S.I.; Miller, S.D. Regulation of Myeloid Cells Function by Nanoparticles. *In preparation.*

- Peters, E.B.; Tsihilis, N.D.; Karver, M.R.; **Chin, S.M.;** Musetti, B.; Ledford, B.T.; Stupp, S.I.; Kibbe, M.R. Atheroma Niche-Responsive Nanocarriers for Immunotherapeutic Delivery. *Advanced Healthcare Materials* **2019**, 1801545.
- Edelbrock, A.N.; Álvarez, Z.; Simkin, D.; Fyrner, T.; **Chin, S.M.;** Sato, K.; Kiskinis, E.; Stupp, S.I. Supramolecular Nanostructure Activates TrkB Receptor Signaling of Neuronal Cells by Mimicking Brain-Derived Neurotrophic Factor. *Nano Letters* **2018**, 18(10) 6237-6347.
- **Chin S.M.***; Synatschke, C.V.*; Liu, S.; Nap, R.J.; Sather, N.A.; Wang, Q.; Álvarez, Z.; Edelbrock, A.N.; Fyrner, T.; Palmer, L.C.; Szleifer, I.; Olvera de la Cruz, M.; Stupp, S.I. Covalent-supramolecular hybrid polymers as muscle-inspired anisotropic actuators. *Nature Communications* **2018**, 9, 2395.
- Savage, A. M.; Ullrich, E.; **Chin, S. M.**; Kiernan, Z.; Kost, C.; Turner, S. R. Synthesis and characterization of double hydrophilic block copolymers containing semi-rigid and flexible segments. *Journal of Polymer Science Part A: Polymer Chemistry* **2015**, *53* (2), 219-227.
- **Chin, S. M.**; He, H.; Konkolewicz, D.; Matyjaszewski, K. Synthesis of triblock and multiblock methacrylate polymers and self-assembly of stimuli responsive triblock polymers. *Journal of Polymer Science Part A: Polymer Chemistry* **2014,** *52* (17), 2548-2555.

ORAL PRESENTATIONS

- **Chin, S.M.** Thermoresponsive Self-Assembled Materials Across Multiple Length Scales. Invited alumni presentation at Carnegie Mellon University Undergraduate Chemistry Seminar, Pittsburgh, PA. Oct. 5, 2018.
- **Chin, S.M.** Liquid Crystalline Behavior of Supramolecular Peptide Assemblies. Invited presentation, Max Planck Institute for Polymer Research, Mainz, Germany. June 21, 2018.
- **Chin, S.M.**; Synatschke, C.V.; Stupp, S.I. Macroscopic Anisotropic Actuation in Muscle-Inspired Polymer-Supramolecular Hybrid Materials. Presented at the 2017 Fall Meeting of the Materials Research Society, Boston, MA, November 29–December 1, 2017; Oral Presentation BM12.05.04.
- **Chin, S.M.** Supramolecular-Covalent Hybrid Polymers as Anisotropic Actuators. Oral presentation at the 2016 Center for Bio-Inspired Energy Sciences annual meeting, Evanston, IL, August 12, 2016.

POSTER PRESENTATIONS

- **Chin, S.M.;** Synatschke, C.V.; Stupp, S.I. Directing Macroscale Actuation of Hybrid Supramolecular-Covalent Polymer Materials using Alignment of Self-Assembled Nanofibers. Presented at the 2018 Bio-Inspired Materials Gordon Research Conference, Les Diablerets, Switzerland, June 23-29, 2018; Poster 23.
- **Chin, S.M.**; Synatschke, C.V.; Liu, S.; Nap, R.; Olvera, M.; Stupp, S.I. Anisotropic actuation in gels of aligned supramolecular-covalent hybrids. Presented at the 252nd National Meeting of the American Chemical Society, Philadelphia, PA, August 21–25, 2016; Poster POLY 408.